Titre: Title:	Numerical and Theoretical Study of Shot Peening and Stress Peen Forming Process
Auteur: Author:	Hong Yan Miao
Date:	2010
Type:	Mémoire ou thèse / Dissertation or Thesis
Référence: Citation:	Miao, H. Y. (2010). Numerical and Theoretical Study of Shot Peening and Stress Peen Forming Process [Thèse de doctorat, École Polytechnique de Montréal]. PolyPublie. https://publications.polymtl.ca/347/

UNIVERSITÉ DE MONTRÉAL

NUMERICAL AND THEORETICAL STUDY OF SHOT PEENING AND STRESS PEEN FORMING PROCESS

HONG YAN MIAO

DÉPARTEMENT DE GÉNIE MÉCANIQUE

ÉCOLE POLYTECHNIQUE DE MONTRÉAL

THÈSE PRESENTÉ EN VUE DE L'OBTENTION

DU DIPLÔME DE PHILOSOPHIAE DOCTOR (Ph.D.)

(GÉNIE MECANIQUE)

JUIN 2010

UNIVERSITÉ DE MONTRÉAL

ÉCOLE POLYTECHNIQUE DE MONTRÉAL

Cette thèse intitulée:

NUMERICAL AND THEORETICAL STUDY OF SHOT PEENING AND STRESS PEEN FORMING PROCESS

présentée par : MIAO Hong Yan

en vue de l'obtention du diplôme de : Philosophiae Doctor

a été dûment accepté par le jury d'examen constitué de :

M. VADEAN Aurelian, Doct., président

M. LÉVESQUE Martin, Ph.D., membre et directeur de recherche

M. PERRON Claude, M.Sc.A, codirecteur de recherche

Mme. ROSS Annie, Ph.D., membre

M. GUAGLIANO Mario, Ing., membre

DEDICATION

To my husband Jiang and my newborn son Michael

ACKNOWLEDGEMENTS

I would like to express my gratitude to my two co-supervisors, Prof. Martin Leveque and Mr. Claude Perron, for their supervision, advice, and guidance, from the early stage of this research, as well as providing me with extraordinary experiences throughout the work. I also thank the members of my graduate committee for their guidance and suggestions.

I acknowledge Aerospace Manufacturing Technology Center (AMTC) of the National Research Center Canada for financial support for this project. I would like to thank all of the employees at the National Research Center who gave me their kind support.

I would especially like to thank Simon Larose at AMTC for his advice and his willingness to share his bright ideas with me, which proved very fruitful and helped me to shape my ideas and research. Thanks again to him for his help in translation process of "Résumé" and "Condensé en français".

I would like also to express my thanks to Yves Fortin at AMTC for his support in the design of the robot program used in my shot peening experiments.

I wish to thank Alexandre Gariepy at École Polytechnique de Montréal for his helpful advice during my research project. My thanks also go to Dave Demers, École Polytechnique de Montréal for his help with my experiments during my pregnancy.

I wish to thank my parents for their encouragement and support over the past years. Finally, I would like to thank my husband, Jiang Guo, for supporting and encouraging me to pursue this degree.

RÉSUMÉ

Le grenaillage de précontrainte est un procédé d'écrouissage largement utilisé dans les industries aérospatiale et automobile pour améliorer la résistance à la fatigue de composants métalliques et ainsi prolonger leur durée de vie utile. La performance et la répétabilité de cette amélioration dépendent largement des paramètres de grenaillage, tels que l'intensité Almen, le taux de recouvrement, la durée du traitement de grenaillage, etc. La méthode d'analyse par éléments finis a été adoptée pour simuler le procédé de grenaillage en raison du développement de plus en plus poussé des méthodes numériques et de l'augmentation des ressources et capacités informatiques disponibles. La plupart des modèles par éléments finis du procédé de grenaillage, tels que les modèles 2D ou les modèles à impact unique, ne peuvent représenter adéquatement ce procédé qui implique un grand nombre d'impacts de billes distribuées de façon aléatoire. Par conséquent, un des objectifs principaux de cette étude a été de développer un modèle 3D capable de simuler ce procédé aléatoire, et d'utiliser ce nouveau modèle afin d'étudier de façon quantitative les relations entre les paramètres de grenaillage et les résultats de ce traitement.

La mise en forme par grenaillage avec application d'un pré-chargement externe est une utilisation particulière du grenaillage de précontrainte lors de la fabrication de composantes à paroi mince. Ce procédé est largement utilisé dans l'industrie aéronautique afin de produire des composantes minces avec des formes géométriques complexes, telles que des revêtements de voilure. La plupart des études publiées portant sur ce procédé consistent en des études expérimentales d'essais et erreurs. Par conséquent, un autre objectif de cette étude a été de développer un modèle numérique afin de simuler ce procédé, et d'investiguer quantitativement les relations entre les conditions de pré-chargement (moment de flexion ou force en tension appliquée) et la forme résultante (flèche maximale résultante ou rayon de courbure).

Un nouveau modèle 3D par éléments finis capable de simuler les impacts de billes distribués de façon aléatoire a été développé afin de simuler de façon dynamique le grenaillage de précontrainte. En utilisant ce modèle aléatoire, des relations quantitatives ont été établies entre l'intensité du jet de billes, le taux de recouvrement, la rugosité induite et le nombre d'impacts, pour une composante en aluminium 2024. Les résultats de simulation montrent que ce nouveau modèle par éléments finis aide à bien comprendre le procédé et permet de mieux prédire les

résultats du grenaillage de précontrainte que les simulations par éléments finis conventionnelles du procédé.

Une étude expérimentale du grenaillage de précontrainte et de la mise en forme par grenaillage avec pré-chargement externe a été conduite afin de valider le nouveau modèle. Les expériences de grenaillage de précontrainte ont permis d'établir des relations quantitatives entre la saturation de la couche superficielle traitée, le taux de recouvrement, la rugosité et le temps de grenaillage pour des éprouvettes en aluminium 2024. Un dispositif de pré-chargement a été conçu pour appliquer des moments en flexion sur les éprouvettes soumises à des tests de mise en forme par grenaillage. La principale conclusion de ces derniers tests de grenaillage est que la flèche induite par le procédé dans la direction d'un pré-chargement en flexion croît avec l'augmentation du moment externe appliqué.

Un modèle par éléments finis en trois étapes (implicite, explicite et explicite) a été développé afin de simuler le procédé de mise en forme par grenaillage avec pré-chargement. Tout d'abord, un calcul implicite a été effectué afin d'obtenir la distribution de contraintes initiale résultant du moment appliqué par le dispositif de pré-chargement. Ensuite, un calcul explicite a été utilisé pour obtenir les contraintes induites par le grenaillage avec pré-chargement. Finalement, un calcul implicite sur un modèle élargi a permis de calculer la flèche induite et le rayon de courbure de la pièce traitée. Ce modèle par éléments finis en trois étapes est le premier modèle permettant de simuler le procédé de mise en forme par grenaillage avec pré-chargement. Il constitue un outil très utile pour contrôler et prédire les résultats du procédé.

Un modèle analytique a également été développé afin d'étudier le procédé de grenaillage et de prédire l'intensité Almen avec utilisation réduite de puissance de calcul. L'utilisation de ce modèle analytique a permis de montrer que différentes combinaisons de paramètres de grenaillage (diamètre de billes et vitesse) peuvent donner une même intensité Almen, tout en générant des profils de contraintes résiduelles différents. Il est par conséquent important de sélectionner différents combinaisons de paramètres, et d'investiguer leur influence sur les résultats du grenaillage.

Des méthodes numériques, expérimentales et analytiques ont été utilisées pour étudier les procédés de grenaillage de précontrainte et de mise en forme par grenaillage avec pré-chargement. Avec l'aide du nouveau modèle par éléments finis développé dans le cadre de cette

étude, l'intensité du jet de billes, la saturation des couches traitées, le taux de recouvrement et la rugosité peuvent être étudiés en détail. Ce nouveau modèle constitue donc un outil pratique pour les concepteurs afin de guider leurs choix de paramètres optimaux de grenaillage. De plus, le nouveau modèle de mise en forme par grenaillage avec pré-chargement constitue un outil unique pour prédire et optimiser ce procédé. Finalement, le modèle analytique du procédé de grenaillage offre un outil simple pour prédire l'intensité Almen en fonction des paramètres de grenaillage.

ABSTRACT

Shot peening is a cold working process widely used to improve the fatigue life of metallic components in the aerospace and automobile industries. The performance and repeatability of this improvement depend greatly on the shot peening parameters, such as Almen intensity, surface coverage, peening time, etc. Finite Element Analysis (FEA) has been adopted to simulate the shot peening process based on the development of computer resources and numerical methods. Most of the existing Finite Element (FE) models, however, such as 2D models and one shot impact models, cannot describe numerous randomly distributed shot flow. Therefore, one goal of this study was to establish a 3D shot peening model that can simulate a random shot peening process and to study the quantitative relationship between peening parameters and peening results.

Stress peen forming is a special application of shot peening that deals with thin target components. Stress peen forming has been widely used in the aeronautics industry to produce thin components with complex shapes, such as wing skins. Most studies of the stress peen forming process have been based on trial and error experiments. Therefore, another objective of this study was to develop a numerical model in order to simulate this process, and to investigate the quantitative relationship between the prebending conditions (prebending moment or pre-stress) and the forming results (resulting arc height or radius of curvature).

A novel 3D FE model that describes randomly distributed shots was developed in order to simulate the dynamic shot peening process. Using this 3D random FE model, a quantitative relationship was established between peening intensity, surface coverage and roughness, with respect to the number of shots, based on the same target component, aluminum 2024. The simulated results show that the novel FE model can help us to understand and predict shot peening results better than the existing conventional FE models.

An experimental study of shot peening and stress peen forming was carried out in order to validate the novel FE model. In shot peening experiments, the quantitative relationships between saturation, surface coverage and roughness, with respect to peening time, were established for aluminum 2024 test strips. A pre-stressing device was designed to apply prebending moments on the strip in order to perform stress peen forming. The principal conclusion was that with increasing prebending moment, the deformed arc height following the prebending direction increases.

A three-step implicit-explicit-implicit FE model was developed to simulate the stress peen forming process. Firstly, an implicit FE calculation was performed to acquire the initial stress distribution resulting from the prebending moment. Secondly, an explicit FE calculation was carried out to obtain the induced stress after shot peening. Finally, an implicit FE model was built to calculate the deformed arc height and radius of curvature of the deformed component. The three-step FE model is the first model that simulates the stress peen forming process. It provides a useful tool to predict the results of stress peen forming.

An analytical model was also developed to study the shot peening process and to predict Almen intensity with reduced use of calculation resources. The study of this analytical model showed that although different combinations of shot peening parameters (shot size and velocity) can produce the same Almen intensity, each combination resulted in a different through thickness residual stress distribution. Therefore, it is important to choose different combinations of shot peening parameters, and to investigate their influence on the shot peening results.

Numerical, experimental and analytical methods were employed to study the shot peening and stress peen forming processes. With the help of the newly developed FE model for the simulation of the shot peening process, the shot peening intensity, saturation, surface coverage, and surface roughness can be studied in detail. Therefore, the new FE model provides a useful tool for designers, to guide their choice of the optimal shot peening parameters. In addition, the newly established FE model of stress peen forming provides a useful tool for prediction and optimization of the stress peen forming process. Finally, the analytical model for calculation of the shot peening process offers a simple tool to predict Almen intensity with respect to shot peening parameters.

CONDENSÉ EN FRANÇAIS

Le grenaillage de précontrainte est un procédé d'écrouissage inventé autour de 1930 et largement utilisé depuis les années 1940 dans les industries automobile et aérospatiale pour améliorer la résistance à la fatigue de composants métalliques et ainsi prolonger leur durée de vie utile. Ce procédé consiste à marteler la surface de la pièce traitée à l'aide d'un jet de grenailles (habituellement sphériques) à haute vitesse. Les impacts répétés déforment de façon marquée la surface, générant des déformations plastiques dans la couche superficielle, ce qui induit un champ de contraintes résiduelles compressives à la surface, de même que des contraintes résiduelles en tension à l'intérieur du composant traité. La couche superficielle de contraintes résiduelles compressives réduit la probabilité de rupture prématurée sous conditions de chargement cycliques et augmente par conséquent la résistance à la fatigue du composant.

De multiples paramètres de grenaillage, tels que les caractéristiques des grenailles ou billes (types, taille, matériau), la vitesse, l'angle d'incidence du jet, les propriétés du matériau traité, le temps d'exposition au grenaillage, etc. ont une influence significative sur les résultats du grenaillage. Cependant, en pratique, deux paramètres de contrôle (intensité du grenaillage et taux de recouvrement) sont utilisés afin d'assurer les performances et la répétabilité du procédé. Ces deux paramètres sont souvent les seuls paramètres spécifiés pour le traitement d'un composant.

L'intensité du grenaillage est reliée à l'énergie cinétique (masse des billes et vitesse) transférée du jet de billes à la surface traitée durant le traitement. Durant la décennie 1940-1950, J.O. Almen a développé une procédure normalisée afin de quantifier l'énergie du jet (Almen et Black, 1963). Remarquant que des éprouvettes métalliques minces soumises au grenaillage se retrouvaient déformées en flexion suite au traitement, il a proposé de considérer la flèche d'une éprouvette soumise à un grenaillage pendant un long temps d'exposition (saturation) afin de mesurer de façon indirecte l'énergie du jet de billes incident. La flèche maximale de l'éprouvette normalisée à saturation constitue, par définition, « l'intensité du grenaillage » ou « l'intensité Almen ». La mesure de l'intensité du grenaillage est effectuée par grenaillage successif d'une série d'éprouvettes normalisées en acier SAE1070 laminé à froid. L'efficacité du traitement de grenaillage dépend largement de l'intensité Almen (voir par exemple Fathallah, 1994 et Herzog et al. 1996), ainsi que du taux de recouvrement (Meguid et al. 2002). Le taux de recouvrement est

simplement défini comme étant la fraction de l'aire totale traitée couverte par des indentations, exprimée en pourcentage.

Durant le grenaillage, les impacts répétés de billes à haute vitesse ne génèrent pas uniquement une couche déformée plastiquement accompagnée de contraintes résiduelles en compression, mais ils augmentent également la rugosité de la surface traitée. Une rugosité accrue présente davantage d'irrégularités, lesquelles créent des concentrations de contraintes et par conséquent une réduction de la vie en fatigue de la pièce traitée (Sharp et al. 1994). Par conséquent, l'efficacité du grenaillage dépend d'un délicat compromis entre son effet bénéfique (génération de contraintes résiduelles compressives) et son effet nuisible (rugosité accrue).

Un effet secondaire du grenaillage de précontrainte est qu'il peut induire des changements géométriques significatifs lors du traitement de composants métalliques minces, tel que noté par J.O. Almen. L'équilibre interne de la pièce traitée requiert que les contraintes résiduelles en compression soient compensées par des contraintes résiduelles en tension ailleurs dans la pièce, soit à l'intérieur de la pièce ou près de la face opposée au traitement. La combinaison de ces contraintes est susceptible de modifier la forme de la pièce traitée. Le procédé de mise en forme par grenaillage est utilisé depuis 1968 pour produire des revêtements de voilures d'ailes avec des géométries complexes (Baughman, 1984). Il est réalisé en grenaillant une seule face ou les deux faces du composant à paroi mince avec des intensités de grenaillage variées, de façon à obtenir la forme désirée.

La mise en forme par grenaillage induit typiquement des formes semi-sphériques, puisque l'effet du procédé – en particulier la courbure induite - est identique dans toutes les directions. La mise en forme de voilures d'ailes, présentant une courbure plus faible dans la direction de la longueur de l'aile que dans la direction de la largeur (corde), nécessite par conséquent l'utilisation d'une technique particulière. La voilure est soumise à un pré-chargement externe en flexion à l'aide d'un outillage spécialisé, tout en étant simultanément soumise au grenaillage. La présence de contraintes dues au pré-chargement externe modifie l'effet du grenaillage, les impacts générant davantage de déformation plastique dans la direction des contraintes en tension générées par l'outillage. Il est ainsi possible de contrôler les courbures induites par le grenaillage, et par conséquent de générer des formes complexes telles que des voilures d'ailes. Les conditions de pré-chargement constituent des paramètres critiques du procédé de mise en forme par grenaillage

au même titre que les paramètres de grenaillage, et nécessitent par conséquent un contrôle approprié. Peu de travaux ont été publiés à propos de la mise en forme par grenaillage. Les quelques études disponibles sont pour la plupart basées sur des résultats expérimentaux et des relations empiriques, et seulement un nombre très réduit d'études (voir par exemple Li, 1981 et Kopp et Ball, 1987) ont considéré l'effet du pré-chargement externe.

L'objectif principal de cette thèse consiste à étudier en détail les procédés de grenaillage de précontrainte et de mise en forme par grenaillage, afin de mieux comprendre l'influence des paramètres des procédés sur le résultat final. Un certain nombre d'études du grenaillage de précontrainte basées sur des simulations numériques par éléments finis et sur des modèles théoriques ont été publiées au cours des 20 ou 30 dernières années, dans un souci de compréhension du procédé et d'optimisation. Cependant, ces études se concentrent pour la plupart sur les contraintes résiduelles générées, sans considérer les autres phénomènes qui influenceront de façon marquée la vie en fatigue, soit la couverture de la surface par des indentations et l'augmentation de la rugosité qui en résulte. Elles négligent également de tenir compte de l'aspect aléatoire du procédé, qui est pourtant susceptible d'influencer les résultats. En effet, les billes sont expulsées de la buse de grenaillage de façon aléatoire, sans en connaître de façon exacte le diamètre, la position, la direction ou la vitesse. Les résultats du grenaillage pourraient donc varier d'une fois à l'autre, et d'un endroit à l'autre à la surface du composant grenaillé. De plus, en raison probablement de la complexité du procédé, aucun modèle numérique de la mise en forme par grenaillage avec pré-chargement extérieur n'est présenté dans la littérature scientifique. Enfin, l'utilisation de ces deux procédés dans un contexte de production industriel implique la mesure de « l'intensité Almen » du jet de billes et du taux de recouvrement pour des fins de contrôle. Aucun lien clair n'a jusqu'à présent été établi entre ces mesures et les paramètres physiques des procédés.

Les sous-objectifs de la thèse sont les suivants:

(1) Développer un modèle 3D par éléments finis considérant l'aspect aléatoire du procédé de grenaillage de précontrainte. Ce modèle permettra d'étudier les relations entre les paramètres physiques du procédé, tels que l'angle d'incidence du jet et le temps d'exposition au grenaillage, avec les paramètres de contrôle du procédé (intensité du grenaillage et taux de recouvrement).

(2) Réaliser une étude expérimentale du grenaillage de précontrainte et de la mise en forme par grenaillage avec pré-chargement extérieur, afin d'établir des relations quantitatives entre l'intensité, le taux de recouvrement, la rugosité et le temps d'exposition, de même qu'entre le pré-chargement appliqué et la forme résultante sur des éprouvettes en aluminium 2024, un alliage typique des applications aéronautiques.

(3) Développer un modèle par éléments finis de la mise en forme par grenaillage avec pré-chargement extérieur.

(4) Développer un modèle analytique du grenaillage afin de prédire l'intensité Almen et les contraintes résiduelles dans l'éprouvette Almen à partir d'une combinaison de paramètres physiques du procédé.

Les modèles par éléments finis existants pour le procédé de grenaillage utilisent des successions d'impacts pour lesquelles la localisation et la séquence des impacts sont définies *a priori*, ce qui est peu représentatif du procédé. Ces modèles permettent une certaine compréhension et prédiction de contraintes résiduelles moyennes induites par le procédé, mais sont d'une utilité fort limitée pour analyser les phénomènes reliés au recouvrement et à la rugosité induite, et pour analyser les variations de résultats inhérentes au procédé.

Un nouveau modèle 3D par éléments finis du procédé a par conséquent été développé dans le cadre de cette thèse. Ce modèle inclut un grand nombre de billes identiques en acier impactant de façon aléatoire une cible en aluminium, avec un angle d'incidence normal ou oblique. Un programme Matlab approprié combiné avec du code en ANSYS APDL (ANSYS Program Design Language) a été utilisé afin de générer les coordonnées initiales et un maillage approprié pour chaque bille dans le jet. Le solveur explicite LS-DYNA a été utilisé pour réaliser les calculs. La taille des éléments dans le maillage a été choisie suite à une étude de convergence, de façon à conserver un temps de calcul acceptable. Les billes ont été considérées rigides dans la simulation en raison de leur dureté et de leur limite d'élasticité nettement plus élevées que celles de la cible. Toutes les billes ont été modélisées avec un même rayon (r = 0.5mm), une même densité, une même vitesse et un même angle d'impact (normal ou oblique, selon les simulations). Une plaque d'aluminium de dimensions 5mm×5mm×3mm a été considérée comme cible. On a considéré que l'aluminium avait un comportement élasto-plastique avec écrouissage isotrope; l'effet éventuel du taux de déformation du matériau a été négligé. Tous les contacts entre les billes ont également

ignorés. Dans toutes les simulations, le centre de chaque indentation a été situé à l'intérieur d'une aire de contact prédéfinie sur la surface. Des simulations ont été effectuées pour 5 différents nombres d'impacts, de façon à pouvoir établir des tendances en fonction du nombre d'impacts et/ou du taux de recouvrement. Pour chaque nombre d'impacts considéré, 5 modèles indépendants ont été générés par le programme Matlab afin d'étudier l'aspect aléatoire du procédé.

L'analyse des résultats de simulation a été réalisée en 4 étapes. Tout d'abord, un profil de contraintes résiduelles moyen a été obtenu pour chaque simulation. Ensuite, on a déterminé de façon analytique la flèche que provoquerait ce profil de contraintes dans une éprouvette d'aluminium de dimensions similaires à celles d'une éprouvette Almen. Ceci a permis de tracer par meilleur ajustement (« best fit ») des courbes reliant le nombre d'impacts et la flèche induite, et d'en trouver le point de saturation, soit l'endroit sur la courbe où la flèche augmente de seulement 10% en doublant le nombre d'impacts. Pour chaque simulation, on a également estimé le taux de recouvrement en considérant que tout point à la surface présentant une déformation plastique supérieure à un seuil prédéterminé (déduit via simulations à une indentation) faisait partie de la surface indentée. Finalement, la rugosité a été estimée en considérant les déplacements verticaux des nœuds des éléments de la surface. Les conclusions suivantes peuvent être tirées des résultats de simulation :

(1) La dispersion de la flèche induite et du taux de recouvrement diminuent lorsque le nombre d'impacts augmente. Cette tendance n'est pas aussi claire pour la rugosité induite.

(2) Dans le cas de grenaillage à incidence normale, le procédé atteint la saturation (en terme de flèche induite) et un taux de couverture de 100% après environ 48 impacts pour la surface étudiée.

(3) Pour un nombre d'impacts donné et une vitesse donnée, les impacts normaux produisent de plus grandes flèches que les impacts obliques. De plus, la saturation est obtenue après un plus grand nombre d'impacts dans le cas d'un jet oblique que dans le cas d'un jet normal.

(4) Dans le cas d'impacts obliques, un taux de recouvrement de 100% est atteint après un plus petit nombre d'impacts, comparativement au procédé à impacts normaux.

(5) Le grenaillage à incidence normale produit une plus grande rugosité que le grenaillage à incidence oblique à saturation de même qu'à taux de recouvrement de 100%.

(6) Des relations empiriques ont pu être établies entre la flèche induite, le taux de recouvrement, la rugosité et le nombre d'impacts.

(7) Les résultats numériques obtenus présentent des tendances similaires aux résultats expérimentaux présents dans la littérature scientifique.

Le modèle 3D développé dans le cadre de cette thèse permet donc de mieux comprendre et prédire les résultats du grenaillage que les modèles conventionnels. Il pourrait donc constituer un outil très utile pour un concepteur, de façon à guider ses choix de paramètres de grenaillage optimaux.

Peu d'études expérimentales ont jusqu'ici tenté d'établir des relations quantitatives entre l'intensité Almen correspondant à un jet de billes, les contraintes résiduelles dans un échantillon donné, le temps d'exposition, le taux de recouvrement et la rugosité. De plus, l'intensité Almen étant basée sur l'utilisation d'éprouvettes normalisées en acier SAE1070, peu de liens ont été établis entre la flèche de ces éprouvettes et celle de l'échantillon d'intérêt. Finalement, aucun article étudiant l'effet d'un pré-chargement externe sur la forme induite par grenaillage n'a pu être trouvé dans la littérature, malgré l'importance fondamentale de cette technique pour la mise en forme de voilures d'ailes d'avions.

Une étude expérimentale a par conséquent été réalisée dans la cadre de la thèse. Les tests ont été effectués sur des éprouvettes ou bandes métalliques en aluminium 2024, un alliage typique des applications aéronautiques, avec des billes de céramique de type Zirshot Z425 (diamètre nominal de 0.425mm) à l'aide de l'équipement suivant, soit d'une machine portable de grenaillage à projection de type BLAKA-1 de la compagnie Baiker AG et d'une buse droite d'un diamètre nominal de ¼ pouce (environ 6mm) montée sur un robot SV3XLong de la compagnie Motoman accompagné d'un contrôleur robot de type XRC2001. La pression et le débit massique des billes ont été mesurés directement par les capteurs de la machine de grenaillage, tandis que la vitesse des billes a été mesurée par un capteur de mesure de vitesses des particules de type Shotmeter. Des profils de contraintes résiduelles ont été obtenus via la technique de diffraction des rayons X, combinée avec électropolissage. Les valeurs mesurées ont été corrigées pour tenir compte de l'effet de l'enlèvement de matière en utilisant les méthodes de compensation et de correction

suggérées dans la norme SAE HS784. Les trajectoires de grenaillage par le robot ont été programmées de façon à avoir un jet de billes normal à la surface traitée, avec une distance constante de 25mm entre l'extrémité de la buse et la surface. Un dispositif de pré-chargement comprenant quatre supports à éprouvettes avec des rayons de courbure différents (R_p= infini, 720 mm, 360 mm et 240 mm) a été utilisé pour les tests de mise en forme par grenaillage avec pré-chargement en flexion.

Les conclusions suivantes peuvent être tirées des résultats des tests :

(1) Pour des conditions de grenaillage similaires, les éprouvettes d'aluminium avec la dimension principale dans la direction du laminage de la plaque originale présentent une plus grande flèche que les éprouvettes découpées perpendiculairement à la direction de laminage. Ceci prouve que la direction de laminage influence les résultats de grenaillage.

(2) Pour les éprouvettes d'aluminium et pour les éprouvettes Almen, la relation entre la flèche à saturation (intensité) et la vitesse des billes est presque linéaire. Les éprouvettes d'aluminium présentent une plus large flèche et un plus court temps d'exposition pour arriver à saturation que les éprouvettes Almen, peu importe la direction du laminage.

(3) Pour un même temps d'exposition, la rugosité de la surface augmente lorsque la vitesse des billes augmente. La relation présente deux étapes, soit une première étape pendant laquelle la rugosité augmente rapidement et de façon presque linéaire, suivi d'une deuxième étape pendant laquelle la rugosité augmente plus lentement jusqu'à atteindre une valeur limite.

(4) Une augmentation de la vitesse des billes entraîne, à saturation, une hausse de la contrainte résiduelle maximale, laquelle est située à une plus grande profondeur. L'épaisseur de la couche superficielle en compression augmente également. Des tendances similaires ont été remarquées en gardant une vitesse des billes constante et en augmentant le temps d'exposition. Cependant, la vitesse des billes et le temps d'exposition ont peu d'effet sur la contrainte résiduelle à la surface.

(5) L'application d'un pré-chargement en flexion lors de la mise en forme par grenaillage augmente de façon significative la flèche induite par le traitement, pour des conditions de grenaillage identiques. Une relation presque linéaire a été constatée entre le moment de

flexion appliqué et la flèche résultante, tant pour la mise en forme de bandes métalliques et que celle d'éprouvettes carrées. La flèche induite dans la direction du pré-chargement augmente de pair avec l'augmentation du moment de flexion appliqué, tandis que la flèche induite perpendiculairement à la direction de pré-chargement diminue.

Un modèle par éléments finis en trois étapes (implicite, explicite puis implicite) a été développé afin de simuler le procédé de mise en forme par grenaillage avec pré-chargement. Le modèle par éléments finis du grenaillage présenté un peu plus haut avec billes impactant de façon aléatoire une surface a été complémenté afin de modéliser la mise en forme. On a considéré que la zone impactée dans ce modèle constituait une zone élémentaire représentative pour une plaque soumise au grenaillage. On a donc dans un premier temps appliqué un pré-chargement en flexion sur le volume représenté, puis simulé les impacts à la surface de ce volume toujours sous chargement en flexion de façon à obtenir les champs de contraintes induites. Ces champs de contraintes ont été appliquées à un second modèle considérant la plaque complète de façon à calculer la déformation géométrique générée par le traitement à partir des contraintes induites.

Ainsi, la première étape a été réalisée à l'aide du logiciel par éléments finis ANSYS. Des champs de pression ont été appliqués aux frontières du volume modélisé afin d'obtenir via un calcul implicite les distributions de contraintes et de déformations résultant du moment appliqué par le dispositif de pré-chargement. On a considéré que les billes étaient immobiles durant cette étape. Après avoir converti tous les éléments du modèle dans un format approprié et transféré les contraintes et déplacements nodaux, un calcul explicite avec LS-DYNA a été exécuté afin de simuler les impacts de billes sur le volume pré-contraint et d'obtenir les contraintes induites par le traitement. Des contraintes moyennes ont été calculées à différentes profondeurs à l'intérieur du volume impacté, de façon à obtenir des profils moyens de contraintes σ_x^c et σ_y^c dans les deux directions principales. Des relations théoriques basées sur quelques hypothèses simplificatrices ont permis d'en déduire les profils de contraintes lorsque le chargement extérieur est retiré. Le principe d'équivalence a alors été utilisé pour déterminer l'effet global de ces profils de contraintes sur une section de la plaque, c'est-à-dire les forces et moments qui devraient être appliqués extérieurement pour générer le même effet sur la section. Finalement, ces forces et moments ont été appliqués aux extrémités d'une plaque rectangulaire, dans un modèle indépendant comprenant uniquement des éléments coques (SHELL181) réalisé sur ANSYS avec calcul implicite. On a considéré que le grenaillage a été effectué de façon uniforme sur cette

plaque. Les changements géométriques obtenus par calcul correspondent aux déformations que générerait le grenaillage avec pré-chargement. Les flèches et courbures induites par le procédé ont ainsi été déterminées dans les deux directions principales.

Ce modèle par éléments finis en trois étapes est le premier modèle permettant de simuler le procédé de mise en forme par grenaillage avec pré-chargement. Il constitue un outil très utile pour contrôler et prédire les résultats du procédé. Employé pour simuler le traitement de bandes métalliques d'aluminium telles que celles utilisées précédemment dans l'étude expérimentale, avec 48 billes frappant de façon normale la surface représentative à 66.2m/s, il a permis de tirer les constatations suivantes :

- La mise en forme par grenaillage génère des contraintes résiduelles compressives sur les deux faces de la composante.
- Par comparaison avec la mise en forme par grenaillage conventionnelle, l'utilisation de pré-chargement génère des contraintes résiduelles plus élevées en surface (sur les faces supérieure et inférieure), de même que des valeurs plus élevées de contrainte maximale en compression et de contrainte maximale en tension.
- Les courbes obtenues par simulation indiquent une relation presque linéaire entre le moment appliqué par le pré-chargement et la flèche induite par le grenaillage. De plus, l'application d'un moment générant des contraintes principalement dans une direction diminue l'effet du grenaillage dans la direction perpendiculaire.
- Les contraintes résiduelles issues de simulation sont conformes aux résultats expérimentaux, prouvant de ce fait la validité de l'approche de modélisation. Les tendances remarquées dans l'étude expérimentale entre le moment appliqué et la flèche induite se retrouvent dans les résultats de simulation.

Un modèle analytique du grenaillage particulièrement adapté à la prédiction de l'intensité Almen d'un jet de billes a été finalement développé. Ce modèle est principalement basé sur un modèle du grenaillage présenté par Li et al. (1991) et complémenté par Shen et al. (2004) pour prédire les contraintes induites dans un solide semi-infini. Quelques améliorations ou corrections au modèle de Li ont été apportées, puis les résultats du modèle prédictif ont été combinés avec l'approche de Guagliano (2001) afin de prédire la déformation correspondante d'une éprouvette Almen.

Dans une première étape du modèle, le champ de déformation correspondant à l'impact d'une bille sur un solide semi-infini est calculé comme si les deux matériaux (bille et cible) étaient purement élastiques. La théorie de contact de Hertz est utilisée pour déterminer les paramètres du contact et les contraintes sont déduites du chargement de Hertz. La vitesse initiale de la bille est reliée à la force maximale exercée par la bille sur la cible pendant le contact selon une approche énergétique. Ensuite, les déformations plastiques dans le régime élasto-plastique sont estimées à l'aide d'un ratio α défini comme étant le ratio entre le rayon d'une indentation lors d'un contact équivalent sur un matériau parfaitement plastique et le rayon de contact maximal lors d'un impact élastique. Ce ratio est utilisé en considérant la courbe élasto-plastique multilinéaire du matériau pour déterminer les proportions respectives de déformations plastiques et élastiques, et en déduire les contraintes totales puis les contraintes résiduelles correspondant à un impact unique. Les champs de contraintes et de déformations correspondant à une succession d'impacts distribués sur la surface traitée sont déduits en remarquant qu'un taux de recouvrement de 100% devrait correspondre à des champs de contraintes et de déformations permanents et continus, avec des contraintes indépendantes de la position en x et y et nulles dans la direction normale à la surface. La prise en compte des conditions d'équilibre interne selon l'approche de Guagliano (2001) permet finalement d'obtenir le profil de contraintes résiduelles qu'on retrouverait dans une pièce de dimensions réelles et de relativement faible épaisseur (comme par exemple une éprouvette Almen) après l'avoir soumise à ce grenaillage, de même que d'obtenir la flèche induite par le traitement.

L'utilisation du modèle analytique pour simuler le grenaillage d'éprouvettes Almen a permis prédire l'intensité Almen correspondant à différentes combinaisons de paramètres, et de tirer conclusions suivantes :

- Les résultats obtenus par le modèle correspondent assez bien aux résultats expérimentaux publiés par Cao et al. (1995), en particulier pour la prédiction de l'intensité Almen.
- La vitesse des billes semble être le paramètre prédominant pour l'intensité Almen. Le matériau dont sont constituées les billes a aussi un effet important.
- L'intensité Almen est approximativement proportionnelle au diamètre des billes pour une vitesse donnée, particulièrement à basse vitesse.

- Des relations empiriques ont été établies afin de relier le diamètre des billes, leur vitesse et l'intensité Almen correspondante pour des billes d'acier et pour des billes de céramique.
- Il n'y a pas de relation biunivoque entre les profils de contraintes résiduelles et les intensités Almen correspondantes. Chaque profil de contrainte résiduelle correspond à une unique intensité, mais une même intensité peut être générée par divers profils de contraintes résiduelles, et donc par différentes combinaisons de paramètres de grenaillage. Ainsi, de petites billes à haute vitesse pourraient produire la même intensité Almen que de grosses billes à faible vitesse, tout en générant une contrainte à la surface et une contrainte maximale compressive plus importantes et une couche de contraintes en compression de plus faible épaisseur.

Ces résultats montrent bien qu'il est important et même primordial de spécifier la taille des billes pour un traitement donné lorsqu'on indique une intensité Almen. Modifier la taille des billes tout en conservant l'intensité Almen pourrait entraîner des résultats non voulus, tels que de plus faibles niveaux de contraintes résiduelles à la surface ou une couche de contraintes en compression de plus faible épaisseur, deux caractéristiques influençant de façon négative la vie en fatigue des composantes traitées. De plus, un mauvais contrôle des paramètres de grenaillage pourrait être problématique, puisque des variations simultanées de plus d'un paramètre de grenaillage pourraient produire une même intensité Almen et par conséquent passer inaperçus. Finalement, rappelons que les tests Almen sont habituellement réalisés sur des éprouvettes normalisées en acier SAE1070. Deux traitements montrant des intensités Almen similaires pourraient induire sur un autre matériau (aluminium par exemple) deux champs de contraintes différant de façon marquée l'un par rapport à l'autre.

En résumé, les procédés de grenaillage de précontrainte et de mise en forme par grenaillage avec pré-chargement ont été étudiés par des méthodes numériques, expérimentales et analytiques dans le cadre de cette thèse. Quatre contributions majeures pour l'optimisation de ces procédés ont été réalisées :

1. Développement d'un modèle 3D par éléments finis prenant compte le caractère aléatoire du procédé, permettant par le fait même d'établir des relations quantitatives entre les principaux paramètres du procédé.

2. Établissement de relations quantitatives entre le moment appliqué et la flèche induite lors de la mise en forme par grenaillage avec pré-chargement, grâce à la réalisation d'une étude expérimentale, qui a également permis de mettre en évidence l'influence de la direction de laminage sur les résultats du grenaillage.
3. Développement d'une approche en trois étapes pour la simulation par éléments finis de la mise en forme par grenaillage avec pré-chargement en flexion. La comparaison des résultats de simulation avec les résultats expérimentaux obtenus précédemment a permis de valider l'approche.
4. Développement d'un modèle analytique permettant de prédire l'intensité Almen et de quantifier les contributions des paramètres de grenaillage.

Les travaux réalisés dans le cadre de cette étude ont permis de réaliser des contributions significatives à la compréhension des procédés de grenaillage et de mise en forme par grenaillage avec pré-chargement. Plusieurs questions d'importances ont cependant été laissées en suspens, et pourraient faire l'objet de recherche supplémentaire. Ainsi, certaines hypothèses devraient être validées ou raffinées afin d'améliorer le modèle aléatoire du grenaillage. Premièrement, la simulation considérait une distance initiale minimale de 0.75mm entre chaque bille, valeur fixée arbitrairement et inférieure au diamètre d'une bille. Une étude supplémentaire devrait donc être réalisée afin de vérifier si la distance minimale entre les billes influence les résultats. Deuxièmement, les dimensions des surfaces et volumes représentatifs ont été également déterminés arbitrairement, et l'influence de ces dimensions sur les résultats présentés devrait par conséquent être investiguée. Troisièmement, les courbes de saturation, de recouvrement et de rugosité issues de simulations numériques devraient être comparées à des courbes expérimentales.

Le modèle par éléments finis en trois étapes de la mise en forme par grenaillage avec pré-chargement considère que les contraintes induites par le grenaillage sont uniformément distribuées sur toute la surface grenaillée de la plaque traitée. Cependant, dans le procédé réel de mise en forme par grenaillage, les contraintes induites par le grenaillage d'une zone donnée ont une influence notable sur les résultats du grenaillage des zones subséquentes. Le champ de contraintes induites n'est donc pas uniforme dans la plaque. Ce phénomène a été mis en évidence par certains tests expérimentaux non présentés dans cette thèse, visant à comparer l'effet d'un

grenaillage réalisé par un robot balayant une surface plusieurs fois à haute vitesse avec l'effet d'un grenaillage réalisé par le même robot balayant une seule fois la surface à basse vitesse. Les courbures et flèches obtenues étaient beaucoup plus uniformes lorsque le robot passait plusieurs fois à haute vitesse. Des études supplémentaires pourraient être réalisées afin de mieux comprendre ce phénomène et de l'intégrer dans le modèle par éléments finis.

TABLE OF CONTENTS

DEDICATION III
ACKNOWLEDGEMENTS IV
RÉSUMÉ V
ABSTRACT VIII
CONDENSÉ EN FRANÇAIS X
TABLE OF CONTENTS XXIII
LIST OF TABLES XXVIII
LIST OF FIGURES XXIX
LIST OF NOMENCLATURE XXXIII
INTRODUCTION 1
CHAPITRE 1 LITERATURE REVIEW 3
1.1 Basic aspects of shot peening 3
1.2 Shot peening process parameters 5
1.3 Shot peening process control methods 7
1.3.1 Almen intensity 7
1.3.2 Surface coverage 8
1.3.3 Surface roughness 9
1.3.4 Influence of Almen intensity and surface coverage on the shot peening effects (residual stress and surface roughness) 10
1.4 Finite element simulation of shot peening 11
1.4.1 Existing Finite Element models 11
1.4.2 Effect of shot peening parameters with FE analysis 13
1.5 Process of peen forming 16
1.5.1 Conventional peen forming 16
1.5.2 Stress peen forming 19
1.6 Summary of the findings 20
CHAPITRE 2 OBJECTIVE AND RATIONALE OF THE PROJECT 22
CHAPITRE 3 SCIENTIFIC APPROACH AND COHERENCE WITH RESEARCH OBJECTIVES 24

3.1 Article 1: On the potential applications of a 3D random finite element model for the simulation of shot peening (Objective 1) 24
3.2 Article 2: Experimental study of shot peening and stress peen forming (Objective 2) 25
3.3 Article 3: A numerical study of the stress peen forming process (Objective 3) 26
3.4 Article 4: An analytical approach to relate shot peening parameters to Almen intensity (Objective 4) 27
CHAPITRE 4 ON THE POTENTIAL APPLICATIONS OF A 3D RANDOM FINITE ELEMENT MODEL FOR THE SIMULATION OF SHOT PEENING 28
4.1 Abstract 28
4.2 Introduction 28
4.3 3D random finite element model 35
4.4 Shot peening intensity and saturation 39
4.4.1 Arc height calculation with induced stress profile 39
4.4.2 Shot peening saturation curve with FEM – normal impacts 40
4.4.3 Shot peening saturation curve with FEM – 60° impact angle 42
4.5 Residual stress profiles of shot peening 45
4.5.1 Residual stress profiles after normal and oblique shot peening 45
4.5.2 Comparison of residual stress profiles with reference models 45
4.6 Shot peening coverage 47
4.6.1 Surface plastic strain after one impact 47
4.6.2 Numerical simulation of peening coverage with FEM – normal impacts 51
4.6.3 Comparison of the simulated coverage with reference studies 53
4.6.4 Numerical simulation of peening coverage with FEM-60° angle impacts 53
4.7 Surface roughness 55
4.7.1 Definition of surface roughness 55
4.7.2 Peening induced surface roughness with FEM – normal impacts 55
4.7.3 Comparison of the surface roughness with reference results 57
4.7.4 Peening induced surface roughness with FEM-60° impact angle 59
4.8 Summary 59
4.9 Suggestions for future work 60

CHAPITRE 5 EXPERIMENTAL STUDY OF SHOT PEENING AND STRESS PEEN FORMING 61
5.1 Abstract 61
5.2 Introduction 61
5.3 Description of shot peening and stress peen forming processes 65
5.3.1 General considerations 65
5.3.2 Shot peening process 66
5.3.3 Stress peen forming process 68
5.4 Shot peening results 69
5.4.1 Saturation studies 69
5.4.2 Surface coverage studies 72
5.4.3 Surface roughness studies 77
5.4.4 Residual stress profiles measured by X-Ray Diffraction Method (XRD) 80
5.5 Stress peen forming results 83
5.5.1 Stress peen forming of narrow strips 83
5.5.2 Residual stress profile after stress peen forming 86
5.5.3 Stress peen forming of square samples 87
5.6 Summary 91
5.7 Conclusions 94
CHAPITRE 6 A NUMERICAL STUDY OF STRESS PEEN FORMING 95
6.1 Abstract: 95
6.2 Introduction 95
6.3 Principle of shot peen forming 98
6.3.1 Peen forming of a rectangular strip 98
6.3.2 Principle of stress peen forming 101
6.4 Numerical model for stress peen forming 102
6.4.1 Description of the finite element model 102
6.4.2 Implicit analysis of prebending 105
6.4.3 Explicit analysis of shot peening process 106
6.4.4 Residual stress profile with stress peen forming 107
6.4.5 Radius of curvature and arc height of stress peen forming 110

6.5 Comparison with experiments 113
6.5.1 Experimental study of stress peen forming 113
6.5.2 Comparison with experimental results 113
6.6 Conclusions 117
CHAPITRE 7 AN ANALYTICAL APPROACH TO RELATE SHOT PEENING PARAMETERS TO ALMEN INTENSITY 118
7.1 Abstract: 118
7.2 Introduction 118
7.3 Analytical prediction of Almen intensity 121
7.3.1 Analytical model for shot peening induced stress in a semi-infinite body 121
7.3.2 Calculation of residual stress for a thin target component 131
7.4 Application 133
7.4.1 Material, geometry and modeling parameters 133
7.4.2 Algorithm for the prediction of induced and residual stress profiles 134
7.4.3 Validation of the efficiency factor $\boldsymbol{\alpha}$ 136
7.4.4 Experimental validation 139
7.5 Potential application 143
7.6 Conclusions 148
CHAPITRE 8 DISCUSSIONS 150
8.1 Discussion of key findings 150
8.1.1 Finding 1: Saturation curve (relationship between resulting arc height and number of shots) was established numerically and experimentally. 150
8.1.2 Finding 2: Surface coverage curve (relationship between surface indentation ratio and number of shots) was established numerically and experimentally. 150
8.1.3 Finding 3: Surface roughness curve (relationship between surface roughness and number of shots) was established numerically and experimentally. 151
8.1.4 Finding 4: Residuals stress profile after shot peening, conventional peen forming and stress peen forming have been simulated, measured and compared. 151
8.1.5 Finding 5: Experimental and numerical study of the stress peen forming process 151
8.1.6 Finding 6: An analytical model was developed to predict Almen intensity. 152
8.2 Discussion of findings in relationship to four articles 152

8.2.1 Discussion of findings in relationship to the first article: On the potential applications of a 3D random finite element model for the simulation of shot peening 152
8.2.2 Discussion of findings in relationship to the second article: Experimental study of shot peening and stress peen forming 153
8.2.3 Discussion of findings in relationship to the third article: A numerical study of the stress peen forming process..... 153
8.2.4 Discussion of findings in relationship to the fourth article: An analytical approach to relate shot peening parameters to Almen intensity 153
CONCLUSIONS..... 154
REFERENCES..... 158

LIST OF TABLES

Table 1.1: Almen strips dimensions (Kirk, 1999). 7
Table 4.1 Relationship between saturation intensity and full coverage for two shot peening cases. 59
Table 5.1: Shot peening process parameters. 66
Table 5.2: Aluminum 2024 Metallurgical Composition. 66
Table 5.3: Average mechanical properties of experimental Al2024. 66
Table 5.4: Results of saturation study on aluminum test strips. 71
Table 5.5: Residual stresses at surface in three cases. 82
Table 5.6: Residual stresses at the surface for the three peening cases under consideration (Unit: MPa). 82
Table 5.7: Relationship between prebending conditions and resulting arc heights. 84
Table 5.8: Prebending parameters and resulting radii for peen formed square strips. 88
Table 5.9: Prebending parameters and resulting arc heights for peen formed square strips. 88
Table 5.10: Relationship between saturation intensity and full coverage for three shot velocities. 94
Table 6.1: Resulting arc heights and radii of curvatures in x and y directions. 111
Table 6.2: Relationship between prebending conditions and peen forming results. 111
Table 7.1: Elastic contact radius and plastic indentation radius calculated by analytical model and FEM. 138

LIST OF FIGURES

Figure 1.1: Schematic illustration of the formation of residual stresses as a consequence of two competitive processes in shot peening. 4
Figure 1.2: Schematic illustration of the residual stress caused by shot peening. 5
Figure 1.3: The effect of the peening parameters on the residual stress profile. 6
Figure 1.4: Almen intensity measurement system (Bernard et al. 2004). 6
Figure 1.5: Schematic saturation curve (Champaigne, 2001). 8
Figure 1.6: Roughness definition. 9
Figure 1.7: Six types of existing models for simulating the shot peening process. 11
Figure 1.8: Residual stress profiles due to shot peening in a thick component. 14
Figure 1.9: Relationship between Residual stress and material constitutive laws. 15
Figure 1.10: Peen forming procedure. 17
Figure 1.11: Schematic illustration of the residual stresses after peen forming. 17
Figure 1.12: Residual stress after peen forming (Han et al. 2002). 19
Figure 1.13: Deflection of the component due to peen forming and stress peen forming. 20
Figure 4.1 Six types of existing models for simulating the shot peening process. 29
Figure 4.2: Random finite element model. 37
Figure 4.3: Representative surface 38
Figure 4.4: Sketch of shot peening on a strip with dimensions $76\text{mm}\times19\text{mm}\times3\text{mm}$. 39
Figure 4.5: Simulated arc heights for normal impacts versus the number of shots. 42
Figure 4.6: Two impact cases. 43
Figure 4.7: Effect of shot peening angle upon the arc heights versus the number of shots. 43
Figure 4.8: Comparison of the residual stress profiles after normal shot peening (case 1) and oblique shot peening (case 2). 44
Figure 4.9: Induced stress profiles calculated from different finite element models. 46
Figure 4.10: Residual stress profiles calculated from different finite element models. 46
Figure 4.11: von Mises equivalent plastic strain contour after one normal shot impact 48
Figure 4.12: von Mises plastic strain profile and indentation profile of the surface nodes 48
Figure 4.13: von Mises equivalent plastic strain contour after one 60° oblique impact 49
Figure 4.14: von Mises equivalent plastic strain contour after one 60° oblique impact 49
Figure 4.15: von Mises plastic strain profile and Uz displacement profile of the surface nodes ..50

Figure 4.16: Shot peening coverage versus the number of shots after normal impacts. 52
Figure 4.17: Relationship between surface coverage and percentage of peen time. 53
Figure 4.18: Shot peening coverage versus the number of shots for normal impacts (case 1) and oblique impacts (case2) respectively.....54
Figure 4.19: *PV* roughness definition: peak-to-valley roughness 55
Figure 4.20: *PV* roughness versus number of shots for normal impacts. 56
Figure 4.21: Relationship between surface roughness and peening time from this numerical study and the experimental results obtained by (Gentil et al. 1987).....57
Figure 4.22: PV roughness versus the number of shots for two shot peening cases.....58
Figure 5.1: Prestressing device with four radii of prebending curvatures 69
Figure 5.2: Resulting arc heights for different numbers of peening passes and fitted saturation curves for aluminum L test strips. 70
Figure 5.3: Relationship between arc height at saturation and shot velocity for aluminum test strips and Almen strips. 71
Figure 5.4: Surface topography obtained by 3D roughness measurement profiler.....73
Figure 5.5 2D grayscale topography of peened surfaces after 1, 2, 4, 8, 16 and 32 peening passes for shot velocity of 34.6 m/s.....73
Figure 5.6: Surface coverage calculated by ImageJ after 1, 2, 4, 8, 16 and 32 peening passes for shot velocity of 34.6 m/s. 74
Figure 5.7: 2D grayscale topography (a, b and c) and surface coverage (d, e and f) calculated by ImageJ after 1, 2 and 4 peening passes for shot velocity of 53.7 m/s. 74
Figure 5.8: 2D grayscale topography (a, b and c) and surface coverage (d, e and f) calculated by ImageJ after after 1, 2 and 4 peening passes for shot velocity of 66.2 m/s.....75
Figure 5.9: 2D color topography of peened surfaces for measurement of shot peening indentations radii at three shot peening velocities. 76
Figure 5.10: Comparison of experimental fitting coverage curves and theoretical Avrami coverage curves for three shot peening velocities.....77
Figure 5.11: Experimentally measured surface average roughness and best fitting curves for three shot velocities. 78
Figure 5.12: Evolution of stress concentration factors with respect to number of passes for different velocities. 79

Figure 5.13: Residual stress profiles after correction for three peening cases. 82
Figure 5.14: Illustration of the relationship between prebending radius and prebending arc height. 83
Figure 5.15: Experimental relationship between arc heights (prebending arc height and resulting arc height) and prebending moments. 85
Figure 5.16: Residual stress profiles in three cases 87
Figure 5.17: Relationship between resulting arc heights in Longitudinal and Transversal directions and prebending moments 89
Figure 5.18: Relationship between resulting arc heights and prebending arc heights vs. prebending moments for three velocities. 90
Figure 6.1: Illustration of the principle of peen forming process 97
Figure 6.2: Sketch of a plate subjected to various moments 100
Figure 6.3: Sketch of a rectangular plate after peen forming 100
Figure 6.4: Finite element model used for stress shot peening simulation. 104
Figure 6.5: Representative surface 104
Figure 6.6: Combined and induced stress profiles after stress peen forming 107
Figure 6.7: Stress profiles after stress peen forming with prebending moment. 108
Figure 6.8: Stress profiles (induced stress and residual stress) of stress peen forming 108
Figure 6.9: Residual stress profiles under four different prebending moments. 109
Figure 6.10: Uz displacements of the strip following x and y directions 110
Figure 6.11: Relationship between prebending moment and peen forming results 112
Figure 6.12: Experimental measured Uz and fitting curve after conventional peen forming and stress peen forming. 114
Figure 6.13: Comparison of FE simulated resulting arc heights and radius of curvature with experimental results 115
Figure 6.14: Comparison of experimental measured residual stress and FEM simulated results under two cases 116
Figure 7.1: Geometry of contacting surfaces. 122
Figure 7.2: Plastic indentation of a rigid shot impacting a perfectly plastic target. 127
Figure 7.3: Schematic diagram for calculating stresses after unloading 129
Figure 7.4: Equilibrium process in thin target component. 133

Figure 7.5: Induced stress, stretching stress, bending stress and residual stress in Almen strip Type A (calculated intensity 8A=0.2mmA). 136
Figure 7.6: Axisymmetric finite element model of a rigid shot impact an infinite target component. 137
Figure 7.7: Contact between rigid shot and target component. 138
Figure 7.8: Comparison of analytical residual stress and published experimental residual stress 141
Figure 7.9: Analytical and experimental relationships between Almen intensity and shot velocity for two shot sizes 142
Figure 7.10: Effect of peening parameters on Almen intensity. 143
Figure 7.11: Calculated residual stresses for different combinations of peening parameters 145
Figure 7.12: Relationship between diameter and velocity for seven different Almen intensities (Almen Type A strip). 146

LIST OF NOMENCLATURE

a	radius of the plastic indentation
a_e	radius of the contact circle
a_e^*	maximum radius of the contact circle
a_p	radius of indentation during the plastic impact
a_p^*	maximum radius of indentation during the plastic impact
A	section area of the target component
$\bar{A}$	shot peening area on the surface of the target component
AH	arc height
$Ah(T)$	reference arc height equation related to peening time
$Ahf(N)$	best fitting arc height equation from the simulated arc heights
AHs	simulated arc height of the strip
Ah_p	prebending arc height
Ah_r	resulting arc height after peen forming
A_s	arc height at saturation
B	width of one peening pass
C	surface coverage
$C_{th}(T)$	theoretical calculated coverage
$Cf(N)$	best fitting coverage function from the simulated coverage
Cs	simulated coverage
d	shot diameter
ds	distance between adjacent shots
e_x^e, e_y^e, e_z^e	principal components of the deviatoric strain tensor in elastic domain

e_x^p, e_y^p, e_z^p	principal components of the deviatoric strain tensor in elastic-plastic domain
E	young's modulus of the target strip
E_H	equivalent Young's modulus
E_s	Young's modulus the shot material
E_T	Young's modulus the target material
E_{tan}	tangent modulus of the target strip
f_x, f_y	arc heights of the component sections parallel to x and y axes
f^{tot}	total arc height of the plate
F_x , M_x	non-equilibrated force and moment calculated from induced stress
h	thickness of target strip
H^1	linear strain-hardening parameter of the target component
HV_m	hardness of the target material
HV_s	hardness of shot
I	moment of inertia of the target component
k	efficiency coefficient related to elastic and thermal dissipation during impact
K_t	stress concentration factor
l	reference length for arc height measurement
l_m	reference distance for measuring Almen intensity
L	length of one peening pass
L_p	length of one peening pass
$\dot{m}$	mass flow rate of shot flow
M_p	prebending moment
M_x, M_y	bending moment in x and y direction, respectively
M_x^{pre}	linear prebending moment in x direction

N	number of random impact shots
N_p	number of peening pass
N_{ps}	saturation numbers of passes
N_{total}	total number of shots for one peening pass
p	pressure of shot flow
p_0	maximum pressure at $r = 0$
$\bar{p}$	average pressure resisting the motion
p_0^*	maximum value of p_0 during elastic impact
$p(r)$	pressure distribution proposed by Hertz for two frictionless elastic solids of revolution in contact
p_0	the maximum pressure
P	total load compressing the solids
PV	surface peak to valley roughness
PVs	simulated surface roughness
$PVf(N)$	best fitting roughness function from the simulated roughness
r	radial distance from the contact center
R	rate of creation of indentations (number of impacts per unit area per unit area)
R	relative radius of the interface
R_1, R_2	initial radii of the two sphere
Ra	average roughness
R_t	maximum peak-to-valley distance
R_v , R_{pe}	highest peak and lowest valley within the sample length for the definition of PV
R_p	radius of prebending curvatures
R_z	surface roughness

R_x, R_y	resulting radius of curvature in x and y direction, respectively
r	radius of shot
$\bar{r}$	average radius of the indentations
s_x^e, s_y^e, s_z^e	principal components of the deviatoric stress tensor in the target material
s_x^p, s_y^p, s_z^p	principal components of the deviatoric stress tensor in the elastic-plastic domain
S_m	average distance between peaks
S_a	surface average roughness
S_{total}	surface area on the target component for one peening pass
S_{rep}	surface of the boundary of the impacting shots
t	thickness of target strip
t_1	depth of maximum compressive residual stress
t_2	depth where the residual stress changes sign (from compressive to tensile)
T	shot peening time
T_f	shot peening time to reach full coverage
U_z	z direction displacement
$\bar{u}_{z1}$, $\bar{u}_{z2}$	normal displacement fields on the surface of the two spheres
v	velocity of shot
V	velocity of shot
V_e	equivalent robot travelling velocity
V_{es}	equivalent robot travelling velocity
V_r	robot travelling velocity
V_{robot}	velocity of the peening robot
V_s	volume of one shot
z	depth under consideration in the target body

Greek

α	ratio of the radius of maximum plastic indentation to the radius of the maximum elastic contact radius
δ	total approach between the centers of the two spheres
δ_1, δ_2	displacements of the centers of the two spheres
δ_p	total approach between the centers of the two bodies
δ^*	maximum approach between the shot and target component
δ_p^*	maximum approach or final depth of indentation
ε_b	strain which corresponds to σ_b
ε_i^e	equivalent strain distribution
ε_i^p	plastic strain calculated from ε_s and ε_i^e
ε_m^e	hydrostatic strain
ε_p	von Mises plastic strain
ε_s	strain corresponding to the yield stress
$\varepsilon_x^e, \varepsilon_y^e, \varepsilon_z^e$	principal strains acting on the elastic target
$\Delta\varepsilon_i^e$	stress corresponding to $\Delta\sigma_i^e$
$\Delta\varepsilon_i^p$	plastic strain calculated from $\Delta\varepsilon_i^e$
θ	shot peening incidence angle
μ	Coulomb friction coefficient between shots and target strip
υ	Poisson's ratio of target strip
υ_S	Poisson's ratio of the shot material
υ_t	Poisson's ratio of the target material
ρ	density of shot
ρ_s, ρ_t	density of shots and target strip, respectively

σ^b	bending stress profile
σ_x^c, σ_y^c	combined stress profile in x and y direction, respectively
σ_i^e	von Mises equivalent stress distribution
σ_m^e	hydrostatic stress
σ_x^e, σ_y^e ,σ_z^e	principal stresses acting on the elastic target
σ_x^i , σ_y^i	linearly distributed initial stress profile in x and y direction, respectively
σ_x^{im}	surface initial stress
σ^{ind}	induced stress profile
σ_x^{ind}, σ_y^{ind}	induced stress profile produced by shot peening in x and y direction, respectively
σ_i^p	plastic stress
σ^s	stretching stress profile
σ^{res}	residual stress profile
σ_x^{res}, σ_y^{res}	residual stress profile after deformation of the strip in x and y direction, respectively
σ_x^{rel}, σ_y^{rel}	relaxation values of σ_x^t and σ_y^t
σ_x^t, σ_y^t ,σ_z^t	transresidual stress
σ_b	ultimate tensile stress of the target material
σ_m	measured residual stress
σ_{max}	maximum compressive residual stress
σ_s	yield stress
σ_{st}	surface tensile stress of a prebent strip
σ_{sur}	surface residual stress
σ_{ten}	maximum tensile residual stress
σ_y	yield stress of target component

$\Delta\sigma_i^e$	tstress that can not be released
$\Delta\sigma_i^p$	stress corresponding to $\Delta\varepsilon_i^p$

Abbreviation

FE	Finite Element
APDL	ANSYS Parametric Design Language
NCI	Normalized 95% Confidence Interval

INTRODUCTION

Shot peening is a cold working process widely used to improve the fatigue life of metal components in the automotive industry and to produce thin components with complex shapes such as wing skins, in the aerospace industry. This process is accomplished by bombarding the surface of a metallic component with shots at a high velocity that induce a layer of plastic deformation near the surface. This plastic deformation leads to a residual compressive stress field in the peened surface, along with increased tensile stress through the thickness. The layer of compressive residual stress reduces the likelihood of premature failure under cyclic loading conditions and therefore improves the fatigue life of the peened component.

Numerous shot peening parameters, such as shot size, type, velocity, pressure, mass flow, incidence angle, material properties of the target component, etc. have great influence on shot peening results. In the industry, two control parameters, peening intensity and surface coverage, have been adopted to characterize the effectiveness and the repeatability of the shot peening process. Peening intensity is related to the amount of kinetic energy (related to the shot mass and velocity) transferred from the shot stream to the target component during the shot peening process. A method widely used to quantify peening intensity is called *Almen intensity* (Almen and Black, 1963). Surface coverage is defined as the ratio of the area covered by peening indentation to the total treated surface area, expressed as a percentage. There is much to be gained by studying these indicators in detail and establishing a direct relationship between them based on the same target component, by analytical, experimental and numerical methods.

During shot peening, the projection of shots at high velocity results not only in compressive residual stress on the peened surface, but also in an increased surface roughness. Higher surface roughness presents more irregularities, which act as stress concentrations and cause a reduction of the fatigue life of the treated component. Therefore, the performance of shot peening will depend on a trade-off between its beneficial effect (compressive residual stresses) and its detrimental effect (surface roughness).

Shot peen forming is a dieless process that has been widely used to form various aircraft component since the 1960's. Conventional peen forming causes the component to form a spherical shape since it induces the same curvatures in both chordwise and spanwise directions. For a wing skin, which has a larger curvature in the chordwise direction than in the spanwise

direction, a technique called stress peen forming is applied. In stress peen forming, the component is elastically pre-bent along the spanwise direction during peen forming. After peen forming, the resulting chordwise curvature will be larger than the spanwise curvature. Most of the investigations of stress peen forming are based on experimental and empirical relationships.

During stress peen forming, not only the shot peening process parameters (shot size, shot velocity and peening time, etc.), but also the prebending conditions (elastic prebending moment) should be controlled to obtain the required deformation of a peened component. Due to the complexity of the process, there is currently no numerical model with the ability to simulate the stress peen forming process that takes into account all these parameters.

The principal objective of this study is to develop and validate predictive tools for the shot peening and (stress) peen forming results. The effect of the shot peening parameters (shot size, material, velocity, etc.) on the peening and forming results (Almen intensity, roughness, coverage, arc height, etc.) are studied by these tools. Both numerical as well as analytical tools are developed and validated by controlled shot peening and peen forming experiments.

This document is organized as follows. Chapter 1 presents a comprehensive review of the state of art of the shot peening and peen forming processes. Chapter 2 presents the rationale and sub-objectives of the project, based on the findings of Chapter 1. The scientific approach and the relationship between the research objectives and the publications resulting from the thesis work are described in Chapter 3. Chapters 4 to 7 present four objectives in the form of four research papers. Each chapter has its own Abstract, Introduction, Methods, Results and Discussion sections. In Chapter 4, a novel 3D random finite element model that considers randomly distributed shot is described. Chapter 5 introduces the experimental study of the shot peening and stress peen forming processes. In Chapter 6, a three-step finite element model is described. The established FE model simulates the stress peen forming process considering the shot peening conditions as described in Chapter 5. An analytical model for the study of the shot peening process and prediction of Almen intensity is described in Chapter 7. Chapter 8 discusses the main findings in this work and the relationship between four articles. The conclusions and the Recommendations are given in the last Chapter.

CHAPITRE 1 LITERATURE REVIEW

1.1 Basic aspects of shot peening

Shot peening is accomplished by bombarding the surface of a metal component with multiple shots at high velocities. Each piece of shot that strikes the material acts as a tiny peening hammer, imparting to the surface a small plastic indentation surrounded by a plastic zone. Once contact between the shot and the target has ceased, the elastically stressed region tends to recover to the fully unloaded state, while the plastically deformed region sustains some permanent deformation. These inhomogeneous elasto-plastic deformations result in the development of a compressive residual stress field in the exposed upper layer. The layer of compressive residual stress reduces the likelihood of premature failure of the metal component under conditions of cyclic loading (Meguid, 1975; Webster and Ezeilo, 2001; Rodopoulos et al. 2004).

Wohlfahrt (1984) described the two competitive residual stress generating processes of shot peening, as shown in Figure 1.1. One is direct plastic elongation of the top layer of the component due to numerous shot indentations, as illustrated at the left hand side of Figure 1.1 (Principle 1). After shot peening, the rz plane (see Figure 1.1) of the target component is divided into two different sections. Section A represents plastic deformation by shot peening while section B represents the region beneath the plastic deformation. The elasto-plastic elongation of the surface layer results in compressive residual stresses with a maximum magnitude at the surface when this effect is the only or predominant one. The second residual stress generating process can be explained as Hertzian pressure which produces plastic deformation beneath the impact surface, as shown at the right side of Figure 1.1 (Principle 2). The residual stress has a maximum value at a distance $z = 0.47a$ below the surface, where a is the radius of the plastic indentation. In practice, the distribution of compressive residual stress after shot peening results from the combined effect of these two competing processes, direct plastic surface deformation and plastic deformation of deeper layers due to the Hertz pressure.

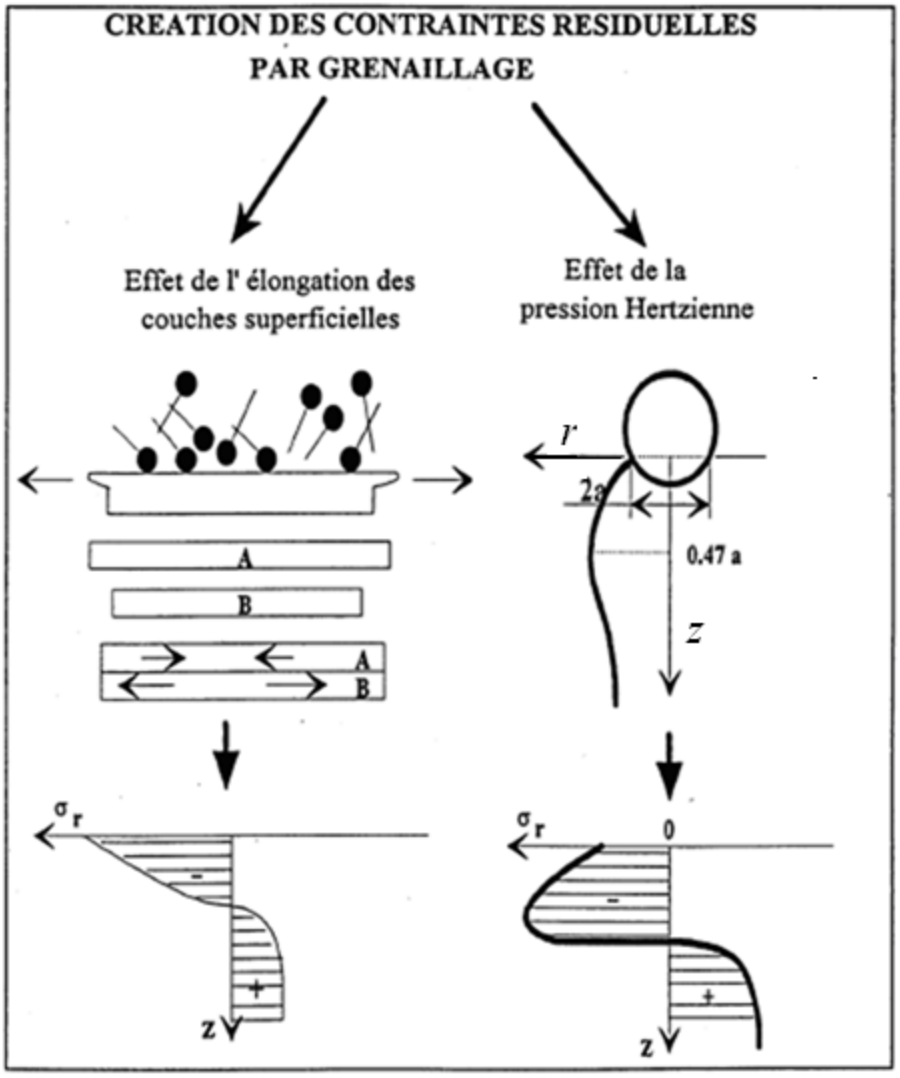

Figure 1.1: Schematic illustration of the formation of residual stresses as a consequence of two competitive processes in shot peening: direct stretching of a surface layer (Principle 1, left) and Hertizan pressure (Principle 2, right) (Slim, 1995).

Figure 1.2 shows a typical residual stress field described by five main terms, namely

- σ_{max}: the maximum compressive residual stress,
- σ_{sur} : the surface residual stress,
- σ_{ten} : the maximum tensile residual stress,
- t_1 : the depth of maximum compressive residual stress, and
- t_2 : the depth where the residual stress changes sign (from compressive to tensile).

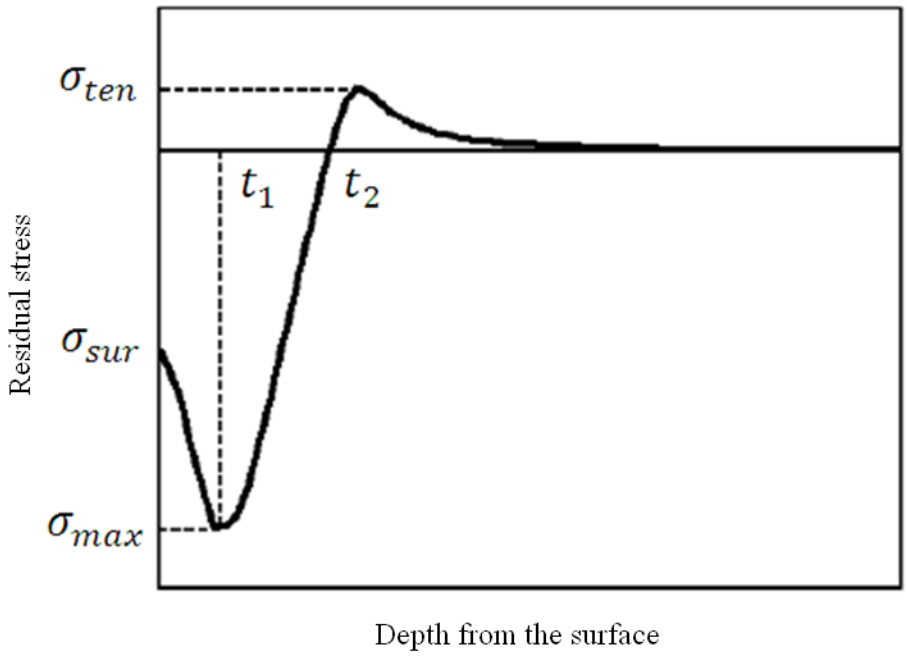

Figure 1.2: Schematic illustration of the residual stress caused by shot peening.

1.2 Shot peening process parameters

Many shot peening parameters are known to have a great influence on the effectiveness of the shot peening treatment. These can be classified into the following three groups (Kyriacou, 1996):

- Shot parameters: Type, size, shape, density, hardness, yield strength, stiffness, etc.
- Target parameters: Hardness, yield strength, stiffness, work hardness, chemical composition, pre-stress condition, etc.
- Flow parameters: Mass flow rate, pressure, velocity, angle of impingement, standoff distance.

Working on fundamental research on shot peening, Herzog et al. (1996) analyzed the effect of shot peening parameters on the resulting residual stress profile. In his study, the influence of the hardness of the target material HV_m , hardness of shot HV_s, shot diameter d, shot velocity v, shot flow mass flow $\dot{m}$, pressure p and peening time t on the residual stress profile was shown schematically in Figure 1.3. In this figure, the directions of the arrows show the influence of these parameters on residual stress profile. Arrow 1 shows that the value of the surface residual stress σ_{sur} increases with the increase of HV_s and HV_m; arrow 2 shows that the value of the

maximum residual stress σ_{max} increases with the increase of v, p, d, t, HV_s and HV_m; arrow 3 shows that the depth of the maximum residual stress t_1 decreases with the increase of HV_m and arrow 4 shows that t_1 increases with the increase of v, p, d, t and HV_s.

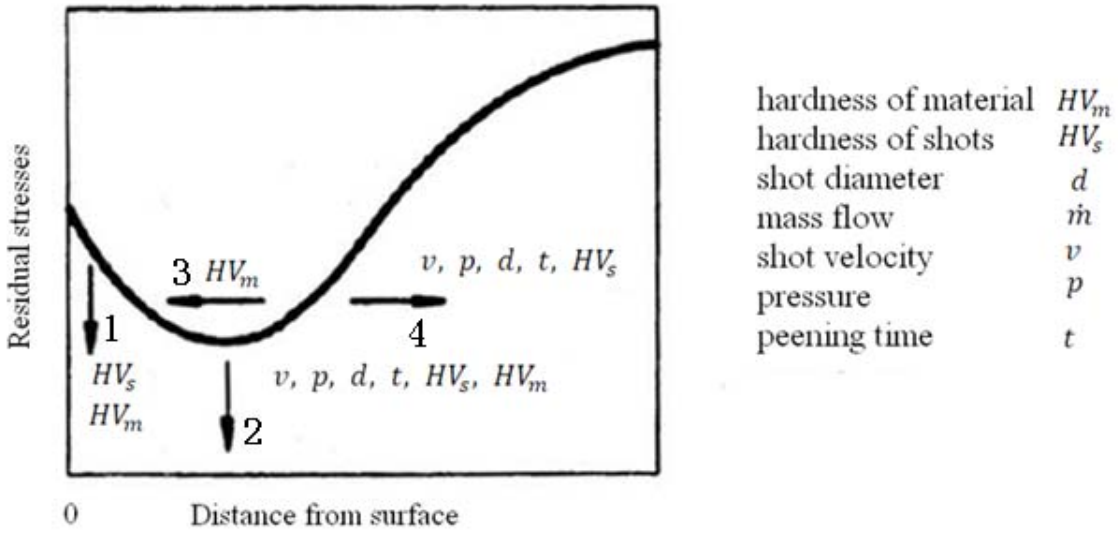

Figure 1.3: The effect of the peening parameters on the residual stress profile (Herzog et al. 1996).

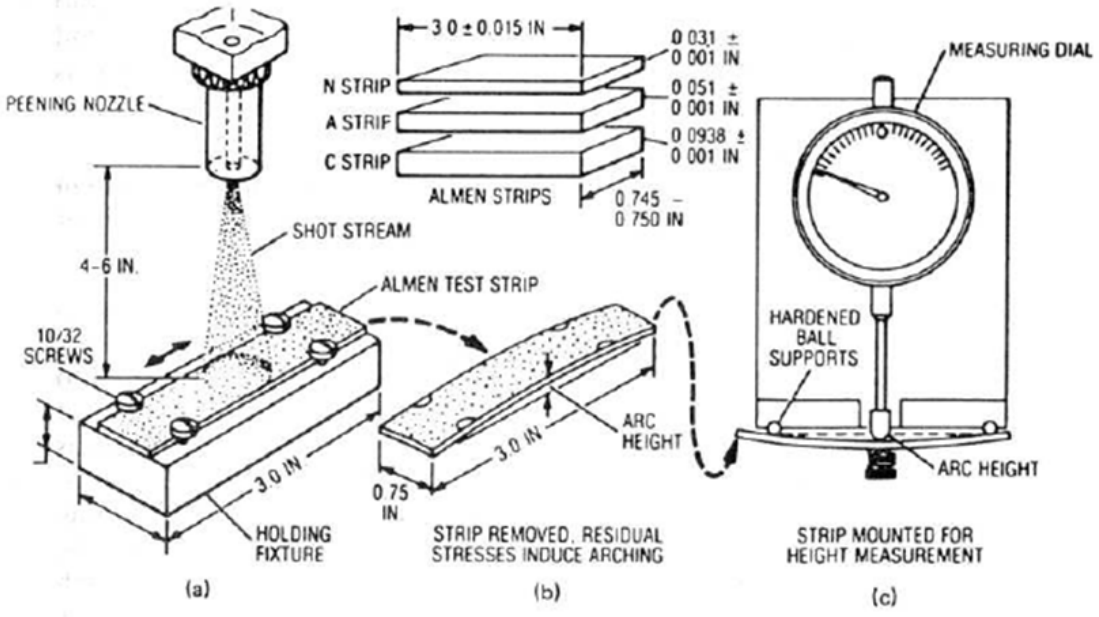

Figure 1.4: Almen intensity measurement system (Bernard et al. 2004).

1.3 Shot peening process control methods

Measurement of Almen intensity and surface coverage are the two main control methods used to ensure the repeatability of the shot peening and peen forming processes in the industry. In this section, these two shot peening control parameters as well as their influence on peening effects are discussed in detail.

1.3.1 Almen intensity

During the 1940's, J.O. Almen developed a standard process to measure the kinematic energy transferred by a shot stream. Shot peener and shot peening specifications refer to this energy as *intensity at saturation*. The measurement of peening intensity is accomplished by determining its effect on standardized test strips, called *Almen strips*, with a standardized tool, called *Almen gage* (Almen and Black, 1963).

Figure 1.4 shows the standard Almen intensity measurement system that consists of three elements. (1)Three different thicknesses of Almen strips of spring steel SAE1070 tempered to 44-50 HRC, as listed in Table 1.1. (2) One steel block (holding fixture) to attach and support the Almen strips during the shot peening process. (3) One gauge capable of reading the arc height of Almen strips.

When a thin piece of metal is submitted to a shot stream on one of its sides (see Figure 1.4 (a)), it bends (convex towards the shot peened side) because of plastic deformations induced by shot peening (see Figure 1.4 (b)). Almen intensity is a measurement of the arc height deflection (inches or millimetres) at the center of Almen strips submitted to a given shot peening process. A higher intensity (higher arc deflection) means that a greater amount of kinetic energy has been transferred to the treated parts.

Table 1.1: Almen strips dimensions (Kirk, 1999).

Strip	Thickness(in)	Length (in)	Width (in)	Use for
N	0.031+/-0.001	3 +/- 0.015	0.745 – 0.750	Low Intensity
A	0.051+/-0.001	3 +/- 0.015	0.745 – 0.750	Average Intensity
C	0.938+/-0.001	3 +/- 0.015	0.745 – 0.750	High Intensity

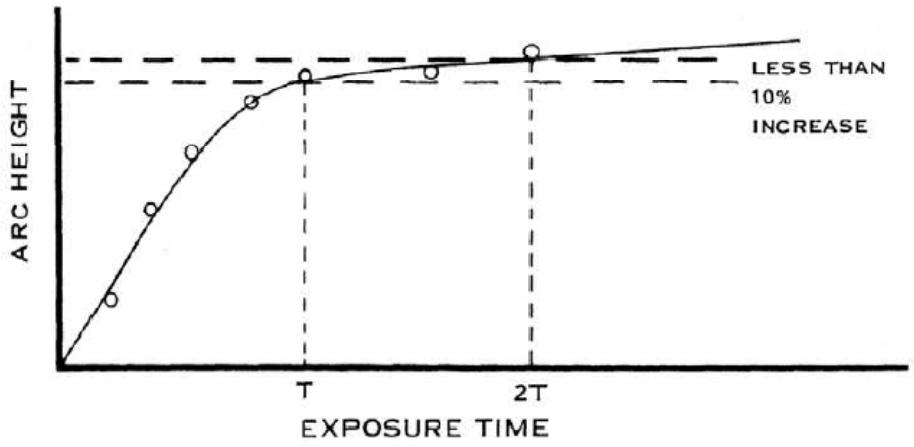

Figure 1.5: Schematic saturation curve (Champaigne, 2001).

In order to determine the Almen intensity of a given process, a certain number of strips must be peened using the same peening parameters but for different exposure times. A saturation curve is then obtained by plotting the arc height deflection of the different strips as a function of exposure time. Saturation time (T) is the earliest point on the curve where doubling the exposure time ($2T$) produces no more than a 10% increase in arc height. Almen intensity is the particular arc height obtained at saturation time (indicated as T in Figure 1.5). Complete procedures can be found in SAEJ442 and SAEJ443.

1.3.2 Surface coverage

Coverage is defined as the ratio of the area covered by peening indentations to the complete surface being treated, expressed as a percentage. Visual inspection is the standard method for coverage evaluation. For practical reasons, the maximum coverage that can be assessed visually is around 98%, since coverage percentages are difficult to discriminate as 100% coverage is approached. Thus 98% surface coverage is usually considered as full coverage according to SAE 2277. Moreover, 200% coverage is defined as peening twice the exposure time required achieving full coverage (98%).

Kirk and Abyaneh (1993), and Kirk (2002, 2005) discussed the theory of coverage developed for random indentations, which assumes that randomly distributed shot particles arrive at the component's surface at a constant rate and create circular indentations of a constant size. A

simplified treatment of the theoretical basis of coverage control is presented, based on the application of an Avrami equation (Kirk and Abyaneh, 1993; Karuppanan et al. 2002).

Karuppanan et al. (2002) presented two theoretical models to predict the development of coverage. One is the Avrami equation which requires determination of indentation radius and shot spread area, the other is the Holdgate model which requires determination of the coverage ratio after an initial interval time of shot peening. All these required parameters are determined from experimental tests.

1.3.3 Surface roughness

Shot peening produces compressive residual stress in the target component, however, it increases surface roughness at the same time. The two most common roughness parameters used in the field of shot peening are peak-to-valley roughness PV and average roughness Ra as shown in Figure 1.6. PV value is defined as the distance between the highest peak R_{pe} and the lowest valley R_v, as in Equation (1.1). Average roughness Ra is defined as the arithmetic average deviation of a surface from a mean line. For a sample length L, it can be obtained with Equation (1.2).

$$PV = R_{pe} + R_v \tag{1.1}$$

$$Ra = \frac{1}{L}\int_0^L |Z(x)|\mathrm{d}x \tag{1.2}$$

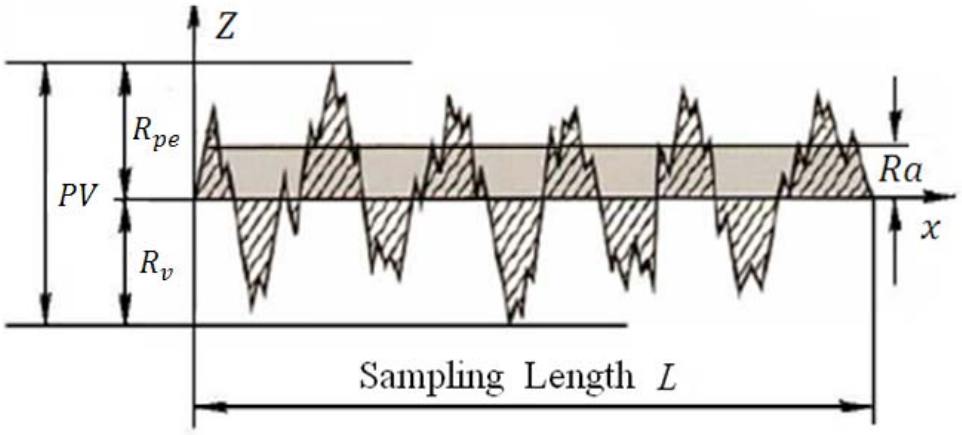

Figure 1.6: Roughness definition.

1.3.4 Influence of Almen intensity and surface coverage on the shot peening effects (residual stress and surface roughness)

Balcar and Maltby (1981) conducted a study showing the influence of Almen intensity on surface roughness. The study was carried out on shot peened A.I.S.I. 316 stainless steel, 2024-T351 and 7075-T6 aluminum alloys, using four different sizes of glass beads and three different projection angles. Bignonnet et al. (1987) studied the influence of surface coverage on the shape of the compressive residual stress field and on surface roughness for two different Almen intensities. Fathallah (1994) investigated the influence of Almen intensity and surface coverage on the shape of the compressive residual stress field. Experiments were conducted with two different shot types. Herzog et al. (1996) studied the influence of Almen intensity on the shape of the compressive residual stress field on shot peened aluminum alloy Al7020 and steel X35CrMo17 specimens, for different shot types. Torres and Voorwald (2002) evaluated the shot peening intensity, residual stress on the fatigue life of AISI 4340 steel.

From these studies, the following conclusions can be drawn:

- *Influence of Almen intensity on residual stress profiles:* Almen intensity had only influence on the depth of the compressive residual stress t_1. With the increase of Almen intensity, t_1 increases, which has beneficial effect in preventing crack propagation. Almen intensity had no significant influence on the surface residual stress σ_{sur} and the maximum residual stress σ_{max} (Fathallah, 1994, Herzog et al. 1996, Torres and Voorwald, 2002).
- *Influence of surface coverage on residual stress profiles:* increasing the surface coverage caused an increase of the compressive residual stress depth t_1 and had no significant influence on the surface residual stress σ_{sur} and the maximum residual stress σ_{max} (Fathallah, 1994, Bignonnet et al. 1987).
- *Influence of Almen on surface roughness:* surface roughness increased with the increase of Almen intensity (Balcar and Maltby, 1981), which has detrimental effect on fatigue life of peened component.
- *Influence of surface coverage on surface roughness:* an increase of surface coverage resulted in an important increase in the surface roughness (Bignonnet et al. 1987).

Since compressive residual stress has beneficial effect, while roughness has detrimental effect, therefore, shot peening results depend on the tradeoff between these two peening results.

1.4 Finite element simulation of shot peening

1.4.1 Existing Finite Element models

Shot peening is a hybrid process involving elasticity and plasticity as well as static and dynamic effects. The theoretical studies of the shot peening process have been rather limited over the past several decades (Al-Obaid, 1995; Kobayashi et al. 1998). Numerical simulation of the process was made possible with the development of the finite element method and the rapid development of computational power. One of the first finite element simulations was carried out by (Al-Obaid,

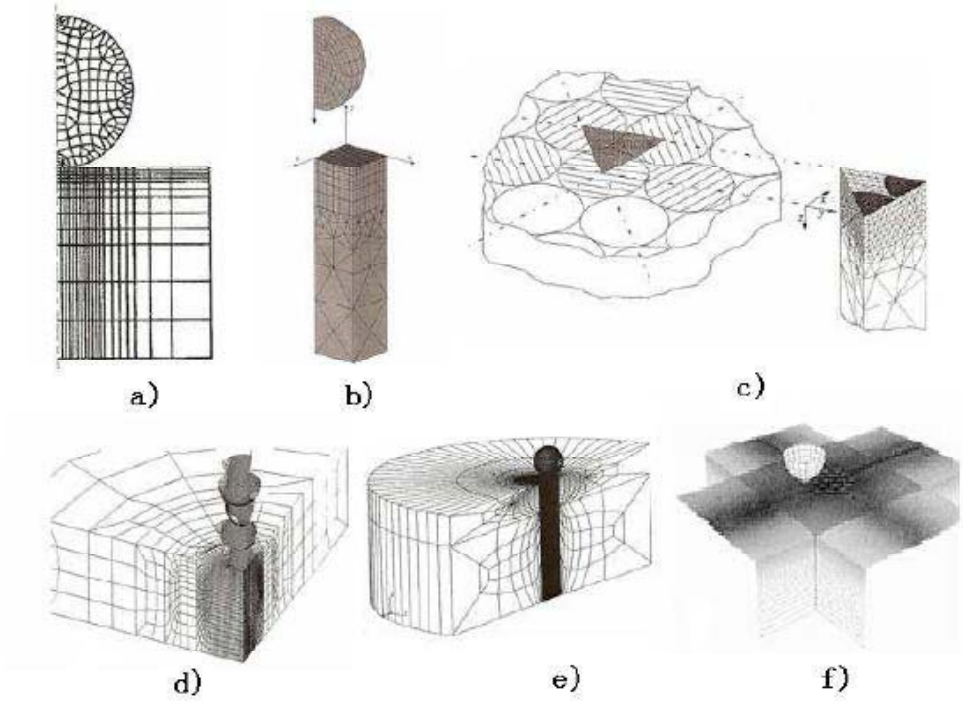

Figure 1.7: Six types of existing models for simulating the shot peening process: a) 2D axisymmtric model (Mori et al. 1994); b) 3D model with four symmetry surfaces (Meguid et al. 2002); c) 3D model with three symmetry surfaces (Schiffner and Droste gen. Helling, 1999); d) 3D model with two symmetry surfaces (Guagliano, 2001); e) 3D model with one symmetry surface (Baragetti, 2001); f) 3D model without symmetry (Schwarzer et al. 2003).

1990b) using 3D isoparametric solid elements and a mesh consisting of nine layers of elements through the thickness of a target plate. Subsequently, six main types of finite element models have been established to simulate the shot peening process:

(1) Mori et al. (1994) introduced an axisymmetric model to simulate the plastic deformation of the workpiece and the shot as shown in Figure 1.7a). Levers and Prior (1995) performed a 2D dynamic analysis with a deformable component and a rigid spherical shot to study the residual stress profile induced by shot peening. Schiffner and Droste gen. Helling (1999) used a similar axisymmetric model for simulating the residual stress profile in an elastic-plastic surface subjected to perpendicular shots with different shot peening parameters. Rouhaud and Deslaef (2002) and Rouhaud et al. (2005) investigated the influence of the shot and component material properties upon the residual stress profiles with a similar axisymmetric model. Meo and Vignjevic (2003) predicted the residual stress profile resulting from the shot peening process with this type of model for welded joints applications.

(2) Meguid et al. (2002) developed a periodic symmetry cell with a square contact surface as shown in Figure 1.7b). The main advantage of this model is its ability to simulate multiple impacts with a reduced model size. Majzoobi et al. (2005) investigated the effects of shot velocity upon the residual stress profile and the development of the shot peening coverage. Meguid et al. (2005) implemented a slightly different cell that consisted of 5 simple unit cells to study the relaxation of peening residual stresses due to cyclic thermo-mechanical overload.

(3) Schiffner and Droste gen. Helling (1999) created a 3D model with an equilateral triangle impact surface and three symmetry surfaces to investigate the effect of adjacent shots, as shown in Figure 1.7c). Their results showed that the interaction between adjacent shots should be taken into account.

(4) Edberg et al. (1995) simulated multiple impingements between the shots and a surface using a 3D model with two symmetry surfaces as shown in Figure 1.7d). Meguid et al. (1999a; 1999b) used this kind of model to study the residual stress profiles resulting from single and twin indentations. The effect of the separation distance between two impinging shots on the equivalent stress contours and residual stresses was presented. Deslaef et al. (2000) and Guagliano (2001) employed a similar model with four impacts (being equivalent to nine impacts due to the symmetry of the problem) to predict residual stresses. Guagliano (2001)

related these stresses to Almen intensity. Al-Hassani et al. (1999) used this type of model to simulate single and multiple impacts with an in-line configuration.

(5) Al-Hassani et al. (1999) developed a half circular 3D finite element model with one symmetry surface as shown in Figure 1.7e) to simulate a single shot impact with an oblique incidence angle. Guagliano et al. (1999) and Baragetti (2001) used a similar model to study the residual stress profiles produced by one and two shot impacts. Hong et al. (2008a) conducted a parametric study based on that model to investigate the effect of shot diameter, impact velocity, incident angle and component material properties on the residual stress profile.

(6) Schwarzer et al. (2003) implemented a 3D model without symmetry boundary condition as shown in Figure 1.7f). This model is more representative than the previous models as it considers independent impacts. Their results showed that the impact sequence has a great influence upon the shot peening results.

Among these six types of models, the axisymmetric model in Figure 1.7a) is the smallest model in terms of degrees of freedom. Therefore, it allows conducting parametric studies of the shot peening process within a relatively short time. However, it does not represent the real shot peening process since all simulated impacts take place over a single location. Figure 1.7b) and c) represent infinite components with fewer elements. In these models, numerous shots impact the component simultaneously due to the symmetry conditions imposed. Models Figure 1.7d) – f) represent more accurately the real shot peening process at the cost of computer resources. In addition, models Figure 1.7a) – d) can only simulate normal impacts. In all of these existing models, the locations and sequence of the multiple shot impacts have been defined a priori (Meguid et al. 2002; Majzoobi et al. 2005; Meguid et al. 2005).

1.4.2 Effect of shot peening parameters with FE analysis

1.4.2.1 Effect of shot velocity and shot size

Al-Obaid (1990b) analyzed the influence of shot velocity on the residual stress profile with a three-dimensional dynamic finite element model that considered the elastoplasticity of the target. Meguid et al. (1999a, 1999b) studied the effect of the shot velocity, size and shape upon the time histories of the equivalent stress trajectories, equivalent plastic strain and unloading residual

stresses with the FE method. Schiffner and Droste gen. Helling (1999) simulated the residual stresses in accordance with the shot peening parameters, such as shot velocity, diameter and material parameters, with an axisymmetric and a 3-Dimensional FE model.

Guagliano (2001) calculated the influence of shot velocity and shot size on the residual stress profiles with a FE model as shown in Figure 1.7d). The simulated results shown in Figure 1.8 indicate that the depth of the maximum compressive residual stress (t_1) and the depth where the residual stress changes sign (t_2) increase with increasing shot velocity and shot diameter. However, with increasing shot velocity, the surface residual stress σ_{sur} decreases. Deslaef et al. (2000) studied various shot peening parameters, such as the shot size and velocity, with the numerical method and by experimentation. The results showed that the residual stress field reached a saturated state after a limited number of impacts. Majzoobi et al. (2005) studied the effect of velocity and peening coverage on the compressive residual stress profiles and the results showed that the residual stress distribution was highly dependent on impact velocity and a uniform state of stress was achieved at a particular shot number.

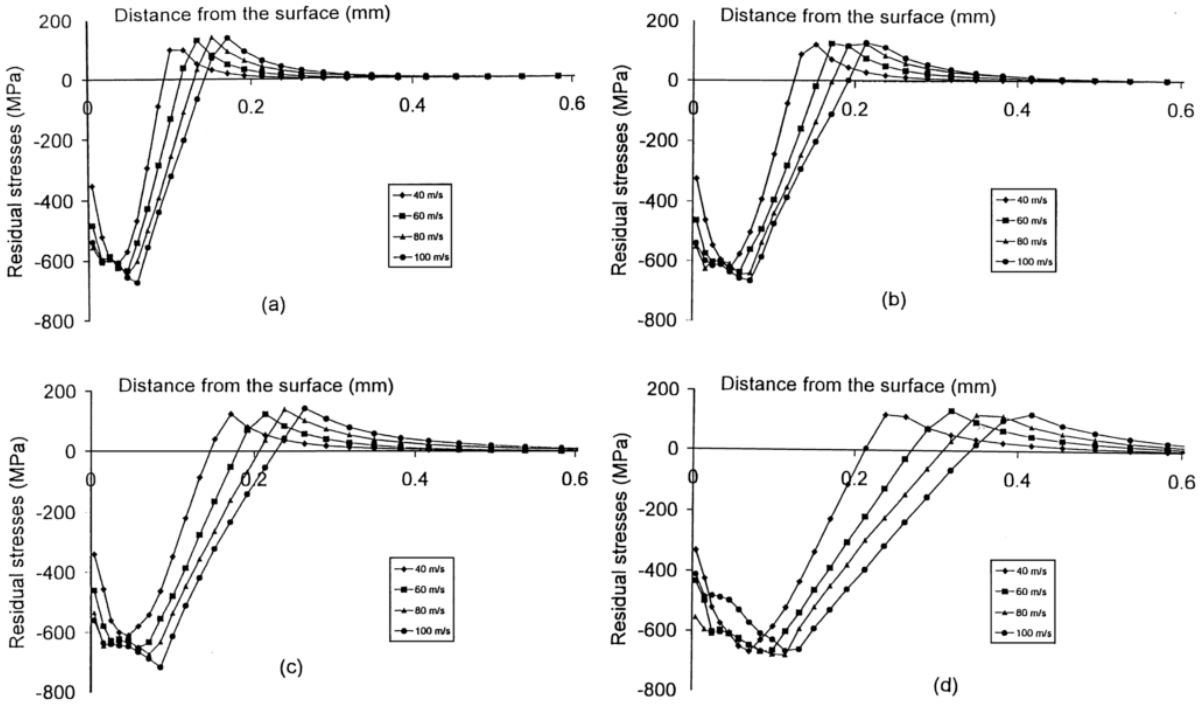

Figure 1.8: Residual stress profiles due to shot peening in a thick component, with different shot diameters and at different shot velocities. (a) Shot diameter 0.3mm, (b) Shot diameter 0.5mm, (c) Shot diameter 0.7mm, (d) Shot diameter 1.0mm (Guagliano, 2001).

1.4.2.2 Effect of material properties

Schwarzer et al. (2003) studied the influence of the material behaviour on residual stress using a 3D finite element model without symmetry. The results showed that higher yield stress caused significantly higher surface and maximum residual stress values. Compared with isotropic material behaviour, the target with kinematic hardening caused a slight reduction of maximum compressive stress. In conclusion, the residual stress produced by shot peening is mainly determined by its yield stress and not by its hardening behaviour.

Rouhaud et al. (2005) studied the effects of target material behaviour on residual stress with a 2D model using multiple shot of radius 0.4mm with velocities 75m/s. Bilinear stress strain constitutive law with different hardening parameters ($H^1 = \frac{\sigma_b - \sigma_s}{\varepsilon_b - \varepsilon_s}$, where σ_b is ultimate tensile stress, σ_s is yield stress, ε_b is strain at ultimate tensile stress and ε_s is strain at yield stress) has been applied in his study. The results of one isotropic hardening model and three kinematic models are shown in Figure 1.9. The analyzed results showed that for the kinematic model, the profile of the residual stress had greatly changed in shape with the change of hardening slope. With increments of hardening slope, the compressive stress near the surface first decreased, and then increased to reach maximum value, and then decreased again to reach a tensile stress. However, for the isotropic model, the surface compressive residual stress increases with the increase of the depth to reach maximum value and then decreases to tensile stress, which was closer to the shape of the experimentally measured residual stress profile as shown in Figure 1.3.

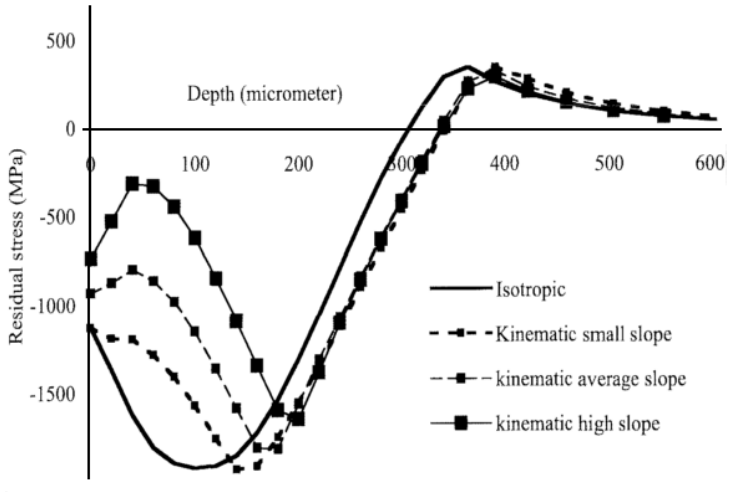

Figure 1.9: Relationship between Residual stress and material constitutive laws (Rouhaud et al. 2005).

1.4.2.3 Effect of friction between shot and component

Meguid et al. (2002) studied the effect of friction with the Coulomb friction model, expressed as

$$F_f = \mu F_n \tag{1.3}$$

where F_f is the friction force, F_n is the normal force and μ is the friction coefficient.

Meo and Vignjevic (2003) studied the effect the friction also with the Coulomb friction model. Significant differences were found in the residual stress field between a frictionless impact and an impact with a coefficient of friction of 0.1. However, the variation of the residual stress and plastic strain was negligible for $0.1 < \mu < 0.5$. Therefore, 0.1 was selected to simulate the Coulomb friction coefficient between the shot and the target. Schwarzer et al. (2003) used a coefficient of friction of 0.4 to describe the contact between the shot and target.

1.5 Process of peen forming

1.5.1 Conventional peen forming

The peen forming technique has been used to curve wing skins since 1968, and ranks as one of the major advances in aircraft manufacturing technique (Baughman, 1984). It is accomplished by peening one or both sides of the component part with varying shot peening intensities so that the part obtains the desired contour shape.

After the surface of the component is repeatedly hit by high velocity shots, a thin plastic layer will cause compressive stress on the top layer and tensile stress beneath the impact points, as shown in Figure 1.10. For a constrained component (*i.e.* clamped at its extremities), this induced stress is in non-equilibrium. After the release of the boundary conditions, a permanent convex curvature will result and the non-equilibrium stress field in the component will be released so that it leads to a balanced residual stress field. Therefore, residual stress can be regarded as the results of an equivalent stretching and bending stresses acting in a manner to balance the induced stresses.

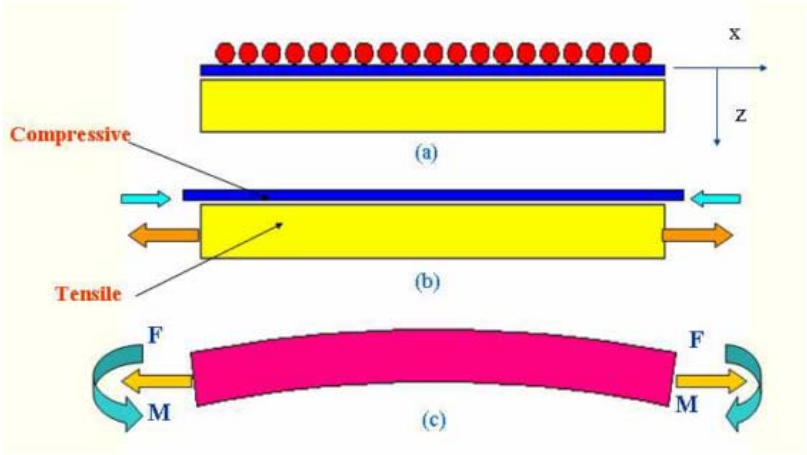

Figure 1.10: Peen forming procedure: (a) Multiple shots impact a thin component. (b) Top plastic deformation and compressive stress. (c) Stretching force F and bending moment M , which cause component to extend and bend.

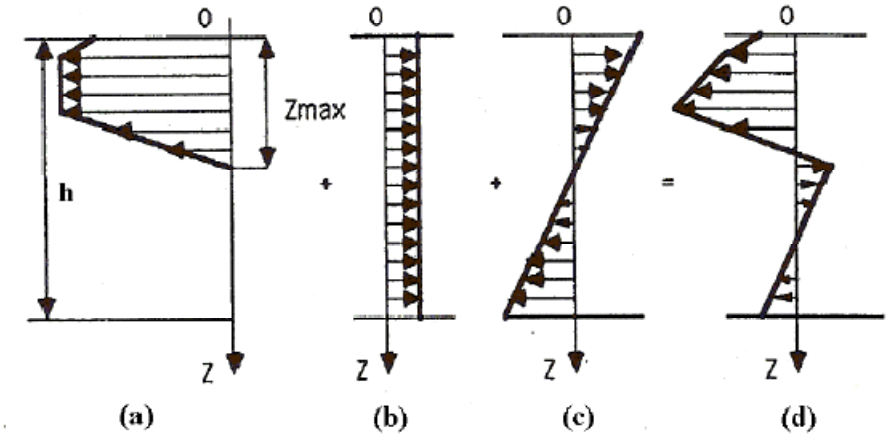

Figure 1.11: Schematic illustration of the residual stresses after peen forming: (a) Induced stress profile σ^{ind}. (b) Stretching stress profile σ^{s}. (c) Bending stress profile σ^{b}. (d) Residual stress profile σ^{res} (Guechichi, 1986).

Guechichi (1986) assumed the distribution of residual stresses in a plate as shown in Figure 1.11. The distribution of the residual stress profile in a thin plate results from the summation of three stress profiles: the induced stress profile caused by shot peening on an infinite plate, Figure 1.11(a); the stretching stress profile, in Figure 1.11(b) and the bending stress profile, in Figure 1.11(c). Therefore:

$$\sigma^{res} = \sigma^{ind} + \sigma^{s} + \sigma^{b} \tag{1.4}$$

Peening induced stresses in a component are complicated and difficult to obtain. Al-Hassani (1981) assumed a cosine function to express the induced stress profile. Vanluchene et al. (1995) and Vanluchene and Cramer (1996) obtained empirical equations from experiments to relate the induced stresses and the arc height (i.e. the deflection) of normalized Almen strips (Almen and Black, 1963). Guagliano (2001) and Han et al. (2002) developed finite element models to predict the induced stress profiles created by shot peening and related these induced stresses to arc heights.

Vanluchene et al. (1995) developed a method to predict the peening pattern and to minimize the peening intensity needed to form a specific shape using a finite element package along with an optimization software. This method simplified the induced stress profile as the sum of a bending stress and a stretching stress and calculated the total induced stress needed on the top and the bottom of the component according to the target forming shape. Several shot peening experiments with different shot peening intensities were carried out in order to relate the induced stresses to the shot peening intensities and the resulting arc heights. Generating a cylinder from a rectangular plate with dimensions of $48\text{in}\times144\text{in}\times0.25\text{in}$ was selected to test the developed software. Percentage errors between 30% to 52% have been obtained at 9 measurement points when compared to the target values.

Han et al. (2002) performed a two-stage explicit/implicit simulation of the peen forming process. At the first stage, the induced stress/strain profile was obtained by employing the finite element approach on a small scale sample problem. At the second stage, this induced profile was applied to the entire workpiece to calculate the final deformation and stress distribution using an implicit static analysis.

Figure 1.12 illustrates the re-distributed equilibrated residual stress profiles for two impact velocities. It is interesting to note that although shot peening was performed only on one side of the component, the forming result presented compressive stress on both sides of the component. These compressive stresses serve to inhibit stress corrosion cracking and to improve fatigue life of the peen formed component.

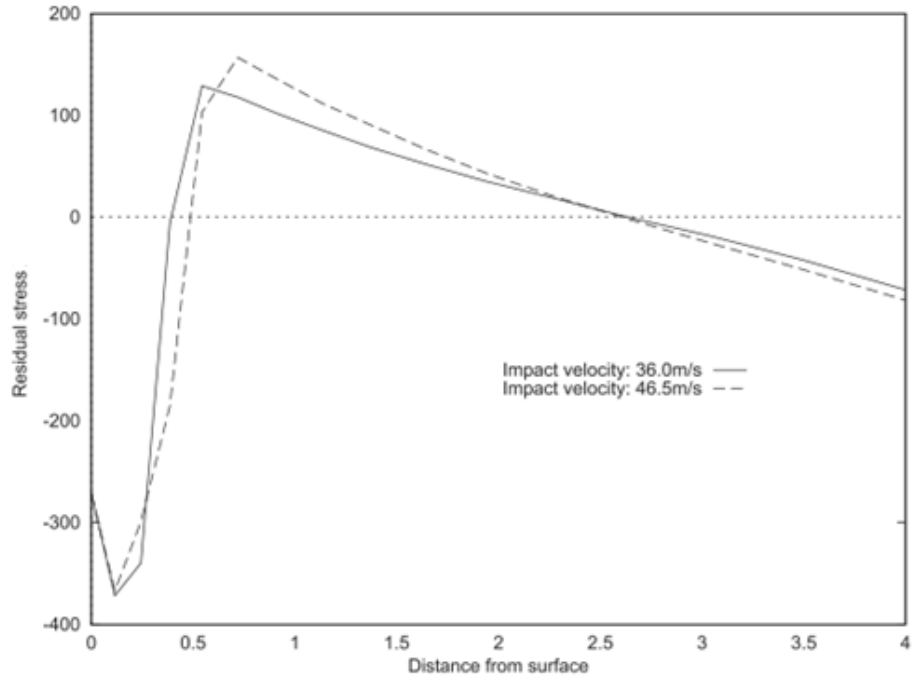

Figure 1.12: Residual stress after peen forming (Han et al. 2002).

1.5.2 Stress peen forming

Conventional peen forming causes the component to acquire a doubly curved shape because it induces an isotropic residual stress distribution in the component and a convex curvature of the component towards the peening direction. For a wing skin, which has a larger curvature in chordwise direction than in spanwise direction, a technique called stress peen forming is applied.

Li (1981) analyzed the features of stress peen forming, described the forming principles and performed experimental studies. The author drew the conclusion from the analysis that if the wing panel is elastically pre-bent in the chordwise direction during peen forming, the chordwise contour curvature will be further increased, and at the same time the spanwise contour curvature will be decreased. Thus the trend in conventional peen forming of a panel taking on a spherical shape can be counteracted by using stress peen forming to a great extent. In addition, the results of experiments showed that the radius of curvature in the pre-bending direction is inversely proportional to the peening pressure, the shot size and the pre-bending value under saturated peen forming conditions.

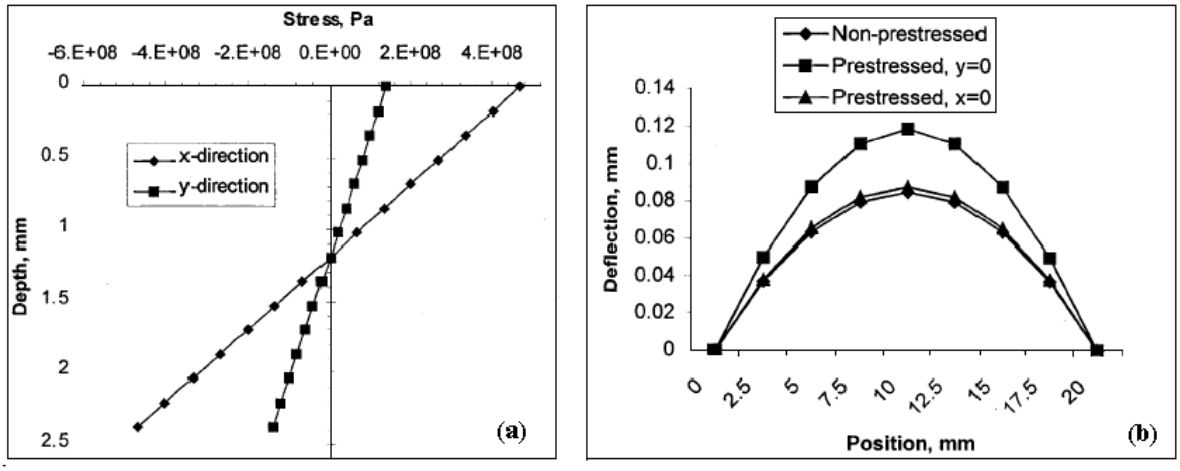

Figure 1.13: Deflection of the component due to peen forming and stress peen forming: (a) Pre-stress values on the component in the x and y directions, respectively. (b) Deflections of the component in the x and y directions under different peen forming conditions (Gardiner and Platts, 1999).

Gardiner and Platts (1999) simulated the induced stress profile involved in stress peen forming by applying temperature distributions in shell elements. In the case of stress peen forming, different temperature profiles following the depth of the component were applied to produce differential effects in the x and y directions, so that different curvatures can be produced in each direction. Figure 1.13 presents the pre-stress condition and the resulting deflections of a square plate with dimensions $20\text{mm} \times 20\text{mm}$. The results show that stress peen forming produced a larger deflection in the pre-stressed direction compared to conventional peen forming.

1.6 Summary of the findings

Shot peening is accomplished by bombarding the surface of the component with numerous shots at high velocities. After shot peening, a layer of compressive residual stress is produced which can postpone crack prorogation and improve the fatigue life of the component. Almen intensity and surface coverage are two important control parameters used to ensure the repeatability of shot peening. Most evaluations of the influence of intensity and surface coverage on the shot peening results were based on experiments that are generally costly, tedious and time consuming. Six types of finite element models have been established to simulate the shot peening process,

with the assumptions that the location and sequence of impacts have no influence on the shot peening results. With these finite element models, the influences of shot velocity, shot type, shot size, shot peening angles, and distance between shot on the shot peening results were studied. In order to simulate the peen forming procedure, an induced stress obtained from explicit analysis was used to calculate residual stress profiles after peen forming. Most of studies of stress peen forming, however, were based on experimental trial and error.

CHAPITRE 2 OBJECTIVE AND RATIONALE OF THE PROJECT

The principal objective of this work is to study numerically, experimentally and analytically the results of the shot peening process and its application to forming. Based on the literature survey performed, four main aspects requiring attention were identified and led to the four sub-objectives studied in this work, namely

1. The literature survey showed that most of the existing numerical analyses did not take into account the stochastic aspect of the shot peening process. The first sub-objective of this study is to develop a new FE model that allows taking into account both the spatial and temporal random nature of the shot stream hitting a metallic surface. Different from all of the existing FE models, this FE model considers numerous randomly distributed peening shots. This should lead to more realistic simulations than the existing models and will allow studying the influence of shot peening parameters (shot diameters, velocity, peening time, etc.) on the shot peening control variables (Almen intensity, coverage, roughness).
2. There is very little experimental data on stress peen forming in the literature. Controlled experiments, where the shot peening parameters are precisely known and where reliable residual stress distributions are obtained would be of considerable interest for validating any predictive tool. The second objective of this study is to perform stress peen forming experiments on aluminum 2024 test strips where the shot peening parameters are rigorously controlled and where residual stress profiles are obtained.
3. There is also very little computational study of stress peen forming. The third objective is to create an Implicit-Explicit-Implicit three-step FE model to simulate the stress peen forming process. With this model, the relationship between the prebending moment and the resulting arc height as well as its influence on the resulting residual stress profile, can be obtained.
4. Finally, although they have the potential of leading to very accurate predictions, computational models are time and resources consuming. It would be a great interest to develop relatively precise analytical tools for predicting the residual stresses and Almen

intensity (which is in fact peen forming). These tools could be used for generating the initial solution in an optimization process where the final tuning is performed with the computational models. The development of such analytical models is the fourth and final objective of this thesis.

At the end of this study, predictive tools for the results of shot peening and peen forming should have been developed and tested. These tools will form a basis for future projects concerned with the optimization of the shot peening and peen forming processes.

CHAPITRE 3 SCIENTIFIC APPROACH AND COHERENCE WITH RESEARCH OBJECTIVES

This thesis is organized into four sections, consisting of the four research articles that were generated from the thesis study in order to reach the four objectives listed at the previous chapter. In the following lines, each article is summarized and it is shown how it meets the objectives set for the project as well as the novelty introduced.

3.1 Article 1: On the potential applications of a 3D random finite element model for the simulation of shot peening (Objective 1)

This article presents a novel 3D shot peening model based on the comparison of the existing FE models. In most of the existing FE models, the shot peening sequence and impact location were defined *a priori*. Therefore, the purpose of this article is to consider the random nature of the shot peening process, which has never been done. This 3D FE model with multiple randomly distributed shots was developed combining a Matlab program with the ANSYS preprocessor. The explicit solver LS-DYNA has been used to simulate the dynamic impingement process.

The main contributions of this paper are:

- Development of a novel 3D FE model with the ability to simulate randomly distributed shots.
- Establishing a relationship between resulting arc height and number of peening shots. With this relationship, shot peening intensity can be simulated.
- Establishing a relationship between surface coverage and number of peening shots.
- Establishing a relationship between surface roughness and number of peening shots.
- Characterization of the influence of peening angle on peening results, such as intensity, surface coverage and roughness, as well as residual stress.

This article was published in the journal *Advances in Engineering Software*, 2009, Vol. 40, pp.1023-1038. The objective of this journal is to communicate recent and projected advances in computer-based engineering techniques. This article was written almost entirely by the author of this thesis.

This article explains the basic concepts and technical terms used in shot peening, such as intensity and coverage, as simulated with the novel 3D FE model. As stated in its title, this paper presents potential applications that are validated in the second paper.

3.2 Article 2: Experimental study of shot peening and stress peen forming (Objective 2)

This article introduces shot peening and stress peen forming experiments designed by the author of this thesis. In this article, the relationship between peening intensity and surface coverage with respect to peening time was established for aluminum 2024.

Another purpose of this article is to perform a stress peen forming process and to determine the quantitative relationship between the prebending moment and the resulting arc height.

The main original contributions of this paper are:

- Establishment of a quantitative relationship between resulting arc height and peening time. With this relationship, shot peening intensity and saturation time can be calculated.
- Establishment of a quantitative relationship between peening surface coverage and peening time.
- Establishment of a quantitative relationship between peening surface roughness and peening time.
- Measurement by X-Ray Diffraction (XRD) of residual stress profiles after shot peening on a thick component, after conventional peen forming and stress peen forming.
- Establishment of a quantitative relationship between prebending conditions (prebending moment) and resulting arc height and radius of curvature with a pre-stressing device designed by the author of this thesis.

This article was accepted by the *Journal of Material Processing Technology*. This journal covers the processing techniques used in manufacturing components from metals and other materials. This article was written almost entirely by the author of this thesis.

This article introduces the shot peening procedure, equipment as well as the shot peening and stress peening results in the experiments. The experimental results under different shot peening

conditions have been used to validate the developed FE models introduced in the first and third papers.

The procedure and the device in the experiments were all designed by the author of this thesis. The operation of the shot peening machine and robot during the shot peening and stress peen forming processes were performed with the help of Dave Demers (Second author of this article), a bachelor student at École Polytechnique de Montréal.

3.3 Article 3: A numerical study of the stress peen forming process (Objective 3)

This article presents a numerical study of the stress peen forming process. In this article, a three-step numerical model was developed to simulate the stress peen forming process.

The main contributions of this paper are:

- Development of an implicit-explicit-implicit FE procedure to simulate stress peen forming successfully. Firstly, an implicit FE model with ANSYS was established to simulate the pre-stress process. Secondly, an explicit FE model was developed, the same as is introduced in the first article (Chapter 4), and was used to simulate the dynamic shot peening process. Finally, an implicit FE model with ANSYS was developed to calculate deformed arc height and radius of curvature after stress peen forming.
- Establishment of a relationship between the prebending moment and the resulting arc height and radius of curvature.
- A comparison is presented of the predicted numerical results with the experimental results presented in article 2 (Chapter 5). The relatively good fit to the experimental results shows that both the novel 3D FE model described in the first article, as well as the three-step FE model described in this article, are both practical and reliable.

This article was submitted to the journal *Advances in Engineering Software*, on April 21st, 2010. The objective of this journal is to communicate recent and projected advances in computer-based engineering techniques. This article was written almost entirely by the author of this thesis.

3.4 Article 4: An analytical approach to relate shot peening parameters to Almen intensity (Objective 4)

This article analyzes the shot peening process theoretically and presents an analytical model based on Hertz contact theory for the prediction of Almen intensity and residual stress distribution for an Almen strip. With this model, the influence of shot peening parameters, such as shot type (steel and ceramic), size, velocity and peening angle on the Almen intensity, can be studied easily.

The main contributions of this article include:

- An explanation of the shot peening principles as well as the internal stress profiles during impingement, after rebound of shot and after the release of boundary conditions of the Almen strip.
- The development of an analytical model that can predict the Almen intensity and shot-induced residual stress for Almen strips, for any combination of peening parameters (shot type, size, velocity, peening angle). The model was solved with MATLAB, the calculation for each case takes only a few seconds, while the calculation with the 3D random FE model takes several days.
- The study of the effect of shot velocity and size on the resulting Almen intensity. These results can be used as a tool for determining the various possible combinations of peening parameters required to obtain given Almen intensities.

This article was submitted to the journal *Surface and Coating Technology* on February 15th 2010. This journal is an international archival journal that publishes scientific papers on surface and interface engineering. This article was written almost entirely by the author of this thesis.

CHAPITRE 4 ON THE POTENTIAL APPLICATIONS OF A 3D RANDOM FINITE ELEMENT MODEL FOR THE SIMULATION OF SHOT PEENING

H.Y. Miao, S. Larose, C. Perron, Martin Lévesque, *Advances in Engineering Software,* 40, pp. 1023-1038, 2009.

4.1 Abstract

Shot peening is a cold-working process that is used mainly to improve the fatigue life of metallic components. Experimental investigation of the mechanisms involved in shot peening is very expensive and complicated. Therefore, the Finite Element (FE) method has been recognized as an effective mean for characterizing the shot peening process and several types of FE models have been developed to evaluate the effects of shot peening parameters. However, in most of the existing FE models, the shot peening sequence and impact location were defined a priori. It is therefore the purpose of this study to consider the random property of the shot peening process. A novel 3D FE model with multiple randomly distributed shots was developed combining a Matlab program with the ANSYS preprocessor. The explicit solver LS-DYNA has been used to simulate the dynamic impingement process. Several potential applications of this novel model such as: the quantitative relationships of the peening intensity, coverage and roughness with respect to the number of shots have been presented. Moreover, simulations with multiple oblique impacts have been carried out in order to compare with results from normal impingements. Our work shows that such a computing strategy can help understanding and predicting the shot peening results better than conventional FE simulations.

4.2 Introduction

Shot peening is a mechanical surface treatment widely used to improve the fatigue life of metallic components in the aerospace and automobile industries. This process is accomplished by bombarding the surface of a metallic component with shots at high velocities. Each shot acts as a tiny peening hammer, compressing and stretching the metallic surface. An indentation surrounded by a plastic region is created during this impingement. The plastic deformation leads to a residual stress profile through the thickness of the component. This residual stress profile is

compressive at the top surface and tensile in the thickness of the component in order to ensure equilibrium. The layer of compressive residual stress reduces the likelihood of premature failure under cyclic loading conditions (Meguid, 1975; Webster and Ezeilo, 2001; Rodopoulos et al. 2004).

Several studies dealt with the theoretical aspects of shot peening (Meguid, 1975; Al-Obaid, 1995; Kobayashi et al. 1998). Numerical simulation of the process was made possible with the development of the finite element method and the rapid development of computational power. Subsequently, six main types of finite element models have been established to simulate the shot peening process:

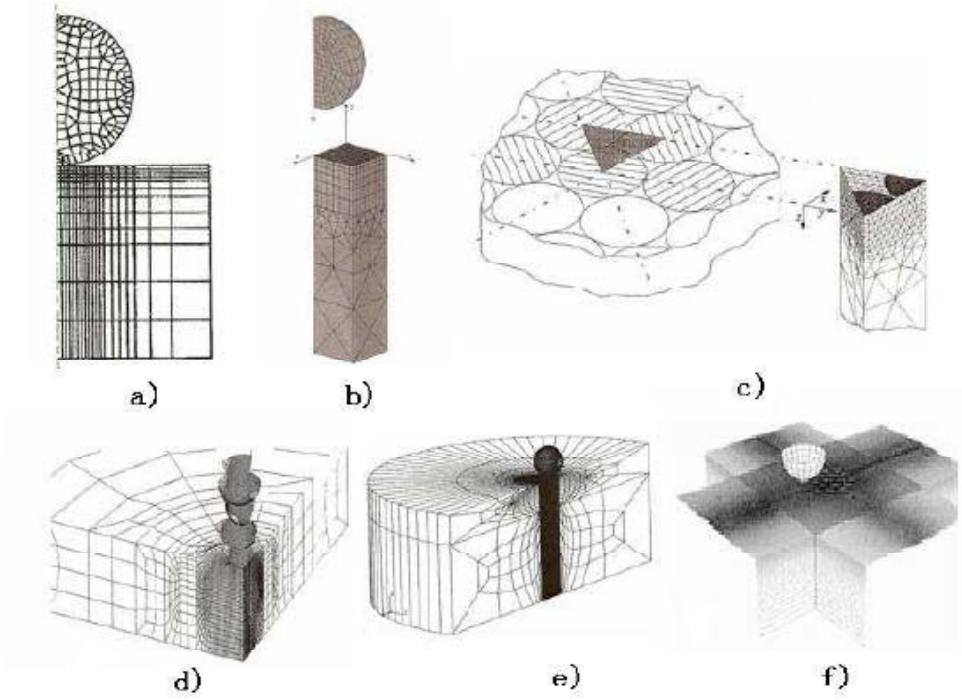

Figure 4.1 Six types of existing models for simulating the shot peening process: a) 2D axisymmtric model (Mori et al. 1994); b) 3D model with four symmetry surfaces (Meguid et al. 2002); c) 3D model with three symmetry surfaces (Schiffner and Droste gen. Helling, 1999); d) 3D model with two symmetry surfaces (Guagliano, 2001); e) 3D model with one symmetry surface (Baragetti, 2001); f) 3D model without symmetry (Schwarzer et al. 2003).

1) Mori et al. (1994) introduced an axisymmetric model to simulate the plastic deformation of the workpiece and the shot as shown in Figure 1.7a). Levers and Prior (1995) performed a 2D dynamic analysis with a deformable component and a rigid spherical shot to study the residual stress profile induced by shot peening. Schiffner and Droste gen. Helling (1999) used a similar axisymmetric model for simulating the residual stress profile in an elastic-plastic surface subjected to perpendicular shots with different shot peening parameters. Rouhaud and Deslaef (2002) and Rouhaud et al. (2005) investigated the influence of the shot and component material properties upon the residual stress profiles with a similar axisymmetric model. Meo and Vignjevic (2003) predicted the residual stress profile resulting from the shot peening process with this type of model for welded joints applications.

2) Meguid et al. (2002) developed a periodic symmetry cell with a square contact surface as shown in Figure 1.7b). The main advantage of this model is its ability to simulate multiple impacts with a reduced model size. Majzoobi et al. (2005) investigated the effects of shot velocity upon the residual stress profile and the development of the shot peening coverage. Meguid et al. (2005) implemented a slightly different cell that consisted of 5 simple unit cells to study the relaxation of peening residual stresses due to cyclic thermo-mechanical overload.

3) Schiffner and Droste gen. Helling (1999) created a 3D model with an equilateral triangle impact surface and three symmetry surfaces to investigate the effect of adjacent shots, as shown in Figure 1.7c). Their results showed that the interaction between adjacent shots should be taken into account.

4) Edberg et al. (1995) simulated multiple impingements between the shots and a surface using a 3D model with two symmetry surfaces as shown in Figure 1.7d). Meguid et al. (1999a; 1999b) used this kind of model to study the residual stress profiles resulting from single and twin indentations. The effect of the separation distance between two impinging shots on the equivalent stress contours and residual stresses was presented. Deslaef et al. (2000) and Guagliano (2001) employed a similar model with four impacts (being equivalent to nine impacts due to the symmetry of the problem) to predict residual stresses. Guagliano (2001) related these stresses to Almen intensity. Al-Hassani et al. (1999) used this type of model to simulate single and multiple impacts with an in-line configuration.

5) Al-Hassani et al. (1999) developed a half circular 3D finite element model with one symmetry surface as shown in Figure 1.7e) to simulate a single shot impact with an oblique incidence angle. Guagliano et al. (1999) and Baragetti (2001) used a similar model to study the residual stress profiles produced by one and two shot impacts. Hong et al. (2008a) conducted a parametric study based on that model to investigate the effect of shot diameter, impact velocity, incident angle and component material properties on the residual stress profile.

6) Schwarzer et al. (2003) implemented a 3D model without symmetry boundary condition as shown in Figure 1.7f). This model is more representative than the previous models as it considers independent impacts. Their results showed that the impact sequence has a great influence upon the shot peening results.

Among these six types of models, the axisymmetric model in Figure 1.7a) is the smallest model in terms of degrees of freedom. Therefore, it allows conducting parametric studies of the shot peening process within a relatively short time. However, it does not represent the real shot peening process since all simulated impacts take place over a single location. Figure 1.7b) and c) represent infinite components with fewer elements. In these models, numerous shots impact the component simultaneously due to the symmetry conditions imposed. Models Figure 1.7d) – f) represent more accurately the real shot peening process at the cost of computer resources. In addition, models Figure 1.7a) – d) can only simulate normal impacts. In all of these existing models, the locations and sequence of the multiple shot impacts have been defined a priori (Meguid et al. 2002; Majzoobi et al. 2005; Meguid et al. 2005).

Numerous shot peening parameters have a great influence on the effectiveness of the shot peening treatment. These can be classified into three groups: shot, target and flow parameters (Kyriacou, 1996):

- Shot parameters: size, shape, integrity, density, hardness, yield strength, stiffness, etc.
- Target parameters: hardness, yield strength, stiffness, work hardening characteristics, chemical composition, pre-stress condition, etc.
- Flow parameters: mass flow rate, shot velocity, angle of impingement, stand-off distance, etc.

The effects of most of these parameters upon the residual stress profiles have been studied by theoretical analysis and finite element method (Al-Obaid, 1990a; Meguid et al. 1999a; Meguid et al. 1999b; Schiffner and Droste gen. Helling, 1999). However, investigations related to shot peening intensity, surface coverage and surface roughness were performed mainly through experiments (Fathallah, 1994; Herzog et al. 1996; Karuppanan et al. 2002; Bignonnet et al. 1987; Clausen and Stangenberg, 1999).

Peening intensity is an important control parameter for the practical shot peening process. It is related to the amount of kinetic energy transferred from the shot stream to a work piece during the shot peening process (Kyriacou, 1996). A method widely used to quantify peening intensity was introduced by John Almen (Almen and Black, 1963) and is called Almen intensity. The method consists in peening a standardized strip of given dimensions and material, called Almen strip, which is fixed to a mounting fixture by means of four roundhead bolts. Once the bolts are removed, the strip will curve towards the peening direction. The resulting arc heights under different shot peening times can be measured. Shot peening saturation is defined as the point, on the curve of peening time versus arc height, beyond which the arc height increases by less than 10% when the peening time doubles. Guagliano (2001) established a relationship between Almen intensity and the shot peening parameters (shot type, shot velocity and shot size) based on the residual stress profiles beneath the centerline of the impact point. Karuppanan et al. (2002) developed an algorithm for determining the saturation point by means of full regression analysis. They applied Equation (4.1) to fit the experimental data

$$Ah(T) = \frac{B}{(T+d)^p} - \frac{B}{d^p} \tag{4.1}$$

where $Ah(T)$ is the arc height, B, d and p are fitting parameters and T is the peening time.

Coverage is defined as the ratio of the area covered by peening indentations to the total treated surface area, expressed in percentage. Similar to the peening intensity, the effectiveness of the peening treatment depends greatly on the peening coverage (Meguid et al. 2002). Most of coverage studies are based on visual inspection and theoretical models. Visual inspection is the standard method for coverage evaluation. For practical purposes, the maximum coverage that can be assessed visually is around 98%, since coverage percentages are difficult to discriminate as 100% coverage is approached. Thus, 98% surface coverage is usually considered as full coverage. Moreover, 200% coverage is defined as peening twice the exposure time required

achieving full coverage (98%) according to SAE J443. Kirk and Abyaneh (1993) and Kirk (2002, 2005) discussed the theory of coverage for random indentations, which assumes that statistically random shot particles arrive at the component's surface at a constant rate and create circular indents of constant size. A simplified treatment of that theory based on the application of an Avrami equation is presented by Kirk and Abyaneh (1993) as:

$$C_{th}(T) = 100 \times \left(-e^{-\pi \bar{r}^2 RT}\right) \tag{4.2}$$

where $C_{th}(T)$ is the theoretical calculated coverage, $\bar{r}$ is the average radius of the indentations, R is the rate of creation of impacts (number of impacts per unit area per unit time) and T is the peening time.

Equation (4.2) was expressed in terms of peening parameters (Kirk and Abyaneh, 1993) and (Karuppanan et al. 2002) as:

$$C_{th}(T) = 100 \times \left(1 - e^{-\frac{3\bar{r}^2 \dot{m} T}{4\bar{A} r^3 \rho_s}}\right) \tag{4.3}$$

where $\dot{m}$ is the mass flow rate of the shots, $\bar{A}$ is the peening area on the treated component, r is the average radius of the shots and ρ_s is the density of the shots.

It is worth noting that Equations (4.2) and (4.3) rely on the assumption that statistically-random shot particles are impinging an infinitely-large plate at a constant rate and creating circular indents of constant size.

The projection of shots at high velocity produces indentations on the surface of the treated material and results in an increased surface roughness. A surface of higher surface roughness presents more irregularities, which act as stress concentrations and cause a reduction of the fatigue life of the treated component (Sharp et al. 1994). In practice, surface roughness parameters are mainly determined with the help of electronic contact (stylus) instruments. However, the measurement results depend strongly on the selections of the scanning length and the limit wavelength (Clausen and Stangenberg, 1999).

Few investigations have been performed to study the effect of the impingement angle upon the shot peening results. Ebenau et al. (1987) conducted an experimental study of the influence of shot peening angle on the residual stress distributions and the bending fatigue behavior. Their results showed that perpendicular shot peening led to a higher fatigue life than peening with an

angle of 45°. Al-Hassani et al. (1999) simulated a single shot impacting the target at an oblique incidence angle with a finite element model. Schwarzer et al. (2003) studied the influence of the impact angle on the residual stress profile by simulating the impacts of 19 shots. The results showed that normal impacts produce both larger surface and larger maximum compressive residual stress values when compared to oblique impacts.

In light with this literature survey, it is possible to list the limitations of the existing studies:

- In most of the existing finite element models, the shot peening sequence and location were defined *a priori* according to a certain pattern. This is of course an over-simplification of the real shot peening process.
- Most of the investigations related to intensity, coverage and roughness were based on experiments and theory. No numerical study has been performed in order to relate them to shot peening time (or number of shots).
- Almen intensity is defined based on Almen strips made of steel SAE1070, which may be different from the practical peened component. Therefore, it is impossible to establish a direct relationship between the development of coverage on Almen strips and that on the practical component.

The objective of this work is to develop a finite element model that can better simulate the real shot peening process. A 3D finite element model with numerous randomly distributed steel shots bombarding an aluminum component at a certain velocity is developed as an example. With this model, the shot peening intensity, saturation, surface coverage, surface roughness and the angle of impingement can be studied in details. The model provides a useful tool for the designer for guiding his choices of the optimal shot peening parameters.

This article is divided into eight sections. Section 4.3 describes a newly developed 3D random finite element model. Sections 4.4 and 4.5 present simulated curves obtained with the 3D random model for saturation and residual stress profiles after normal and oblique shot peening. Sections 4.6 and 4.7 deal with surface coverage and surface roughness, respectively. Section 4.8 concludes the work and the last section lists future works.

4.3 3D random finite element model

During the shot peening process, numerous shots impact the component at random locations and in a random sequence. The finite element model developed in this paper consists of a large number of identical shots impinging an aluminum target at normal or oblique incidence angles, randomly. In order to simulate these randomly distributed shots, a Matlab program combined with ANSYS APDL (ANSYS Program Design Language) were used to generate the random coordinates of each shot. Explicit solver LS-DYNA has been used to simulate the dynamic impingement process.

It is assumed that all shots are rigid due to their relatively high yield and hardness values, when compared to the target material (Meguid et al. 1999b). All the shots have the same radius ($r = 0.5\text{mm}$), density ($\rho_s = 7800\text{kg/m}^3$), velocity ($v = 50\text{m/s}$) and impact angles (90° or 60°). An aluminum plate with dimensions $5\text{mm} \times 5\text{mm} \times 3\text{mm}$ was selected as the target component in this shot peening model. A Coulomb friction coefficient $\mu = 0.2$ was defined between the shots and the target component since its influence on the residual stresses and plastic strains is negligible for $0.1 < \mu < 0.5$ (Meo and Vignjevic, 2003).

The aluminum is assumed to obey an elasto-plastic behavior with isotropic hardening. In the simulation, the elastic modulus $E = 71.7\text{GPa}$, the Poisson's ratio $\upsilon = 0.33$, the density $\rho_t = 2810\text{kg/m}^3$, the initial yield stress $\sigma_y = 503\text{MPa}$ and the linear strain-hardening parameter $H^1 = 3.3\text{GPa}$ have been selected in the FE calculation. In this study, the potential strain rate sensitivity of the material was not taken into account. Similar assumption were used by other authors for the simulations of the shot peening process (Meguid et al. 1999b; Guagliano, 2001; Rouhaud et al. 2005 and Hong et al. 2008a).

For this 3D non-symmetrical model with multiple shots, the most important limitation in the calculation is the solution time. It is therefore important to use an appropriate meshing since the minimum element size determines the total solution time in the explicit finite element code. After convergence study, an impact area of $2\text{mm} \times 2\text{mm} \times 1\text{mm}$ was discretized into a fine mesh with elements of dimensions $0.05\text{mm} \times 0.05\text{mm} \times 0.05\text{mm}$. Reduced one-node integration was used to decrease the computational time. These simulations required approximately 1GB of RAM. In this

paper, the shot peening parameters, the dimensions of target plate and the material properties of aluminum plate were fixed for the sake of simplicity.

In order to study the relationships between intensity, coverage, roughness and the number of shots, the simulations corresponding to 5 different numbers of shot impacts N= {6, 12, 24, 48 and 96} were carried out. The initial coordinates of these shots were generated with a Matlab program. The origin of the coordinates system is located at the center of the aluminum plate top surface. The z-axis is directed towards the depth direction of the component and the x- and y-axes are along the model sides (see Figure 4.2a). In the case of normal impingement, the coordinates of the center of each shot are obtained by:

$$\begin{aligned} x &= -0.75 + 1.5 \times \mathrm{rand}(1,1) \\ y &= -0.75 + 1.5 \times \mathrm{rand}(1,1) \\ z &= -0.5 - (N-1) \times 0.5 \times \mathrm{rand}(1,1) \end{aligned} \tag{4.4}$$

where $\mathrm{rand}(1,1)$ is a uniform pseudo-random number generator in the interval [0, 1]. After automatic and random generation of shot center position, spherical shots were created and meshed. Then a velocity of 50m/s in the z direction was applied to all shots and the simulation was started.

In the case of 60° oblique impingement, the coordinates of each shot are obtained by:

$$\begin{aligned} y &= -0.75 + 1.5 \times \mathrm{rand}(1,1) \\ x &= -0.75 - (N-1) \times 0.5 \times \mathrm{rand}(1,1) \\ z &= -0.75 + 1.5 \times \mathrm{rand}(1,1) + (z - 0.5)/\tan(60°) \end{aligned} \tag{4.5}$$

For better comparison with normal impacts, the shot velocity was kept constant at $50\mathrm{m/s}$. Thus, a velocity of $50 \times \cos(60°)\mathrm{m/s}$ in x the direction and a velocity of $50 \times \sin(60°)\mathrm{m/s}$ in the z direction were applied to all shots to represent a 60° oblique incidence.

For both cases, the centers of the indentations are located in an area of $1.5\mathrm{mm} \times 1.5\mathrm{mm}$. The coordinates of the first sphere were randomly generated with Equation (4.4) or (4.5). Then for each new sphere, if the distances between all the existing spheres are greater than an assumed value $0.75\mathrm{mm}$, the sphere is accepted. Otherwise, the sphere is rejected and the coordinates of a new sphere are generated until the distance condition mentioned above is reached. This minimum distance value has been set arbitrarily and we believe that it might have some influence upon the final results. Such consideration is let for future studies. In addition, only the contacts between

the shots and the aluminum target have been defined. The contacts between the shots, such as the impact shots and the rebound shots, are ignored for simplicity. Therefore, the shot stream thus simulated could be interpreted as an effective stream. Finally, an APDL code was written with the Matlab program in order to automatically mesh the shots in ANSYS. For each number of shots under investigation, five models were generated in order to study the random aspects of the peening process.

Figure 4.2 shows the model thus developed. Figure 4.2(a) presents 24 random shots perpendicularly impacting the component, Figure 4.2(b) presents 24 random shots impacting the component with an oblique angle of 60° in the xz-plane. The displacements normal to the bottom and four side surfaces of the target block were fixed. The top surface was free.

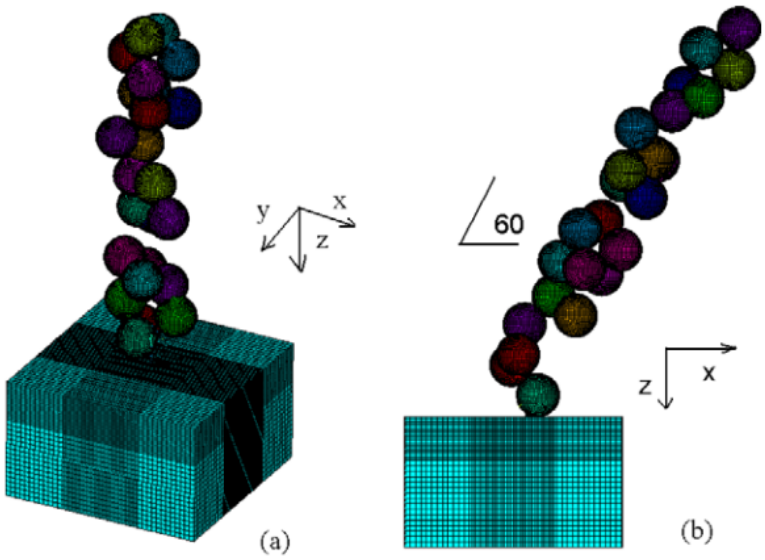

Figure 4.2: Random finite element model: (a) multiple shots impinging an aluminum component at normal incidence; (b) multiple shots impinging an aluminum component at 60° angle of incidence.

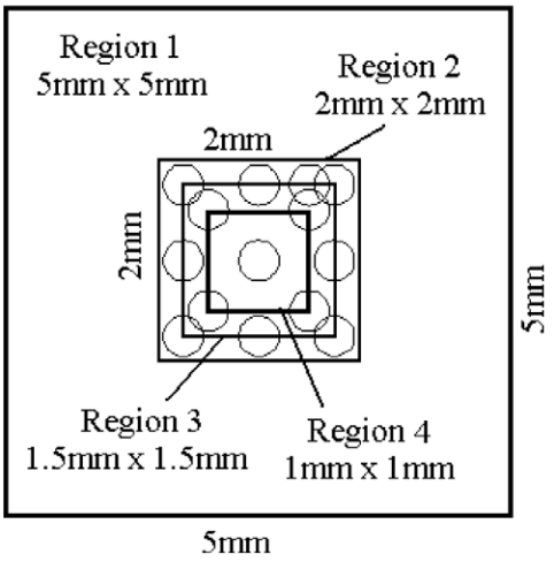

Figure 4.3: Representative surface. (Region 1: aluminum surface. Region 2: fine element region. Region 3: boundary of the shots centers. Region 4: representative surface.)

Figure 4.3 presents the surface impact region and the representative surfaces for the intensity, coverage and roughness studies described in the following sections. Region 1, with dimensions 5mm×5mm, is the total target component for the simulation. Region 2, with dimensions 2mm×2mm, is the boundary of the impacting shots. All the shot centers lie within Region 3, of dimensions 1.5mm×1.5mm. Region 4, with dimensions 1mm×1mm, is selected as the representative surface for studying the surface coverage and roughness. A volume of 1mm×1mm×3mm is selected as a representative volume to study the average induced stress profile, saturation and intensity. All these dimensions were chosen arbitrarily since our objective is to study the influence and the usefulness of simulating random impacts. The problem of defining a simulation area that is representative of the whole component is let for future investigation.

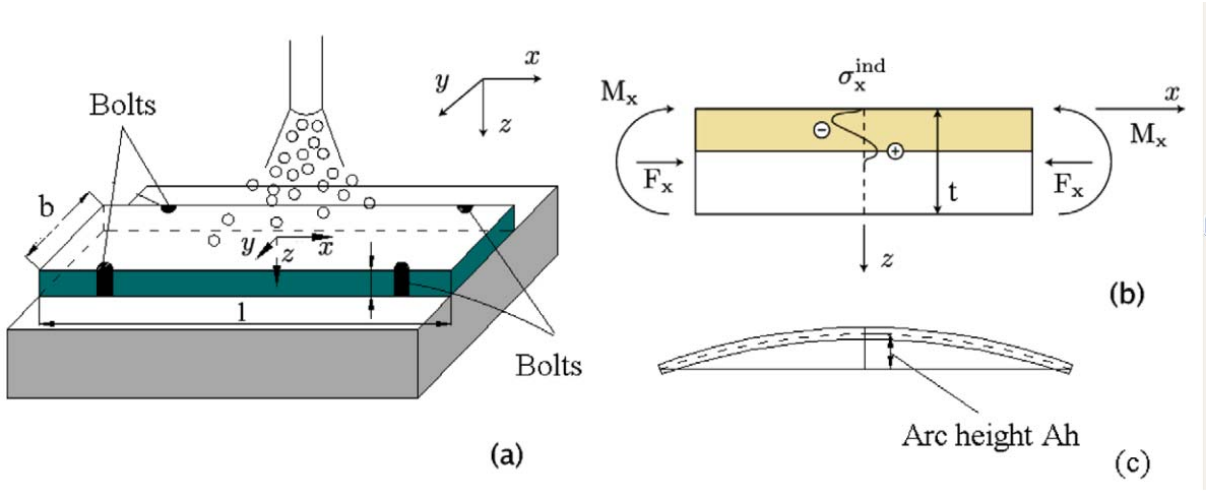

Figure 4.4: Sketch of shot peening on a strip with dimensions 76mm×19mm×3mm. (a) Shot peening of a strip with bolts. (b) Induced stress profile in the strip. (c) Arc height of the deformed strip.

4.4 Shot peening intensity and saturation

4.4.1 Arc height calculation with induced stress profile

The Almen intensity is usually determined with standard Almen steel strips. In practice, however, shot peening can be applied on different materials such as aluminum. In this paper, a shot peening saturation curve on an aluminum plate was simulated.

In order to simulate a saturation curve, an aluminum strip with dimensions 76mm×19mm× 3mm is fixed with bolts as shown in Figure 4.4(a). As peening takes place, gradual plastification of the component surface layers produces an induced stress profile in x-direction σ_x^{ind} as shown in Figure 4.4(b).

The induced stress profile in Figure 4.4(b) is not self-equilibrated and tends to stretch and bend the strip. Therefore, a compressive force F_x and a bending moment M_x must be applied on the strip by the rigid support in order to maintain the strip in a flat shape. Equations (4.6) and (4.7) are the force and moment equilibrium equations for this case, namely

$$\int_0^t \sigma_x^{ind}\, b\mathrm{d}z + F_x = 0 \tag{4.6}$$

$$\int_0^t \sigma_x^{ind} \left(\frac{t}{2} - z\right) \mathrm{b}\mathrm{d}z + M_x = 0 \tag{4.7}$$

where $b = 19\text{mm}$ is the width and $t = 3\text{mm}$ is the thickness of the strip.

After the release of the rigid constraints due to the support and bolts, the originally flat strip will stretch and bend, as shown in Figure 4.4(c). The superposition principle is used in order to calculate the resulting bending. It is assumed that the strip is subjected to the inverse of the force and moment calculated from Equations (4.6) and (4.7) by using the theory of elasticity. Therefore, the residual stress profile after the deformation of the strip can be calculated as:

$$\sigma_x^{res} = \sigma_x^{ind} + \frac{F_x}{A} + \frac{M_x\left(\frac{t}{2} - z\right)}{I} \tag{4.8}$$

where A is section area of the target component and I is the moment of inertia of the target component.

Finite element simulation of such a strip with a bending moment and a stretching force induced by shot peening showed that the influence of the stretching force on the arc height is negligible. Therefore, in the following study, only the bending effect of the strip has been considered in order to calculate the arc height. For this specific rectangular strip, the length is four times the width, so the arc height along the length is 16 times of which along the width. Therefore, only the result along the length direction is considered and expressed as:

$$AHs = \frac{3M_x l^2}{2Ebt^3} \tag{4.9}$$

where $l = 76\text{mm}$ is the length of the strip.

4.4.2 Shot peening saturation curve with FEM – normal impacts

Five dynamic simulations were performed for each number of shots N = {6, 12, 24, 48 and 96}. For each of these simulations, σ_x^{ind} were averaged over the whole xy-plane of the representative volume in the z direction. In order to obtain these average induced stress profiles, $9 \times 9 = 81$ uniformly distributed paths following the depth of the plate in the representative volume were defined by ANSYS General Postprocessor. SX values were interpolated into each of these 81 paths respectively. Then the average values of SX for constant depths were calculated from these 81 paths to represent σ_x^{ind}. Arc heights can be calculated with Equations (4.7) and (4.9) with these averaged induced stress profiles.

Figure 4.5 presents the 25 arc heights calculated from simulation results AHs. An equation of the form:

$$AHf(N) = \frac{p_1 N^2 + p_2 N}{N + q_1} \tag{4.10}$$

is fitted according to a least squares criterion through these 25 simulated values. A regression coefficient $R^2 = 0.9812$ has been obtained in this case. With the help of Equation (4.10), it is possible to calculate a saturation point, beyond which when the number of shots doubles, the arc height increases by 10% with the Fminsearch function in Matlab.

It was found that the arc height reaches saturation for N = 48 and for an intensity of 1.1409mm. Therefore, our model predicts that saturation of this specific aluminum strip, according to the Almen intensity definition, is reached after 48 shots for the shot peening conditions we have simulated.

A 95% confidence interval on the mean value of arc height has been computed for each number of shots. Then, the width of this confidence interval has been normalized with respect to the mean value and is presented in Figure 4.5. This normalized confidence interval is used as an indication of the relative scatter as the number of shots increases. It can be seen from the figure that the relative scatter decreases significantly as the number of shots increases. This might be explained by the fact that the induced stress field becomes more uniform as the number of shots increases.

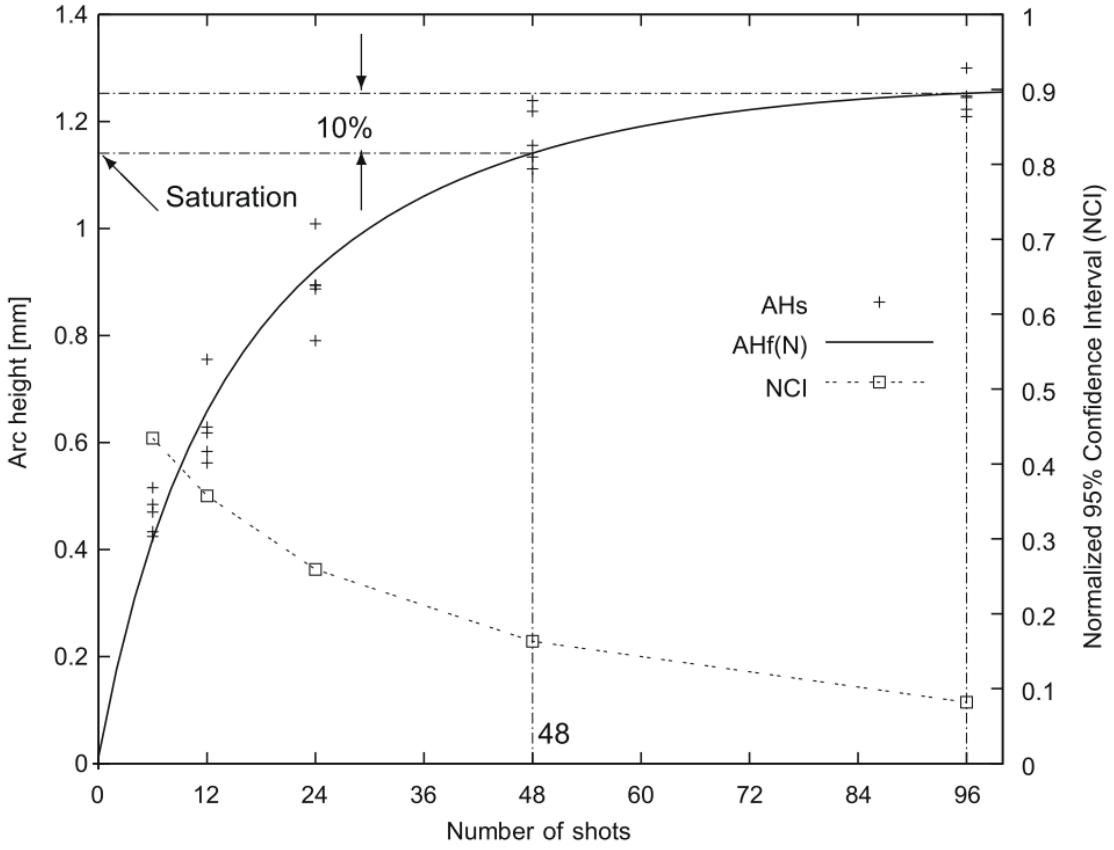

Figure 4.5: Simulated arc heights for normal impacts versus the number of shots.

4.4.3 Shot peening saturation curve with FEM – 60° impact angle

Shot peening impact angle has a significant influence on the shot peening results. Most of the existing finite element models can be used to investigate the influence of shot size and velocity. However, few of them are suitable for the investigation of the influence of the peening angle because of symmetry considerations.

Figure 4.6 presents the general case with normal impacts (case 1) and oblique impacts (case 2). For normal impacts (case 1), shots have an impingement angle of 90° with respect to the x-axis in the xz-plane. For oblique impacts (case 2), shots have an impingement angle of 60° with respect to the x-axis in the xz-plane. For oblique impacts, 5 random simulations for each N= {6, 12, 24, 48 and 96} were performed to obtain average induced stress profiles and arc heights. Equation (4.10) was fitted through these 25 arc heights data with a regression coefficient $R^2 = 0.9603$. Shot peening saturation was obtained for N=78, which corresponds to a deflection of 0.8137mm.

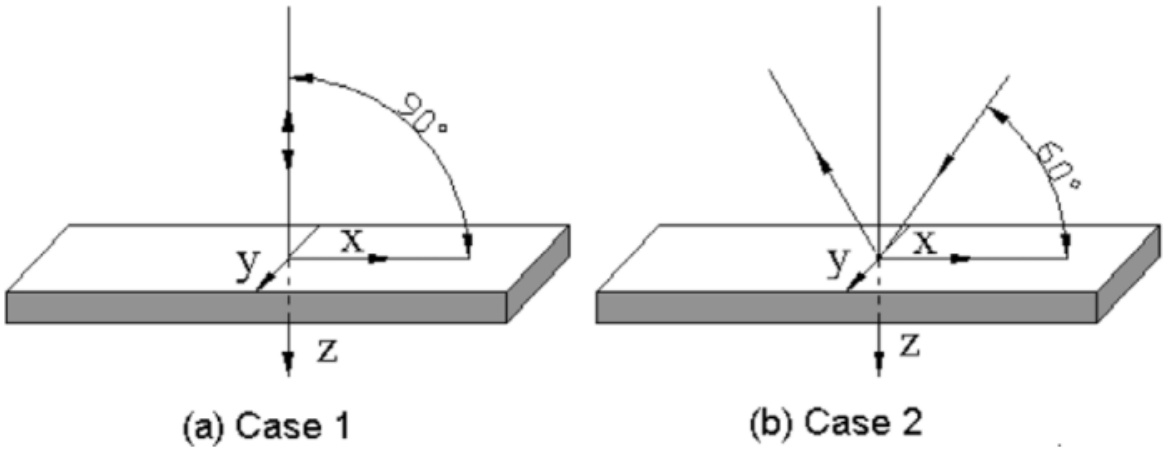

Figure 4.6: Two impact cases: (a) normal impact; (b) oblique impact with 60° impact angle with respect to x-axis in the xz-plane.

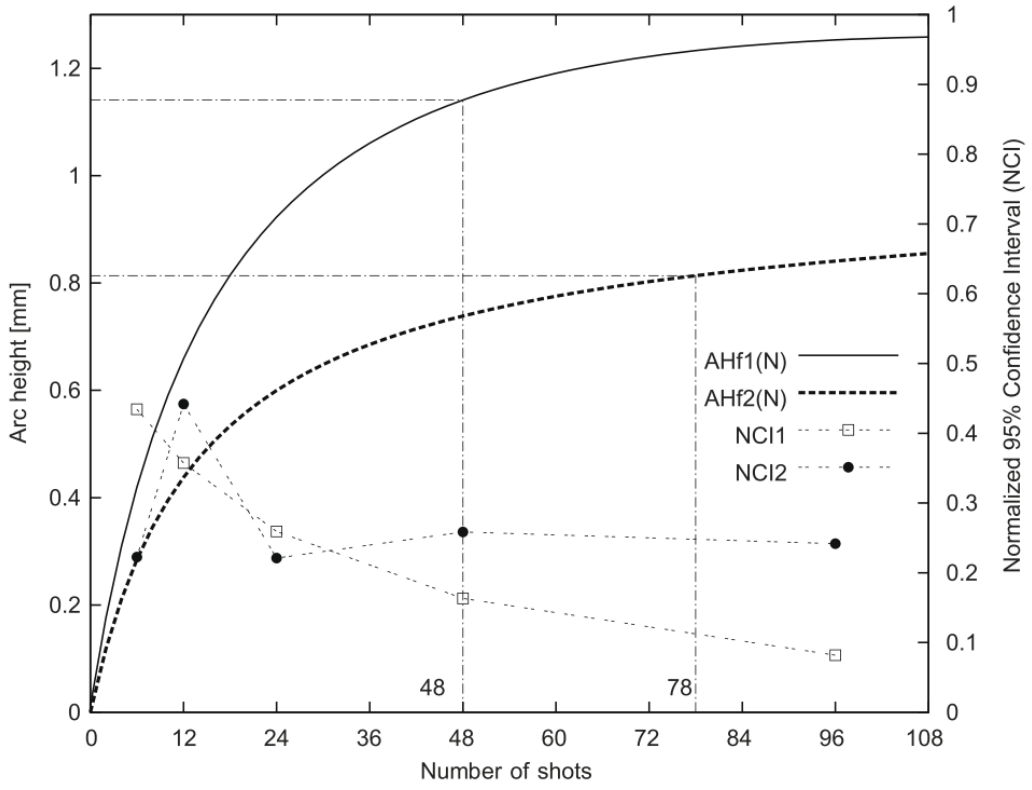

Figure 4.7: Effect of shot peening angle upon the arc heights versus the number of shots for two shot peening cases as shown in Figure 4.6. $AHf1(N)$) and $AHf2(N)$ are fitting Equation (4.10) for normal impact and oblique impact respectively; NCI1 and NCI2 are normalized 95% confidence interval for these two cases respectively.

Figure 4.7 presents the saturation curves for these normal impacts and oblique impacts. It can be seen that the deflection at saturation (intensity in the case of Almen strips) decreases when the impact angle decreases, while the peening time to reach saturation increases. The 95% confidence intervals on the mean values have been computed for oblique impacts. As for the normal impacts, it can be found that the Normalized Confidence Interval decreases globally as the number of shots increases. However, for the oblique impact, its variation is not monotonous. The reason for such behaviour is not clear but could be related to the random property of the process and simulation. A reasonable assumption would be that an increased number of simulations would reduce the scatter in simulation results.

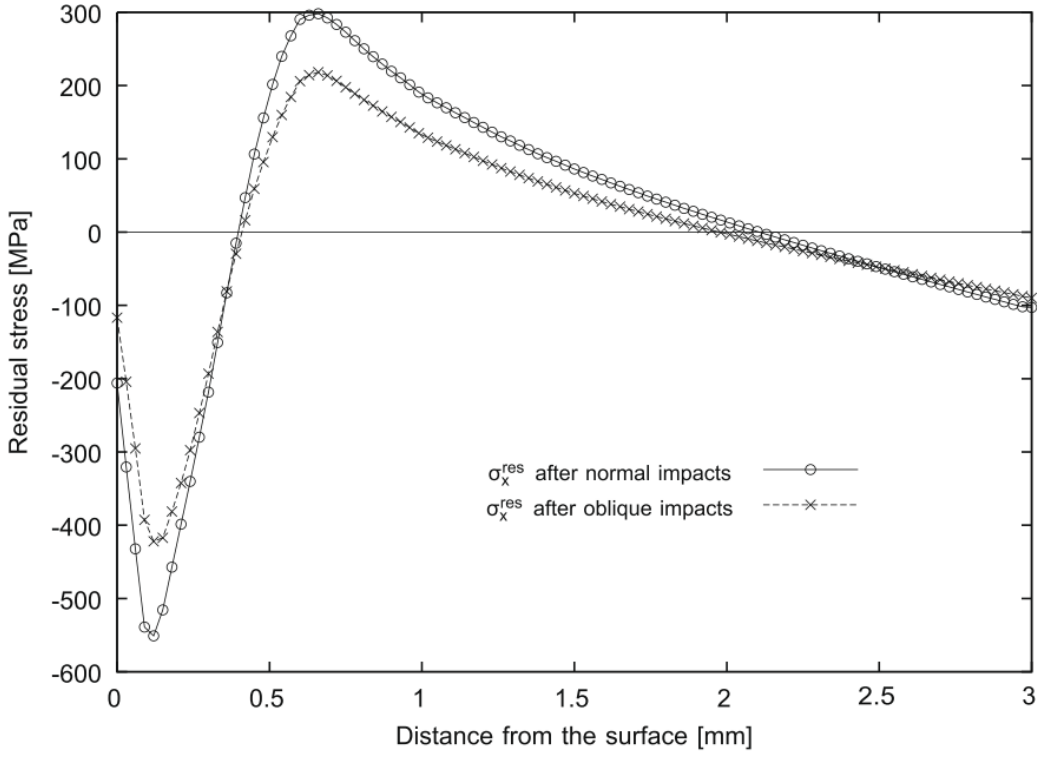

Figure 4.8: Comparison of the residual stress profiles σ_x^{res} after normal shot peening (case 1) and oblique shot peening (case 2) respectively with shot radius $r = 0.5\text{mm}$, shot velocity $v = 50\text{m/s}$ and number of shots N= 48.

4.5 Residual stress profiles of shot peening

4.5.1 Residual stress profiles after normal and oblique shot peening

Figure 4.8 compares the residual stress profiles σ_x^{res} calculated from the induced stress profiles, after 48 normal and oblique impacts, with Equation (4.8). For these two cases, the residual stress is compressive at both the top and bottom surfaces of the component. This result is typical for shot peening on thin components. Normal peening produces higher maximum compressive residual stress and higher surface compressive residual stress.

4.5.2 Comparison of residual stress profiles with reference models

Figure 4.9 and Figure 4.10 present the induced and residual stress profiles calculated with different finite element methods. In these two figures, curve (1) represent σ_x^{ind} and σ_x^{res} beneath the impact point of model (b) in Figure 4.1 with one shot impact. Curves (2) and (3) represent σ_x^{ind} and σ_x^{res} beneath the centerline of model (d) in Figure 4.1 after five shot impacts. The sequences and impact locations of the five shots are as in (Guagliano, 2001) with an indentation distance $ds = 0.4$mm and $ds = 0.3$mm, respectively. Curves (4) are σ_x^{ind} and σ_x^{res} and obtained for the new model introduced in this paper, for 48 shots.

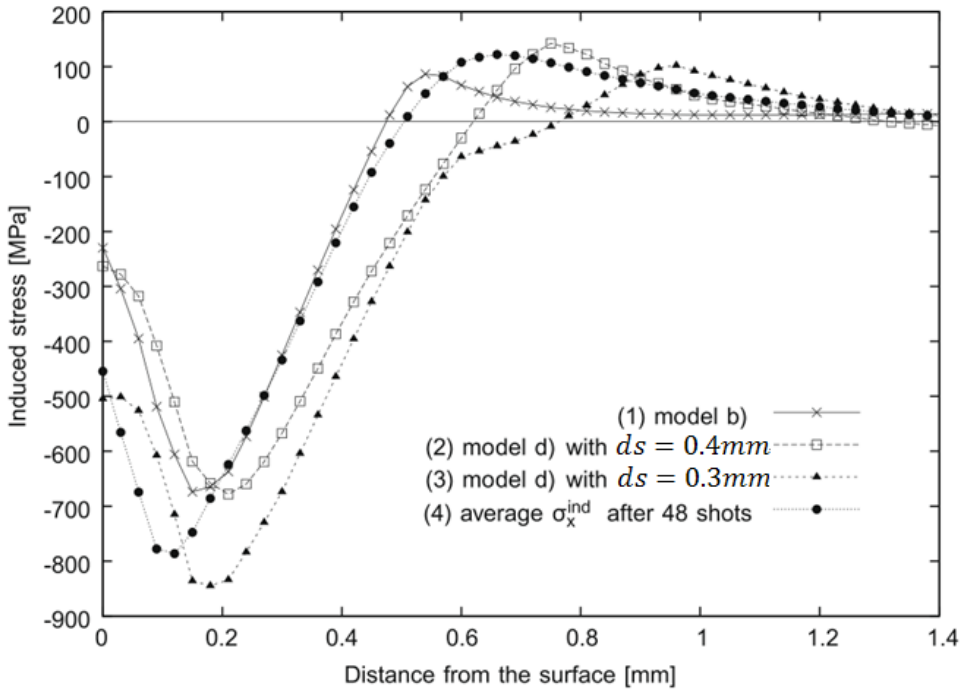

Figure 4.9: Induced stress profiles σ_x^{ind} calculated from different finite element models with shot radius $r = 0.5\text{mm}$, shot velocity $v = 50\text{m/s}$ and for normal shot peening.

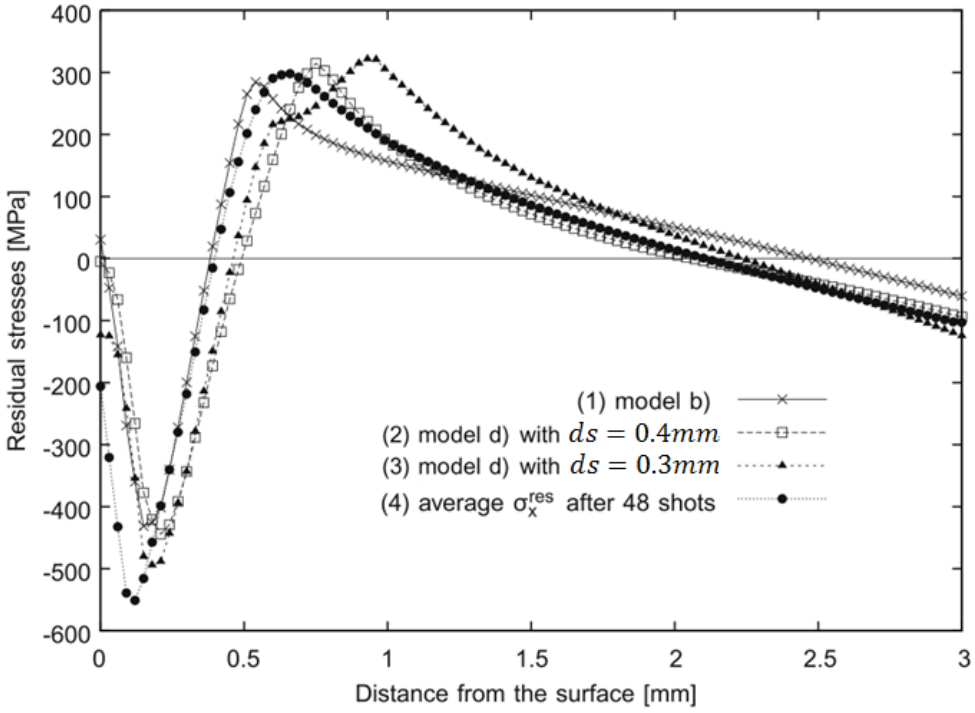

Figure 4.10: Residual stress profiles σ_x^{res} calculated from different finite element models with shot radius $r = 0.5\text{mm}$, shot velocity $v = 50\text{m/s}$ and for normal shot peening.

It can be seen from these curves that significantly different results can be obtained for the various modeling strategies tested in this study. For both σ_x^{ind} and σ_x^{res}, very different results can be obtained for the surface and maximum compressive stresses. In addition, curves (2) and (3) show that the shot location can have a significant effect on the σ_x^{ind} and σ_x^{res} profiles. We believe that the new model introduced in this study will lead to more representative results than the previous models since it is based on more realistic hypotheses. This will be verified in future works with X-Ray Diffraction measurements.

4.6 Shot peening coverage

4.6.1 Surface plastic strain after one impact

Shot peening coverage is defined in terms of surface plastic indentation as introduced in Section 4.2. Two simple shot peening simulations with one shot were performed in order to compare the plastic indentations produced by one normal impact and one oblique impact with the model developed in this paper.

Figure 4.11 presents the von Mises equivalent plastic strain contour in the xz-plane passing through the model center after one normal impact. The results show that the maximum plastic strain is beneath the impact point.

Figure 4.12 shows the equivalent plastic strain and U_z displacement profiles at the component surface. A pile up around the indentation can be observed. Considering that the pile up is not part of the indentation, the boundary of the indentation can be defined as the contour line with null U_z displacement. From that definition, an indentation of radius $\bar{r} = 0.2\text{mm}$ was obtained for this shot peening case. In addition, the von Mises equivalent plastic strain is equal to 0.027 at the boundary of the indentation. Therefore, we considered all points on the surface with the von Mises equivalent plastic strain larger than 0.027 as impacted material. This definition allows evaluation of peening coverage after single and multiple impacts.

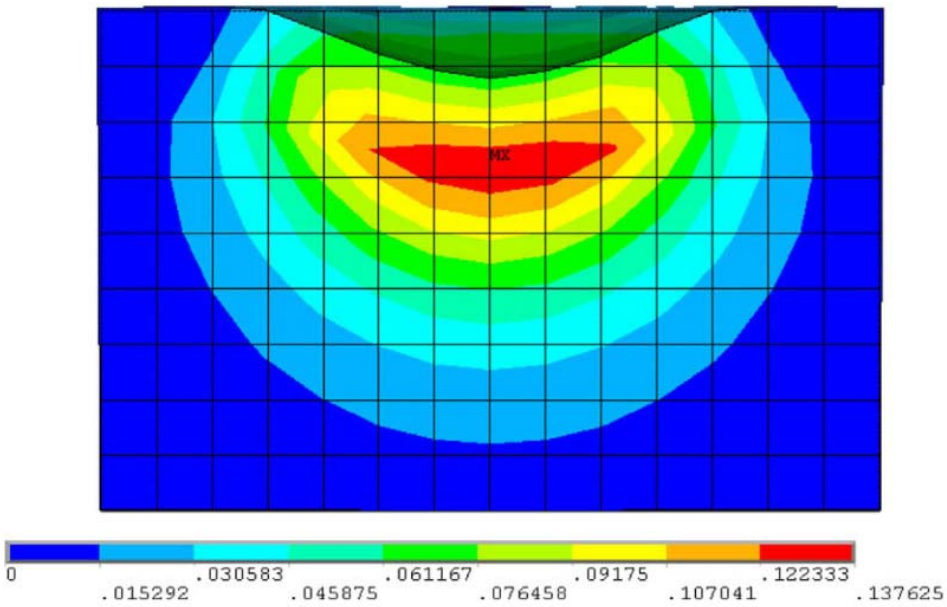

Figure 4.11: von Mises equivalent plastic strain contour after one normal shot impact (cutting in the xz plane).

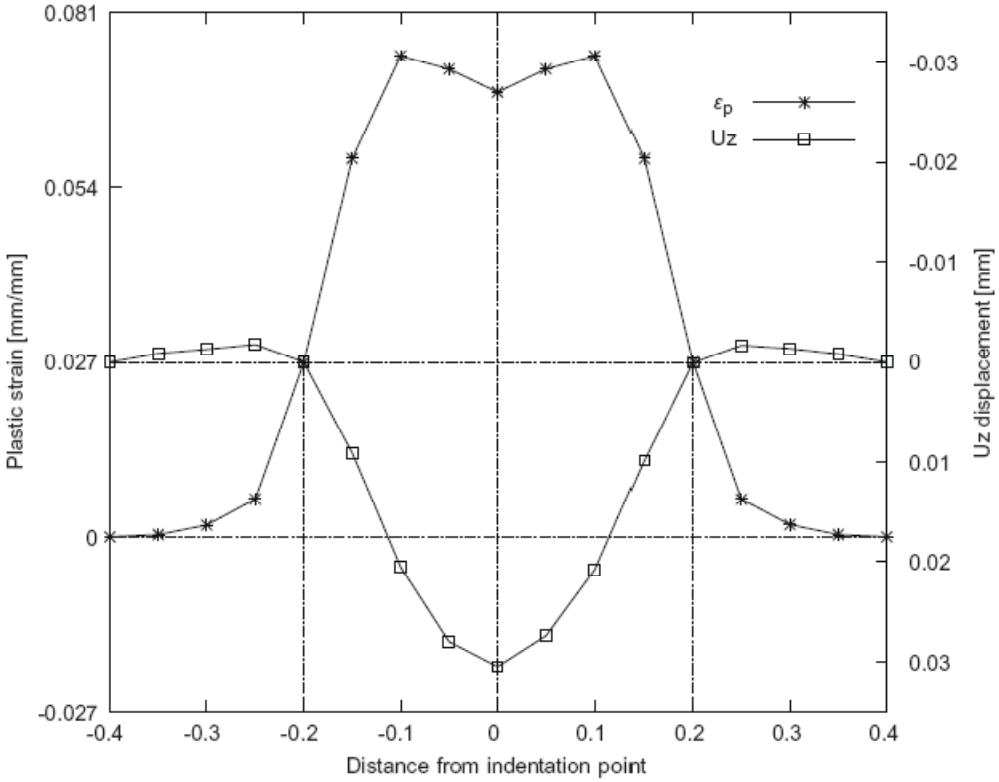

Figure 4.12: von Mises plastic strain profile and indentation profile of the surface nodes (with y=0 and z=0) after one normal impact

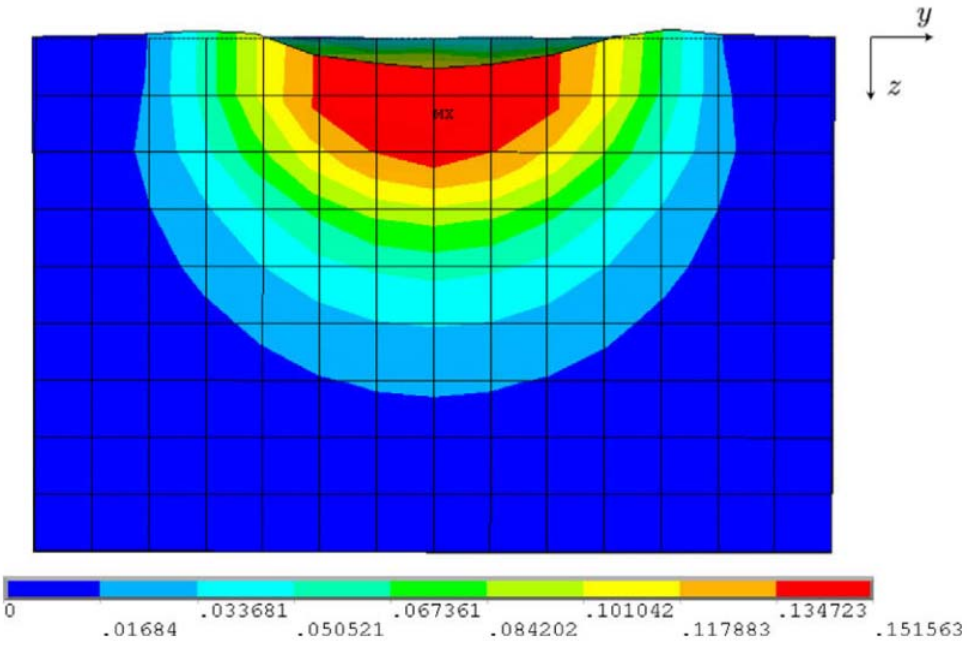

Figure 4.13: von Mises equivalent plastic strain contour after one 60° oblique impact (cutting in the yz-plane).

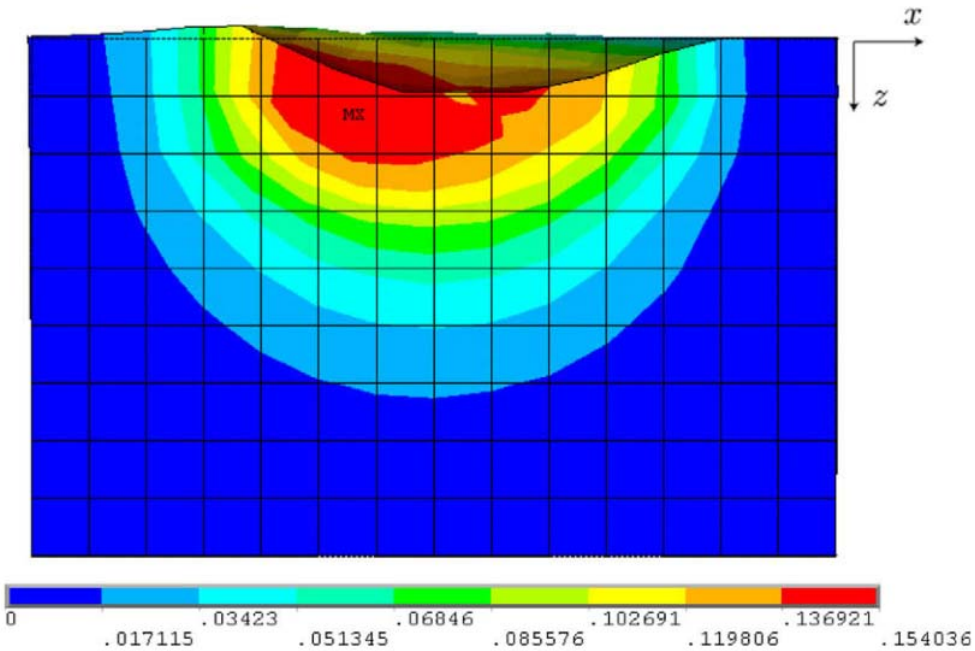

Figure 4.14: von Mises equivalent plastic strain contour after one 60° oblique impact (cutting in the xz-plane).

Figure 4.13 and Figure 4.14 present von Mises equivalent plastic strain contours after one shot impact for oblique impacts in the yz-plane and in the xz-plane respectively. Similar to the results of the normal impact, the plastic strain contour in the yz-plane is symmetric. However, the plastic strain contour in the xz-plane is no longer symmetric.

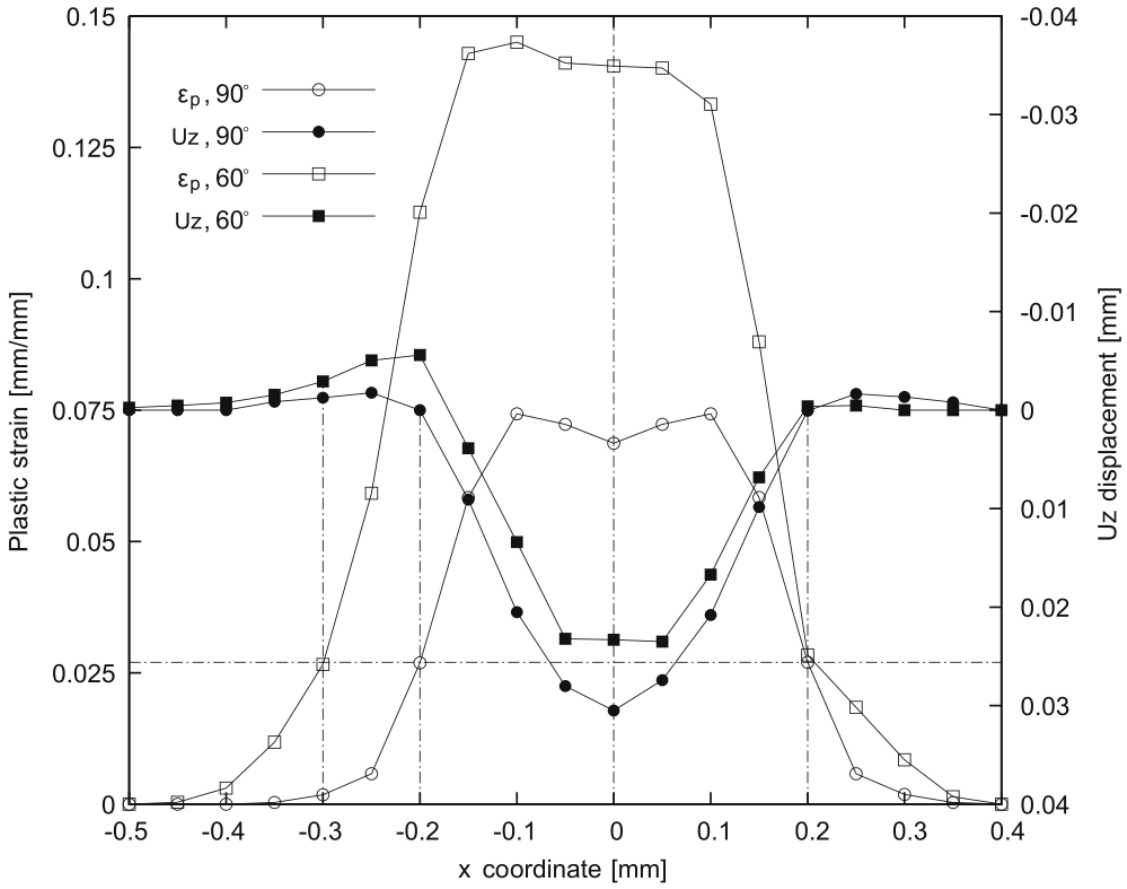

Figure 4.15: von Mises plastic strain profile and U_z displacement profile of the surface nodes (with y=0 and z=0) for normal peening and oblique peening respectively. (ε_p,90° represents plastic strain after one normal impact; U_z, 90° represents U_z after one normal impact; ε_p, 60° represents plastic strain after one oblique impact; U_z, 60° represents U_z after one oblique impact).

Figure 4.15 presents the comparison of von Mises plastic strain and U_z displacement profiles of the nodes with $y = 0$ and $z = 0$ for cases 1 and 2. This figure clearly shows that the surface plastic indentation profiles after a normal or an oblique impingement are quite different:

- The surface plastic strains after a normal impact are smaller than after an oblique impact.
- In the case of a normal impact, the surface plastic strain contour is symmetric while it is not in the case of an oblique impact. For an oblique impact, the plastic strain has a larger value on the side whose normal is along the shot trajectory than on the other side.
- In the case of a normal impact, a plastic strain value $\varepsilon_p^* = 0.027$ reveals an indentation with a diameter 0.4mm, while in the case of an oblique impact, a plastic strain value $\varepsilon_p^* = 0.027$ relates to a plastic indentation with a width equal to 0.5mm in the x direction for this specific case. In addition, on the left hand side of Figure 4.15, it seems that $\varepsilon_p^* = 0.027$ is not inside the crater left by the indentation but in the pile up. It can be seen from Figure 4.15 that it is difficult to define the value of a plastic strain that belongs to an impacted region for an oblique shot.

4.6.2 Numerical simulation of peening coverage with FEM – normal impacts

In our model, numerous shots impact the surface of the component following a random sequence and at random locations. The plastic strain related to indentations on the top layer of the component can be related to shot peening coverage. von Mises equivalent plastic strains for the 441 nodes on the representative surface of the component were obtained through simulations for different number of shots impacts. Shot peening coverage was approximated as the ratio of the number of nodes with von Mises plastic strains larger than 0.027 to the total number of nodes on the representative surface (441). The sensitivity of peening coverage with respect to this definition is let for future study.

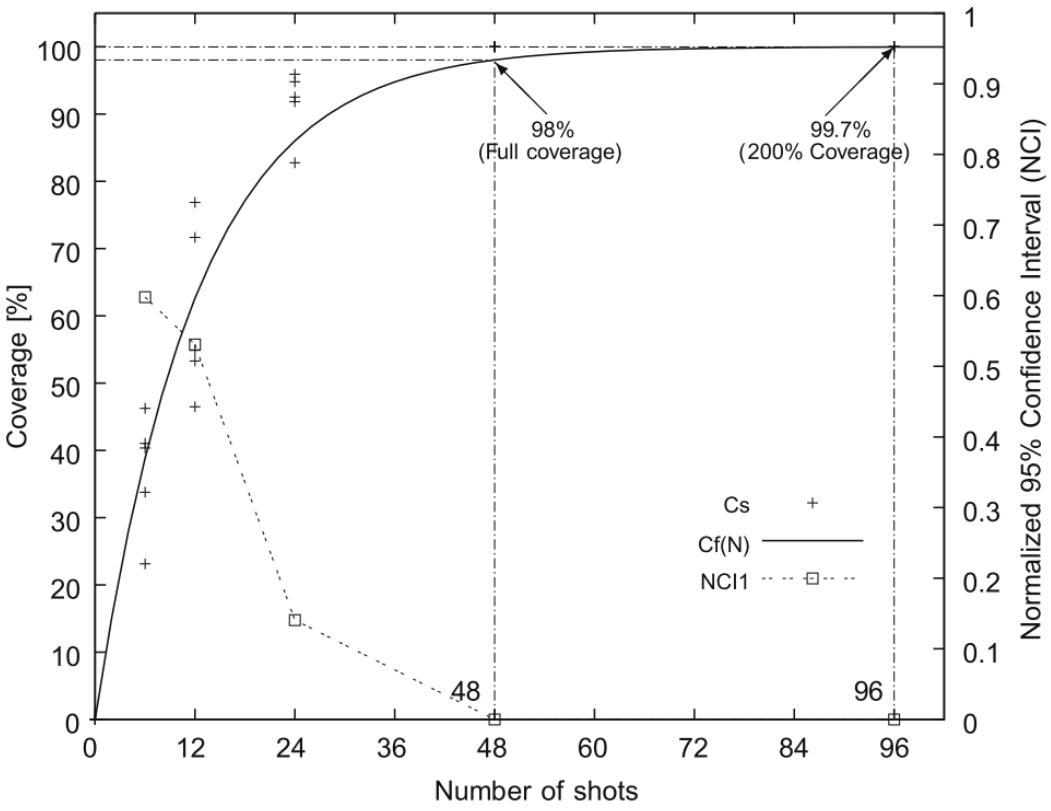

Figure 4.16: Shot peening coverage versus the number of shots after normal impacts.

Figure 4.16 presents the 25 simulated coverage results Cs for N= {6, 12, 24, 48 and 96}. An Avrami Equation (4.11) of the form

$$Cf(N) = 100 \times (1 - e^{-mN}) \tag{4.11}$$

was fitted through this data with a fitting parameter m = 0.082 and led to a regression coefficient $R^2 = 0.969$. From Avrami Equation $Cf(N) = 100 \times (1 - e^{-0.082N})$, full coverage (98% coverage or Cf= 98%) is obtained for N=48 under these peening conditions and 200% coverage (twice the duration of full coverage) is obtained for N= 96.

Normalized 95% confidence intervals of the mean values for each N = {6, 12, 24, 48 and 96} are shown in Figure 4.16. It can be seen that the scatter in the results decreases with the increase of the number of shots.

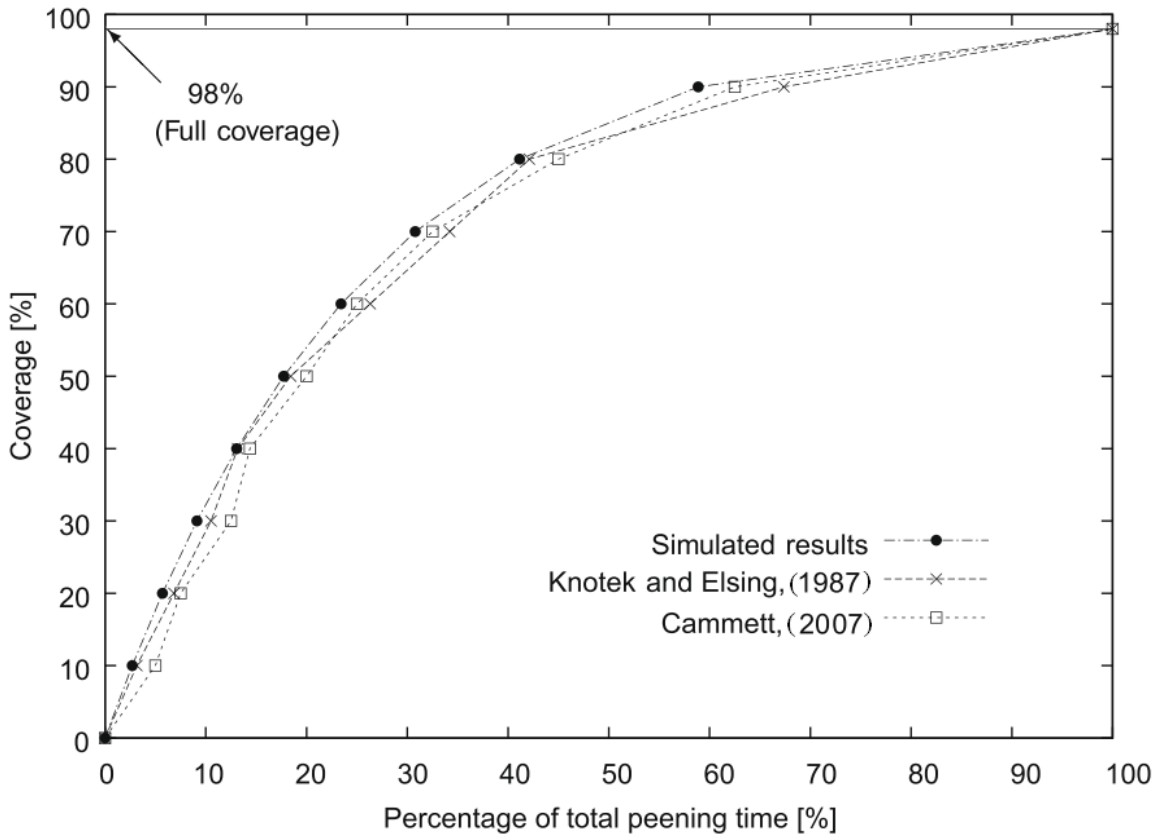

Figure 4.17: Relationship between surface coverage and percentage of peen time.

4.6.3 Comparison of the simulated coverage with reference studies

Figure 4.17 presents curves showing the relationship between the surface coverage and the percentage of total peening time, defined as the ratio of the number of shots to the total number of shots for 98% surface coverage (full coverage). The curves shown in Figure 4.17 summarize the experimental results obtained by Knotek and Elsing (1987), where steel shots with $r = 0.9\text{mm}$ are impacted at the 50CrV4 steel with $v = 52\text{m/s}$ and by Cammett (2007), where S280 steel shots are impacted at the 4340 steel with intensity equal to 9A, as well as the simulated results in this study. It can be seen that very consistent results can be obtained.

4.6.4 Numerical simulation of peening coverage with FEM-60° angle impacts

In the case of oblique impacts, the coverage study is based on the aforementioned assumption that all surface points where the von Mises equivalent plastic strain is larger than 0.027 are considered as pertaining to the impacted area. Therefore, a fitting Equation (4.11) through the

simulated data led to fitting parameter $m = 0.11$ with a regression coefficient $R^2 = 0.979$. It can be calculated from the equation that full coverage (98%) is reached after 36 random shots. We recall that a more detailed study would be required for defining a more realistic criterion for the computation of coverage for the case of oblique impacts.

Figure 4.18 presents curves fitted through the data points for normal impacts and oblique impacts. It can be seen that shot peening with an angle of incidence of 60° reaches full coverage earlier than with normal impacts. This is likely to be due to the fact that a larger plasticized area is induced on the surface in the case of oblique impact as shown in Figure 4.15.

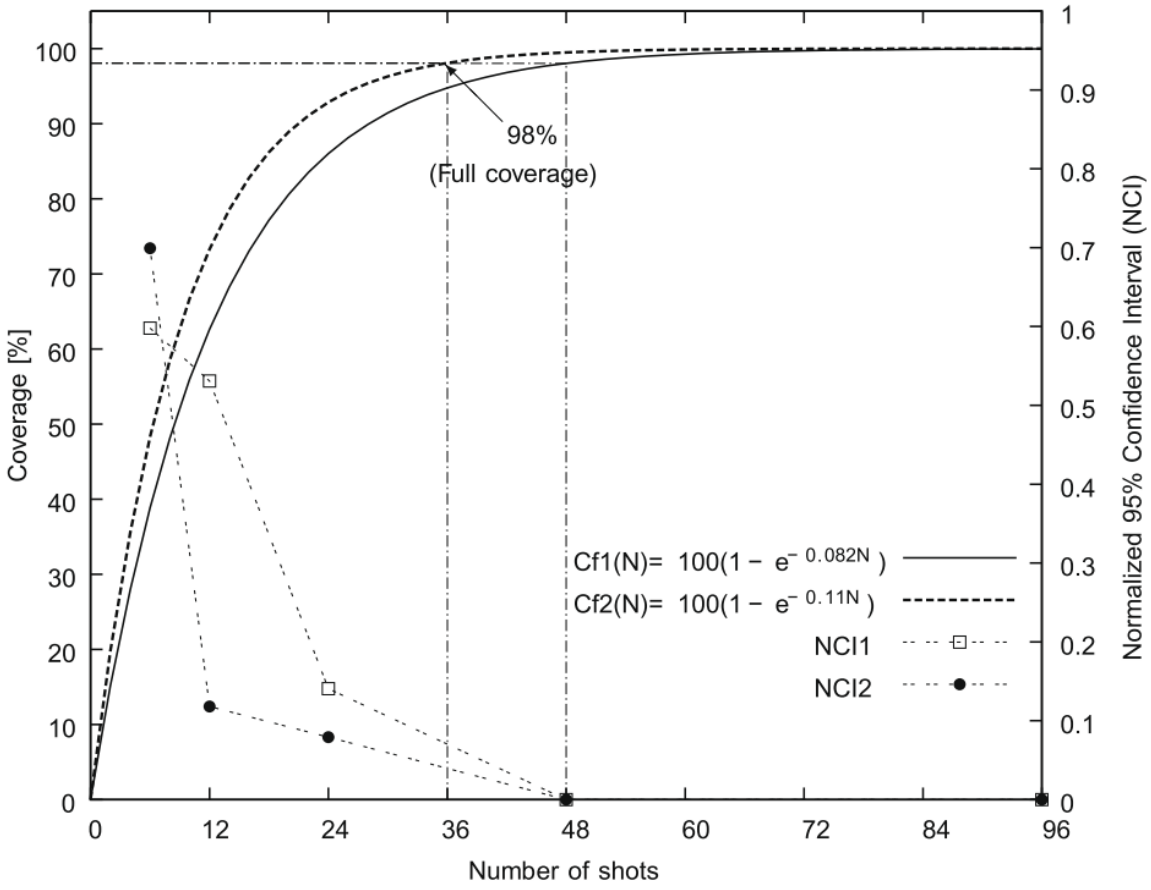

Figure 4.18: Shot peening coverage versus the number of shots for normal impacts (case 1) and oblique impacts (case2) respectively.

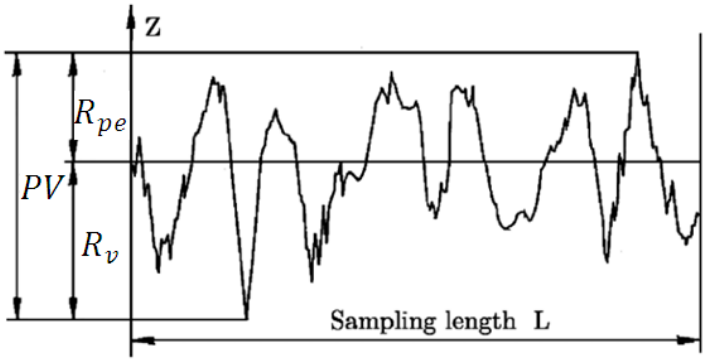

Figure 4.19: *PV* roughness definition: peak-to-valley roughness (Clausen and Stangenberg, 1999).

4.7 Surface roughness

4.7.1 Definition of surface roughness

One of the most common roughness parameters used in the field of shot peening is the peak-to-valley roughness (PV) as shown in Figure 4.19 (Clausen and Stangenberg, 1999). PV value is defined with Equation (4.12) as the distance between the highest peak R_{pe} and the lowest valley R_v within the sampling length,

$$PV = R_{pe} + R_v \tag{4.12}$$

4.7.2 Peening induced surface roughness with FEM – normal impacts

After multiple random impacts, the z direction displacements of the nodes on the representative surface can be used to evaluate the surface roughness. Simulated surface roughness PVs can be approximately obtained as:

$$PVs = \max(U_z) - \min(U_z) \tag{4.13}$$

where $\max(U_z)$ and $\min(U_z)$) are the highest peak and the lowest valley within the reference area.

Figure 4.20 presents 25 values of roughness PVs from simulation after 6, 12, 24, 48 and 96 random impacts. As for the intensity study (Section 4.4), an equation of the form:

$$PVf(N) = \frac{p_1 N^2 + p_2 N}{N + q_1} \tag{4.14}$$

was fitted through the data and led to $R^2 = 0.9849$. In addition, the Normalized 95% Confidence Interval on the mean value has been computed for each number of shots. It can be seen that the relative scatter increases slightly as the number of shots increases. One possible explanation for this behaviour could be that as the number of shots increases, the possibility of creating a deeper valley or a higher peak increases. Such behaviour is also consistent with the fact that PVs is computed with the extreme values rather than with average quantities.

From Figure 4.20, it can be seen that the development of roughness can be divided into two main stages. During stage I, roughness increases rapidly as each impact creates an isolated indentation and independent peaks and valleys. During stage II, many indentations are superimposed so that roughness increases at a slower rate.

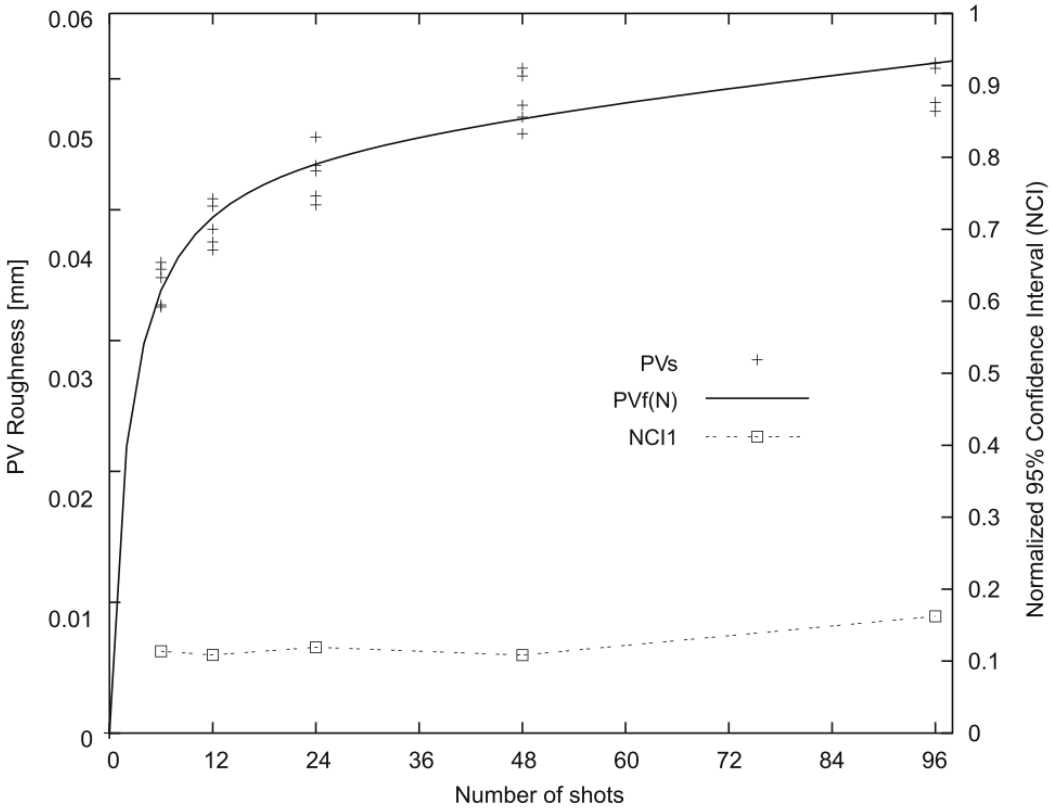

Figure 4.20: *PV* roughness versus number of shots for normal impacts.

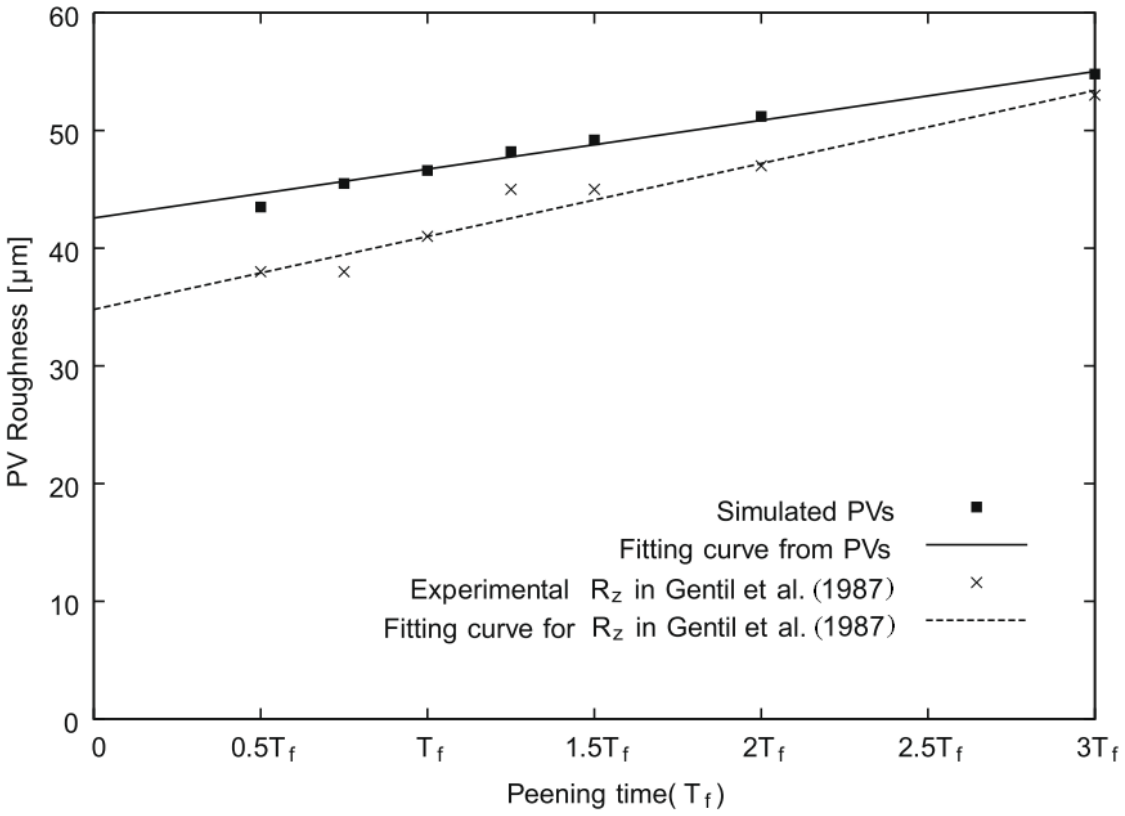

Figure 4.21: Relationship between surface roughness and peening time from this numerical study and the experimental results obtained by (Gentil et al. 1987).

4.7.3 Comparison of the surface roughness with reference results

By combining the relationship between coverage and number of shots obtained from Figure 4.16 (Equation (4.11)) and the relationship between roughness and number of shots obtained from Figure 4.20 (Equation(4.14)), it is possible to establish the relationship between the simulated surface roughness and the peening time as well as the relationship between the simulated surface roughness and the surface coverage .

Figure 4.21 compares the relationship between surface roughness and peening time from this numerical study and the experimental results obtained by Gentil et al. (1987). In the study of Gentil et al. (1987), a linear function of the form $Rz = 34.8 + 6.2T_f$ was used for best fitting the experimental results with regression coefficient $R^2 = 0.94$. In this study, a linear equations with the form $PV = 42.5 + 3.98T_f$ was used for best fitting the simulated results with a regression coefficients $R^2 = 0.98$. In this figure, T_f represents peening time to reach full coverage;

$0.5T_f$ represents half peening time of T_f, which corresponds to 86% coverage; $2T_f$ and $3T_f$ represent twice and three times T_f.

In the study of Gentil et al. (1987), steel shots with $r = 0.7\text{mm}$ impacted E460 steel; in our model, steel shots with $r = 0.5\text{mm}$ impacted aluminum strip. However, it can be seen that the numerical results and reference experimental results present similar tendencies.

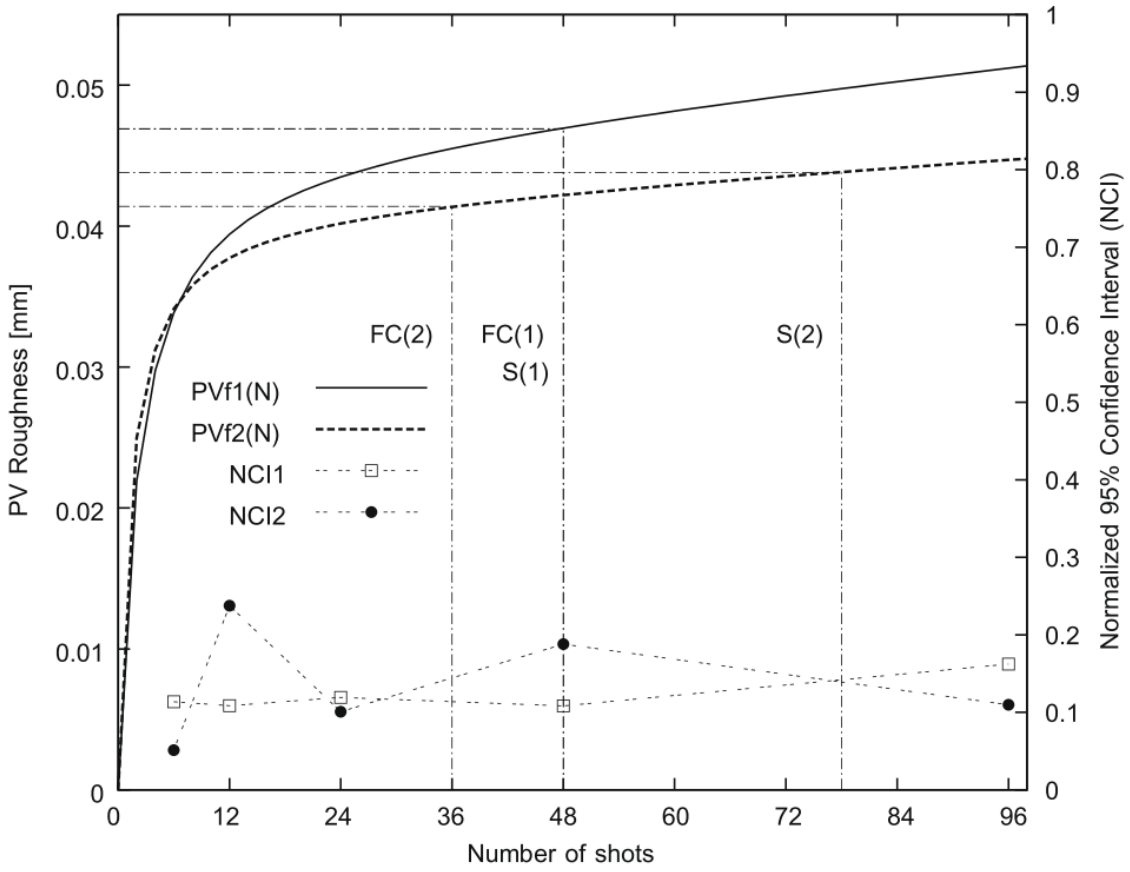

Figure 4.22: PV roughness versus the number of shots for two shot peening cases. $PVf1(N)$ is PV roughness for normal impacts; $PVf2(N)$ is PV roughness for oblique impacts; NCI1 is Normalized 95% Confidence Interval width for normal impacts; NCI2 is Normalized 95% Confidence Interval width for oblique impacts.

Table 4.1 Relationship between saturation intensity and full coverage for two shot peening cases.

Peening angle	Saturation				Full Coverage (98%)			
	Number	Arc height (mm)	Cove-rage (%)	*PV* (mm)	Number	Arc height (mm)	Cove-rage (%)	*PV* (mm)
Normal	48	1.1409	98	0.0469	48	1.1409	98	0.0469
Oblique (60°)	78	0.8137	99.9	0.0438	36	0.6837	98	0.0411

4.7.4 Peening induced surface roughness with FEM-60° impact angle

Equation (4.14) was fitted through the data obtained for PVs after 60° oblique impacts. A regression coefficient $R^2 = 0.9814$ was obtained. Figure 4.22 presents the fitted $PVf(N)$ equations for normal impacts and oblique impacts respectively.

With the fitted equations, it is possible to calculate the PV values corresponding to saturation and full coverage for the two shot peening cases. In Figure 4.22, $S(1)$ and $FC(1)$ represent saturation and full coverage with N=48 for normal impacts, $S(2)$ represents saturation for oblique impacts with N= 78; $FC(2)$ represents full coverage with N = 36 for oblique impacts.

4.8 Summary

A 3D random model was developed to simulate shot peening intensity, surface coverage and surface roughness with normal and oblique impacts. For each of these quantities, an empirical relationship has been obtained in order to relate them to the number of shots. With these equations, (a) the arc height, coverage and roughness values at saturation, (b) the arc height, coverage and roughness values at full coverage can be calculated separately.

Table 4.1 summarizes these simulated results for this specific shot peening case (shot velocity $v = 50\text{m/s}$, shot radius $r = 0.5\text{mm}$). It can be seen from Table 4.1 and Figure 4.22 that:

(1) For the case of normal shot peening, the process reaches saturation and full coverage after approximately 48 impacts. Since these two parameters are based on the study of the same target material (aluminum), full coverage and saturation are very consistent.

(2) For the same number of impacts, normal impacts produce larger arc heights than oblique impacts. In addition, more shot impacts are required to reach saturation with oblique impacts than with normal impacts.

(3) In the case of oblique impacts, shot peening reaches full coverage with less shots, when compared to normal shot impacts. We recall that this result depends greatly on the criterion used for discriminating peened and unpeened area.

(4) When compared with oblique impacts, shot peening at normal impacts induces larger surface roughness at saturation and at full coverage. This is consistent with the results shown in Figure 4.15, where the difference between the peak and valley caused by one normal impact is larger than that caused by one oblique impact.

4.9 Suggestions for future work

Shot peening is widely used for improving the fatigue life of metallic component, but this ability depends greatly on the shot peening effectiveness, such as shot peening intensity, surface coverage and surface roughness. The contribution of present work is the development of a numerical model to simulate all of these shot peening results and to establish a relationship between all of them. Table 4.1 shows the kind of conclusions that can be drawn from such an exercise.

Our model is based on several assumptions and simplifications that require to be considered in future works, such as: the influence of the representative surface, the definition of the plastic strain used for computing the coverage, the influence of the distance between each shots and the influence of the impact between each shots, etc. Material properties were assumed for the target aluminum component. An experimental program should be undertaken in order to obtain realistic constitutive properties for this material. Nevertheless, we believe that our work is useful in the sense that it shows the potential information and results that can be obtained from the simulations we have performed. In addition, refinement of the models will lead to new understanding of the shot peening process and this might lead to a significant impact in the shot peening industry. This is therefore the motivation for conducting the studies listed above.

CHAPITRE 5 EXPERIMENTAL STUDY OF SHOT PEENING AND STRESS PEEN FORMING

H. Y. Miao, D. Demers, S. Larose, C. Perron, Martin Lévesque, accepted by *Journal of material processing technology*.

5.1 Abstract

Shot peening is a cold working process widely used to improve fatigue life of aerospace and automobile components. Stress peen forming is widely used in the aeronautic industry to produce thin components with complex shapes, involving double curvatures, such as wing skins. In this paper, quantitative relationships between the saturation, surface coverage and roughness with respect to peening time have been established based on aluminum Al2024 test strips. The influences of peening velocity and peening time on the resulting residual stress profiles have been experimentally presented. The quantitative relationships between the prebending moment and the resulting arc heights of narrow strips and square strips have been experimentally investigated. Experimental results show that with the increases of the prebending moment, the resulting arc height following the prebending direction increases and the tendency is almost linear. Quantitative equations of the saturation, coverage and roughness as well as the relationship between the prebending moment and resulting arc height can be used for the optimization of shot peening and stress peen forming process.

5.2 Introduction

Shot peening is a cold working process widely used to improve the fatigue life of metallic components and to induce curvature of thin aeronautic components, such as wing skins. Numerous shot peening parameters, such as shot size, type, velocity, incidence angle, material properties of the target component, etc. have a great influence on the effectiveness of the treatment. The repeatability of the shot peening process is usually measured using two control parameters: Almen (peening) intensity and peening coverage.

Peening intensity is related to the amount of kinetic energy transferred from the shot stream to a work piece during the shot peening process (Kyriacou, 1996). A method commonly used to quantify peening intensity was introduced by Almen and Black (1963) and is called Almen test.

The method consists of peening a standardized SAE1070 spring steel test strip of given dimensions and material (Almen strip) that is clamped to a mounting fixture by means of four roundhead bolts. This strip is of dimensions $76\text{mm} \times 19\text{mm}$ for three available thicknesses (type A: 1.29 mm, type N: 0.79 mm and type C: 2.39 mm). Once the bolts are removed, the Almen strip will curve towards the peening direction. The resulting arc heights under different shot peening times can be measured by a dedicated measuring equipment called Almen gauge. Shot peening saturation is defined as the point on the curve of peening time versus arc height beyond which the arc height increases by less than 10% when the peening time doubles. The Almen intensity, or peening intensity, is by definition the arc height of the Almen strip at shot peening saturation. Complete procedures and specifications of intensity measuring equipment can be found in SAE standards SAE-J442, SAE-J443 and SAE-AMS 2430. Karuppanan et al. (2002) adopted an algorithm for determining the saturation point by means of full regression analysis. They applied Equation (5.1)

$$Ah(T) = \frac{B}{(T+d)^p} - \frac{B}{d^p} \tag{5.1}$$

to fit experimental data, where $Ah(T)$ is the arc height, B, d and p are fitting parameters and T is the peening time.

Coverage is defined as the ratio of the area covered by peening indentations to the total treated surface area, expressed in percentage. Visual inspection is the standard method for coverage evaluation. For practical purposes, the maximum coverage that can be assessed visually is around 98%, since coverage percentages are difficult to discriminate as 100% coverage is approached. Thus, 98% surface coverage is usually considered as full coverage according to SAE J2277. Moreover, 200% coverage is defined as peening twice the exposure time required achieving full coverage (98%). Kirk and Abyaneh (1993) and Kirk (2002, 2005) discussed the theory of coverage for random indentations, which assumes that randomly distributed shot particles reach the component's surface at a constant rate and create circular indents of constant size. A simplified treatment of that theory based on the application of an Avrami equation is presented by Kirk and Abyaneh (1993) as

$$C_{th}(T) = 100 \times \left(-e^{-\pi \bar{r}^2 RT}\right) \tag{5.2}$$

where $C_{th}(T)$ is the theoretical calculated coverage, $\bar{r}$ is the average radius of the indentations, R is the rate of creation of impacts (number of impacts per unit area per unit time) and T is the peening time.

Equation (5.2) was expressed in terms of peening parameters (Kirk and Abyaneh, 1993) and (Karuppanan et al. 2002) as:

$$C_{th}(T) = 100 \times \left(1 - e^{-\frac{3\bar{r}^2 \dot{m} T}{4\bar{A} r^3 \rho_s}}\right) \tag{5.3}$$

where $\dot{m}$ is the mass flow rate of the shots, $\bar{A}$ is the peening area on the treated component, r is the average radius of the shots and ρ_s is the density of the shots.

Shot peening improves the fatigue life by introducing compressive residual stress in near surface region which hinders cracks propagation. However, the projection of shots at high velocity produces indentations on the surface of the treated material and results in an increased surface roughness which reduces the fatigue life of the treated component (Sharp et al. 1994). Therefore, the performance of shot peening will depend on a tradeoff between its beneficial effects (compressive residual stress) and its detrimental effects (surface roughness) (Curtis et. al. 2003). A surface with higher surface roughness presents more irregularities, which act as stress concentrations to accelerate the nucleation and early propagation of microcracks. In practice, surface roughness parameters are mainly determined with the help of electronic contact (stylus) instruments. The measurement results depend strongly on the selections of the scanning length and the limit wavelength (Clausen and Stangenberg, 1999). An elastic stress concentration factor K_t related to surface roughness can be calculated as (Curtis et. al. 2003)

$$K_t = 1 + 2.1\frac{R_t}{S_m} \tag{5.4}$$

where R_t represents the maximum peak-to-valley distance and S_m represents the average distance between peaks.

Shot peening of a thin component induces a curvature towards the peening direction. Almen intensity measurement is a common use of this phenomenon. The use of shot peening to induce a shape is called peen forming. It is a dieless process which has been widely used to form various aircraft components since the 1960's (Baughman, 1984; Kopp and Ball, 1987 and Tatton, 1987).

Conventional peen forming usually induces a spherical shape in the peened component as normal shot impacts create an isotropic effect in isotropic material. For a wing skin, which has a larger curvature in chordwise direction than in spanwise direction, a technique called stress peen forming can be applied. In stress peen forming, the component is elastically pre-stressed (usually stretched or bent) before and during peening. In the case of wing forming, wing panels can be pre-bent along the chordwise direction during peen forming. After peen forming, the resulting curvature along the chordwise direction will thus be larger than that along the spanwise direction. It is possible to obtain the target curvature in the chordwise direction with a small curvature in the spanwise direction.

Most of the stress peen forming process is based on experimental trials and errors and few investigations of stress peen forming have been performed to relate the prebending moments or forces and the resulting curvatures. (Baughman, 1984) and (Kopp and Ball, 1987) introduced the principles of elastic stress peen forming with prebending moment or prestretching force. (Barrett and Todd, 1984) showed that the elastic pre-stressing technique increases the maximum compressive residual stress when compared with conventional peen forming. Li (1981) presented experimental results of stress peen forming under different values of prebending moments. Gardiner and Platts (1999) simulated various stress profiles (induced, residual, etc.) involved in stress peen forming by using temperature profiles.

According to this literature survey, it is possible to list the limitations of the existing studies:

(1) Almen intensity is defined based on Almen strips made of steel SAE1070, which are different from the practical peened components. Therefore, it is impossible to establish a direct relationship between the coverage and saturation of an Almen strips and the material being treated.

(2) Most of the investigations of Almen intensity, coverage and roughness were conducted separately. No direct relationship between these parameters and shot peening time was obtained through experimental investigation.

(3) For stress peen forming, the relationship between the prebending moments and the curvatures of the deformed component has not been studied in details.

The first objective of this work is to experimentally study the shot peening control parameters (saturation and coverage) and shot peening effects (residual stress and roughness) in details. With

experimental data, the quantitative relationship between the shot peening intensity, coverage, roughness and peening time on the same target material can be established. In addition, residual stress profiles for different peening parameters, such as shot velocity, saturation peening time, full coverage peening time are presented. The second objective of this paper is to present the effect of the prebending moments on the peen forming results. The relationship between the prebending moments and the resulting arc heights of narrow and square components are obtained.

This article is divided into six sections. Section 5.3 introduces devices and parameters in the shot peening and stress peen forming experiments performed in this study. Section 5.4 presents the shot peening results including saturation curve, coverage curve, roughness curve as well as residual stress profiles. Section 5.5 shows the relationship between prebending moment and resulting arc heights in narrow strip and square strips. Section 5.6 discusses the experimental results and conclusions are presented in section 5.7.

5.3 Description of shot peening and stress peen forming processes

5.3.1 General considerations

Shot peening and stress peen forming process were performed with a BLAKA-1 portable blasting machine (#CH8152 GLATTGRUGG), a Motoman Model robot (Motoman SV3X Long) and a robot controller (XRC 2001). Ceramic Zirshot Z425 shots with approximate Young's modulus $E = 300\text{GPa}$, Poisson's ratio $\upsilon = 0.27$ and density $\rho_s = 3850\text{kg/m}^3$ were used in the experiments. Table 5.1 lists the three cases of shot peening parameters used in this study. The pressure and mass flow of the shots were measured directly by the pressure and mass flow meters of the "Baiker" machine. The velocity of the shot flow was measured by shot velocity measurement device "Shotmeter" sold by Progressive Technologies (Barker, 2005). The diameter of the nozzle was 6mm and the standoff distance between nozzle and target was of 25mm. Normal impingement of shots was considered in the experiments.

Table 5.2 lists the metallurgical composition of target material Al2024 used in the experiments, which was manufactured by standard lamination process. This fabrication method stretches the grain in one preferential direction (longitudinal) which could bring mechanical properties anisotropy and could significantly modify the peening results. Samples were cut from 1.6mm thick 2024-T3 aluminum sheets 200 and from 12.5mm thick 2024-T351 aluminum plates. For

each of the two samples thicknesses, three longitudinal (L) and three transverse (T) directions tensile tests have been performed on MTS 810 material testing machine to evaluate the mechanical properties of the material. Therefore, a total twelve tensile tests have been performed.

Table 5.1: Shot peening process parameters.

Case #	Set pressure (kPa)	Set mass flow (kg/min)	Measured shot velocity (m/s)
1	37.9	0.4	34.6
2	96.5	0.4	53.7
3	155.1	0.4	66.2

Table 5.2: Aluminum 2024 Metallurgical Composition.

	Al	Cr	Cu	Fe	Mg	Mn	Other	Si	Ti	Zn
(%)	90.7 - 94.7	0.10	3.80 – 4.90	0.50	1.20 – 1.80	0.30 – 0.90	0.15	0.50	0.15	0.25

Table 5.3: Average mechanical properties of experimental Al2024.

	Thick sample (12.5mm)			Thin sample (1.6mm)			Difference between thin and thick samples in L direction (%)
	L	T	Difference between L and T (%)	L	T	Difference between L and T (%)	
E (GPa)	74.3	74.1	0.27	78.5	74.5	5.08	5.35
σ_s (MPa)	370.8	332.9	10.22	394.4	364.4	7.61	5.98
σ_b (MPa)	468.7	483.1	2.98	528.7	503.4	4.78	11.35
ε_b (%)	23.6	19.7	16.53	17.3	17.6	2.20	26.70

Table 5.3 shows the average results of three samples in L and T directions for two thicknesses, respectively. The thin component has higher Young's modulus E, yield stress σ_s, Ultimate tensile stress σ_b and lower elongation at UTS ε_b when compared with thick component. For both thick and thin components, yield stress σ_s in L direction is larger than that in T direction.

5.3.2 Shot peening process

In shot peening experiments, peening time incrementation can be defined by either considering one peening pass over each surface location ($N_p = 1$) and different robot travelling velocities ($V_r = 320, 160, 80, 42, 20$ and 10mm/s) or considering different numbers of peening passes

($N_p = 1, 2, 4, 8, 16\ and\ 32$) and only one robot travelling velocity $V_r = 320\text{mm}/s$. Comparison of these two methods on aluminum test strips has been performed as a preliminary test. Results showed that both methods can produce similar peening results (both coverage and resulting arc height) on aluminum test strips with dimensions $76\text{mm} \times 19\text{mm} \times 1.6\text{mm}$. That is to say, peening results considering one peening pass ($N_p = 1$) at relatively slow travelling velocity ($V_r = 10\text{mm}/s$.) were in close agreement with peening results considering 32 peening passes $N_p = 32$) at high travelling velocity ($V_r = 320\text{mm}/s$). This robot travelling velocity will be considered as nominal travelling velocity in this paper. Therefore, for any number of peening passes N_p, an equivalent robot travelling velocity V_e corresponding to one peening pass ($N_p = 1$) can be calculated with Equation:

$$V_e = \frac{320}{N_p} \tag{5.5}$$

Four categories of shot peening experiments were performed:

(1) For each of the three shot peening velocities ($34.6\text{m/s}, 53.7\text{m/s}, 66.2\text{m/s}$), three Almen tests were performed on standard SAE1070 steel (Almen) strips (Type A with dimensions $76\text{mm} \times 19\text{mm} \times 1.29\text{mm}$). Saturation curves and Almen intensities were obtained by peening with a constant robot travelling velocity $V_r = 320\text{mm}/s$ for six different numbers of peening passes ($N_p = 1, 2, 4, 8, 16$ and 32). Therefore, a total of 54 (6passes $\times$ 3velocities $\times$ 3repetitions) Almen strips have been tested.

(2) The influence of the material grains orientations on the peening-induced arc height was investigated by conducting saturation studies using two sets of aluminum test strips, with the longest dimension in longitudinal direction (L test strips) and transverse direction (T test strips) respectively. Aluminum test strips with dimensions $76\text{mm} \times 19\text{mm} \times 1.6\text{mm}$ were peened with robot travelling velocity $V_r = 320\text{mm}/s$ for six different numbers of peening passes ($N_p = 1, 2, 4, 8, 16$ and 32). For each combination of peening parameters, robot parameters (three shot velocities) and type of test strips (L and T test strips), three samples were peened for repeatability concerns. Therefore, 54 (6passes $\times$ 3velocities $\times$ 3repetitions) L and 54 T test strips were prepared to study the influence of the material grains orientations on the resulting deformed arc heights, respectively.

(3) Three aluminum plates with dimensions $200\text{mm} \times 150\text{mm} \times 12.5\text{mm}$ were peened with three shot velocities to study the influence of shot velocity on the surface coverage and roughness. On each plate, six regions with dimensions $200\text{mm} \times 25\text{mm} \times 12.5\text{mm}$ have been peened with six peening passes ($N_p = 1, 2, 4, 8, 16$ and 32), respectively, with the robot travelling velocity $V_r = 320\text{mm}/s$ to study the influence of the number of passes on the surface coverage and roughness.

(4) Two aluminum plates with dimensions $200\text{mm} \times 75\text{mm} \times 12.5\text{mm}$ were peened with shot velocities $v = 34.6\text{m}/s$, $53.7\text{m}/s$ and $66.2\text{m}/s$ until saturation for evaluating the influence of shot velocity on residual stress. A third aluminum plate with dimensions $200\text{mm} \times 75\text{mm} \times 12.5\text{mm}$ was peened with shot velocity $v = 66.2\text{m}/s$ until full coverage to study the influence of peening time on residual stress.

5.3.3 Stress peen forming process

For these experiments, the robot velocity was set so that saturation is reached in one pass. This velocity V_e is calculated from Equation (5.5) by using the number of passes required for saturation obtained at Section 5.3.2, for each shot velocity.

Figure 5.1 presents the pre-stressing device with four radii of prebending curvatures ($R_p = \infty, 720\text{mm}, 360\text{mm}, 240\text{mm}$) designed for the stress peen forming. Two categories of experiments were performed with this device:

(1) For each shot velocity, four groups of four aluminum strips (two L test strips and two T test strips) with dimensions $76\text{mm} \times 19\text{mm} \times 1.6\text{mm}$ were fixed on the prestressing device. Therefore, 24 aluminum L test samples and 24 aluminum T test samples were tested. The strips were elastically deformed with radii of the prebending curvatures equal to $\infty, 720\text{mm}, 360\text{mm}$ and 240mm, respectively.

(2) Four square strips with dimensions $76\text{mm} \times 19\text{mm} \times 1.6\text{mm}$ were prebent on the prestressing device along the longitudinal direction of the strip with radii of the prebending curvatures equal to $\infty, 720\text{mm}, 360\text{mm}$ and 240mm, respectively. For each shot velocity, experiments were performed three times to ensure repeatability. 36 aluminum samples were therefore tested.

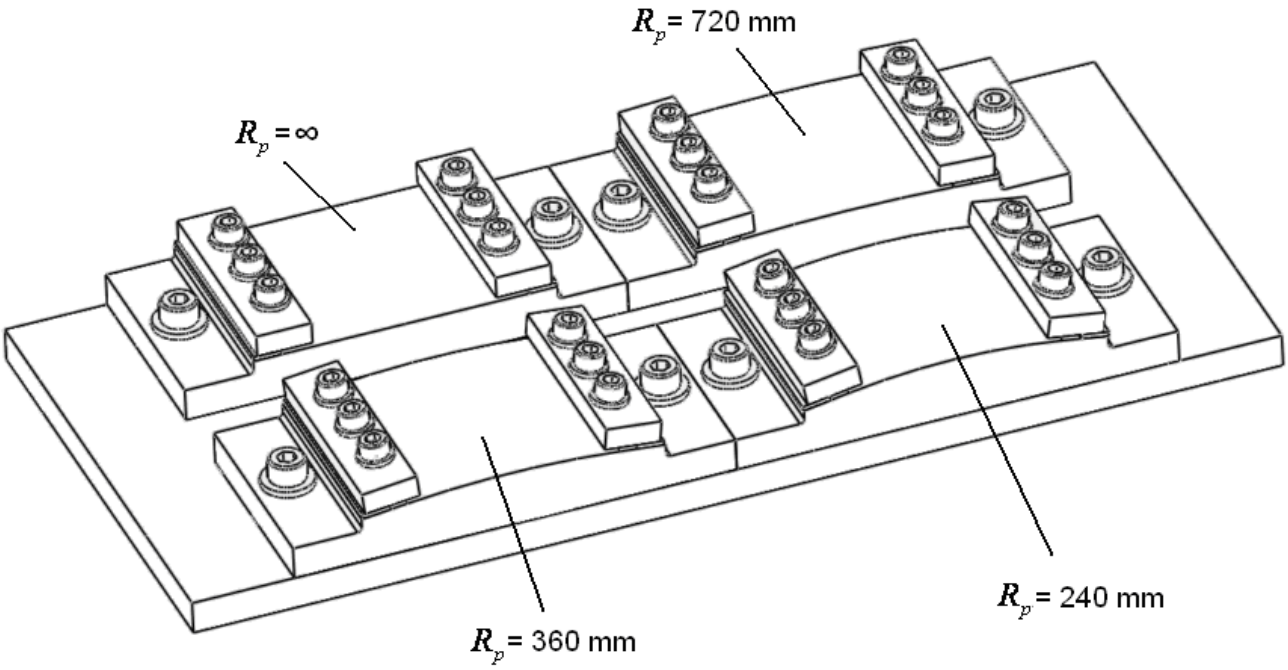

Figure 5.1: Prestressing device with four radii of prebending curvatures ($\infty, 720\text{mm}, 360\text{mm}$ and 240mm) used in the stress peen forming experiments: clamping the samples on the device induces prebending moments.

5.4 Shot peening results

5.4.1 Saturation studies

Almen gauge was used to measure the deformed arc heights of Almen strip ($76\text{mm} \times 19\text{mm} \times 1.29\text{mm}$) and aluminum test strip ($76\text{mm} \times 19\text{mm} \times 1.6\text{mm}$) for different peening times (number of passes). It should be noted that Almen gauge measures the total arc heights between specific lengths of the strip 31.75mm in the longitudinal direction and 15.87mm in the transverse direction, respectively) (SAE-J442). Figure 5.2 presents the 54 measured resulting arc heights of aluminum L test strips for the three shot velocities under investigation. For each shot velocity, with the 18 measured results for $N_p = 1, 2, 4, 8, 16$ and 32 (three repetitions for each number of pass), the quantitative relationship between the resulting arc heights and the number of passes was best fitted using Equation (5.6) as:

$$AH = \frac{at}{b+t} \tag{5.6}$$

where AH is arc height, t is number of passes and a, b are fitting parameters.

For each saturation curve, saturation time (number of passes) and the arc height at saturation time (aluminum intensity) were calculated and listed in Figure 5.2. Very similar curves were obtained for the other test strips and are not reported here.

Table 5.4 lists the arc height at saturation A_s and saturation numbers of passes N_{ps} for aluminum L and T test strips as well as for Almen strips type A for each velocity. With the number of robot passes at saturation N_{ps}, the equivalent robot travelling velocities V_{es} can calculated using Equation (5.5). Therefore, for three shot velocities, equivalent robot travelling velocities for the saturation of the aluminum L test strips are 34mm/s, 47mm/s and 55mm/s, respectively.

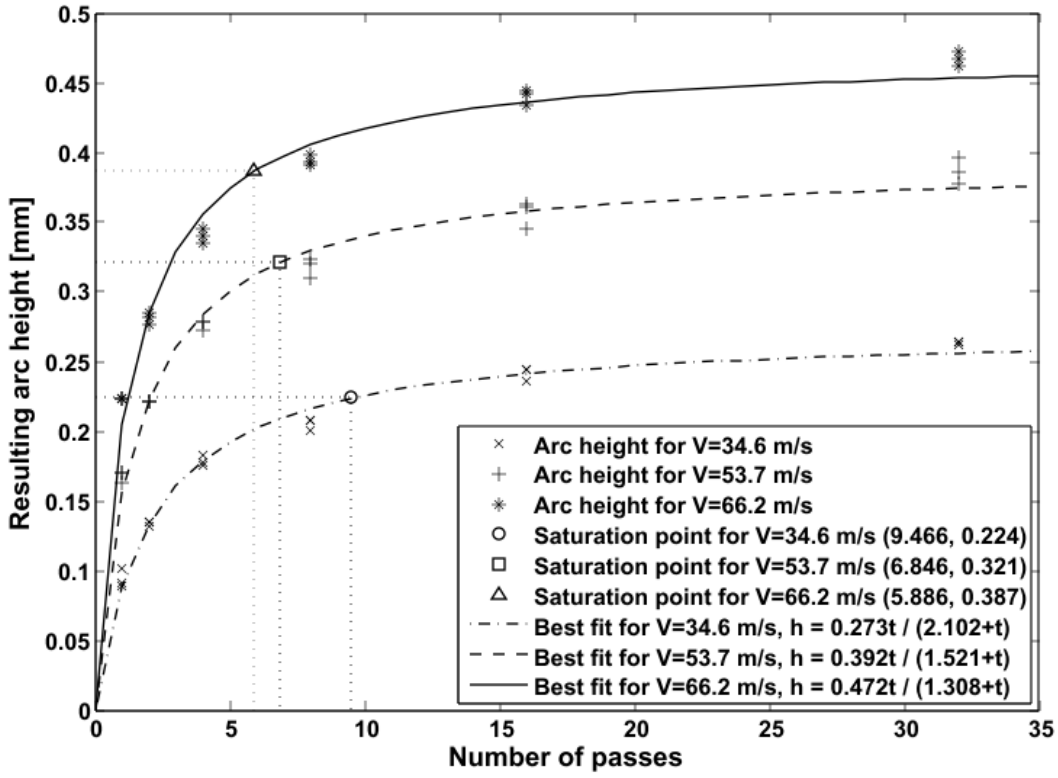

Figure 5.2: Resulting arc heights for different numbers of peening passes and fitted saturation curves for aluminum L test strips (with longitudinal direction equals to 76mm and transverse direction equals to 19mm) for three shot peening velocities.

Table 5.4: Results of saturation study on aluminum test strips (L represents aluminum L test strip, T represents aluminum T test strip) and Almen strip (Type A).

Shot velocity (m/s)	**Arc height at saturation A_s (mm)**			**Saturation time (number of pass N_{ps})**			**Equivalent robot velocity for saturation of aluminum L test strips $V_{es} = 320/N_{ps}$ (mm/s)**
	L	**T**	**Almen strips**	**L**	**T**	**Almen strips**	
34.6	0.224	0.209	0.127	9.466	9.919	23.219	34
53.7	0.321	0.308	0.189	6.846	6.673	12.178	47
66.2	0.387	0.376	0.220	5.886	6.119	8.304	55

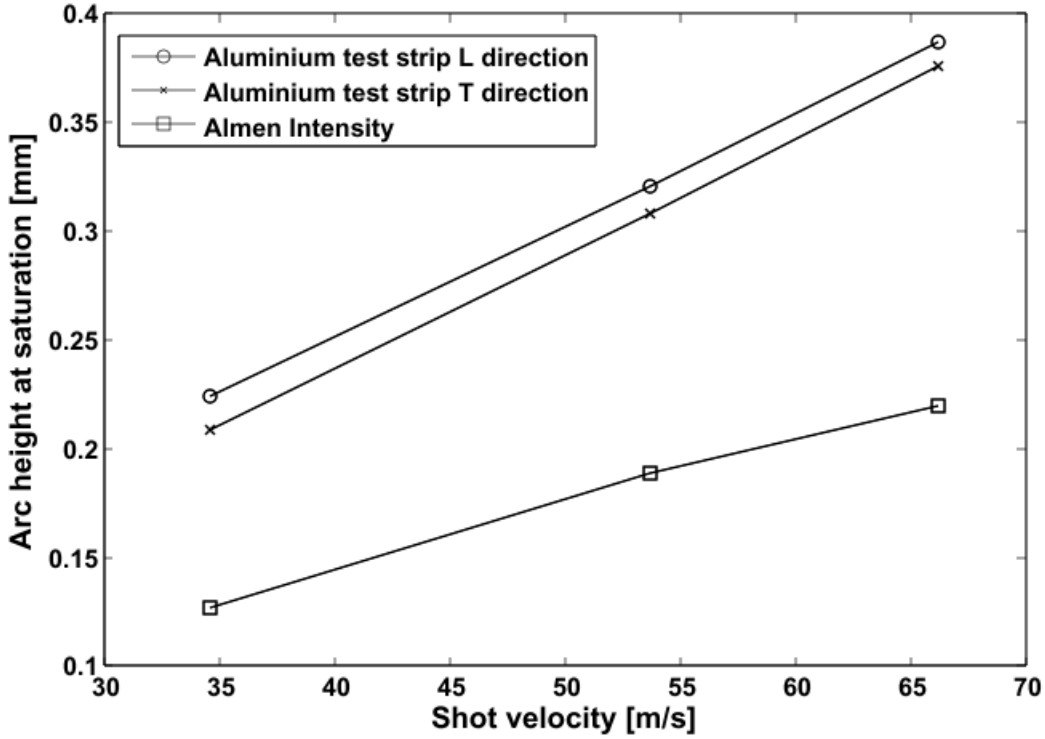

Figure 5.3: Relationship between arc height at saturation and shot velocity for aluminum test strips and Almen strips.

From Table 5.4, it can be found that for each shot peening velocity, arc height at saturation of aluminum test strips (both L and T) are all larger than the corresponding arc height at saturation for Almen strips (Almen intensities). This is due to the fact that aluminum 2024 has a lower modulus of elasticity (more compliant) than Almen 1070 steel strip. Therefore, for the same peening energy, larger deformations can be produced in aluminum test strips than in Almen strips. In addition, for each shot velocity, the arc height at saturation of aluminum L test strip is larger than that of T test strips. This is explainable by the difference in the mechanical properties of the material as shown in Table 5.3 for thin components. For aluminum 2024-T3 with thickness of 1.6mm, tensile test results show that yield stress (σ_s) and ultimate tensile stress (σ_b) in longitudinal direction are larger than those in transverse direction. That is to say, for the same peening energy (shot velocity), induced stress produced by shot peening is larger in L direction than in T direction (Wang et al. 1998). Therefore, the deformed arc height, which can be calculated from the induced stress profiles (Miao et al. 2009) is larger in L direction than that in T direction.

Figure 5.3 presents the relationships between arc height at saturation and shot velocity for aluminum test strips (L and T) and Almen strips. It can be found that for both materials, arc height at saturation increases with the increase of shot peening velocity. The relationship is almost linear, which is consistent with the experimental results presented by Cao et al. (1995).

5.4.2 Surface coverage studies

Taylor Hobson stylus profiler (Talysurf Series 2) was used to measure 3D surface topography for 18 shot peening conditions (six different numbers of peening passes for three shot velocities). For each shot peening condition, measurements on a $5\text{mm} \times 5\text{mm}$ shot peened aluminum surface with 400×400 measurement points was performed to evaluate surface coverage and roughness.

Figure 5.4 shows two example surface topography results with shot velocity of 34.6m/s after 1 and 32 numbers of peening passes, respectively. It can be found that more random indentations were produced after numerous peening passes, which results in larger surface coverage and roughness.

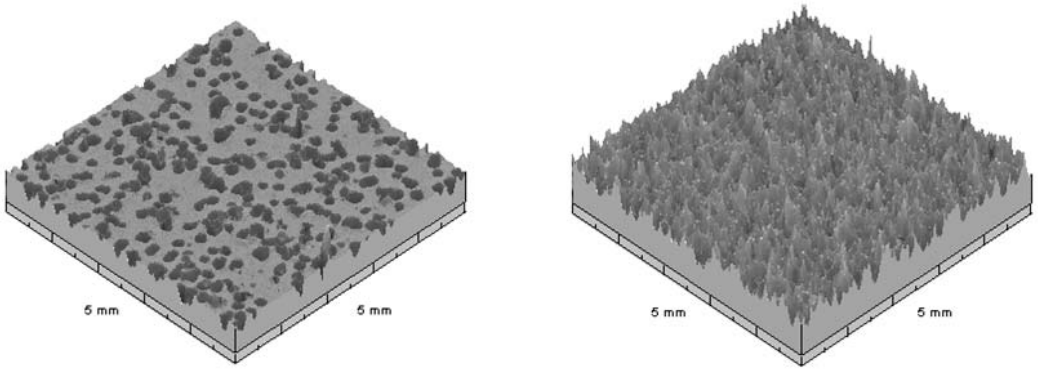

(a) V = 34.6 m/s, 1 pass (b) V = 34.6 m/s, 32 passes

Figure 5.4: Surface topography obtained by 3D roughness measurement profiler. (a) After one peening pass. (b) After 32 peening passes.

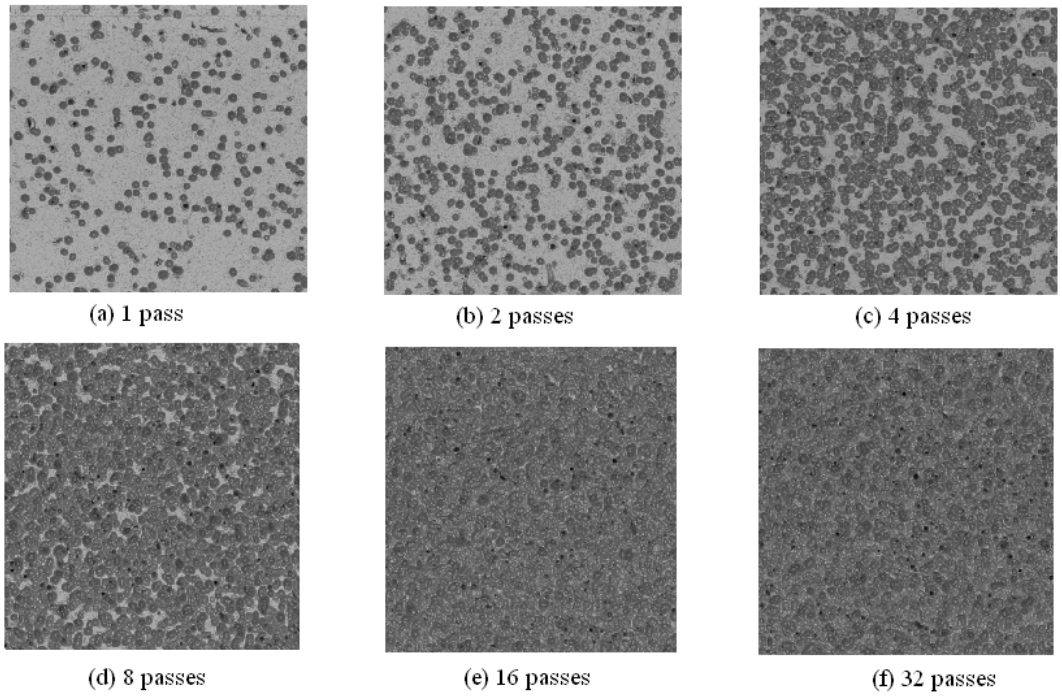

Figure 5.5 2D grayscale topography of peened surfaces after 1, 2, 4, 8, 16 and 32 peening passes for shot velocity of 34.6 m/s.

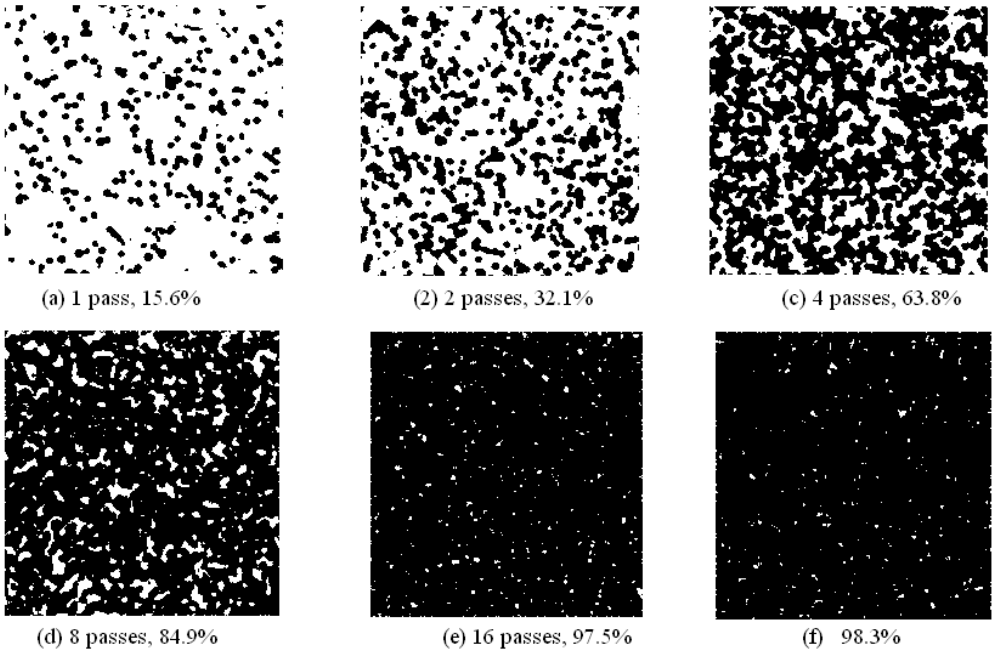

Figure 5.6: Surface coverage calculated by ImageJ after 1, 2, 4, 8, 16 and 32 peening passes for shot velocity of 34.6 m/s.

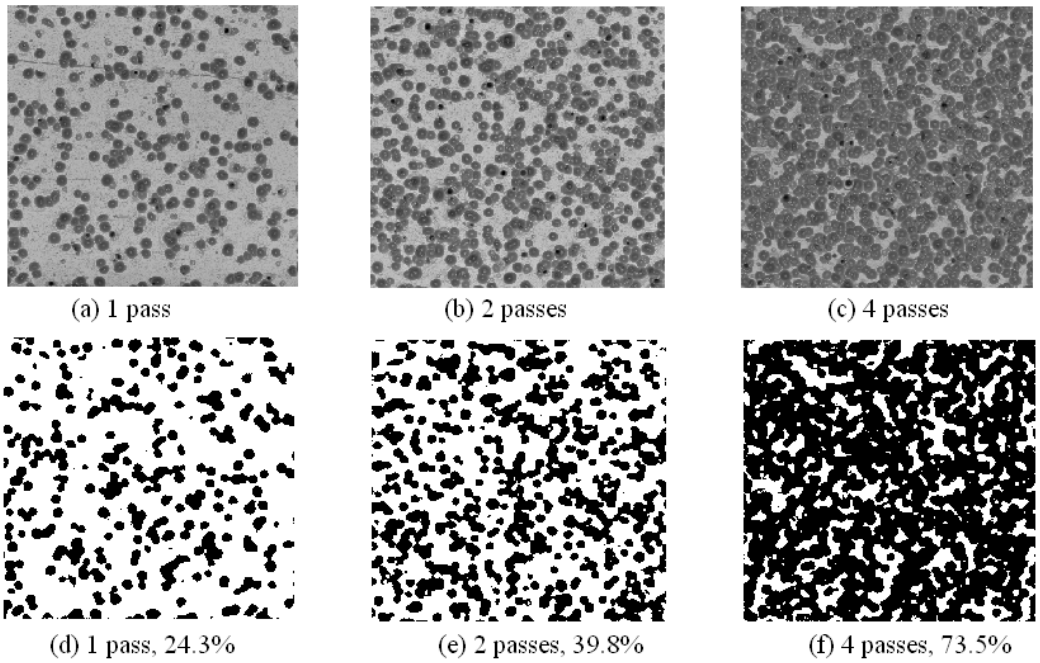

Figure 5.7: 2D grayscale topography (a, b and c) and surface coverage (d, e and f) calculated by ImageJ after 1, 2 and 4 peening passes for shot velocity of 53.7 m/s.

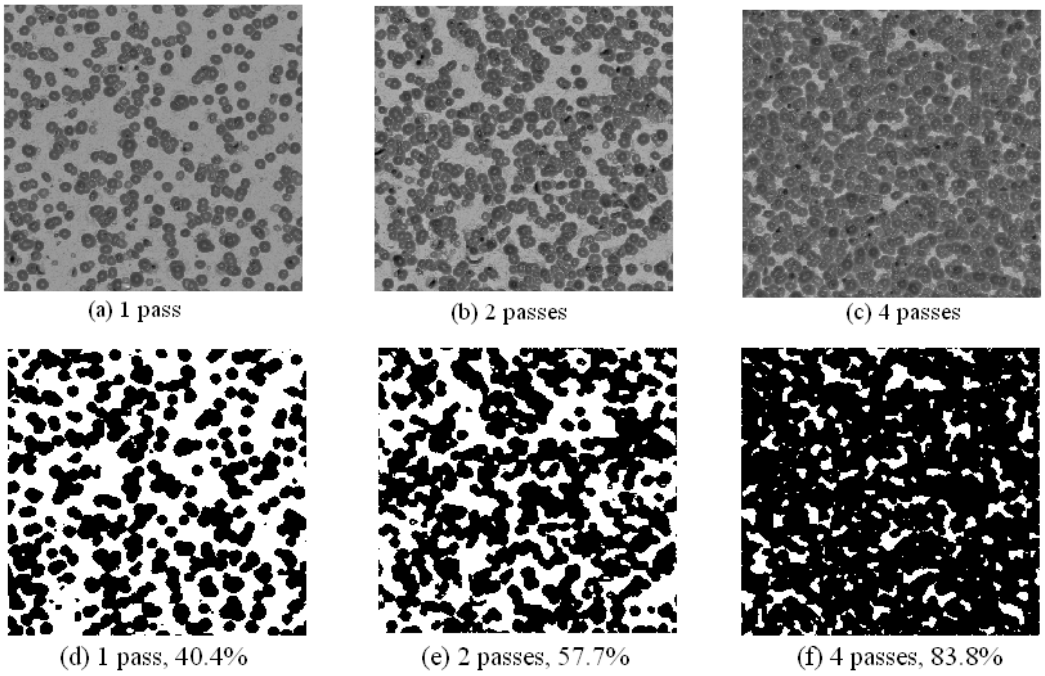

Figure 5.8: 2D grayscale topography (a, b and c) and surface coverage (d, e and f) calculated by ImageJ after after 1, 2 and 4 peening passes for shot velocity of 66.2 m/s.

ImageJava software was use to evaluate surface coverage form surfaces topography images obtained from profiler. Figures 5.5, 5.6, 5.7 and 5.8 present 2D measured topography images as well as evaluated surface coverages by ImageJ after different number of peening passes for three shot velocities. It becomes very difficult to evaluate coverage percentage as 100% is approached since it is hard to distinguish between peened and unpeened areas. Therefore, for shot velocities of $53.7\mathrm{m}/s$ and $66.2\mathrm{m}/s$, only the images after 1, 2 and 4 passes have been presented. For the visual evaluation of the coverage, standard assumption of considering 98% coverage as full coverage remains in this study.

With these visual evaluations of the surface coverage, the relationship between the coverage and the number of peening passes was obtained with a best fitting Avrami as

$$C = 100(1 - e^{-at}) \tag{5.7}$$

where C is coverage, t is the number of peening passes and a is a fitting parameter.

Avrami theoretical model expressed in Equation (5.7) was used to validate the experimental evaluation of the coverage. Before the validation, average radii of indentations for each peening velocity were measured using magnified images from the profiler as shown in Figure 5.9. For

each velocity, five indentation radii were measured to obtain the average value. The average radii of five indentations radii are 0.1302mm, 0.176mm and 0.191mm for the three shot velocities under investigation ($34.6\text{m}/s$, $53.7\text{m}/s$ and $66.2\text{m}/s$). It can be found that the radius of indentation increases with the increase of the shot velocity.

Figure 5.10 compares the experimental fitting coverage curves from Equation (5.7) as well as the theoretical Avrami coverage curves calculated from Equation (5.7) for different shot peening velocities. From Figure 5.10 (a), (b) and (c), it can be found that the experimental fitting curves are consistent with the theoretical curves. Figure 5.10 (d) compares the influence of the shot velocities on surface coverage curves. It shows that for same numbers of peening passes, surface coverage increases with the increase of shot velocity.

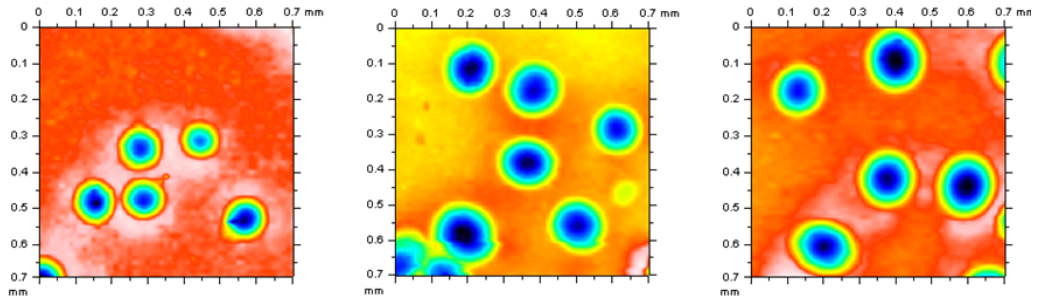

(a) Velocity = 34.6 m/s (b) Velocity = 53.7 m/s (c) Velocity = 66.2 m/s

Figure 5.9: 2D color topography of peened surfaces for measurement of shot peening indentations radii at three shot peening velocities (For each velocity, five indentation radii are measured to obtain the average value).

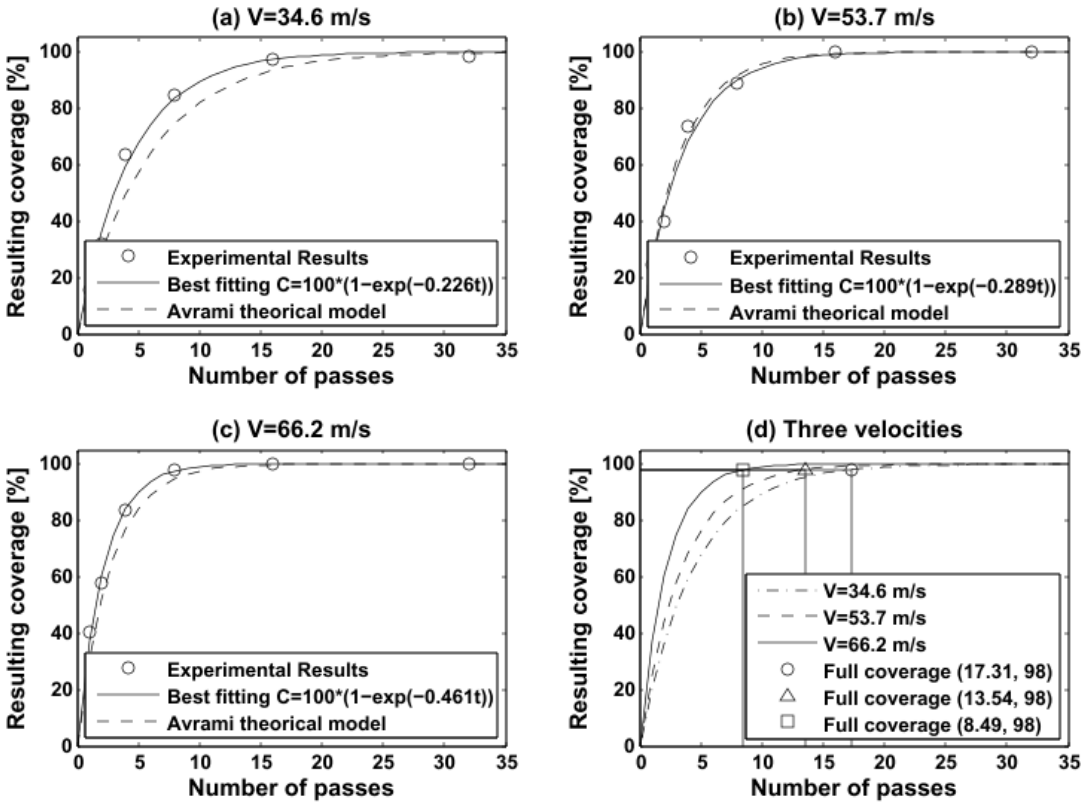

Figure 5.10: Comparison of experimental fitting coverage curves and theoretical Avrami coverage curves for three shot peening velocities. (a) Shot velocity equals to $34.6\mathrm{m}/s$. (b) Shot velocity equals to $53.7\mathrm{m}/s$. (c) Shot velocity equals to $66.2\mathrm{m}/s$. (d) Effect of shot velocity on coverage curves.

5.4.3 Surface roughness studies

With 3D measured surface roughness data, the relationship between surface average roughness and surface stress concentration factor with respect to the number of peening passes can be obtained. The surface average roughness parameter S_a represents the average amplitude of the peaks and valleys of the measured.

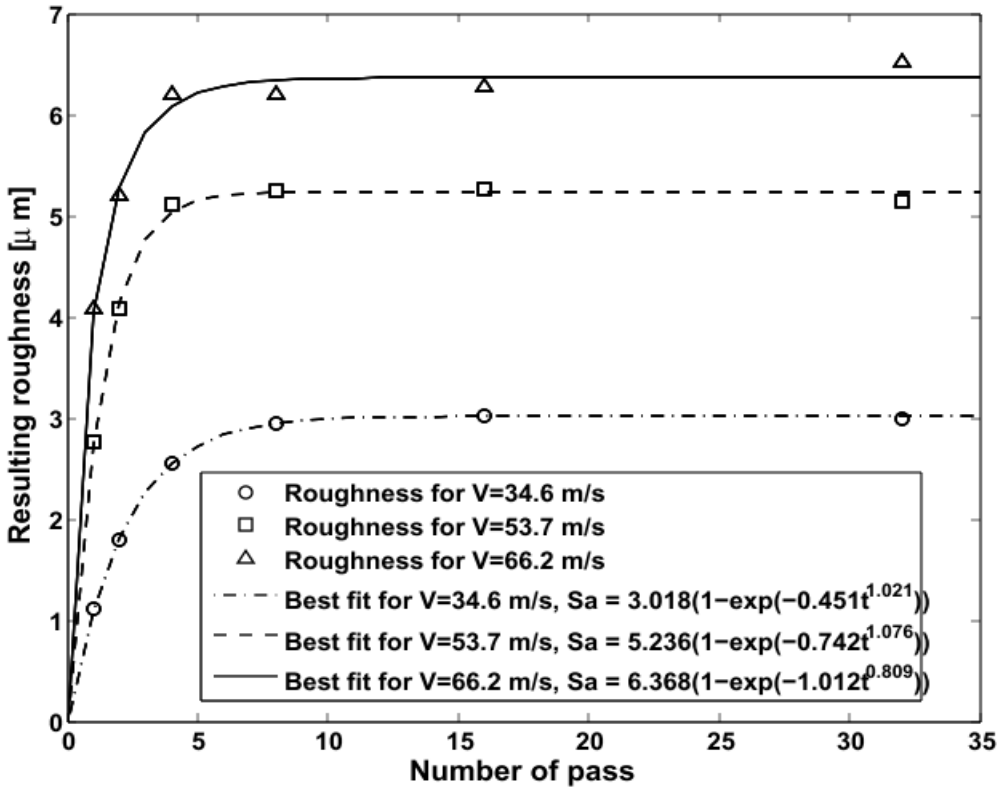

Figure 5.11: Experimentally measured surface average roughness and best fitting curves for three shot velocities.

Figure 5.11 presents 18 experimentally measured surface average roughness for 18 shot peening conditions, as well as the best fitting average roughness curves with respect to number of pass with Equation (5.8) for each shot velocity:

$$S_a = a(1 - e^{-bt^c}) \tag{5.8}$$

where t is the number of peening passes, a, b and c are fitting parameters.

From Figure 5.11, it can be found that the surface average roughness increases with the increase of shot velocity for identical number of peening passes. In addition, the development of the surface average roughness can be divided into two main stages. During stage I, roughness increases rapidly as each impact creates an isolated indentation and independent peaks and valleys. During stage II, many indentations are superimposed so that roughness increases at a slower rate.

Stress concentration factor K_t is calculated from the experimentally measured maximum peak to valley distance (R_t) and the average distance between peaks (S_m) with Equation (5.4). Discrimination between long-range height variations and short-range height variations such as R_t and S_m was accomplished based on a 2D measurement length of 5mm in this experiment. For each of the 18 shot peening conditions, five measurement repetitions were preformed to obtain R_t and S_m. Therefore, five K_t could be calculated.

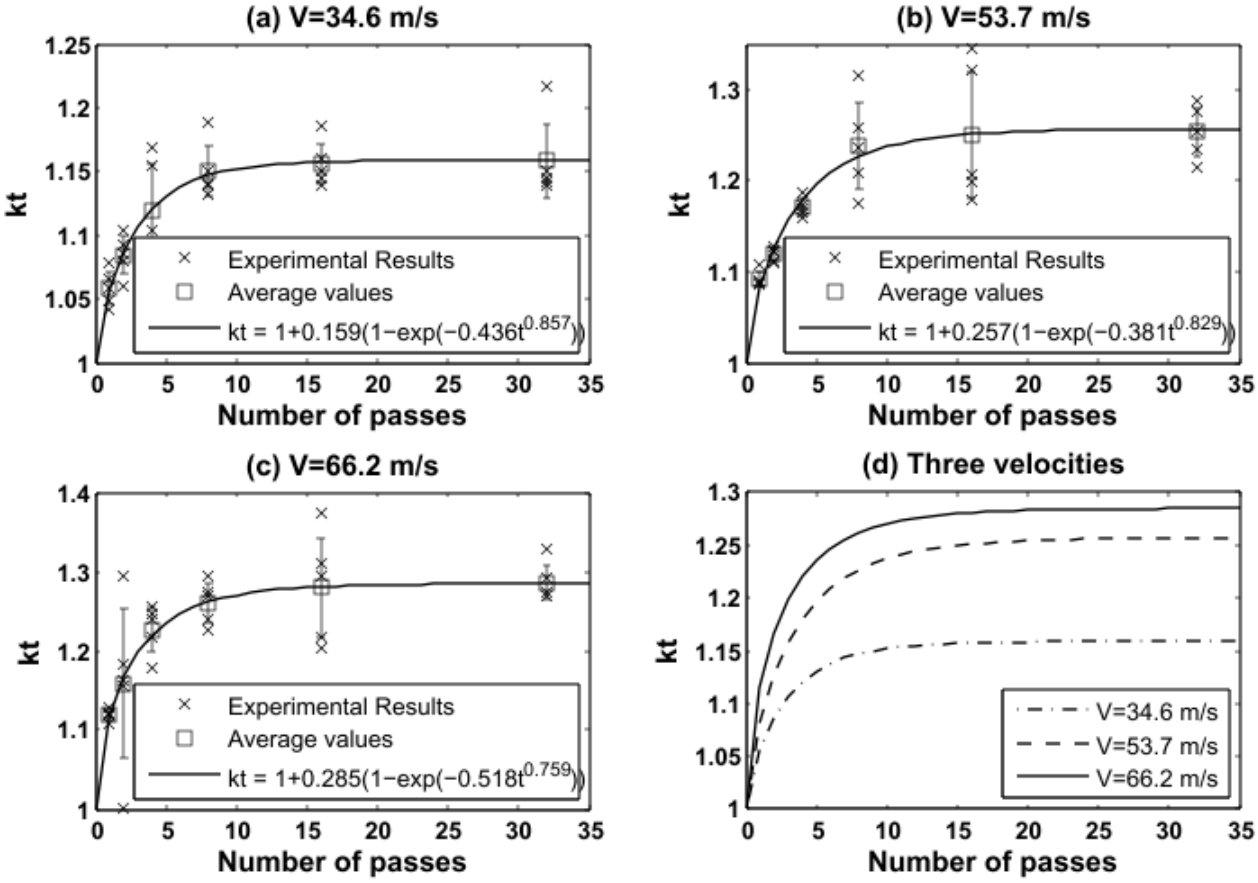

Figure 5.12: Evolution of stress concentration factors *Kt* with respect to number of passes for different velocities. (a) Shot velocity equals to $34.6\mathrm{m}/s$. (b) Shot velocity equals to $53.7\mathrm{m}/s$. (c) Shot velocity equals to $66.2\mathrm{m}/s$. (d) Evolution of stress concentration factor curves for three shot velocities.

Figure 5.12 shows the five calculated stress concentration factors K_t as well as the average value of K_t for each shot peening condition. For each shot peening velocity, Equation (5.9) can be used to best fit the relationship between the experimental stress concentration factors with respect to the number of passes:

$$K_t = 1 + a(1 - e^{-bt^c}) \tag{5.9}$$

where t is the number of peening passes, a, b and c are fitting parameters.

It can be seen from Figure 5.12 that the stress concentration factor increases with the increase of shot velocity. In addition, similar to the surface average roughness, development of the stress concentration factor can be divided into two main stages. During stage I, K_t increases rapidly while during stage II, K_t increases at a slow rate until a stabilized value.

5.4.4 Residual stress profiles measured by X-Ray Diffraction Method (XRD)

X-Ray diffraction method has been employed to measure residual stress profiles corresponding to three different shot peening conditions in Al2024-T351 12.5mm thick strips:

Case 1: Shot peening velocity $v = 34.6\text{m}/s$ and robot travelling velocity for saturation $V_{es} = 34\text{mm}/s$ (as listed in Table 5.4);

Case 2: Shot peening velocity $v = 66.2\text{m}/s$ and robot travelling velocity for saturation $V_{es} = 55\text{mm}/s$ (Table 5.4);

Case 3: Shot peening velocity $v = 66.2\text{m}/s$ and robot travelling velocity for full coverage $V_{ef} = 29\text{mm}/s$ (corresponds to number of peening passes $N_{ef} = 11.15$ in Figure 5.10).

For residual stresses at each depth within the samples, the surface material was electropolished with a diameter of 12mm and the irradiated/sampled spot for the X-Ray beam was with a diameter of 2mm. Therefore, the measured residual stress for each depth is an average value over a circular surface of 2mm in diameter. The measured residual stress values have been compensated using gradient correction and material removal correction method as in SAE HS784. Equation (5.10) is used to best fit this experimental data:

$$\sigma^{res} = A\exp\left[\frac{-2(x-x_d)^2}{W^2}\right] + B \tag{5.10}$$

where σ^{res} is the residual stress, x is the depth beneath the surface, $A + B$ is the maximum residual stress, W is the width of the curve and x_d is the depth of the maximum residual stress (Curtis et. al. 2003). Values of the fitting parameters for the three cases under consideration are presented in Table 5.5.

Figure 5.13 presents measured residual stress values (after correction) as well as the best fitting curves for the three cases studied. The following conclusions can be drawn from this figure:

(1) For saturation speeds (Case 1 and Case 2), with the increase of shot velocity, the maximum compressive residual stress increases. In addition, the depth of maximum compressive residual stress and the thickness of the layer with compressive residual stress are increased.

(2) For the same peening velocity (Case 2 and Case 3), more peening time, which means more impact energy can increase the maximum compressive residual stress, and increase the depth of maximum compressive residual stress as well as the thickness of the layer with the compressive residual stress.

(3) For all three cases, the residual stress at the top surface of the component (from 0 to 0.06mm) is quite similar.

In order to study the surface residual stresses in these three cases, two measurements at each top surface of the component have been performed and compared.

Table 5.6 lists for the three peening cases the measured surface residual stresses (no correction of gradient) for two different locations as well as the average values. These results suggest that the residual stresses are fairly uniform at the surface.

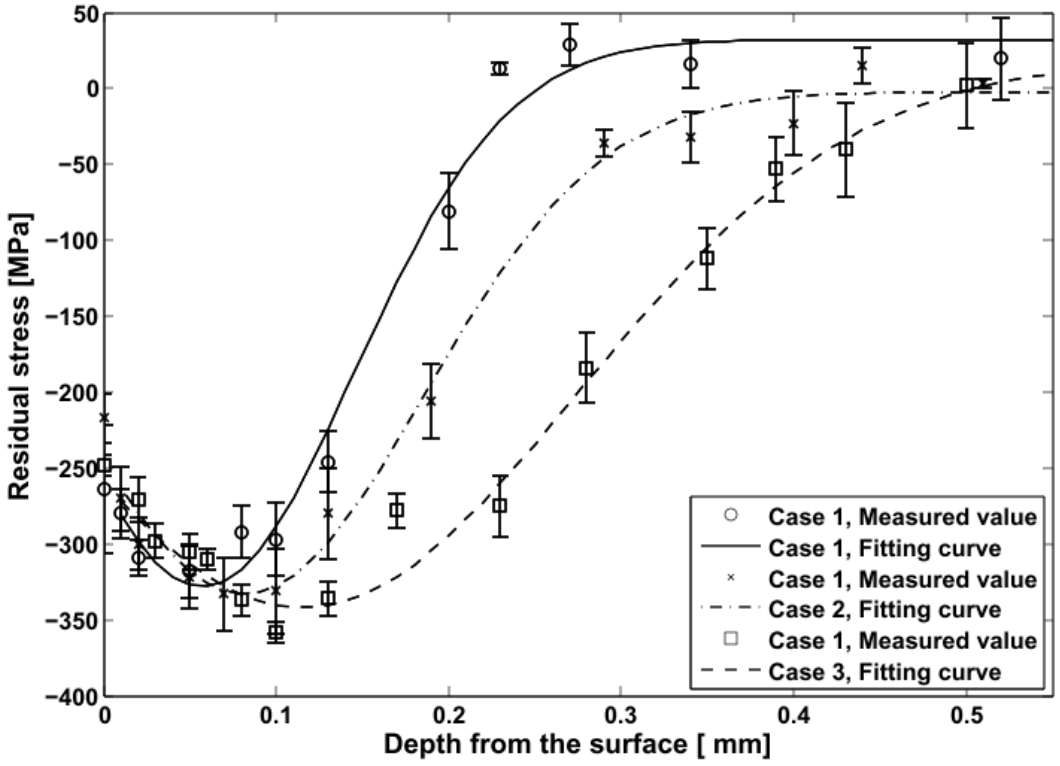

Figure 5.13: Residual stress profiles after correction for three peening cases.

Table 5.5: Residual stresses at surface in three cases.

	A (MPa)	B (MPa)	x_d (mm)	W (mm)	R^2
Case 1	-360.7	32.25	0.0571	0.177	0.9814
Case 2	-330.8	-2.373	0.08161	0.2073	0.9845
Case 3	-354.6	18.64	0.1151	0.3203	0.9851

Table 5.6: Residual stresses at the surface for the three peening cases under consideration (Unit: MPa).

	Location 1	**Location 2**	**Average**
Case 1	-296± 10	-284± 9	-290± 9
Case 2	-275±6	-290± 3	-283± 5
Case 3	-286±4	-274± 8	-280± 6

5.5 Stress peen forming results

5.5.1 Stress peen forming of narrow strips

Aluminum L test strips and T test strips with the same dimension as Almen strips (76mm × 19mm × 1.6mm) have been chosen in this study for simplification of arc height measurement. Significant parameters for the peen forming tests can be calculated as follows.

Figure 5.14 illustrates the parameters introduced in the relationship that can be obtained by a geometrical analysis between the prebending radius R_p and the prebending arc height Ah_p, expressed by Equation (5.11):

$$R_p{}^2 = (R_p - Ah_p)^2 + \left(\frac{l}{2}\right)^2 \tag{5.11}$$

where l is the reference length for arc height measurement, which is equal to 31.75mm in this case. Since $Ah_p \ll R_p$, Equation (5.11) can be rewritten as Equation (5.12):

$$Ah_p = \frac{l^2}{8R_p} \tag{5.12}$$

Prebending moment can be calculated with Equation (5.13) (Miao et al. 2009):

$$M_p = \frac{EI}{R_p} = \frac{Ebt^3}{12R_p} \tag{5.13}$$

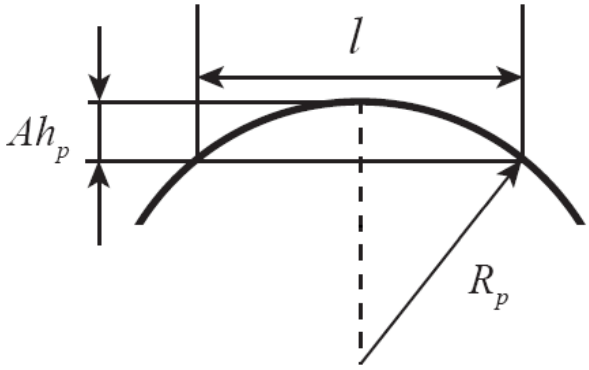

Figure 5.14: Illustration of the relationship between prebending radius and prebending arc height.

where E is Young's Modulus of aluminum strip (76.5GPa), the average value of thin L and T aluminum strips as shown in Table, I is the moment of inertia, b is the width of the strip (19mm) and t is the thickness of the strip (1.6mm).

The surface tensile stress of a prebent strip σ_{st} can be calculated with Equation (5.14):

$$\sigma_{st} = \frac{M_p \times {}^{t}/_{2}}{I} \tag{5.14}$$

Table 5.7 lists the prebending arc heights Ah_p, prebending moments M_p, surface tensile stresses σ_{st} and resulting arc heights measured by Almen gauge for peen forming tests performed under four prebending radii ($R_p = \infty, 720\text{mm}, 360\text{mm}, 240\text{mm}$), shot velocity of $66.2\text{m}/s$ and for a robot travelling velocity $V_{es} = 55\text{mm}/s$ (ensuring saturation of the aluminum strips).

It can be seen from Table 5.7 that the maximum surface stress σ_{st} produced by the maximum prebending moment is 255MPa, which is less than the yield stress of aluminum 2024 listed in Table 5.3. The prebending of the strip is therefore entirely elastic for the range of prebending arc height under consideration.

Table 5.7: Relationship between prebending conditions and resulting arc heights.

Radius of prebend R_p **(mm)**	**Prebend arc height** Ah_p **(mm)**	**Prebend moment** M_p **(N·mm)**	**Surface stress** σ_{st} **(MPa)**	**Resulting arc height** Ah_r **(mm)** $v = 66.2\text{m}/s$			
				L-test strip with Longitudinal prebending		**T-test strip with Transverse prebending**	
				TEST 1	**TEST 2**	**TEST 1**	**TEST 2**
∞	0	0	0	0.3759	0.3658	0.3429	0.3632
720	0.175	689	85	0.4521	0.4674	0.4343	0.4420
360	0.350	1378	170	0.5969	0.5867	0.5537	0.5791
240	0.525	2067	255	0.7010	0.7163	0.6629	0.6782

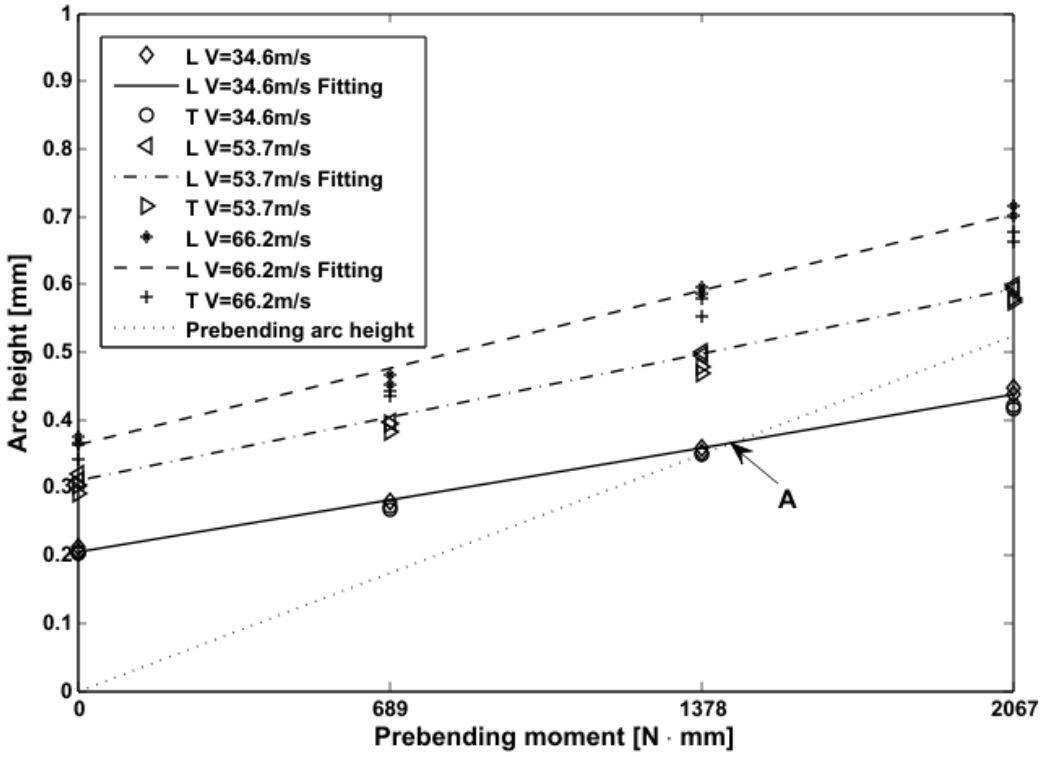

Figure 5.15: Experimental relationship between arc heights (prebending arc height and resulting arc height) and prebending moments.

Figure 5.15 presents the prebending arc heights and the resulting arc heights for three shot velocities as a function of the prebending moments. For each velocity and prebending moment, two L test strips and two T test strips were peened. It can be found that, similar to the saturation study, resulting arc heights of L test strips are larger than those of T test strips for identical prebending moments. In addition, for each shot velocity, a linear best fitting curve from 8 resulting arc heights data in longitudinal direction was obtained to represent the relationship between the prebending moments and the resulting arc heights. The fitting curves show that the resulting arc height increases almost linearly with the increase of the prebending moment. Furthermore, for shot velocities $v = 53.7\mathrm{m}/s$ and $v = 66.2\mathrm{m}/s$, all resulting arc heights are larger than the prebending arc heights. However, for shot velocity $v = 34.6\mathrm{m}/s$, there exists a specific prebending moment (Point A) with identical prebending and resulting arc heights. According to the best-fitting curve for shot peening velocity equals to $34.6\mathrm{m}/s$, both prebending and resulting arc heights equal to $0.367\mathrm{mm}$ at Point A while the prebending moment equals to $1445.5\mathrm{N}\cdot\mathrm{mm}$. This result suggests that a controlled shot peening combined to an accurate

prestressing device could produce the same final arc height as the prebending arc height. This finding could be of particular interest for practical applications.

5.5.2 Residual stress profile after stress peen forming

Two additional residual stress profiles have been measured by XRD after conventional peen forming (without prebending moment) and after stress peening forming (with prebending moment). The two cases studied are:

(1) ***Case 4:*** Al2024-T3 strip with dimensions of $76\text{mm} \times 19\text{mm} \times 1.6\text{mm}$, peened with shot velocity of $v = 66.2\text{m}/s$, robot travelling velocity of 55mm/s and for conventional peen forming.

(2) ***Case 5:*** Al2024-T3 strip with dimensions of $76\text{mm} \times 19\text{mm} \times 1.6\text{mm}$, peened with shot velocity of $v = 66.2\text{m}/s$, robot travelling velocity of 55mm/s and for a prebending moment of $2067\text{N} \cdot \text{mm}$.

For each case, two identical samples have been prepared. Correction for stress relaxation and redistribution as a result of material removal via electro-polishing was performed as per SAE HS784. However, it is difficult to compensate the stress release when the correction becomes large. Therefore, for each case, the residual stresses for depth (0 to 0.8mm) were measured from the convex side on a first sample and residual stresses for depth (0.8mm to 1.6mm) were measured from concave side on the second sample.

Figure 5.16 shows the residual stress profiles for Cases 2 (strip with thickness 12.5mm, peened with shot velocity of $v = 66.2\text{m}/s$, robot travelling velocity of 55mm/s), 4 and 5. It can be seen from the figure that:

(1) Shot peening on thick component produces compressive residual stress only at the top surface of the component (Case 2), while peen forming produces compressive residual stress on both top and bottom surfaces of the strip (Cases 4 and 5). Larger tensile residual stress can be induced in the middle of the strip after peen forming.

(2) With respect to conventional peen forming (Case 4), stress peen forming (Case 5) has larger compressive residual stress on both top and bottom surfaces. It also leads to high tensile stresses in the middle layer of the strip.

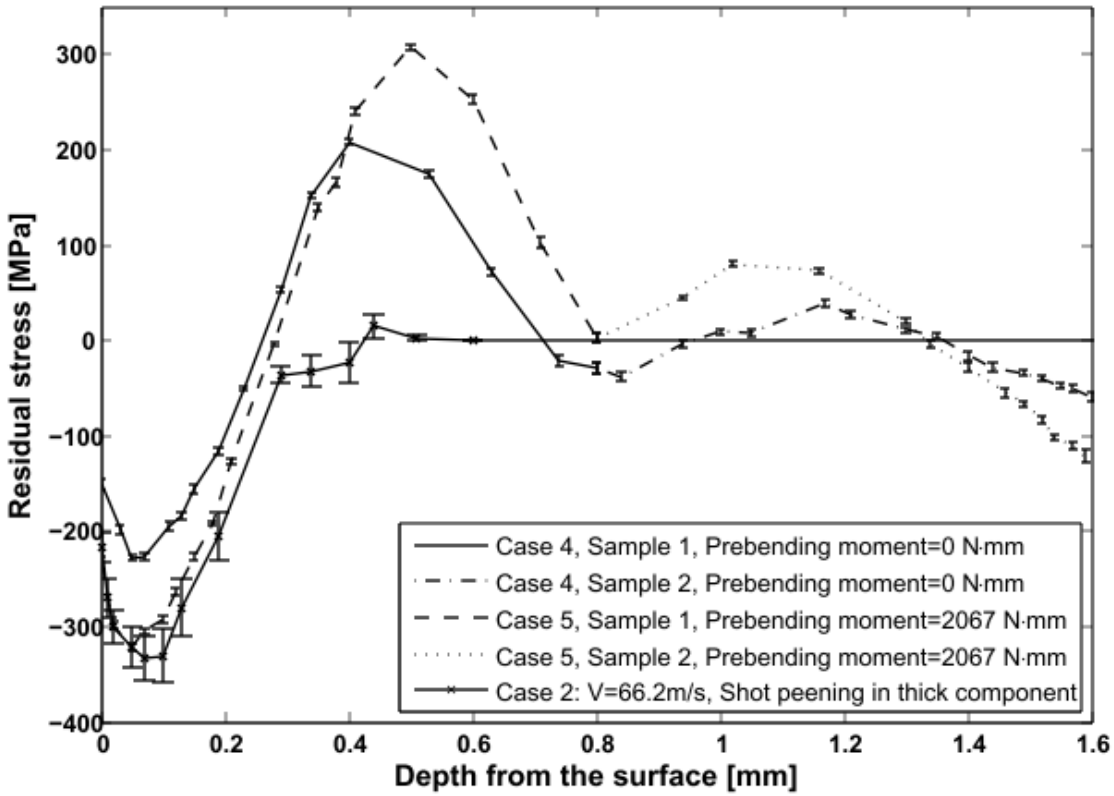

Figure 5.16: Residual stress profiles in three cases: conventional peen forming on 1.6mm thick strip ($M_p = 0\text{N} \cdot \text{mm}$), stress peen forming on 1.6mm thick strip ($M_p = 2067\text{N} \cdot \text{mm}$) and shot peening of 12.5mm thick component.

5.5.3 Stress peen forming of square samples

Table 5.8 lists the relationship between the prebending values in the longitudinal direction (prebending radii, prebending moments and surface stresses) and the resulting radii of curvature in longitudinal and transverse directions for square strips ($76\text{mm} \times 19\text{mm} \times 1.6\text{mm}$) with shot velocity of $66.2\text{m}/s$ and robot travelling velocity of 55mm/s. Similar to that for narrow strips, the prebending moment M_p is calculated using Equation (5.13) with $b = 19\text{mm}$ and the surface stress σ_{st} is calculated with Equation (5.14).

The resulting radius of curvature following the centerline of the square plate is calculated from the measured deformation data measured by the surface profiler in the longitudinal and transverse directions, respectively.

From Table 5.8, it can be seen that with the increase of the prebending moment, the resulting radius of curvature decreases in Longitudinal direction and increases in Transverse direction.

Table 5.9 lists the relationship between the prebending values (prebending radii, prebending arc height) and the resulting arc height for the cases listed in Table 5.8.

The prebending arc heights Ah_p and resulting arc heights Ah_r are calculated using Equation (5.12) with reference length $l = 76\text{mm}$. The results show that with the increase of the prebending moment, the resulting arc height increase in Longitudinal direction and decreases in transverse direction.

Table 5.8: Prebending parameters and resulting radii for peen formed square strips.

Radius of prebending R_p (mm)	**Prebending moment M_p (N·mm)**	**Surface stress σ_{st} (MPa)**	**Resulting radius of curvature (mm) $v = 66.2\text{m}/s$**					
			Longitudinal resulting radius (mm)			**Transverse resulting arc radius (mm)**		
			Test 1	**Test 2**	**Test 3**	**Test1**	**Test**	**Test 3**
∞	0	0	541	513	520	606	605	600
720	2756	85	371	372	370	668	670	675
360	5512	170	279	274	272	895	848	834
240	8268	255	218	216	217	1054	1043	1032

Table 5.9: Prebending parameters and resulting arc heights for peen formed square strips.

Radius of prebending R_p (mm)	**Prebending arc height Ah_p (mm)**	**Resulting arc height Ah_r (mm) $v = 66.2\text{m}/s$**					
		Longitudinal resulting arc height (mm)			**Transverse resulting arc height (mm)**		
		Test 1	**Test 2**	**Test 3**	**Test 1**	**Test 2**	**Test 3**
∞	0	1.336	1.406	1.386	1.191	1.194	1.204
720	0.8507	1.947	1.938	1.95	1.081	1.077	1.070
360	1.7014	2.592	2.629	2.648	0.806	0.852	0.866
240	2.5521	3.307	3.333	3.320	0.685	0.692	0.699

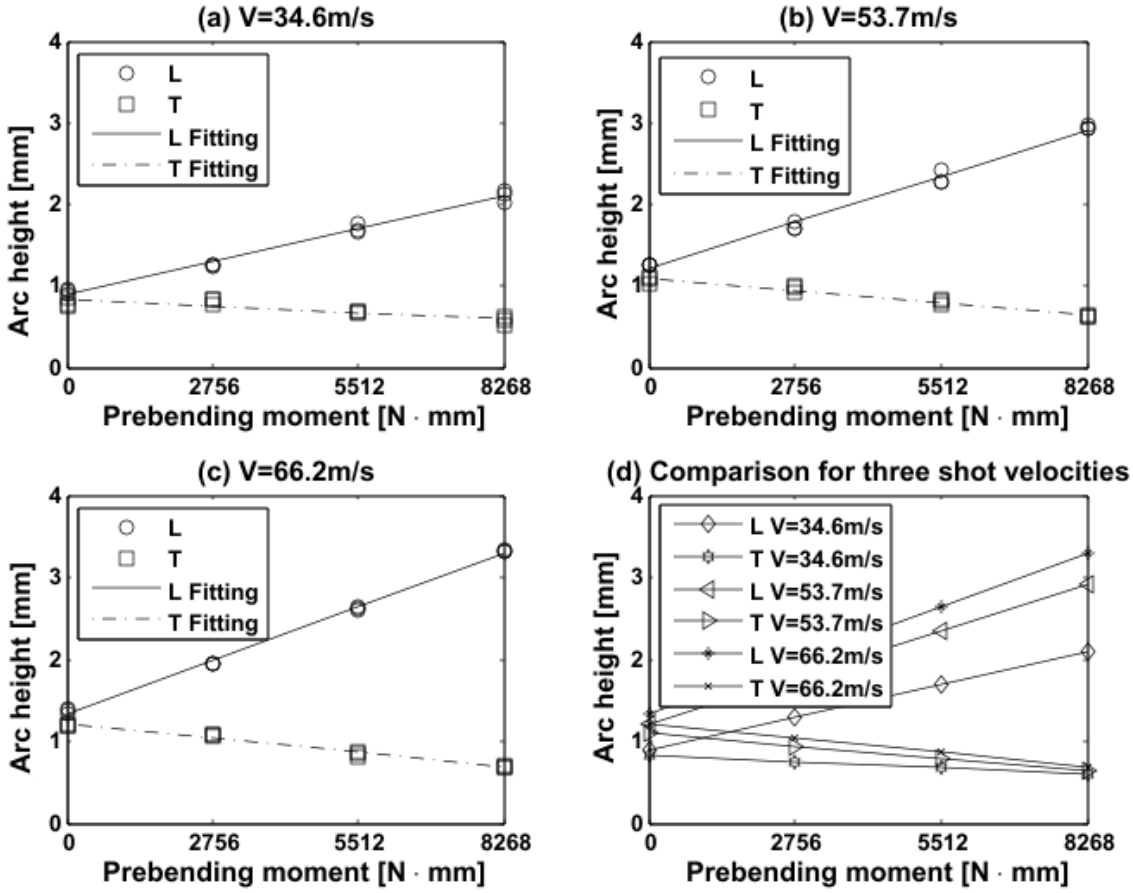

Figure 5.17: Relationship between resulting arc heights in Longitudinal and Transversal directions and prebending moments. (a) Shot velocity equals to $34.6\mathrm{m}/s$. (b) Shot velocity equals to $53.7\mathrm{m}/s$. (c) Shot velocity equals to $66.2\mathrm{m}/s$. (d) Comparison of resulting arc heights for three shot velocities.

Figure 5.17 shows the relationship between the resulting centerline arc heights with respect to the prebending moments. For each shot peening velocity and each prebending moment, three resulting arc heights in longitudinal and transverse directions have been presented respectively. In addition, linear regression have been used to best fitting the relationships between the resulting arc heights and the prebending moments in both directions. It can be seen that for the three shot peening velocities, the resulting arc height in longitudinal direction increases with the increase of the prebending moments while the resulting arc height in transverse direction decreases with the increase of the prebending moments. All of these results reflect the tendencies that were obtained experimentally by (Li, 1981).

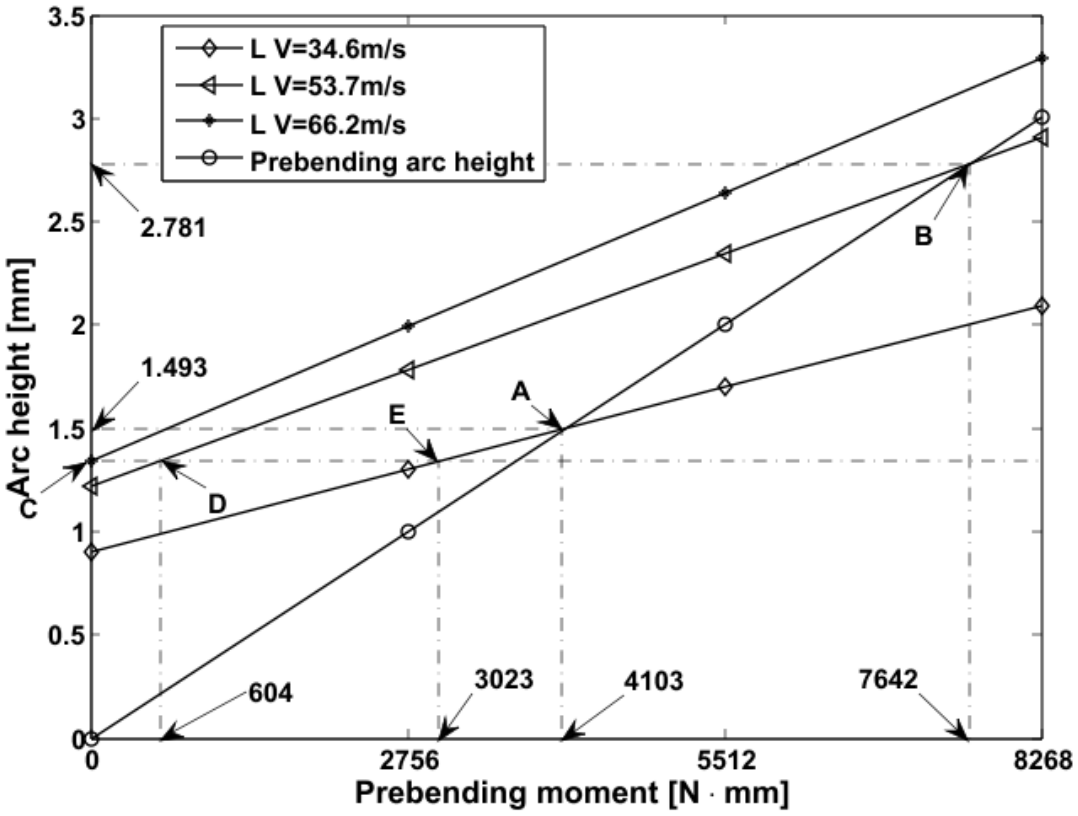

Figure 5.18: Relationship between resulting arc heights and prebending arc heights vs. prebending moments for three velocities. (Point A: identical prebending moment of $4116\text{N}\cdot\text{mm}$ and resulting arc heights of 1.493mm for shot velocity of $34.6\text{m}/s$. Point B: identical prebending moment of $7666\text{N}\cdot\text{mm}$ and resulting arc heights of 2.781mm for shot velocity of $53.7\text{m}/s$. Point C, D and E: identical resulting arc heights of 1.34mm with prebending moments of $0,\ 540\text{N}\cdot\text{mm}$ and $2934\text{N}\cdot\text{mm}$ for three shot velocities $34.6\text{m}/s$, $53.7\text{m}/s$ and $66.2\text{m}/s$, respectively).

Figure 5.18 presents the prebending arc heights and resulting arc heights in the longitudinal direction as a function of the prebending moments for three shot velocities. It can be found that with the increase of the shot peening velocity, the resulting arc height increases. For shot velocity $v = 66.2\text{m}/s$, all resulting arc heights are larger than the prebending arc heights, however, for both shot velocities $v = 34.6\text{m}/s$ and $v = 53.7/s$, there exists specific points **A** and **B**, where the resulting arc heights are equal to the prebending arc heights. With the help of the prebending technique, the same deformed arc heights can be obtained under different shot peening conditions. For example, points **E**, **D** and **C** represent resulting arc height 1.34mm obtained from

three shot peening velocities ($v = 34.6\text{m}/s,\ v = 53.7/s$ and $v = 66.2\text{m}/s$) with three different prebending moments $0,\ 604\text{N}\cdot\text{mm}$ and $3023\text{N}\cdot\text{mm}$, respectively. It is well known that higher shot peening velocity requires more peening energy and can also produce larger surface roughness which has detrimental effect on the fatigue life of the peened component. Therefore, stress peen forming offers an alternative where the prebending values and the shot peening parameters could potentially be selected in order to obtain the desired shape while minimizing the shot peening energy and maximizing the fatigue life of the peened component.

5.6 Summary

Shot peening experiments on aluminum 2024 with ceramic shots have been performed to study peening intensity, surface coverage and surface roughness with different shot peening velocities. Experimental results can be summarized as:

(1) Shot peeing time can be evaluated either by one pass of robot peening N_p for different robot peening velocities V_r or by different numbers of peening passes N_p for the same robot peening velocities V_r. Experimental results show that both methods can produce the same surface coverages and resulting arc heights on aluminum test strips. For any number of peening passes N_p the equivalent robot peening velocity V_e can be calculated with Equation(5.5).

(2) For the same peening conditions, aluminum L test strip produces larger resulting arc height than T test strip. This result means that the rolling direction of the aluminum strip has an influence on the shot peening results.

(3) When compared to Almen standard strips, both aluminum L test strip and T test strip present larger intensity and a shorter peening time to reach saturation.

(4) For both aluminum and Almen strips, the relationships between intensities and shot peeing velocities are almost linear.

(5) With the increase of shot peening velocity, the radii of the plastic indentation increase**,** which can explain why the increase of the peening velocity decreases the full coverage peening time. With the help of the radii of the plastic indentations, Avrami equations can

be used for predicting the relationship between the coverage and peening time (number of peening passes).

(6) For the same peening time, both surface average roughness S_a and surface stress concentration factor K_t increase with the increase of the peening velocity. In addition, their relationships present two main stages: during stage I, roughness increases rapidly and during stage II, roughness increase slowly and stabilizes.

(7) For saturation peening time, with the increase of shot peening velocity, the maximum compressive residual stress, the depth of the maximum compressive residual stress as well as the depth of the compressive residual stress increase. For the same peening velocity, the increase of the peening time can increase the maximum compressive residual stress, the depth of the maximum compressive residual stress as well as the depth of the compressive residual stress. However, both peening velocities and peening time have few influence on the surface residual stress.

With the experimental results of the peening intensity, surface coverage and surface roughness, quantitative relationships have been obtained in order to relate them to peening time (number of passes). With Equations (5.6), (5.7), (5.8) and (5.9), the values of resulting arc height (AH), coverage (C) and roughness (S_a and K_t) at saturation and at full coverage can be calculated separately. Table 5.10 summarizes these simulated results for this specific shot peening case. It should be noted that the results of the aluminum L test strip have been considered since little difference have been presented between L and T test strips.

It can be seen from Table 5.10 that:

i. With the increase of the shot peening velocity, the peening time (number of passes) to reach saturation and full coverage decrease, while the arc heights, surface roughness (S_a and K_t) at saturation and at full coverage increase.

ii. The ratio of the peening time to reach full coverage and the peening time to reach saturation is of 2.17, 1.86 and 1.89 for shot peening velocities $v = 34.6\mathrm{m}/s$, $v = 53.7/s$ and $v = 66.2\mathrm{m}/s$, respectively. In general, these values are close to 2 for all three cases, which means the peening time of full coverage is twice the peening time to reach saturation. Since full coverage is easier to evaluate, peening operator could find full

coverage time and divides by two to obtain the effective time with respect to saturation, for the materials and conditions listed in this study.

Stress peen forming experiments on both narrow strips (aluminum L and T test strips) with dimensions of $76\text{mm} \times 19\text{mm} \times 1.6\text{mm}$ and square strips with dimensions of $76\text{mm} \times 76\text{mm} \times 1.6\text{mm}$ have been performed. Experimental results show that:

1) When compared to conventional peen forming, stress peen forming produces larger resulting arc height under the same peening conditions for both narrow and square strips.
2) Similar to the saturation study, for the same stress peen forming conditions, L test strip produce larger resulting arc height than T test strip.
3) The relationship between the prebending moments and the resulting arc heights are almost linear for both narrow and square strips. For narrow strips, the resulting arc height increases with the increase of the prebending in the longitudinal direction. For the square strips, the resulting arc height following the longitudinal direction increases with the increase of the prebending moment. However, the resulting arc height following the transverse direction decreases with the increase of the prebending moment.
4) For narrow strip (L test strip), a controlled shot peening process combined with a prebending device can be designed to produce the same resulting arc height as the prebending arc height. For square strip, stress prebending can produce same resulting as prebending arc heights along longitude direction. Different peening velocities combined with different prebending moments can produce same designed resulting arc height, as points E, D and C in Figure 5.18. Therefore, with the help of the prebending device, it is possible to reduce peening energy and improve fatigue life of the peened component.
5) Under same forming condition, stress peen forming requires less peening energy and produces less surface stress concentration factor therefore can improve fatigue life of deformed component.

Table 5.10: Relationship between saturation intensity and full coverage for three shot velocities.

Shot Velocity v (m/s)	**Saturation**					Full Coverage (98%)				
	N	**Arc height AH (mm)**	**Coverage C (%)**	S_a **(µm)**	K_t	N	**Arc height AH (mm)**	**Coverage C (%)**	S_a **(µm)**	K_t
34.6	9.466	0.224	83.4	2.98	1.15	20.59	0.248	98	3.01	1.16
53.7	6.846	0.321	87.7	5.22	1.22	12.79	0.350	98	5.24	1.25
66.2	5.886	0.387	87.3	6.28	1.25	11.15	0.422	98	6.36	1.27

5.7 Conclusions

Almen intensity and surface coverage are two important parameters to evaluate the shot peening process. However, different from surface coverage, which is based on the peened material, Almen intensity is based on standard Almen strip (spring 1070). In this paper, experimental study of intensity and surface coverage on aluminum 2024 have been performed to relate them with the peening time. One contribution of this work is to develop quantitative relationships between arc height and coverage with respect to the number of peening passes. With these equations, the number of passes to reach saturation as well as to reach full coverage can be calculated.

Compressive residual stresses have beneficial effect for the improvement of the fatigue life of the peened component. However, surface roughness has detrimental effect on the fatigue life of the peened component. In this paper, the influence of the shot peening velocities and peening time on the residual stress profile as well as their influence on the surface roughness have been experimentally measured and presented. Peen forming has been recognized as a suitable manufacturing process for various aircraft components. Stress peen forming is a prevailing technique for the forming of wing skins. Another contribution of present work is to establish a quantitative relationship between the prebending moment and resulting arc height based on experimental results. With this relationship, the prebending moment can be predicted to achieve the required deformed curvature or arc height.

CHAPITRE 6 A NUMERICAL STUDY OF STRESS PEEN FORMING

H. Y. Miao, S. Larose, C. Perron, Martin Lévesque, submitted to the journal *Advances in Engineering Software,* on April 21th, 2010.

6.1 Abstract:

Stress peening forming is widely used in the aeronautics industry to induce curvatures in wing skins. Most of the investigations of stress peen forming are empirical and experimental. In this paper, a three steps numerical model that can simulate this process was developed. First, an implicit Finite Element Analysis (FEA) with ANSYS where a prebending moment along the spanwise direction of the component was performed. Then, an explicit FEA with LS-DYNA simulating shot impacts on the pre-stressed component was executed in order to obtain the resulting stresses inside the component. Finally, an implicit FEA with ANSYS was performed for calculating the arc heights and the curvature radii of the component in chordwise and spanwise directions. Numerical analysis of the process shows that the prebending moments have an influence not only on the residual stress profiles but also on the curvatures of the deformed component in chordwise and spanwise directions. This model establised the relationship between the prebending moment and the resulting arc heights and residual stress profiles. The numerical strategies developed in this paper supply a useful tool for studying and optimizing the stress peening process.

6.2 Introduction

Shot peen forming is a dieless process which is and has been widely used to form various aircraft components since the 1960's (Baughman, 1984; Kopp and Ball, 1987; Tatton, 1987). The forming process is achieved by bombarding the surface of a component with high speed particles that induce a thin layer of plastic deformations near the surface. These plastic deformations induce an isotropic residual stress distribution in the component and a convex curvature of the component towards the peening direction. Conventional peen forming causes the component to acquire a doubly curved shape because its induces the curvatures in all directions. For a wing skin, which has a larger curvature in chordwise direction than in spanwise direction, a technique called stress peen forming is applied to reduce the generation of parasitic curvatures. In stress

peen forming, the component is elastically pre-bent along spanwise direction during peen forming. After peen forming, the resulting chordwise contour curvature will be larger than the spanwise contour curvature.

Several theoretical and numerical works have been performed to study the residual stress distribution and the deformation of a component after conventional peen forming. Al-Hassani (1981) used the assumption that the residual stress profile is the sum of an equivalent stretching stress and an equivalent bending stress acting in a manner to balance the induced stresses. Induced stresses are defined as the internal non-equilibrated stresses that develop in a rigidly constrained component subjected to shot peening (Al-Obaid, 1990a; Vanluchene et al. 1995). Residual stresses are the self-equilibrated stresses that remain inside the component after the removal of all external constraints. Peening induced stresses in a component are complicated and difficult to obtain. Al-Hassani (1981) assumed a cosine function to express the induced stress profile. Vanluchene et al. (1995) and Vanluchene and Cramer (1996) obtained empirical equations from experiments to relate the induced stresses and the arc height (i.e. the deflection) of normalized Almen strips (Almen and Black, 1963). Meo and Vignjevic (2003) employed an axi-symmetric Finite Element (FE) model to obtain the induced stress profile by simulating the impact of a single rigid sphere on an elastic-plastic work-piece. Hong et al. (2008a) conducted a parametric study with a 3D FE model to investigate the effect of shot diameter, impact velocity, incident angle and component material properties on the resulting induced stress profile. Guagliano, (2001) and Han et al. (2002) developed finite element models to predict the induced stress profiles created by shot peening and related these induced stresses to arc heights. As defined in SAE Standards J442, Almen intensity is defined as the arc height of a normalized Almen strip at the point where when shot peening time doubles, the arc height increases by less than 10%.

Most of the investigations of stress peen forming are based on experiments and empirical relationships. Baughman (1984) and Kopp and Ball (1987) introduced the principles of elastic stress peen forming with prebending moment or pre-stretching force. Barrett and Todd (1984) showed that the elastic pre-stressing technique increases the maximum compressive residual stress when compared to conventional peen forming. Li (1981) presented experimental results of stress peen forming under different values of prebending moments. Gardiner and Platts (1999)

simulated the various stress profiles (induced, residual, etc.) involved in stress peen forming by using temperature profiles.

In these previous works the relationship between the prebending parameters and the curvatures of the component has not been studied in details. Our objective in this paper is to address this issue. A finite element model suitable for simulating the stress peen forming process is established firstly. Then residual stress profiles, curvature radii and arc heights of a deformed component are calculated. In addition, the effects of prebending moment on these quantities are studied. Finally, model predictions are compared with the corresponding experiments.

This article is divided into five sections. Section 6.3 presents the features and the basic principles used in the stress peen forming numerical models. Section 6.4 presents the numerical models used to calculate the peen forming results under different prebending conditions. Section 6.5 compares the simulated arc height and residual stress with experimental results. Finally, Section 6.6 concludes the work.

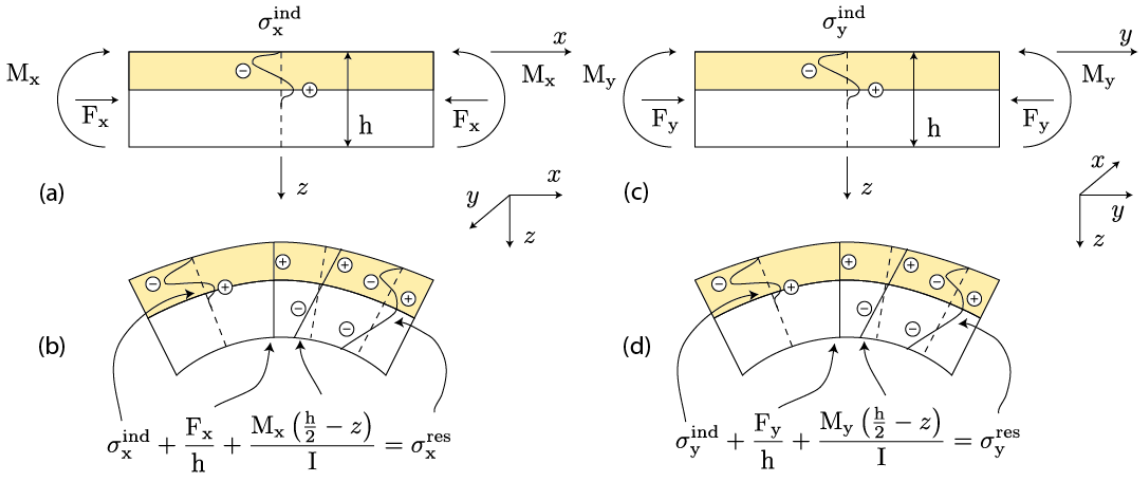

Figure 6.1: Illustration of the principle of peen forming process. (a) Induced stress profile in x direction σ_x^{ind} produced by shot peening in a fixed strip with a linear compressive force F_x and a linear bending moments M_x. (b) Extended and bent strip after release of boundary force and moment in x direction. (c) Induced stress profile in y direction σ_y^{ind} produced by shot peening in a fixed strip with a linear compressive force F_y and a linear bending moments M_y. (d) Extended and bent strip after release of boundary force and moment in y direction.

6.3 Principle of shot peen forming

6.3.1 Peen forming of a rectangular strip

Figure 6.1 illustrates the principle of the conventional peen forming of a rectangular strip, where F_x and F_y are linear compressive forces, M_x and M_y are linear bending moments, h is the thickness of the plate, σ_x^{ind} and σ_y^{ind} are induced stress profiles, $I = h^3/12$ is the moment of inertia, σ_x^{res} and σ_y^{res} are residual stress profiles. Firstly, a flat component is rigidly constrained during shot peening. As peening takes place, gradual plastification of the component surface layers produces induced stress profiles in x direction σ_x^{ind} and in y direction σ_y^{ind} as shown in Figure 6.1(a) and (c). These induced stresses are not self-equilibrated. Then after the release of the boundary constrains (F_x, F_y and M_x, M_y), the strip tends to extend and bend, as shown in Figure 6.1(b) and (d), which corresponding to producing tensile stresses (F_x/h and F_y/h) and bending stresses ($M_x(h/2 - z)/I$ and $M_y(h/2 - z)/I$) for equilibrium. Finally residual stress profiles after peen forming (σ_x^{res} and σ_y^{res}) can be calculated with equations shown in Figure 6.1(b) and (d).

Linear compressive forces F_x, F_y and linear bending moments M_x, M_y are applied on the component by the rigid support in order to maintain the component in a flat shape. It should be noted that the subscripts refer to the direction of the axial stress induced by these forces. For example, in Figure 6.1(a), M_x induces a linear axial stress in x direction even though it is actually oriented along y. After the release of the rigid constraints due to the support, the originally flat component will stretch and bend, as shown in Figure 6.1(b) and (d). The superposition principle is used in order to calculate the resulting stretching and bending. It is assumed that the component is made of an elasto-plastic material with hardening. The solutions (stresses, strains, displacements, etc.) of an initially unloaded flat component subjected to the inverse of the forces and moments illustrated in Figure 6.1 (a) and (c) (called Problem 2) are added to the solutions of the problems depicted in the same figures (called Problem 1). In order to apply this principle, it is assumed that adding the stresses of Problem 2 to the stresses of Problem 1 does not lead to further yielding when taking into account the hardening that took place at Problem 1. The compressive forces and the bending moments used for keeping the component flat can be expressed as:

$$F_x = -\int_0^h \sigma_x^{ind}\,\mathrm{d}z \tag{6.1}$$

$$F_y = -\int_0^h \sigma_y^{ind}\,\mathrm{d}z \tag{6.2}$$

$$M_x = -\int_0^h \sigma_x^{ind}\left(\frac{h}{2}-z\right)\mathrm{d}z \tag{6.3}$$

$$M_y = -\int_0^h \sigma_y^{ind}\left(\frac{h}{2}-z\right)\mathrm{d}z \tag{6.4}$$

where $z = 0$ at the top surface.

As introduced by Al-Hassani (1981), residual stresses in x and y directions can be calculated with Equations (6.3) and (6.4), namely

$$\sigma_x^{res} = \sigma_x^{ind} + \frac{F_x}{h} + \frac{M_x(\frac{h}{2}-z)}{I} = \sigma_x^{ind} - \frac{1}{h}\int_0^h \sigma_x^{ind}\,\mathrm{d}z - \frac{(\frac{h}{2}-z)}{I}\int_0^h \sigma_x^{ind}\left(\frac{h}{2}-z\right)\mathrm{d}z \tag{6.5}$$

$$\sigma_y^{res} = \sigma_y^{ind} + \frac{F_y}{h} + \frac{M_y(\frac{h}{2}-z)}{I} = \sigma_y^{ind} - \frac{1}{h}\int_0^h \sigma_y^{ind}\,\mathrm{d}z - \frac{(\frac{h}{2}-z)}{I}\int_0^h \sigma_y^{ind}\left(\frac{h}{2}-z\right)\mathrm{d}z \tag{6.6}$$

Since, in theory, $\sigma_x^{ind} = \sigma_y^{ind}$ for conventional peen forming, Equations (6.5) and (6.6) can be written as:

$$\sigma^{res} = \sigma^{ind} + \sigma^{s} + \sigma^{b} \tag{6.7}$$

where σ^s is stretching stress and equals to $\frac{F_x}{h}$, σ^b is bending stretch and equals to $\frac{M_x(\frac{h}{2}-z)}{I}$.

Figure 6.2 presents a sketch of the bending moments applied to a rectangular plate with dimensions $l \times b \times h$. M_x represents a linear bending moment along y direction (spanwise), M_y represents a linear bending moment along x direction (chordwise). This generic figure presents the loads applied in the implicit finite element model of a rectangular plate for the calculation of the arc heights as well as the curvature radii of the deformed component.

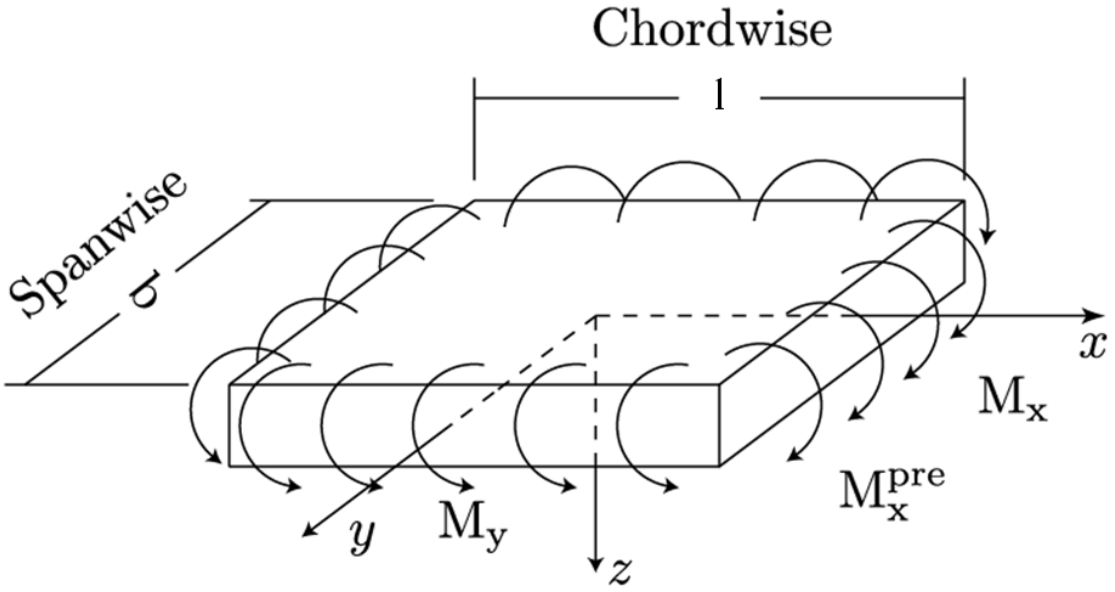

Figure 6.2: Sketch of a plate ($l \times b \times h$) subjected to various moments (linear prebending moment M_x^{pre} and linear bending moments M_x and M_y.)

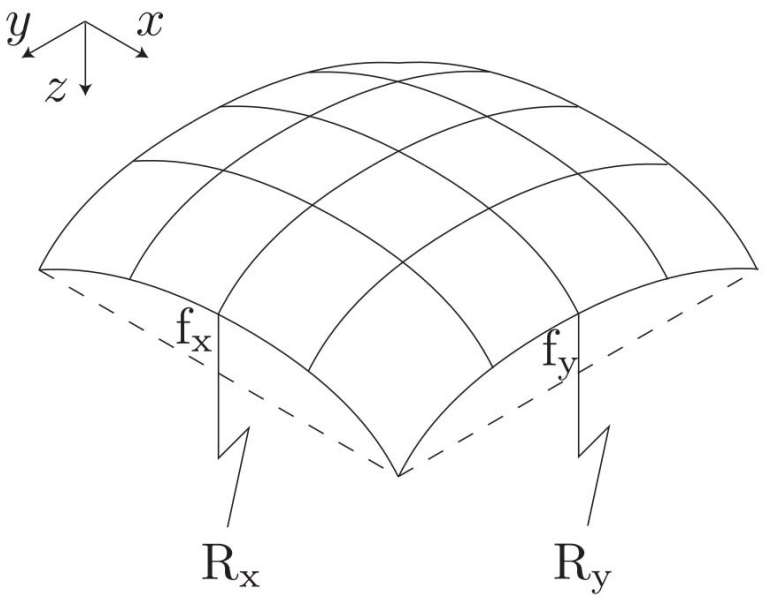

Figure 6.3: Sketch of a rectangular plate after peen forming: R_x, f_x are in xz plane, R_y, f_y are in yz plane.

Figure 6.3 shows a deformed component after peen forming. f_x, f_y are the arc heights of the component sections parallel to x and y axes caused by the bending moments M_x and M_y. The total arc height of the plate is defined as:

$$f^{tot} = f_x + f_y \tag{6.8}$$

For a strip with dimensions as Almen strip, the total arc height f^{tot} can be measured experimentally using Almen gauge with $l = 31.75\text{mm}$ and $b = 15.87\text{mm}$. R_x and R_y represent the curvature radii of the component sections parallel to x and y axes caused by the bending moments M_x and M_y.

6.3.2 Principle of stress peen forming

Stress peen forming is usually performed in the following order. First, the prebending moment is applied. In our case, a linear prebending moment M_x^{pre} is applied (see Figure 6.2). Then, the boundaries of the component are rigidly fixed in order to maintain the initial curvature. The component is subjected to shot peening and finally, the constraints are removed.

In this paper, the prebending moment is assumed to only cause an elastic deformation of the component. Therefore, a linearly distributed initial stress profile σ_x^i can be calculated using Equation (6.9), namely

$$\sigma_x^i = \frac{M_x^{pre}(\frac{h}{2} - z)}{I} \tag{6.9}$$

This initial stress has a maximum tensile value at $z = 0$, which is defined as σ_x^i. In practice, this maximum tensile stress can be calculated with the reading of a strain gage and be used as the control parameter of the prebending moment. It is therefore associated to the prebending moment value in our study. In this study, it is assumed that the plate is free in y direction and, therefore, the initial stress is assumed to be $\sigma_y^i = 0$.

A three-steps FE Implicit-Explicit-Implicit calculation procedure is used to simulate shot peening on a prestressed component and the resulting deflection for a plate subjected to peen forming. First, an implicit analysis is performed to obtain the initial stress distribution and the deformation of the component under prebending. Since the material treated has an elastoplastic behavior, the intensity of the initial stress profile should have a significant influence on the plastic deformation

induced by shot peening, and hence, on the final shape of the component. Second, an explicit analysis is performed to acquire the various internal stresses at the various stages of the peen forming process and to calculate the bending moments (M_x and M_y) due to shot peening. Finally, another implicit analysis is performed to calculate the resulting arc heights and the curvature radii of the component in chordwise and spanwise directions resulting from bending moments.

Equations (6.10) and (6.11) introduce the combined stresses σ^c as the sum of the initial stress σ^i caused by the prebending moment and the induced stress σ^{ind} caused by shot peening:

$$\sigma_x^c = \sigma_x^i + \sigma_x^{ind} \tag{6.10}$$

$$\sigma_y^c = \sigma_y^i + \sigma_y^{ind} \tag{6.11}$$

The combined stresses σ_x^c and σ_y^c are obtained from explicit FE simulation. They represent the stress distribution in the component after shot peening and prior to the removal of the boundary constraints. The induced stress in a pre-stressed component can be calculated from:

$$\sigma_x^{ind} = \sigma_x^c - \sigma_x^i \tag{6.12}$$

$$\sigma_y^{ind} = \sigma_y^c \tag{6.13}$$

Substituting Equations (6.12) and (6.13) into Equations (6.5) and (6.6) leads to the residual stresses in x and y directions separately. Bending moments M_x and M_y are obtained by substituting Equations (6.12) and (6.13) into Equations (6.3) and (6.4). Then the arc heights and radii of curvatures resulting from stress peen forming can be obtained from third step of implicit FE.

For all these equations, it can be seen that setting $M_x^{pre} = 0$ leads to the equations for conventional peen forming. In the following studies, these results were used to simulate both conventional and stress peen forming.

6.4 Numerical model for stress peen forming

6.4.1 Description of the finite element model

Both implicit solver ANSYS and explicit solver LS-DYNA were used to simulate stress peen forming according to the three-steps approach described in the previous section.

The finite element model shown in Figure 6.4 has been used for the first and second steps of the simulation. An Implicit-to-Explicit sequence solution was used to study the effect of the prebending moment M_x^{pre} on the structure dynamic response. 48 randomly distributed ceramic shots with radius $r = 0.25\text{mm}$, velocity $v = 66.2\text{m/s}$ are impacting a high strength aluminum 2024. The number of shots (48) was calculated with Equation (6.14) according to experiments as described in section 5.3:

$$N = \frac{N_{\text{total}}}{S_{\text{total}}} S_{\text{rep}} = \frac{\dot{m} L \rho_s V_s / V_{\text{robot}}}{L_p B_p} S_{\text{rep}} \tag{6.14}$$

where N_{total} is the total number of shots for one peening pass, S_{total} is the surface area on the target component for one peening pass, $\dot{m}$ is the mass flow of the shot flow, which is equal to 0.4kg/min, L_p is the length of one peening pass and is equal to 100mm, V_{robot} is the velocity of the peening robot to reach saturation in Aluminum 2024 in experiments for same peening condition and equals to 55mm/s, ρ_s is the density of shot and equals to 3850kg/m^3, V_s is the volume of one shot, B_p is the width of one peening pass and equals to 10mm, S_{rep} is the surface of the boundary of the impacting shots and equals to $1\text{mm} \times 1\text{mm}$ as shown in Figure 6.5.

The initial coordinates of these shots were generated with a Matlab program as described in Miao et al. (2009). The dimensions of the aluminum target was $2.5\text{mm} \times 2.5\text{mm} \times 1.6\text{mm}$. Coordinate (0,0,0) was located on the middle top surface of the target. In order to reduce calculation time, a relatively small vertical distance of $0.2r$ between each shot has been assumed. The influence of this distance on the results has been ignored and is left for the future study.

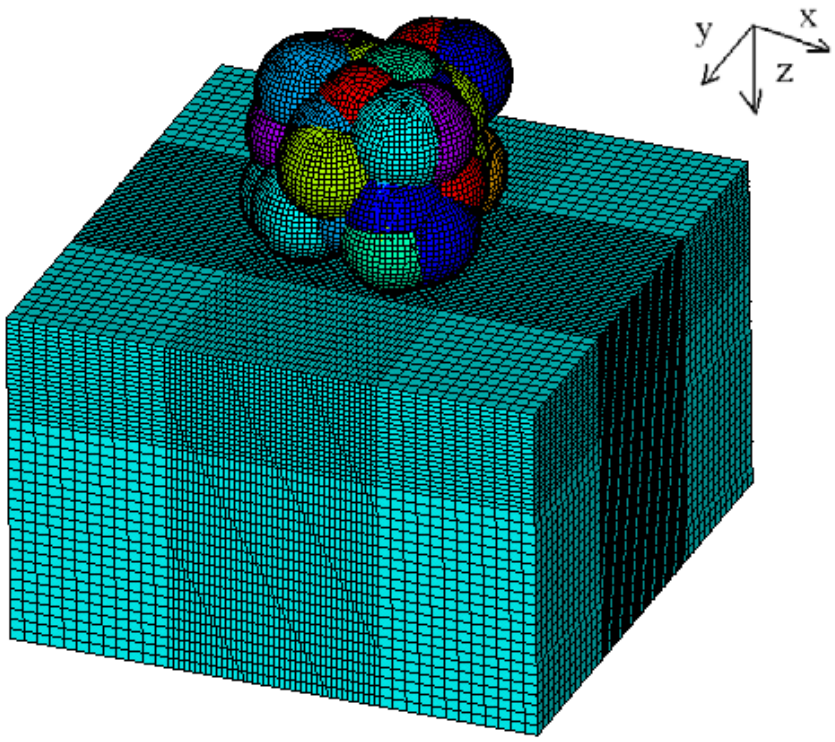

Figure 6.4: Finite element model used for stress shot peening simulation.

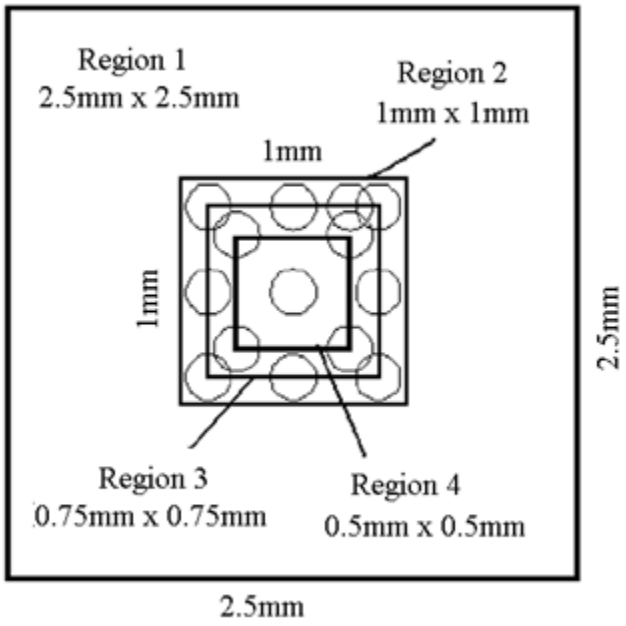

Figure 6.5: Representative surface (Region 1: aluminum surface; Region 2: fine element region; Region 3: boundary of the shots centers; Region 4: representative surface).

Figure 6.5 presents the surface impact region and the representative surfaces for the study of the induced residual stresses. Region 1, with dimensions $2.5\text{mm} \times 2.5\text{mm}$, is the total target component for the simulation. Region 2, with dimensions $1\text{mm} \times 1\text{mm}$, is the boundary of the impacting shots. All the shot centers lie within Region 3, of dimensions $0.75\text{mm} \times 0.75\text{mm}$. A volume of $0.5\text{mm} \times 0.5\text{mm} \times 1.6\text{mm}$ is selected as a representative volume to study the average induced stress profile

In this procedure, ANSYS implicit elements SHELL181 (for shot) and SOLID185 (for component) were converted to explicit elements SHELL163 (for shot) and SOLID164 (for component) in LS-DYNA. Element size of shot and the top surface of the component were set to 0.025mm after a convergence study. The ceramic shots were assumed to be rigid due to their relatively high rigidity and hardness values when compared to that of the target aluminum (Meguid et al. 1999a). The density of the ceramic shots was set to $\rho_s = 3850\text{kg/m}^3$. A bilinear isotropic elastoplastic constitutive theory with an elastic modulus $E = 76.5\text{GPa}$, Poisson's ratio $\upsilon = 0.33$, density $\rho_t = 2800\text{kg/m}^3$, yield stress $\sigma_y = 379\text{MPa}$ and tangent modulus $E_{tan} = 810\text{MPa}$ were selected to represent the aluminum material properties. These numbers were obtained from tensile testing on the target material. Potential strain rate effects of the aluminum material were neglected.

For the third part of the simulation, ANSYS implicit elements SHELL181 were used to simulate an aluminum strip of dimensions $31.75\text{mm} \times 15.87\text{mm} \times 1.6\text{mm}$. This dimension of the strip was selected in order to compare the deformed arc height of the strip with experimental measured value by Almen gauge. Bending moments M_x and M_y from Equations (6.3) and (6.4) (as presented in Figure 6.2) were applied on four sides of the strip in order to calculate the resulting deflection after stress peen forming. Coordinate (0,0,0) was located on the middle of the strip and the node at this point was fixed in x, y, z and $ROTz$ directions.

6.4.2 Implicit analysis of prebending

In the static prebending analysis, all the nodes on the shot were fixed. The nodes on the bottom surface of the component with $x = 0$ were fixed in z direction to prevent rigid movement. Linear pressure gradients with a slope of $\{0,\ 85/1.6,\ 170/1.6 \text{ or } 255/1.6\}\text{MPa/mm}$ along z direction were applied on the right surface of the component ($x = 1.25\text{mm}$) and linear pressure gradients

of slope of {0, -85/1.6, -170/1.6 or -255/1.6}$\mathrm{MPa/mm}$ along z direction were applied on the left surface of the component ($x = -1.25\mathrm{mm}$). These pressure lead to surface initial stress σ_x^{im}={0, 85, 170 or 255} MPa on the top surface and $M_x^{pre} = \{0,\ 36.3,\ 72.6,\ 108.9\}\mathrm{N}$ according to Equation (6) evaluated for $z = 0$.

6.4.3 Explicit analysis of shot peening process

The initial stress distribution and nodal displacements obtained from implicit analysis were transferred to the explicit model. The four side and the bottom surfaces of the component were fixed. Then, the model was subjected to 48 shot impacts with an initial velocity $v = 66.2\mathrm{m/s}$.

Figure 6.6 presents the results obtained from the Implicit and Explicit sequence solution with $M_x^{pre} = 108.9\mathrm{N}$ (see Figure 6.2), which corresponds to $\sigma_x^{im} = 255\mathrm{MPa}$. The average combined stress profiles σ_x^c and σ_y^c were averaged over the whole xy-plane of the representative volume with dimensions $0.5\mathrm{mm} \times 0.5\mathrm{mm} \times 1.6\mathrm{mm}$ (Region 4 in Figure 6.5) in the z direction after Explicit calculation by LS-DYNA.

In order to obtain these average combined stress profiles, $9 \times 9 = 81$ uniformly distributed paths following the depth of the plate in the representative volume were defined by ANSYS General Postprocessor. SX and SY values were interpolated into each of these 81 paths, respectively. Then the average values of SX and SY for constant depths were calculated from these 81 paths to represent σ_x^c and σ_y^c respectively. Then the average induced stress profiles σ_x^{ind}, σ_y^{ind} can be calculated with Equations (6.12) and (6.13), respectively.

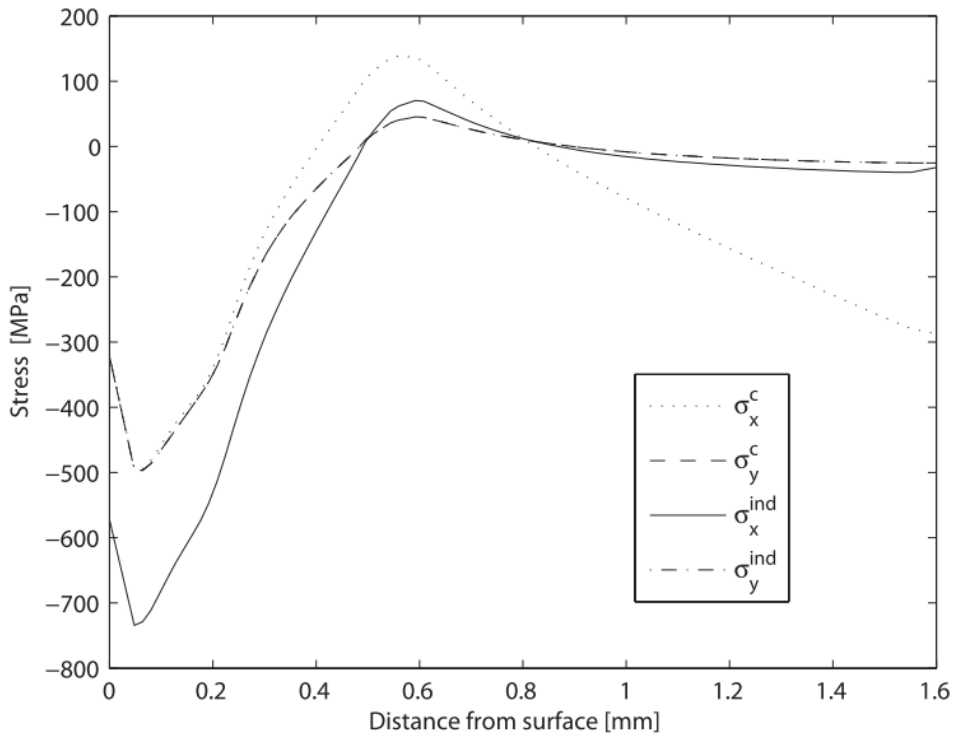

Figure 6.6: Combined and induced stress profiles after stress peen forming with $M_x^{pre} = 108.9\text{N}$.

It can be seen from Figure 6.6 that there is little difference between σ_x^c and σ_y^c at the top layer of the component. On the other hand, at the bottom layer of the component, the value of σ_x^c is approximately equal to the initial bending stress. σ_x^{ind} has larger maximum and surface compressive stresses than σ_y^{ind}. They both show similar values at the deepest layer of the component.

6.4.4 Residual stress profile with stress peen forming

Figure 6.7 presents each term of Equation (6.7) used for calculating the residual stress profile σ_x^{res} for stress peen forming with prebending moment $M_x^{pre} = 108.9\text{N}$. Similar results can be obtained for σ_y^{res}. It is clearly seen that compressive residual stresses were obtained both at the top and at the bottom surfaces of the component.

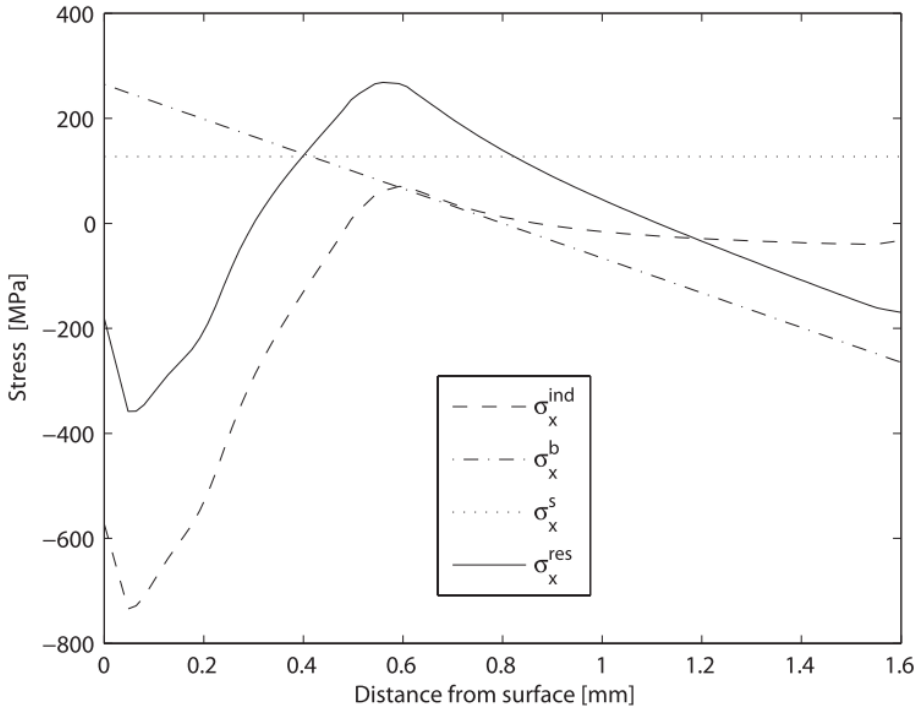

Figure 6.7: Stress profiles after stress peen forming with prebending moment $M_x^{pre} = 108.9\text{N}$.

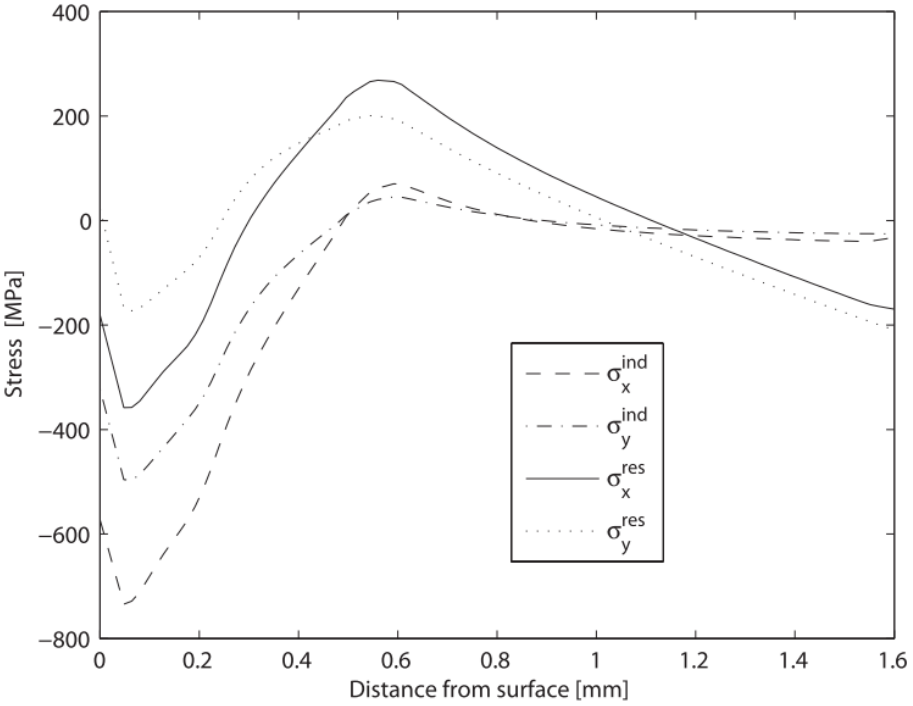

Figure 6.8: Stress profiles (induced stress and residual stress) of stress peen forming with prebending moment $M_x^{pre} = 108.9\text{N}$.

Figure 6.8 presents the induced stresses σ_x^{ind}, σ_y^{ind}, and the residual stress profiles σ_x^{res}, σ_y^{res} with prebending moment $M_x^{pre} = 108.9\text{N}$ ($\sigma_x^{im} = 255\text{MPa}$). Due to the difference between σ_x^{ind} and σ_y^{ind}, σ_x^{res} and σ_y^{res} were quite different at the top layer of the component. σ_x^{res} has larger maximum compressive stress and top surface compressive stress than σ_y^{res}. In addition, both σ_x^{res} and σ_y^{res} have compressive residual stresses at the bottom surface of the component.

Figure 6.9 presents the evolution of the residual stresses obtained following the procedure previously established. It can be seen from the figure that prebending has a significant influence on the residual stresses distribution in the component. With the increase of the prebending moment, the surface and maximum compressive σ_x^{res} increases gradually, the maximum compressive residual stress decreases gradually. The compressive residual stress values in chordwise direction produced by stress peen forming were larger than those obtained from conventional peen forming.

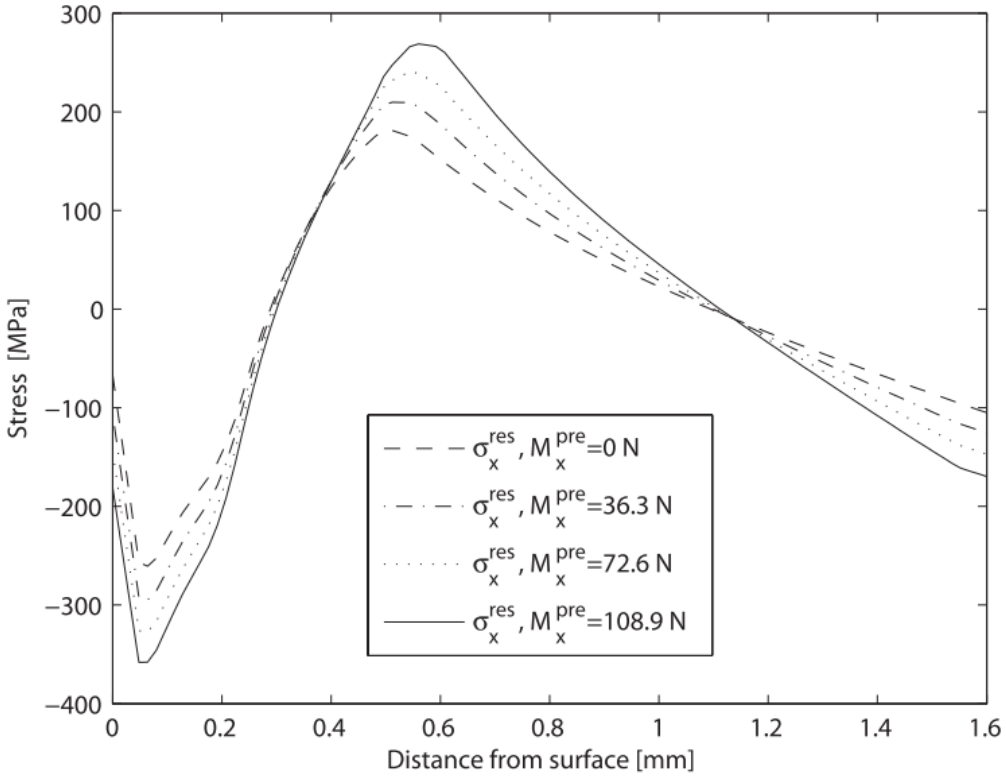

Figure 6.9: Residual stress profiles under four different prebending moments.

6.4.5 Radius of curvature and arc height of stress peen forming

Figure 6.10 presents the U_z displacements of nodes with $y = 7.935\text{mm}$ and $x = 15.875\text{mm}$ after FE calculation for conventional peen forming ($M_x^{pre} = 0$) and stress peen forming ($M_x^{pre} = 108.9N$), respectively. With these U_z displacement values, the arc heights f_x, f_y can be calculated directly and the curvature radii R_x and R_y can obtained by best fitting with a circle and are listed in Table 6.1. It can be found that stress peen forming produces larger arc height (smaller radius of curvature) in the prebending direction (x direction) compared with conventional peen forming. While in the direction vertical to prebending moment (y direction), prebending moment has less influence.

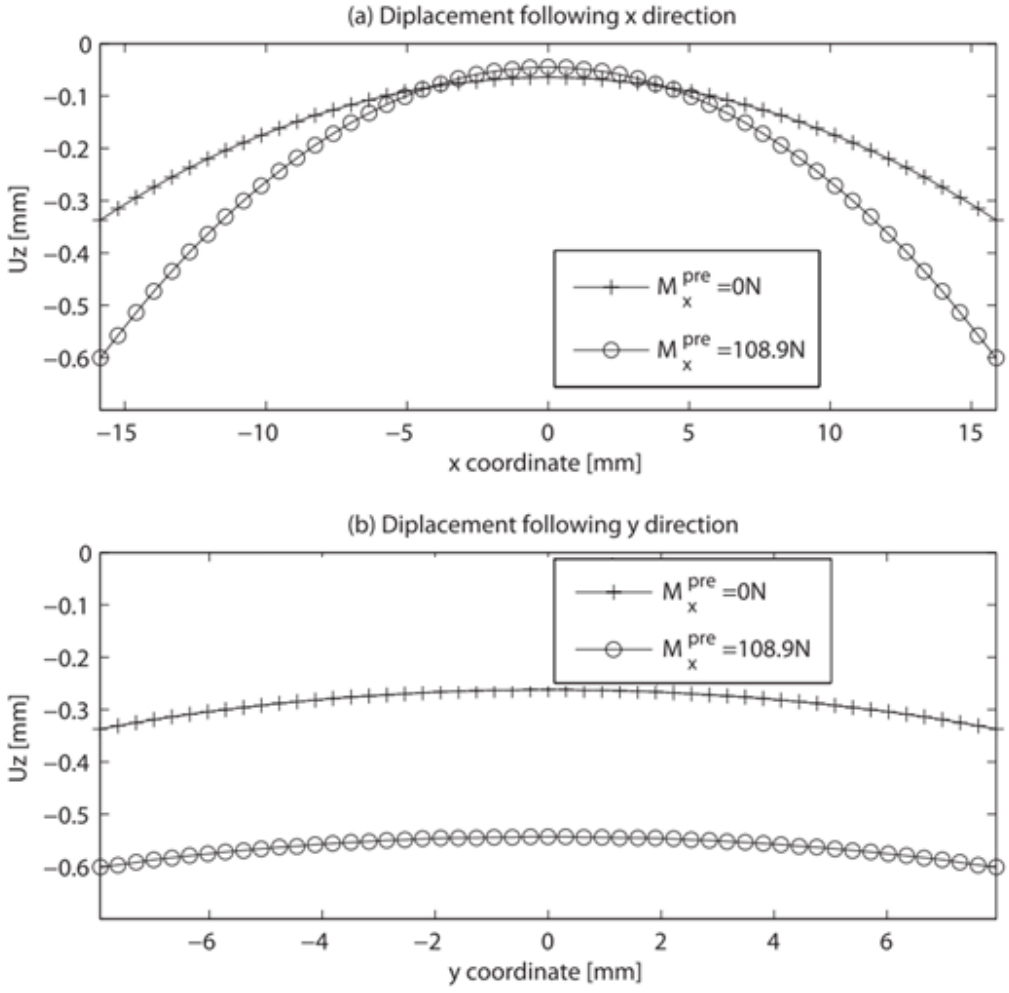

Figure 6.10: U_z displacements of the strip following x and y directions after conventional peen forming ($M_x^{pre} = 0$) and stress peen forming ($M_x^{pre} = 108.9N$).

Table 6.1: Resulting arc heights and radii of curvatures in x and y directions.

Prebending moment (N**)**	**Arc height (** mm **)**		**Radius of curvature (**mm**)**	
M_x^{pre}	f_x	f_y	R_x	R_y
0	0.2227	0.0638	455.57	454.46
108.9	0.4689	0.0468	226.97	547.47

Table 6.2: Relationship between prebending conditions and peen forming results.

Prebending moment M_x^{pre} **(** N **)**	**Surface stress** σ_s **(** MPa**)**	**Radius of prebend** R_x^{pre} **(** mm **)**	**Bending moment (** N**)**		**Resulting arc height (** mm **)**			**Radius of curvature (** mm **)**	
			M_x	M_y	f_x	f_y	f^{tot}	R_x	R_y
0	0	∞	65.31	69.92	0.28	0.075	0.36	455.57	454.46
36.3	85	720	80.37	71.04	0.35	0.070	0.42	358.75	464.85
72.6	170	360	96.36	72.04	0.45	0.060	0.51	278.80	474.61
108.9	255	240	112.93	72.8	0.55	0.050	0.60	226.97	499.80

Table 6.2 lists the bending moments M_x and M_y, resulting arc heights f_x, f_y and f^{tot} as well as curvature radii R_x and R_x under four different prebending conditions ($M_x^{pre} = \{0,\ 36.3,\ 72.6,\ 108.9\}$N). M_x and M_y were calculated using Equations (6.3) and (6.4). f_x, f_y, R_x and R_y were obtained from implicit FE analysis. Prebending radius of curvature R_x^{pre} in Table 6.2 can be calculated from prebending moment as:

$$R_x^{pre} = \frac{EI}{M_x^{pre}} = \frac{Eh^3}{12M_x^{pre}} \tag{6.15}$$

It can be seen from Table 6.2 and Figure 6.11 that:

- In the case conventional peen forming ($M_x^{pre} = 0$), M_x should be equal to M_y. The little difference between these two quantities might be due to the randomness of the shots distribution.
- In the case of stress peen forming ($M_x^{pre} = 36.3$N, 72.6N or 108.9N), the radius of curvature R_x is smaller than R_y.

- Radius of curvature R_x decreases with the increase of prebending moment, while radius of curvature R_y increases with the increase of prebending moment.
- Compared with conventional peen forming ($M_x^{pre} = 0$), stress peen forming produces smaller R_x and larger R_y. R_x decreases with the increase of prebending moment, and R_y increases with the increase of prebending moment.

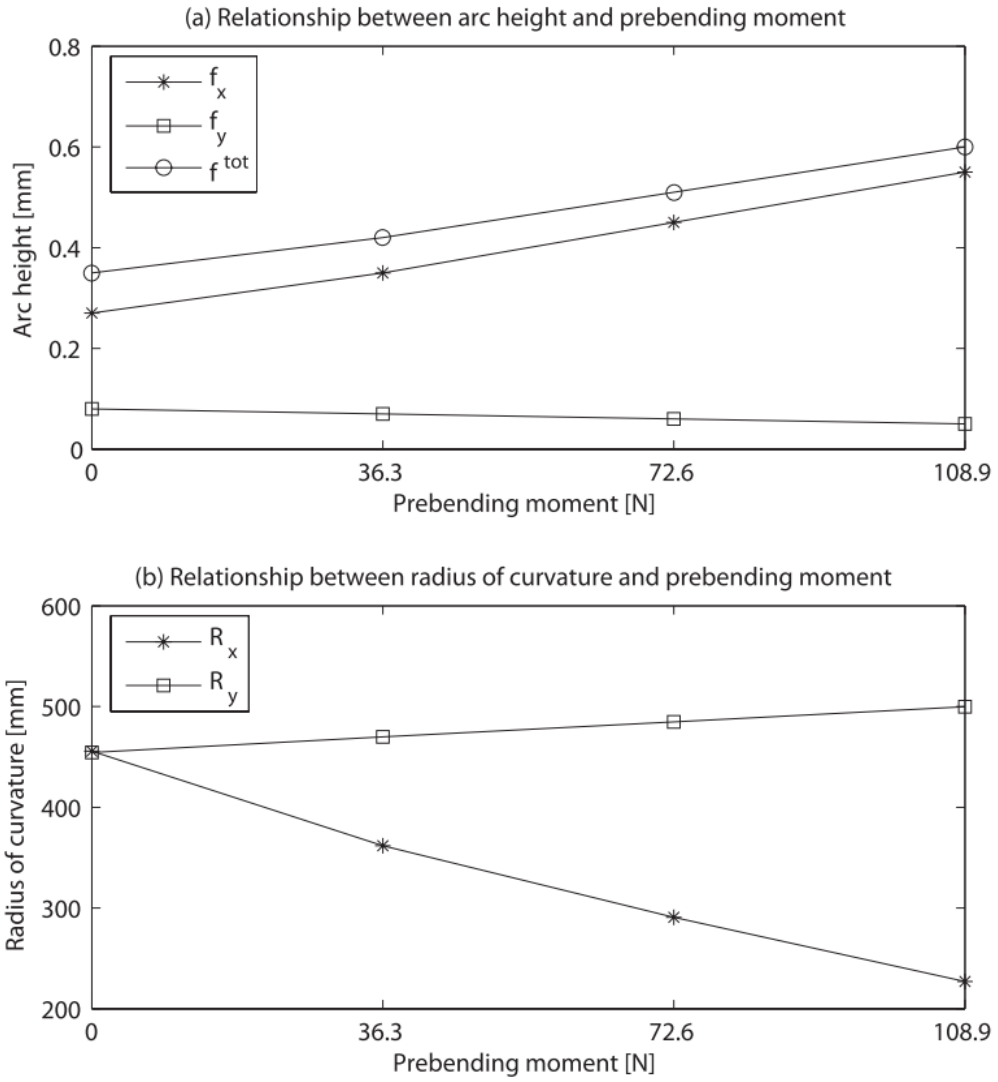

Figure 6.11: Relationship between prebending moment M_x^{pre} and peen forming results. (a) Relationship between prebending moment M_x^{pre} and resulting arc heights f_x, f_y and f^{tot}. (b) Relationship between prebending moment M_x^{pre} and resulting radii of curvatures R_x and R_y.

Figure 6.11 plots the relationship between prebending moment M_x^{pre} and resulting arc heights f_x, f_y and f^{tot} as well as resulting radii of curvatures R_x and R_y. All of these results reflect the tendencies that were obtained experimentally by (Li, 1981).

6.5 Comparison with experiments

6.5.1 Experimental study of stress peen forming

Stress peen forming process were performed with a BLAKA-1 portable blasting machine (#CH8152 GLATTGRUGG), a Motoman Model robot (Motoman SV3X Long) and a robot controller (XRC 2001). Ceramic Zirshot Z425 shots were used in the experiments. The pressure of the shots stream was set to 22.5Psi, and the mass flow of the shots was set to 0.4kg/min. The velocity of the shot flow was 66.2m/s and was measured by shot velocity measurement device "Shotmeter" sold by Progressive Technologies. The diameter of the nozzle was 6mm and the standoff distance between nozzle and target was of 25mm. Shots having a normal trajectory with respect to the target surface were considered in the experiments. The robot moving velocity was set to 55mm/s for aluminum 2024 strip with dimensions $76\text{mm} \times 19\text{mm} \times 1.6\text{mm}$ to reach saturation. The prestressing device as shown in Figure 5.1 with four radii of prebending curvatures ($R_x^{pre} = \infty$, 720 mm, 360 mm and 240 mm) has been designed for the stress peen forming. Four aluminum strips with dimensions $76\text{mm} \times 19\text{mm} \times 1.6\text{mm}$ were fixed on the prestressing device. Aluminum strips with dimensions $76\text{mm} \times 19\text{mm} \times 1.6\text{mm}$ have been selected in the experiments for the simplification of arc height measurement. The strips were elastically deformed following the prestressing device.

6.5.2 Comparison with experimental results

Figure 6.12 presents experimental measured U_z displacement of the deformed strip along prebending direction after conventional peen forming ($M_x^{pre} = 0$) and stress peen forming ($M_x^{pre} = 108.9\text{N}$). For each case, 13 points along prebending direction with a total length of 60mm were measured by Taylor-Hobson's PGI-840 profilometer and read manually. A circle with a radius R_x can be used to best fit these 13 measured values for each case. Similar to FE simulated results in Figure 6.10(a), stress peen forming produces smaller resulting radius of curvature compared with conventional peen forming.

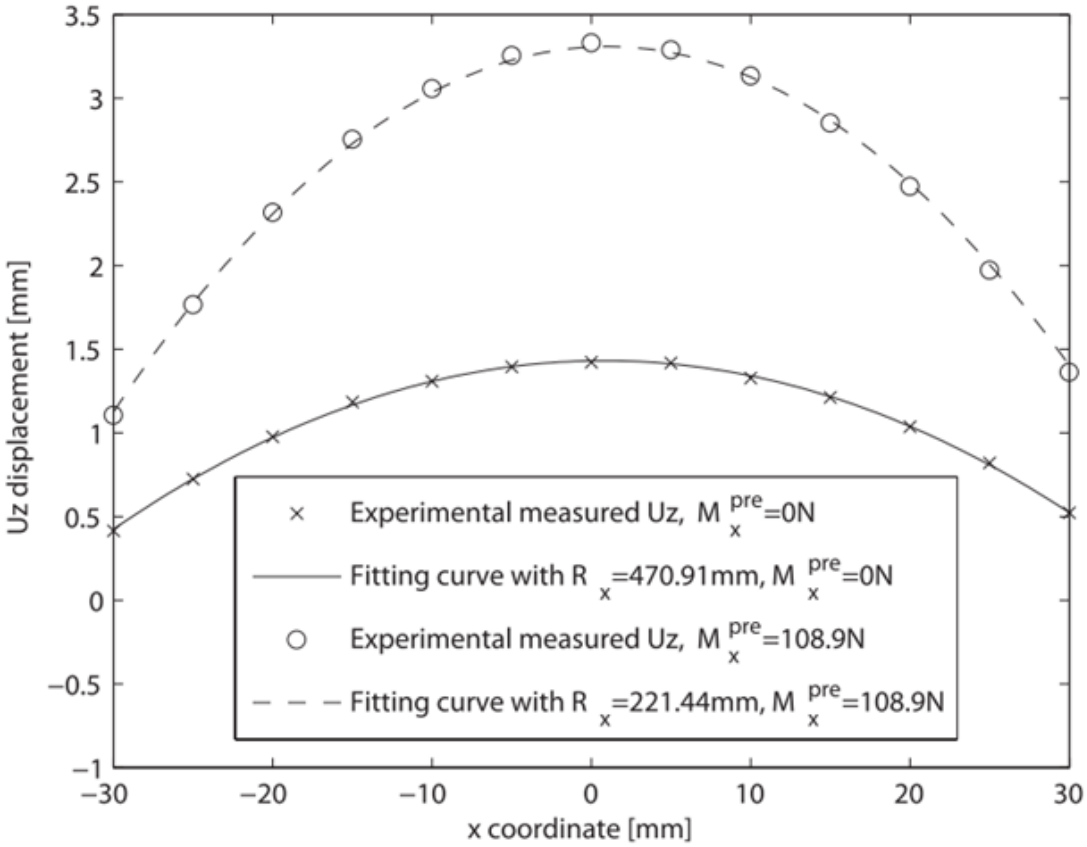

Figure 6.12: Experimental measured U_z and fitting curve after conventional peen forming ($M_x^{pre} = 0$) and stress peen forming ($M_x^{pre} = 108.9$N).

Figure 6.13 compares the experimental measured arc height and fitted radius of curvature R_x with FE simulated results under four different prebending moments $M_x^{pre} = \{0,\ 36.3,\ 72.6,\ 108.9\}$N. In Figure 6.13(a), the resulting total arc heights were measured by Almen gauge and were compared with the simulated resulting arc height f^{tot}. In Figure 6.13(b), four best fitting radii of curvatures from experimental measured data were compared with four best fitting radii of curvatures from FE calculated U_z displacement. It can be seen that, for both arc heights and radius of curvature R_x, the simulated results are consistent with the experimental results. In addition, both experimental and simulated results present same tendency for the relationship between prebending moment and resulting arc height and radius of curvature. That is to say, resulting arc height f^{tot} increases with the increase of the prebending moment and resulting radius of curvature R_x decreases with the increase of the prebending moment.

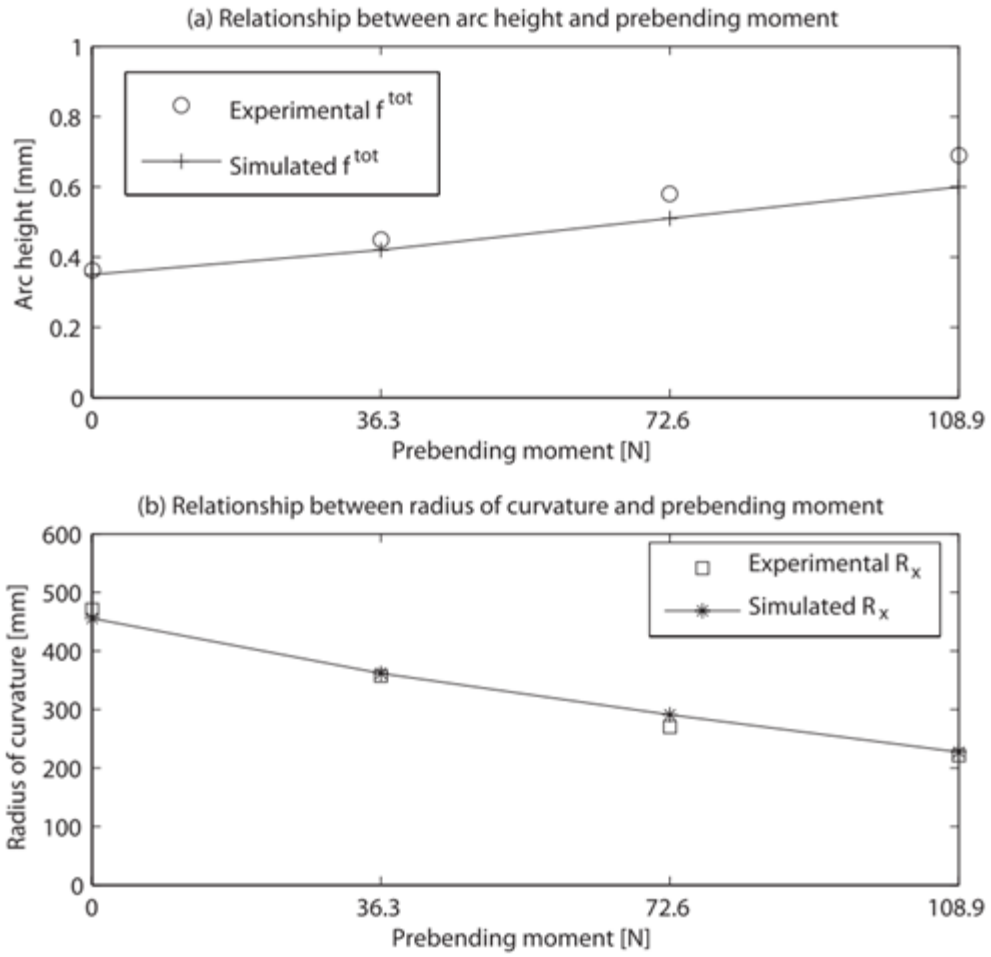

Figure 6.13: Comparison of FE simulated resulting arc heights and radius of curvature with experimental results (a) Relationship between prebending moment and resulting arc height from experiment and FE simulation. (b) Relationship between prebending moment and resulting radius of curvature from experiment and FE simulation.

Residual stress profiles under conventional peen forming ($M_x^{pre} = 0\text{N}$) and stress peen forming ($M_x^{pre} = 108.9\text{N}$) have been measured in PROTO Manufacturing company with equipment LXRD using X-Ray Diffraction method. Correction for stress relaxation and redistribution as a result of material removal via electro-polishing was performed as per SAE HS784. However, it is difficult to compensate the stress release when correction becomes large. Therefore, for each case, the residual stress for depth (0 to 0.8mm) were measured from the convex side on a first sample and residual stress for depth (0.8mm to 1.6mm) were measured from concave side on the second sample. Figure 6.14 compares experimental measured and FE simulated residual stress profiles under these two cases.

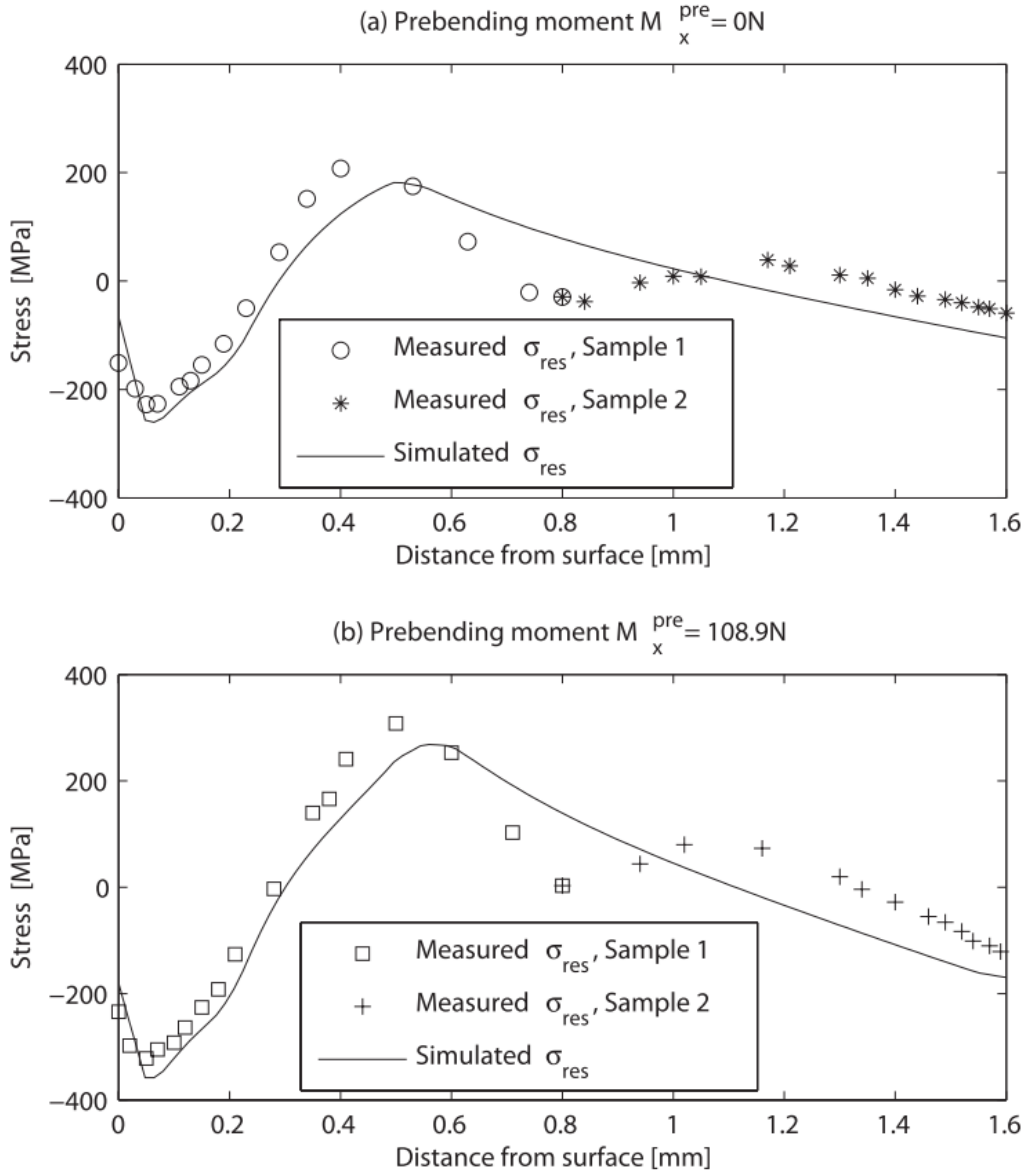

Figure 6.14: Comparison of experimental measured residual stress and FEM simulated results under two cases. (a) Conventional peen forming with $M_x^{pre} = 0\text{N}$. (b) Stress peen forming with $M_x^{pre} = 108.9\text{N}$.

It can be seen from Figure 6.14 that:

- The simulated residual stresses are consistent with the experimental results, which means that the developed the three-steps FE model can be used to study conventional peen forming and stress peen forming process effectively.

- Peen forming process produces compressive residual stress not only on the top surface but also on the bottom surface of the component.
- When compared with conventional peen forming, stress peen forming produces larger surface residual stress (both top and bottom surface of strip) and maximum compressive residual stress.
- When compared with conventional peen forming, stress peen forming induces larger maximum tensile residual stress inside the component.

6.6 Conclusions

Stress peen forming is widely used in curving aircraft wing skins but the process remains almost strickly empirical. The contribution of our work is the application of the computational Implicit and Explicit strategies for studying this engineering problem. With this newly developed tool, the relationship between prebending values and residual stress profiles, arc heights curvature radii and of the deformed component can be studied in details. The method developed in this paper led to a useful tool to control and predict stress peening forming process results. For certain desired deformed shape, shot peening parameters such as shot size, shot velocity and prebending values can be selected and optimized before peen forming.

In this paper, only a rudimentary analysis of stress peen forming has been performed based on several assumptions and limitations. Ongoing and future works will be dealing with the optimization of the 3D randomly distributed shot peening model, which includes model representation size and distance between random shots.

CHAPITRE 7 AN ANALYTICAL APPROACH TO RELATE SHOT PEENING PARAMETERS TO ALMEN INTENSITY

H. Y. Miao, S. Larose, C. Perron, Martin Lévesque, submitted to the journal *Surface and Coating Technology* on February 15th, 2010.

7.1 Abstract:

The shot peening process is widely used in the automotive and aerospace industries to improve the fatigue strength of metal components by introducing near-surface plastic strains and compressive residual stresses. This mechanical treatment is primarily controlled by monitoring Almen (peening) intensity, which corresponds to the arc height at saturation of standardized test strips exposed to the shot stream. However, the same Almen intensity may be obtained by using small shots impacting the surface at high velocity or by using large shots impacting the surface at low velocity. This paper describes a model for predicting Almen intensity based on an analytical model for shot peening residual stresses. Theoretical results for different sets of peening parameters were consistent with published experimental results and revealed that although different combinations of shot peening parameters can produce the same Almen intensity, each combination resulted in a different through thickness residual stress distribution.

7.2 Introduction

Shot peening is a mechanical surface treatment widely used in the automotive and aerospace industries to improve the fatigue life of metallic components. A shot stream hammers the metal surface and induces a compressive residual stress layer, which reduces the likelihood of premature failure under cyclic loading conditions. The effectiveness and repeatability of the shot peening process is usually measured using two control parameters: peening coverage and Almen (peening) intensity. Numerous shot peening parameters (shot size, type, velocity, incidence angle, material properties of the target component, etc.) have a great influence on the effectiveness of the treatment.

Almen intensity is related to the amount of kinetic energy transferred from the shot stream to a target component during the shot peening process (Kyriacou, 1996). The method commonly used to quantify peening intensity was introduced by Almen and Black (1963). It consists of peening a

standardized SAE1070 spring steel test strip (Almen strip) clamped to a mounting fixture by means of four roundhead bolts. This strip is of dimensions $76\text{mm} \times 19\text{mm}$ for three available thicknesses (type A: 1.29mm, type N: 0.79mm and type C: 2.39mm). After peening, when the fixing bolts are removed, the test strip bends towards the peening direction due to the plastic deformation induced by shot peening. The degree of strip deflection (expressed as strip arc height) due to different peening times is measured using a dedicated measuring equipment called Almen gauge. In order to determine the intensity of a given peening process, a number of Almen strips are peened using the same peening parameters for different exposure times according to SAE specifications. A saturation curve is obtained by plotting the strip arc height as a function of peening exposure time. Saturation is defined as the point on the curve beyond which the arc height increases by less than 10% when the peening time is doubled. Almen intensity is defined as the arc height at saturation. Complete procedures and specification of intensity measuring equipment can be found in SAE standards SAE-J442, SAE-J443 and SAE-AMS 2430.

Flavenot and Niku-Lari (1977), Al-Hassani (1982, 1984) and Guagliano (2001) related the peening-induced test strip arc height to the residual stress profile in a peened thin component by envisaging that a bending moment and a stretching force were internally generated to balance the peening-induced stress (source stress), thus providing equilibrium in the free component. The bending moment and stretching force cause bending and axial elongation, which are manifested in the deflection of the component. A cosine function was assumed by Flavenot and Niku-Lari (1977) to represent both the residual stress in a semi-infinite component and the induced stress in a thin component.

Guechichi (1986) developed a theoretical model to predict residual stress introduced by shot peening, based on Hertz theory of contact and an elasto-plastic calculation method (Zarka and Casier, 1979); Zarka and Inglebert, 1985). In his model, shot peening parameters such as shot velocity, shot diameter and target material were considered. Khabou et al. (1989) improved Guechichi's model by considering different constitutive laws for the target material. They obtained good results for 7075 aluminum alloy by using a compound rheological model with two blocks having coupled yield thresholds. Fathallah et al. (1998) extended the model one step further by considering the effect of the tangential friction between the shot and the treated material as well as the angle of impingement. The calculated residual stress profiles using

different coefficients of friction and angles of impingement showed a good correlation with experimental data from the literature.

Li et al. (1991) developed a simplified analytical model for calculating the compressive residual stress field due to shot peening. The predicted results showed good agreement with experiments. However, in their model, the shot peening process was considered as a quasi-static case, which could not take into account the velocity of the shot. In addition, an empirical relationship between the experimental plastic radius and the equivalent static load of shot peening was required. Shen et al. (2004) improved the model proposed by Li et al. (1991) by calculating a theoretical plastic radius as in Al-Hassani (1984), using the equation of motion of a rigid spherical shot impinging upon a rigid perfectly plastic target and a geometrical relationship between the indentation plastic radius and indentation depth. When compared to the model of Li et al. (1991), the model of Shen et al. (2004) considered more shot peening parameters, such as the size and velocity of the shot and as the characteristics of the target material.

As opposed to existing studies, this paper presents a combined analytical model for both investigating the influence of shot peening parameters on the resulting Almen intensity and on the residual stress in the Almen strip. The model incorporates the models of Li et al. (1991) and Shen et al. (2004) to predict the induced stress in a semi-infinite target component (described in Section 7.3.1 below). The approach of Guagliano (2001) is then used to predict residual stresses and deformed arc height in the Almen strip (described in Section 7.3.2 below). Section 7.4 compares the predicted Almen intensity and residual stress distributions with experimental results obtained from the literature. Section 7.5 presents a parametric study of Almen intensity. Conclusions are presented in Section 7.6.

7.3 Analytical prediction of Almen intensity

7.3.1 Analytical model for shot peening induced stress in a semi-infinite body

7.3.1.1 Hertz contact theory and impact between elastic sphere and semi-infinite elastic body

The loading introduced by shot peening in the model developed by Li et al. (1991) and complemented by Shen et al. (2004) is based on Hertz theory of contact. Fundamental equations are recalled below.

It is assumed that the shot is elastic and the target is a semi-infinite elastic body. This situation can be considered as a particular application of Hertzian contact between two elastic spheres. The boundary condition for normal displacements within the circular contact area of two contacting spheres (see Figure 7.1) can be written as (Johnson, 1985, p.92):

$$\bar{u}_{z1}(r) + \bar{u}_{z2}(r) = \delta - \left(\frac{1}{2R}\right) r^2 \tag{7.1}$$

where $\bar{u}_{z1}(r)$ and $\bar{u}_{z2}(r)$ are the normal displacement fields on the surface of the two spheres, r is the radial distance from the contact center, δ is the total approach between the centers of the two spheres with the relationship $\delta = \delta_1 + \delta_2$, where δ_1 and δ_2 are the displacements of the centers of the two spheres, respectively. R is the relative radius of the interface with relationship $\left({}^{1}/_{R}\right) = \left({}^{1}/_{R_1}\right) + \left({}^{1}/_{R_2}\right)$, where R_1 and R_2 are the initial radii of the two spheres, respectively.

The pressure distribution $p(r)$ proposed by Hertz for two frictionless elastic solids of revolution in contact can be expressed as (Johnson, 1985, p.60):

$$p(r) = p_0 \left[1 - \left(\frac{r}{a_e}\right)^2\right]^{1/2} \tag{7.2}$$

where p_0 is the maximum pressure at $r = 0$ and a_e is the contact radius. This pressure distribution gives rise to normal displacements at the surface of a body (Johnson, 1985, p.61):

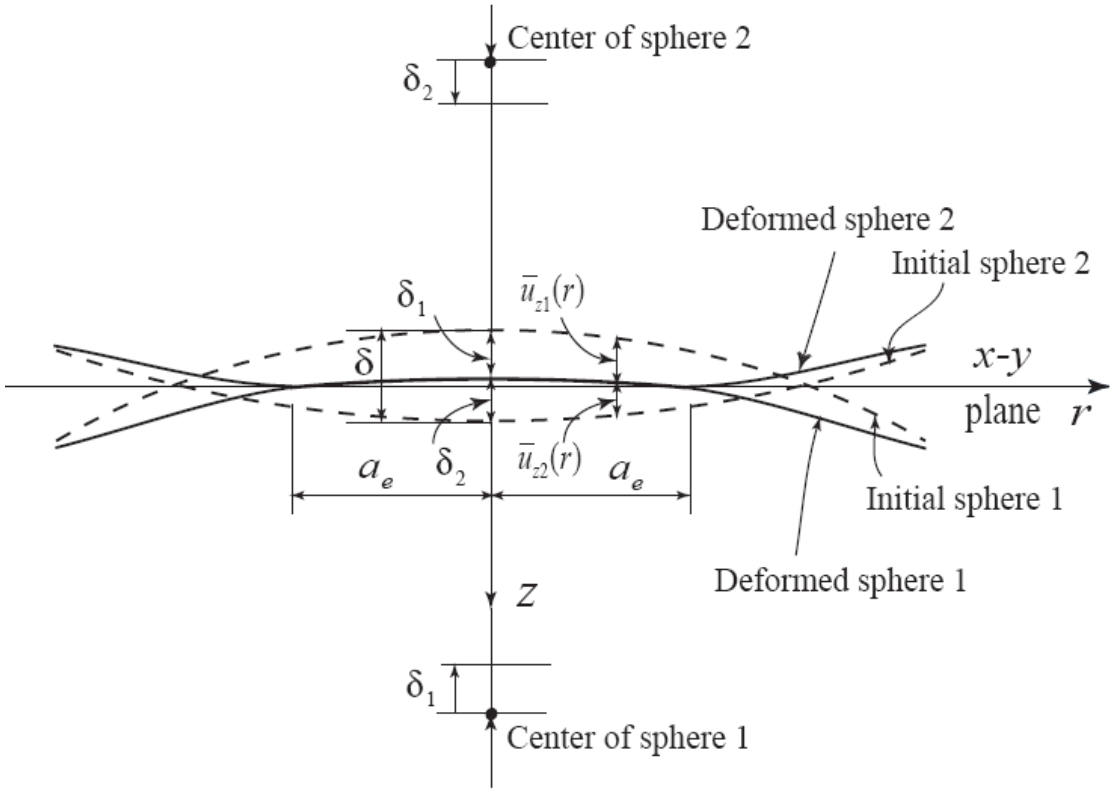

Figure 7.1: Geometry of contacting surfaces. The dotted lines represent the initial envelopes of the spheres. After contact, the two spheres adjust (shown by the solid lines) to avoid penetration ($R_1$and R_2 are the initial radii of the two spheres, is the radial distance from the contact center, $\bar{u}_{z1}(r)$ and $\bar{u}_{z2}(r)$ are the normal displacement fields on the surface of the two spheres, δ_1 and δ_2 are the displacements of the centers of the two spheres, a_e is the radius of the contact circle).

$$\bar{u}_z(r) = \frac{1-\upsilon^2}{E}\frac{\pi p_0}{4a_e}(2a_e^2 - r^2),\ r \le a_e \tag{7.3}$$

where υ and E are the Poisson's ratio and Young's modulus of the body, respectively.

The pressure distribution acting on the second body is equal to that on the first, so that by substituting Equation (7.1) into (7.3) we get (Johnson, 1985, p.92):

$$\frac{\pi p_0}{4a_e E_H}(2{a_e}^2 - r^2) = \delta - \left(\frac{1}{2R}\right)r^2 \tag{7.4}$$

where an equivalent Young's modulus E_H is defined for simplification as:

$$\frac{1}{E_H} = \frac{1-{\nu_S}^2}{E_S} + \frac{1-{\nu_T}^2}{E_T} \tag{7.5}$$

where E_s and υ_S are the Young's modulus and the Poisson's ratio of the shot material, respectively, and E_T and υ_T are the Young's modulus and the Poisson's ratio of the target material, respectively.

From Equation (7.4) we get the total approach between the centers of the two spheres with $r = 0$:

$$\delta = \frac{\pi a_e p_0}{2E_H} \tag{7.6}$$

and the radius of the elastic contact circle with $r = a_e$ as:

$$a_e = \frac{\pi p_0 R}{2E_H} \tag{7.7}$$

Combining Equation (7.6) and Equation (7.7), we obtain:

$$a_e = \sqrt{\delta R} \tag{7.8}$$

The total load P compressing the solids is related to the pressure distribution by (Johnson, 1985, p.92):

$$P = \int_0^{a_e} p(r)\, 2\pi r dr = \frac{2\pi {a_e}^2 p_0}{3} \tag{7.9}$$

Combining Equation (7.6), Equation (7.8) and Equation (7.9), P can also be expressed as function of δ:

$$P = \left(\frac{4E_H}{3}\right) R^{1/2} \delta^{3/2} \tag{7.10}$$

In the case of shot peening, a shot is impinged at a flat target component, which is defined as a semi-infinite target in this study. Therefore, the relationship $\left(1/R\right) = \left(1/R_1\right) + \left(1/R_2\right) = \left(2/D\right)$ is applied in the following equations.

The characteristics of the impact between the shot and the target component are described using an energy approach. We consider that the initial kinetic energy of the impinging shot is mostly converted into elastic work during the impact:

$$k \cdot \frac{1}{2}\left(\frac{\pi \rho D^3}{6}\right)(V\sin\theta)^2 = \int_0^{\delta^*} P \mathrm{d}\delta = \int_0^{\delta^*} \left(\frac{4E_H}{3}\right)\left(\frac{D}{2}\right)^{1/2} \delta^{3/2} \mathrm{d}\delta \tag{7.11}$$

where D, ρ and V correspond to the shot diameter, density and shot velocity, θ is the shot peening incidence angle with respect to the x-y plane, δ^* is the maximum approach between the

shot and target component and k is an efficiency coefficient related to elastic and thermal dissipation during impact. Following Iida (1984), we consider here that the characteristics of the indentation are mainly function of the normal component of velocity onto the surface. The value of k is taken as 0.8 (Johnson, 1972).

When integrating the right hand side of Equation (7.11), we obtain the expression for δ^*:

$$\delta^* = \frac{D}{2}\left(\frac{5}{4}\pi k\rho\frac{(V\sin\theta)^2}{E_H}\right)^{2/5} \tag{7.12}$$

Using Equation (7.8), the maximum contact radius a_e^* can be expressed as:

$$a_e^* = \frac{D}{2}\left[\frac{5}{4}\pi k\rho\frac{(V\sin\theta)^2}{E_H}\right]^{\frac{1}{5}} \tag{7.13}$$

The maximum value of p_0 during elastic impact p_0^* can be obtained by substituting Equation (7.13) into Equation (7.7):

$$p_0^* = \frac{1}{\pi}\left[40\pi k\rho {E_H}^4 (V\sin\theta)^2\right]^{\frac{1}{5}} \tag{7.14}$$

We can notice that for a normal impact between two spheres of the same material (with Young's modulus E_D and Poisson's ratio υ_D), assuming $k = 1.0$, Equation (7.13) reduces to

$$a_e^* = \frac{D}{2}\left[\frac{5}{2}\pi\rho V^2\frac{(1-{\upsilon_D}^2)}{E_D}\right]^{\frac{1}{5}} \tag{7.15}$$

as proposed by Davies (1949).

7.3.1.2 Stress-strain analysis of elastic contact

The equations in this section will be developed for the exact moment of maximum indentation, corresponding to δ^*, a_e^* and p_0^*. However, similar relationships can be obtained for any moment of the impact by replacing these maximum values with their corresponding instantaneous values δ, a_e and p_0 inside Equations (7.16) to (7.19).

Following Hertz theory, the stresses reach their maximum along the *z*-axis passing through the center of the contact area in the target body, where they can be expressed as (Johnson, 1985, p.62):

$$\sigma_x^e(z) = \sigma_y^e(z) = -p_0^*\left[-\frac{1}{2}A(z) + (1+\nu)B(z)\right] \tag{7.16}$$

$$\sigma_z^e = -p_0^* A(z) \tag{7.17}$$

with:

$$A(z) = \left[1 + \left(\frac{z}{a_e^*}\right)^2\right]^{-1} \tag{7.18}$$

$$B(z) = 1 - \frac{z}{a_e^*}\tan^{-1}\left(\frac{a_e^*}{z}\right) \tag{7.19}$$

σ_x^e, σ_y^e and σ_z^e are the principal stresses acting on the elastic target and z is the depth under consideration in the target body.

The von Mises equivalent stress distribution σ_i^e can be calculated from the principal stresses as:

$$\sigma_i^e = \left\{\left[(\sigma_x^e - \sigma_y^e)^2 + (\sigma_y^e - \sigma_z^e)^2 + (\sigma_z^e - \sigma_x^e)^2\right]^{1/2}\right\}/\sqrt{2} \tag{7.20}$$

According to Hooke's law, the principal strains in the target material are expressed as:

$$\varepsilon_x^e = \varepsilon_y^e = \frac{1}{E_T}\left[\sigma_x^e - \nu_T(\sigma_y^e + \sigma_z^e)\right] \tag{7.21}$$

$$\varepsilon_z^e = \frac{1}{E_T}\left[\sigma_z^e - 2\nu_T\sigma_y^e\right] \tag{7.22}$$

The equivalent strain ε_i^e can be obtained directly through Hooke's law as:

$$\varepsilon_i^e = \frac{\sigma_i^e}{E_T} \tag{7.23}$$

The hydrostatic stress and strain can be written as:

$$\sigma_m^e = \frac{1}{3}(\sigma_x^e + \sigma_y^e + \sigma_z^e) \tag{7.24}$$

$$\varepsilon_m^e = \frac{1}{3}(\varepsilon_x^e + \varepsilon_y^e + \varepsilon_z^e) \tag{7.25}$$

The principal components of the deviatoric stress tensor in the target material can be expressed as:

$$s_x^e = s_y^e = \sigma_x^e - \sigma_m^e = \frac{1}{3}\sigma_i^e \tag{7.26}$$

$$s_z^e = \sigma_z^e - \sigma_m^e = -\frac{2}{3}\sigma_i^e = -2s_x^e \tag{7.27}$$

In a similar way, the principal components of the deviatoric strain tensor are derived as:

$$e_x^e = e_y^e = \frac{1}{3}(1+\nu_T)\varepsilon_i^e \tag{7.28}$$

$$e_z^e = -\frac{2}{3}(1+\nu_T)\varepsilon_i^e = -2e_x^e \tag{7.29}$$

7.3.1.3 Elastic-plastic analysis of the loading process

In the elastic-plastic deformation stage, calculation of strains and stresses in an elasto-plastic region presents a difficult theoretical problem. Li et al. (1991) introduced the following simplified method. In a first step, the strain field is calculated as if the material was purely elastic. Then, the plastic strain in the elasto-plastic deformation stage is obtained from the strain field produced by the purely elastic impact and from the characteristics of a perfectly plastic impact using an empirical formulation introducing an efficiency factor α as:

$$\varepsilon_i^p = \begin{cases} \varepsilon_i^e & \text{for } \varepsilon_i^e \le \varepsilon_s \\ \varepsilon_s + \alpha(\varepsilon_i^e - \varepsilon_s) & \text{for } \varepsilon_i^e > \varepsilon_s \end{cases} \tag{7.30}$$

α is defined as the ratio of the radius of maximum plastic indentation a_p^* to the radius of the maximum elastic contact radius a_e^* (Li et al. 1991), ε_s is the strain corresponding to the yield stress σ_s.

The geometric characteristics of the plastic indentation are calculated assuming a rigid shot impinging upon a rigid perfectly plastic target. The determination of a_p^* involves the equation of motion of the shot during a normal contact with the target surface (Al-Hassani, 1984):

$$\frac{4\pi}{3}\rho R^3 \frac{dV}{dt} = -\pi {a_p}^2 \bar{p} \tag{7.31}$$

where $\bar{p}$ is the average pressure resisting the motion and a_p is the radius of indentation during the plastic impact. Using δ_p as the total approach between the centers of the two bodies, $V = \frac{d\delta_p}{dt}$ and $\frac{dV}{dt} = V\frac{dV}{d\delta_p}$, Equation (7.31) can be rewritten as

$$\frac{4\pi}{3}\rho R^3 V \frac{dV}{d\delta_p} = -\pi {a_p}^2 \bar{p} \tag{7.32}$$

This equation can be solved with the use of a geometrical relationship for the plastic indentation, as illustrated in Figure 7.2:

$$R^2 = {a_p}^2 + (R-\delta_p)^2 \tag{7.33}$$

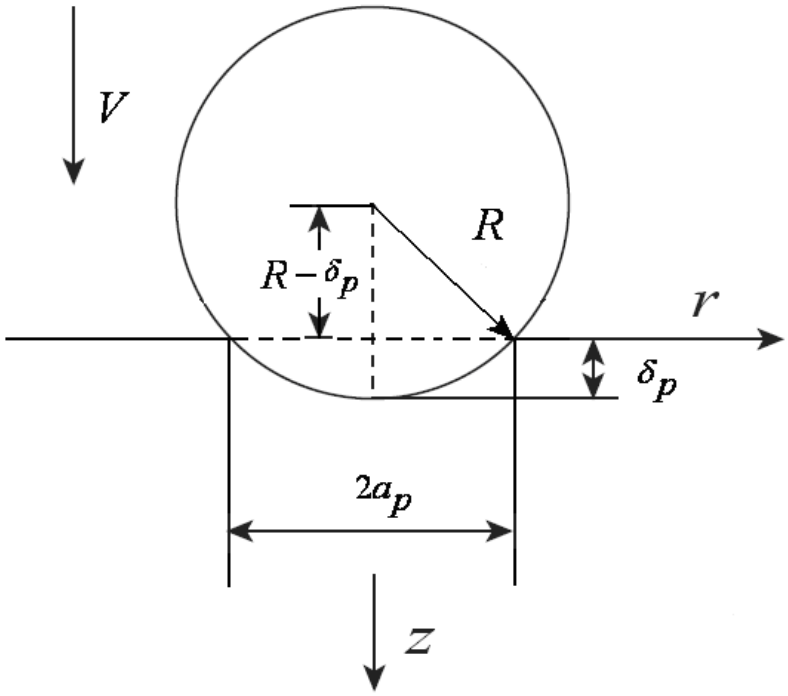

Figure 7.2: Plastic indentation of a rigid shot impacting a perfectly plastic target.

With the assumption that $R \gg \delta_p$, ${\delta_p}^2$ is ignored in Equation (7.33). Therefore, Equation (7.34) is obtained:

$$a_p = \sqrt{2\delta_p R} \tag{7.34}$$

Integrating Equation (7.32) with the help of Equation (7.34), while assuming full plasticity conditions in which $\bar{p}$ remains constant and equal to $3\sigma_s$ (Tabor, 1951) during the impingement, we obtain the maximum approach or final depth of indentation δ_p^* as:

$$\delta_p^* = \sqrt{\frac{2\rho R^2 V^2}{9\sigma_s}} \tag{7.35}$$

Then, combining Equations (7.34) and (7.35) we can obtain the following expression for the maximum plastic radius a_p^* in the case of normal impact:

$$a_p^* = R\left(\frac{8\rho V^2}{9\sigma_s}\right)^{\frac{1}{4}} \tag{7.36}$$

In the general case of an impact with incidence angle θ, Equation (7.36) becomes

$$a_p^* = R\left(\frac{8\rho(V\sin\theta)^2}{9\sigma_s}\right)^{\frac{1}{4}} \tag{7.37}$$

Once the strains are calculated, the stresses can be calculated according to the elastic-plastic stress-strain curve (Figure 7.3):

$$\sigma_i^p = \begin{cases} \sigma_i^e & \text{for} \quad \varepsilon_i^p < \varepsilon_s \\ \sigma_s + H^1(\varepsilon_i^p - \varepsilon_s) & \text{for} \quad \varepsilon_s \le \varepsilon_i^p < \varepsilon_b \\ \sigma_b & \text{for} \quad \varepsilon_i^p \ge \varepsilon_b \end{cases} \tag{7.38}$$

in which H^1 is a linear strain-hardening parameter, σ_b is the ultimate tensile stress of the target material, ε_b is the strain which corresponds to σ_b and ε_s is the elastic strain which corresponds to yield stress and is calculated as:

$$\varepsilon_s = \frac{\sigma_s}{E_T} \tag{7.39}$$

Since the simplified analysis for the strain assumed an elastic material, it is assumed that their relationships in the elastic-plastic domain are valid:

$$e_x^p = e_y^p = \frac{1}{3}(1+\nu_T)\varepsilon_i^p \tag{7.40}$$

$$e_z^p = -\frac{2}{3}(1+\nu_T)\varepsilon_i^p = -2e_x^p \tag{7.41}$$

According to Ilyushin's elastic-plastic theory (Ilyushin, 1948):

$$s_{ij}^p = \frac{1}{1+\nu_T}\frac{\sigma_i^p}{\varepsilon_i^p}e_{ij}^p \tag{7.42}$$

Then, the principal components of the deviatoric stress tensor in the elastic-plastic domain are:

$$s_x^p = s_y^p = \frac{1}{1+\nu_T}\frac{\sigma_i^p}{\varepsilon_i^p}e_x^p = \frac{1}{3}\sigma_i^p \tag{7.43}$$

$$s_z^p = -\frac{2}{3}\sigma_i^p = -2s_x^p \tag{7.44}$$

With the expressions for stress and strain in the elastic-plastic domain, expressions for the induced stress in the target material after unloading are be derived in the next section.

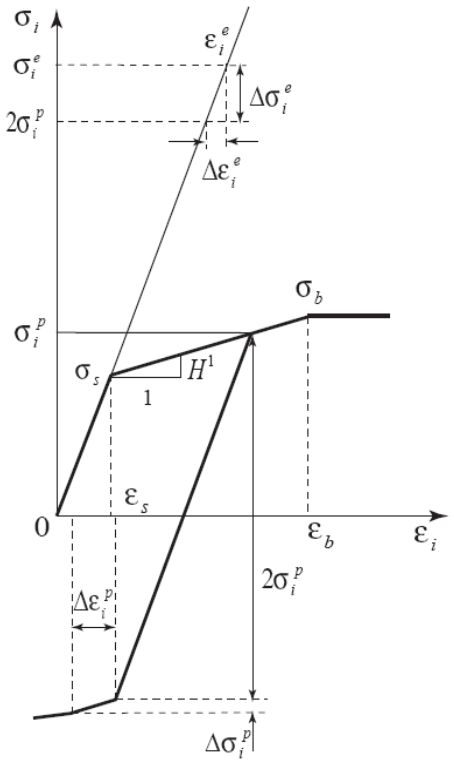

Figure 7.3: Schematic diagram for calculating stresses after unloading (σ_s is yield stress, σ_b is ultimate tensile stress , σ_i^e is von Mises equivalent elastic stress, σ_i^p is the plastic stress, $\Delta\sigma_i^e$ is the stress that can not be released , $\Delta\sigma_i^p$ is the stress corresponding to $\Delta\varepsilon_i^p$, ε_s is elastic strain corresponding to σ_s , ε_b is ultimate tensile strain corresponding to σ_b , ε_i^e is elastic strain corresponding to σ_i^e , ε_i^p is plastic strain calculated from ε_s and ε_i^e , $\Delta\varepsilon_i^e$ is the stress corresponding to $\Delta\sigma_i^e$, $\Delta\varepsilon_i^p$ is the plastic strain calculated from $\Delta\varepsilon_i^e$ and H^1 is a linear strain-hardening parameter).

7.3.1.4 Calculation of the transresidual and induced stresses after unloading

A clear distinction must be made at this point between stresses in the target material after successive loading and unloading of a single shot, which will be called transresidual stresses, and stresses after full shot peening coverage (100% coverage), which will be called induced stresses.

Assuming that (1) the target material is an isotropic hardening material, (2) the shot-induced deformation is small, (3) unloading is an elastic process before reversed yielding starts and (4) the hydrostatic stresses do not introduce plastic deformation, the transresidual stress can be calculated from the following relations:

$$\sigma_{ij}^{t} = \begin{cases} 0 & \text{for } \sigma_i^e < \sigma_s \\ s_{ij}^{p} - s_{ij}^{e} & \text{for } \sigma_s \le \sigma_i^e \le 2\sigma_i^p \end{cases} \tag{7.45}$$

These relations can be expressed in the three principal directions x, y and z as:

$$\sigma_x^t = \sigma_y^t = \frac{1}{3}\left(\sigma_i^p - \sigma_i^e\right) \text{ for } \sigma_s \le \sigma_i^e \le 2\sigma_i^p \tag{7.46}$$

$$\sigma_z^t = -2\sigma_x^t \tag{7.47}$$

When $\sigma_i^e > 2\sigma_i^p$, the target material will experience reversed yielding and hardening. Firstly, a stress of $2\sigma_i^p$ is elastically unloaded, then reversed yielding takes place. However, some stresses could not be released, namely:

$$\Delta\sigma_i^e = \sigma_i^e - 2\sigma_i^p \tag{7.48}$$

The elastic strains related to $\Delta\sigma_i^e$ are:

$$\Delta\varepsilon_i^e = \frac{\Delta\sigma_i^e}{E} \tag{7.49}$$

Then, as was done for the elastic-plastic contact, the elastic-plastic strains are assumed to be:

$$\Delta\varepsilon_i^p = \alpha\Delta\varepsilon_i^e \tag{7.50}$$

Then, the corresponding stress $\Delta\sigma_i^p$ can be obtained by considering the multilinear stress-strain curve of the target material as:

$$\Delta\sigma_i^p = H^1\Delta\varepsilon_i^p \tag{7.51}$$

Equation (7.51) assumes that reverse yielding induces only small strains. In the case of reverse yielding with large strains (e.g. due to shots impacting at very high velocity), $\Delta\sigma_i^p$ should be obtained using the elastic-plastic stress-strain curve (Figure 7.3) considering the presence of σ_b during reverse yielding. Finally, the transresidual stresses when $\sigma_i^e > 2\sigma_i^p$ can be obtained as:

$$\sigma_x^t = \sigma_y^t = \frac{1}{3}\left(\sigma_i^p - 2\sigma_i^p - \Delta\sigma_i^p\right) \tag{7.52}$$

$$\sigma_z^t = -2\sigma_x^t \tag{7.53}$$

After full shot peening coverage (100% coverage), the deformation field is assumed to be steady and continuous. The target component is assumed to retain a plane surface, i.e. ε_x, ε_y are zero and

the non-zero stress and strain components will be independent of *x* and *y*. Therefore, at full coverage:

$$\sigma_x = \sigma_y = f(z) \tag{7.54}$$

$$\sigma_z = 0 \tag{7.55}$$

$$\varepsilon_x = \varepsilon_y = 0 \tag{7.56}$$

$$\varepsilon_z = f_1(z) \tag{7.57}$$

The transresidual stresses do not satisfy these equilibrium conditions and must be partially relaxed. In accordance with Hooke's law, the relaxation values of σ_x^t and σ_y^t can be calculated as:

$$\sigma_x^{rel} = \sigma_y^{rel} = \frac{\nu}{1-\nu}\sigma_z^t \tag{7.58}$$

The induced stresses corresponding to 100% peening coverage (σ^{ind}) can be calculated as:

$$\sigma_x^{ind} = \sigma_y^{ind} = \sigma_x^t - \sigma_x^{rel} = \sigma_x^t - \frac{\nu}{1-\nu}\sigma_z^t = \frac{1+\nu}{1-\nu}\sigma_x^t \tag{7.59}$$

$$\sigma_z^{ind} = 0 \tag{7.60}$$

It is believed that these induced stresses are a good approximation of the induced stresses at saturation (in the sense of Almen intensity) and can therefore be used to calculate the theoretical Almen intensity.

7.3.2 Calculation of residual stress for a thin target component

The induced stress profile obtained in the previous section is based on a semi-infinite target body. It is however not self-equilibrated and stresses would thus be redistributed afterward if applied to a thin strip since the non-equilibrated stress field would tend to stretch and bend it. Therefore, when performing an Almen test, a compressive force F_x and a bending moment M_x must be applied by the rigid support on the Almen strip in order to maintain it in a flat shape, as shown in Figure 7.4. The resulting residual stress profile can be calculated with equations introduced by Al-Hassani (1982). Equations (7.61) and (7.62) are the force and moment equilibrium equations for this case, namely:

$$\int_0^h \sigma_x^{ind} b \mathrm{d}z + F_x = 0 \tag{7.61}$$

$$\int_0^h \sigma_x^{ind} (\frac{h}{2} - z) b \mathrm{d}z + M_x = 0 \tag{7.62}$$

where b is the width and h is the thickness of the strip.

After the release of the rigid constraints due to the support and bolts, the originally flat strip will stretch and bend. The superposition principle is used in order to calculate the resulting bending. It is assumed that only elastic stresses occur during this post-treatment release and that the flat component is subjected to the inverse of the force and moment calculated from Equations (7.61) and (7.62). The residual stress profile after deformation of the strip can therefore be calculated with Equation (7.63) :

$$\sigma_x^{res} = \sigma_x^{ind} + \sigma_x^s + \sigma_x^b = \sigma_x^{ind} + \frac{F_x}{A} + \frac{M_x(\frac{h}{2} - z)}{I} \tag{7.63}$$

where σ_x^s is the stretching stress calculated from stretching force F_x and σ_x^b is the bending stress calculated from bending moment M_x.

Finite element simulation of such a strip with a bending moment and a stretching force induced by shot peeing showed that the influence of the stretching force on the arc height is negligible. Therefore, in the following study, only the bending effect along the length direction is considered in order to calculate the arc height (Guagliano, 2001 and Miao et al. 2009):

$$\mathrm{ArcHeight} = \frac{3 M_x {l_m}^2}{2 E b t^3} \tag{7.64}$$

where $l_m = 31.75\mathrm{mm}$ is the reference distance for measuring Almen intensity.

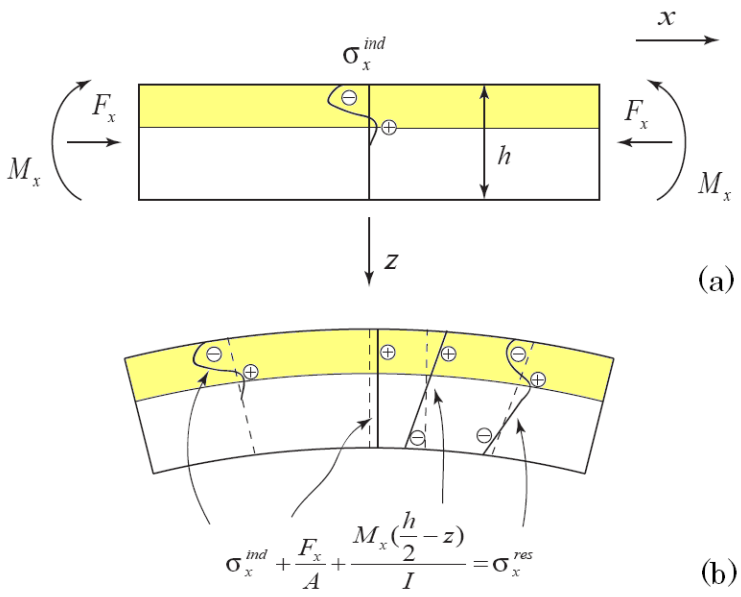

Figure 7.4: Equilibrium process in thin target component: (a) Peened component constrained in flat shape by rigid support, σ_x^{ind} is the induced stress profile in a constrained strip. (b) Deformed shape and residual stress profile after release from the rigid support, F_x and M_x are stretching force and bending moment with respect to the stretching stress and bending stress, respectively. σ_x^{res} is residual stress in the free strip.

7.4 Application

7.4.1 Material, geometry and modeling parameters

The model developed at Section 7.3 was used to obtain theoretical values of Almen intensities for different combinations of peening parameters. Almen strips of type A, used most often for peening with cast metal or cut wire shots, were considered with dimensions $76\text{mm} \times 19\text{mm} \times 1.29\text{mm}$. The material for Almen strips, SAE1070 spring steel, is assumed to obey an elasto-plastic behavior with isotropic hardening, a bilinear stress-strain relationship capped with ultimate tensile stress (UTS) and to have the following properties: Young's modulus $E = 200\text{GPa}$, Poisson ratio $\upsilon = 0.31$, yield stress $\sigma_s = 1120\text{MPa}$, ultimate tensile stress $\sigma_b = 1270\text{MPa}$ and elongation at UTS $\varepsilon_b = 8.2\%$ (Guagliano, 2001). The linear strain-hardening parameter H^1 (see Figure 7.3) was calculated based on these values.

Shots were considered elastic in all calculations. Both steel and ceramic shots were studied, with the following material properties:

- ***For steel shot:*** Young's modulus $E_s = 210\text{GPa}$, density $\rho_s = 7800\text{kg/m}^3$ and Poisson's ratio $\upsilon_s = 0.31$.
- ***For ceramic shot:*** Young's modulus $E_s = 300\text{GPa}$, density $\rho_s = 3850\text{kg/m}^3$ and Poisson's ratio $\upsilon_s = 0.27$.

In addition, different velocities, radius and shot peening angles were studied in order to determine their influence on Almen intensity.

7.4.2 Algorithm for the prediction of induced and residual stress profiles

In this section, an algorithm for the prediction of induced and residual stress profiles in an Almen strip (type A) impacted by 0.4mm diameter steel shots with an incoming velocity 45m/s is presented as an example. A discretization value of $1\mu\text{m}$ along the z-axis was chosen for this example.

(i) Input parameters:

- **Almen strip:** $E_t = 200\text{GPa}$, $\upsilon_t = 0.31$, $\sigma_s = 1120\text{MPa}$, $\sigma_b = 1270\text{MPa}$, $\varepsilon_b = 8.2\%$, $H^1 = (\sigma_b - \sigma_s)/(\varepsilon_b - \varepsilon_s)$, where ε_s is calculated with Equation (7.39).
- **Steel shot:** $E_s = 210\text{GPa}$, $\rho_s = 7800\text{kg/m}^3$, $\upsilon_s = 0.31$, $D = 0.4 \times 10^{-3}\text{m}$.
- **Contact parameters:** $k = 0.8$, E_H is calculated with Equation (7.5).
- **Peening conditions:** $\theta = 90^o$, $V = 45\text{m/s}$.

(ii) Step1: Elastic contact analysis

- Calculate a_e^* with Equation (7.13), p_0^* with Equation (7.14).
- For each location along the z-axis through the strip thickness, and using a discretization of $1\mu\text{m}$, evaluate $\sigma_x^e(z)$, $\sigma_y^e(z)$ and $\sigma_z^e(z)$ with Equations (7.16) and (7.17), σ_i^e with Equation (7.20) and ε_i^e with Equation (7.23).

(iii) Step2: Elastic-plastic analysis

- Calculate a_p^* with Equation (7.37). Calculate $\alpha = a_p^*/a_e^*$, ε_i^p with Equation (7.30) and σ_i^p with Equation (7.38).

(iv) Step3: Transresidual stress (after loading for one shot)

- If $\sigma_i^e < \sigma_s$, σ_{ij}^t=0;
- If $\sigma_s \leq \sigma_i^e \leq 2\sigma_i^p$, calculate σ_x^t, σ_y^t and σ_z^t with Equations (7.46) and (7.47).
- If $\sigma_i^e > 2\sigma_i^p$, calculate $\Delta\sigma_i^e$ and $\Delta\varepsilon_i^e$ with Equations (7.48) and (7.49), $\Delta\varepsilon_i^p$ and $\Delta\sigma_i^p$ with Equations (7.50) and (7.51), σ_x^t, σ_y^t and σ_z^t with Equations (7.52) and (7.53).

(v) Step4: Induced stress (after loading for full peening coverage)

- Calculate induced stresses σ_x^{ind} and σ_y^{ind} with Equation (7.59).

(vi) Step5: Residual stress prediction and arc height

- Calculate F_x and M_x with Equations (7.61) and (7.62), residual stress σ_x^{res} with Equation (7.63), then arc height with Equation (7.64).

Figure 7.5 presents the calculated induced stresses, stretching stresses, bending stresses and residual stresses in the Almen strip (type A) for the example presented above. The calculated Almen intensity for this combination of parameters was 8A (0.2mm A). The induced stresses have compressive values only on the top layer of the target component. The residual stress profile is the final equilibrated stress profile after the release of the constraints. When compared to the induced stresses, the residual stresses have compressive values at both top and bottom surfaces of the target component. For a semi-infinite body or a fixed strip, the elongation and bending of the strip can be neglected. Therefore the induced stresses can be regarded as the residual stresses in the semi-infinite body or the fixed strip.

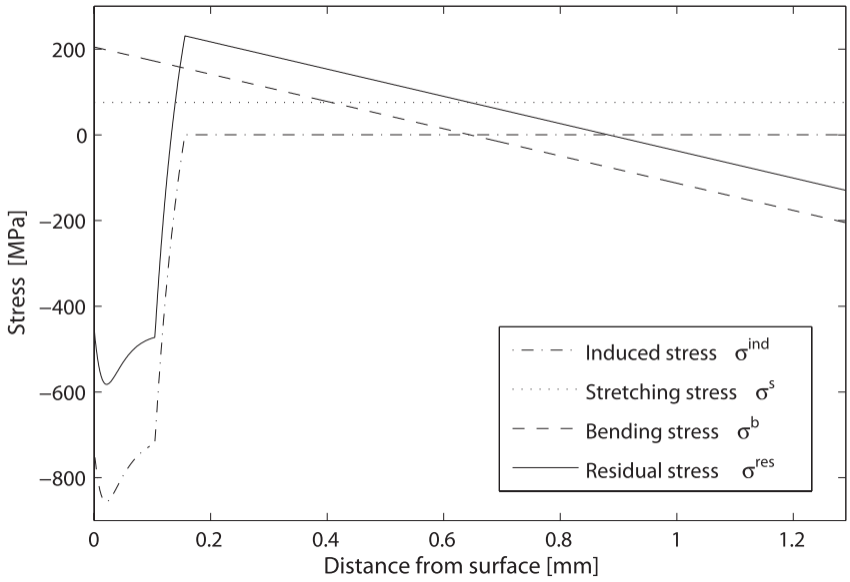

Figure 7.5: Induced stress, stretching stress, bending stress and residual stress in Almen strip Type A (calculated intensity 8A=0.2mmA).

7.4.3 Validation of the efficiency factor α

The axisymmetric finite element model shown in Figure 7.6 was developed by ANSYS to validate the parameter α defined in Section 7.4.2. The model considered the same shot peening parameters as in Section 7.4 (a rigid shot with diameter D equals to 0.4mm and velocity equals to 45m/s). The target component was represented by a cylinder with radius and depth equal to $3D$, including a fine mesh in the contact region of radius and depth equal to D. The element size was approximately 0.02mm for the entire model, except in the contact regions of the shot and target component where fine elements of size 0.005mm were used. An elastic and a rigid perfectly plastic targets were successively considered to calculate the elastic contact radius a_e^* and the plastic indentation radius a_p^*, respectively.

For elastic target, a material with Young's modulus $E = 200\text{GPa}$ and Poisson ratio $\upsilon = 0.31$ was defined. The rigid perfectly plastic material behaviour was approximated by an isotropic hardening material model with negligible strain at yield stress, with the following properties: Young's modulus $E = 2 \times 10^5\text{GPa}$, Poisson ratio $\upsilon = 0.31$, yield stress $\sigma_s = 1120\text{MPa}$ and linear strain-hardening parameter $H^1 = 0$.

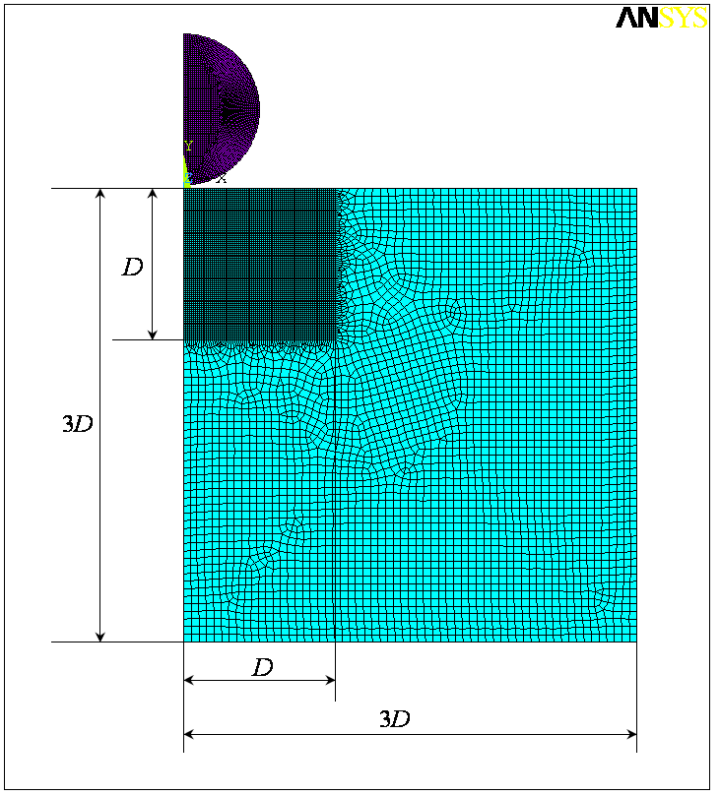

Figure 7.6: Axisymmetric finite element model of a rigid shot impact an infinite target component.

Figure 7.7 (a) and (b) present the contact between the rigid shot and the elastic target. The maximum contact radius is approximately $a_e^* = 0.041\text{mm}$. After shot rebound, the indentation disappears. Figure 7.7 (c) and (d) show the contact between a rigid shot and the rigid perfectly plastic target. The radius of indentation is calculated by considering the location of the first point with zero vertical displacement. Indentations with radii $a_p^* = 0.0615\text{mm}$ were obtained both during impact and after rebound.

Table 7.1 lists the maximum contact radius in the elastic domain a_e^* and the maximum plastic radius a_p^* calculated using the analytical model and using FEM, respectively. It can be found that although a_e^* and a_p^* are slightly different, the efficiency factor α calculated from both approaches are very consistent.

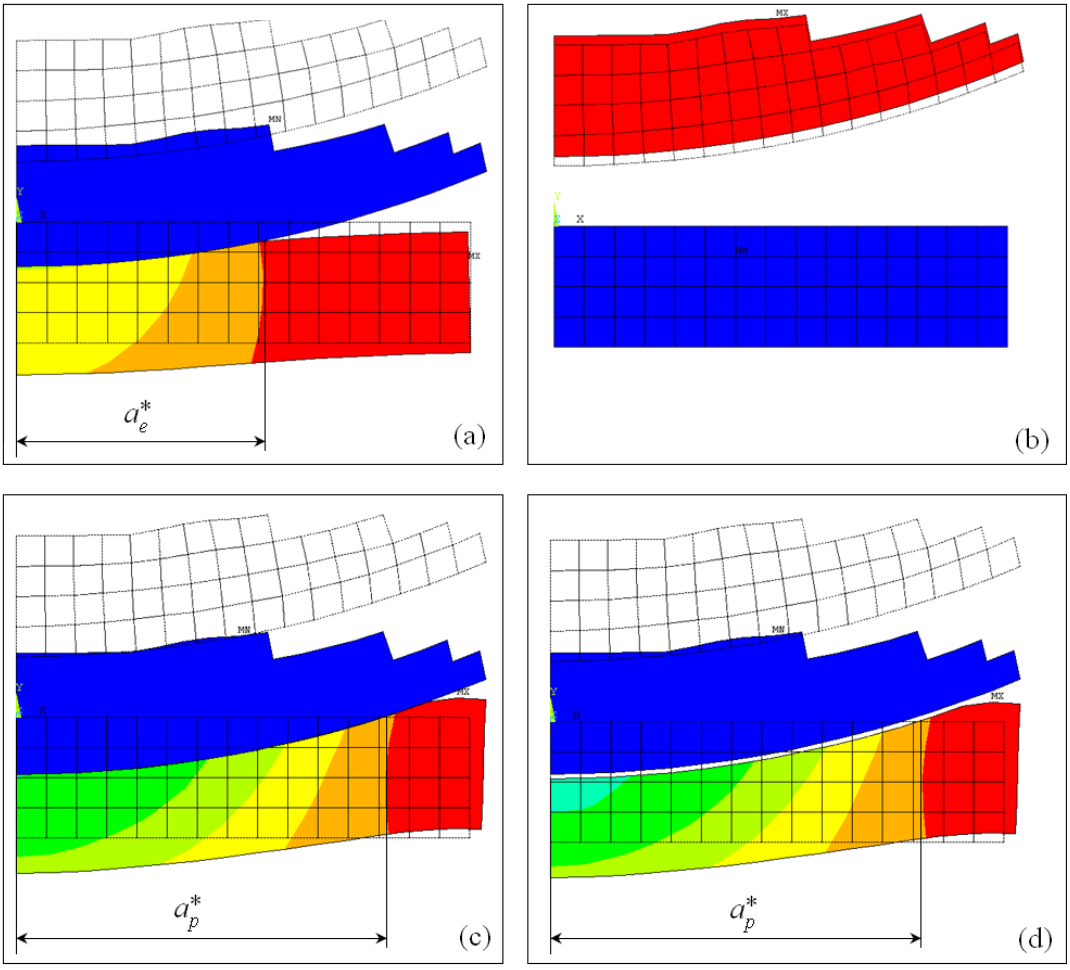

Figure 7.7: Contact between rigid shot and target component: (a) rigid shot impacting an elastic target – at maximum compression; (b) rigid shot impacting an elastic target– after rebound; (c) rigid shot impacting a perfectly plastic target –at maximum compression; (d) rigid shot impacting a perfectly plastic target – after rebound.

Table 7.1: Elastic contact radius and plastic indentation radius calculated by analytical model and FEM.

	a_e^* (mm)	a_p^* (mm)	$\alpha = a_p^*/a_e^*$
Analytical values (Equation (7.13) for a_e^* and Equation (7.37) for a_p^*)	0.0425	0.0660	1.55
FEM values	0.041	0.0615	1.5

7.4.4 Experimental validation

Figure 7.8 compares theoretical stress profiles with published experimental residual stress profiles from Cao et al. (1995) for constrained Almen strips and free Almen strips, respectively. The experimental size range of the steel shots was $355\sim420\mu m$, the Almen intensity was 8A (0.2mm), shot velocity was determined as $45m/s$ by means of an optical method and the number of peening passes is indicated in the figure. In order to simulate the experimental Almen intensity of 8A(0.2mm), we assumed steel shots of diameter $400\mu m$, with shot velocity of $45m/s$ impacting at normal incidence angle in the theoretical calculation.

The experimental stresses were measured by Cao et al. (1995) in the center of Almen strips (type A) in the longitudinal direction using an X-ray diffraction instrument SET-X. Depth distribution was obtained by successive electrolytic removal of material layers. The published results did not include correction of residual stresses due to material removal. Such correction on the published experimental data was however performed as part of the current work. Considering that thin layers Δz were removed, it can be assumed that the stress is homogeneous in the layer. Corrected stresses were thus calculated using the following approximate formula (Lu, 1996):

$$\sigma(z_1) = \sigma_m(z_1) - 4\sigma_m(z_1 + \Delta z)\frac{\Delta z}{z_1 + \Delta z} \tag{7.65}$$

where $\sigma(z_1)$ and $\sigma_m(z_1)$ are the corrected stress and measured stress at depth z_1 from the opposite surface, respectively and $\sigma_m(z_1 + \Delta z)$ is the measured stress at depth $z_1 + \Delta z$ (i.e. closer to the surface where material removal took place).

Figure 7.8(a) and (c) compare the measured stress (uncorrected stress) and corrected stress profiles in constrained strips and free strips, respectively. In both cases, corrected measurements were slightly smaller than published measurements and the analytical prediction will be compared with the corrected measurements.

Figure 7.8 (b) compares the analytical induced stress profile and the corrected residual stress in constrained strips after two different number of peening passes. In this figure, the induced stresses obtained using the theory presented in Section 7.3.1 can be regarded as residual stresses in a fixed strip. It can be seen that the analytical results are in relatively good agreement with the corrected results. However, some differences can be noticed between the theoretical and the

corrected residual stresses at the surface and from 0.12mm to 0.20mm from the surface. These differences might be attributed to:

The experimental fixturing allowing small deflection of constrained strips. Theoretical induced stresses correspond to residual stresses in a semi-infinite component, without any stretching or bending. This is assumed equivalent to the stresses in a fully constrained strip. However, Almen strips subjected to a blast of shots undergo deformation and small deflection while they are still constrained by the fixing screws, as shown by Cao et al. (1995). This deflection reduces the surface stress that is to be experimentally measured. Fully constraint strips would probably present larger surface stresses, closer to the predicted values.

The model not considering repeated peening passes. The model considers only one impact; the stresses and strains induced by this impact are uniformly distributed throughout the entire Almen strip and relaxed. However, experimental residual stresses after 12 and 48 peening passes show that the depth of the compressive residual stress layer increases with the increase of the number of pass. Modifying the model to take into account multiple passes or multiple impacts over the same point would probably increase the thickness of the layer with plastic strain, thus increasing the depth of the compressive residual stress layer

Figure 7.8 (d) compares the analytical residual stress profile and the experimental residual stress in free strips after correction. It can be seen that in the free Almen strip, the equilibrated residual stresses calculated by model are reasonably consistent with the corrected experimental stresses. The analytical results are especially close to corrected experimental stresses at depth ranges of about 0.05mm to 0.10mm. The differences between the experimental and analytical results for free strips could be explained by reason 2) presented above.

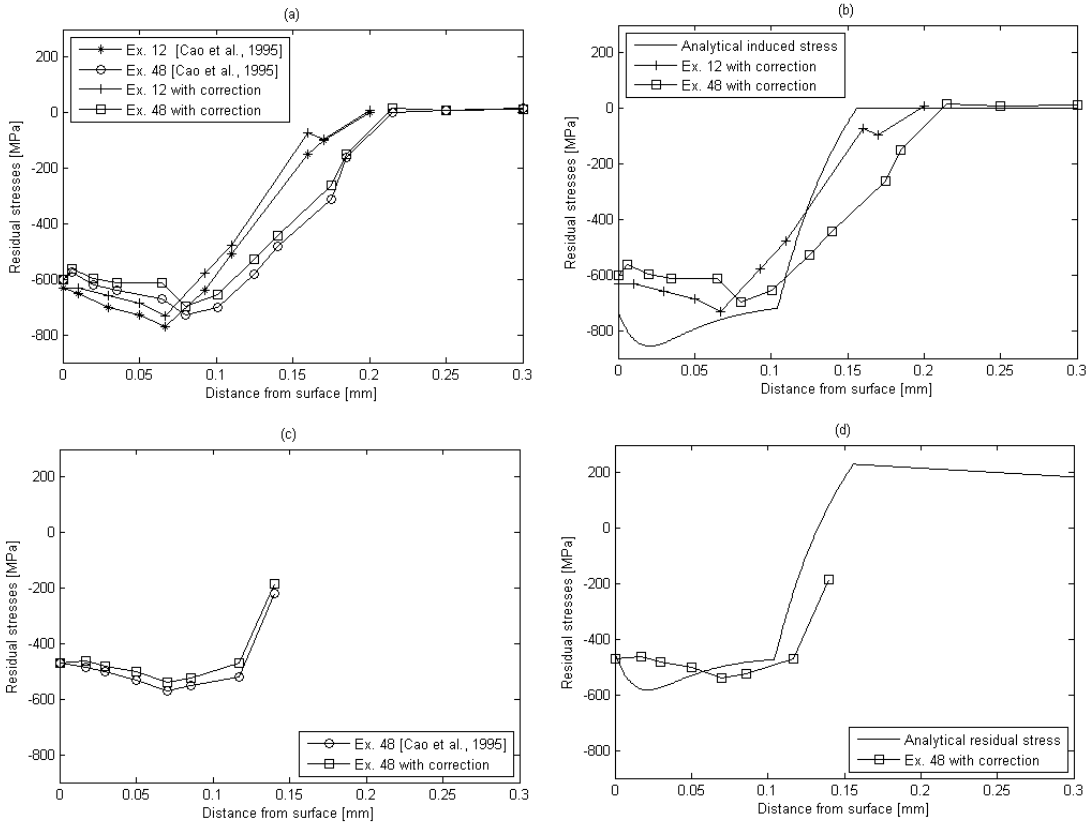

Figure 7.8: Comparison of analytical residual stress and published experimental residual stress (Cao et al. 1995) in Almen Type A strips for: (a) Measured stresses and corrected stresses in constrained strips after 12 passes and after 48 passes. (b) Analytical induced stress, corrected stress in constrained strips after 12 passes and after 48 passes. (c) Measured stresses and corrected stresses in free strips after 48 passes. (d) Analytical residual stress and corrected stress in free strips after 48 passes.

Figure 7.9 shows predicted and experimental Almen intensity as a function of shot velocity for two shot sizes: (a) S110 steel shots (nominal diameter D_{nom}=0.279mm, average diameter D_{ave}=0.356mm), and (b) S170 steel shots (D_{nom}=0.423mm, D_{ave}=0.504mm).

In both cases, the average shot diameter was used for calculation. Figure 7.9(b) shows that the analytical results for the larger shot (S170) are very similar to the experimental results of (Cao et al. 1995). Figure 7.9(a) indicates that the model slightly overestimates the Almen intensity for small S110 shot (D=0.356mm) at low velocity and underestimates at higher velocity. Possible explanations for this phenomenon include:

- Increased interference effect at low velocity in the experiment causes a decrease of the average impact velocity as well as a decrease of Almen intensity (Hong et al. 2008b).
- Friction effect between shots and surface hasn't been considered in the model.
- A constant efficiency coefficient parameter has been assumed in the model. For different peening condition, might be influenced by shot size, velocity and peening angle, etc.

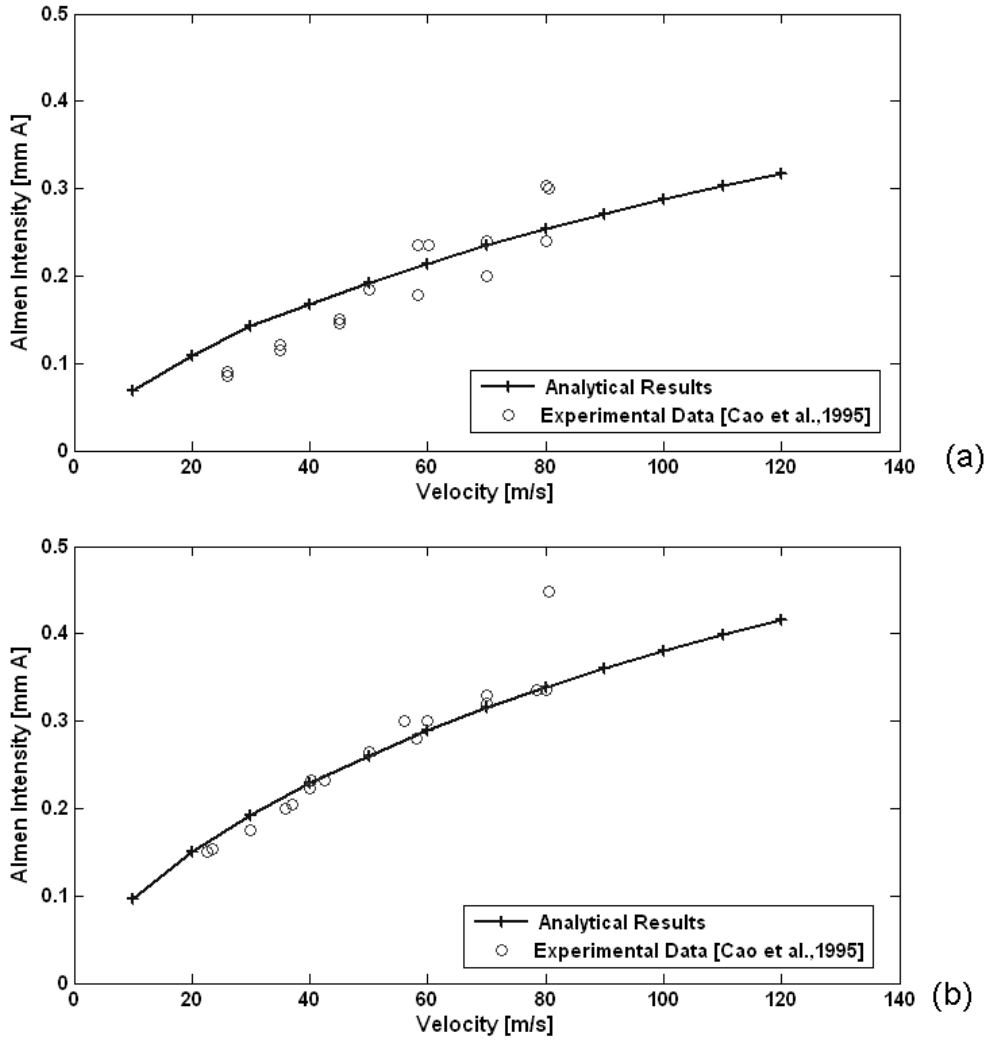

Figure 7.9: Analytical and experimental relationships between Almen intensity and shot velocity for two shot sizes: (a) S110 shot (D_{ave}=0.356mm) and (b) S170 (D_{ave}=0.504mm).

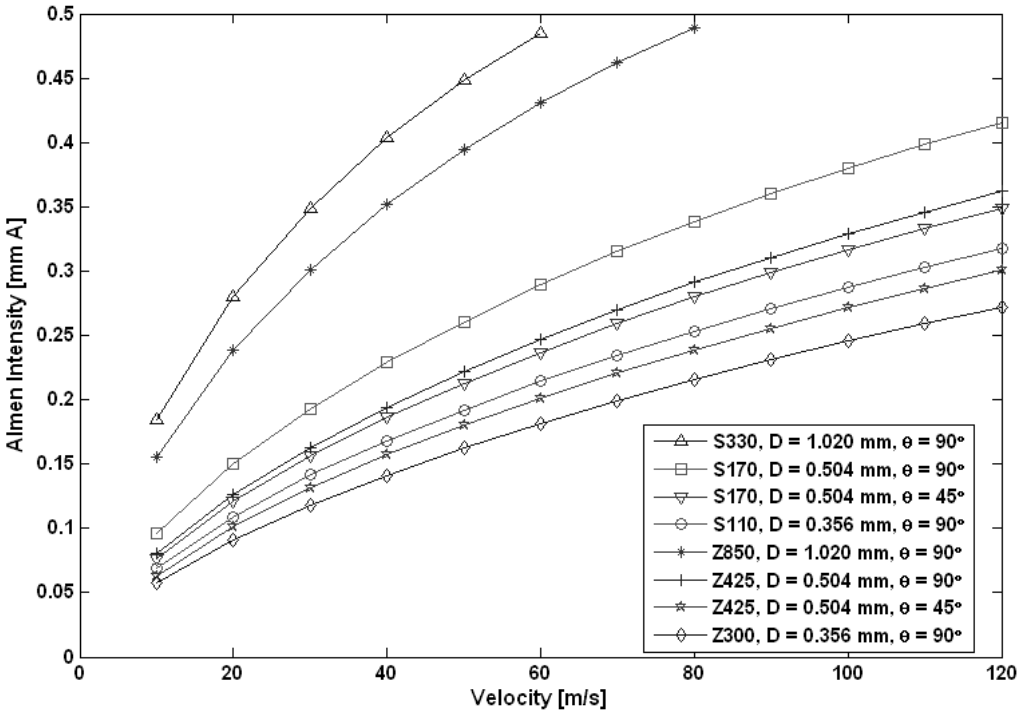

Figure 7.10: Effect of peening parameters on Almen intensity. S330, S170 and S110 represent three types of steel shots with diameter equal to 0.356mm, 0.504mm and 1.020mm, respectively. Z850, Z425 and Z300 represent three types of ceramic shots with diameter equal to 0.356mm, 0.504mm and 1.020mm, respectively. For S170 and Z450, two peening angles 45º and 90º have been considered.

7.5 Potential application

Figure 7.10 shows the predicted variation of Almen intensity with shot velocity for various peening parameters. Two shot materials (steel and ceramic) and two peening angles (45^o and 90^o) were investigated. For each shot material, three commercially available shot sizes were studied (steel shots: S110, S170 and S330, and the closest available sizes for ceramic shots: Z300, Z425 and Z850).

Results in Figure 7.10 indicate that shot velocity is the predominant peening parameter for Almen intensity. For a given combination of shot size, material and peening angle, a variation of shot velocity from to was shown to increase the resulting Almen intensity by a minimum ratio of 2.65. The corresponding minimum ratio was 4.32 for a variation of shot

velocity from 10 m/s to 120 m/s. Shot material also has a substantial effect on Almen intensity. Steel shots produced larger Almen intensities for each combination of shot size and peening angle under consideration, with a difference in Almen intensity between the two shot materials ranging from 11% to 17% and an average difference of 15%. The Almen intensity was found to be approximately proportional to shot diameter, especially at low velocities. Finally, peening angle induces a scale factor on the shot velocity.

The Almen intensity induced by a peening treatment with shot velocity V and peening angle $\theta = 45°$ corresponds to the Almen intensity with shot velocity $V\sin 45°$ and peening angle $\theta = 90°$. This phenomenon suggested by the model may not be completely representative of the real shot peening process since the model ignores friction effects as well as interference effects between incident and reflected shots.

Figure 7.11 compares the calculated residual stress profiles in Almen strips for normal impacts of steel shots, considering three combinations of shot size and velocity: (i) S110(0.356mm), shot velocity 53.5m/s; (ii) S170(0.504mm), shot velocity 31.8 m/s; (iii) S330(1.02mm), shot velocity 11.4 m/s. Each combination resulted in the same Almen intensity (0.2mm A). This figure indicates that no one-to-one correspondence exists between residual stress profile and Almen intensity. Each residual stress profile corresponds to a unique Almen intensity, while a given Almen intensity can be related to various residual stress profiles with underlying peening parameters. Combination (i) with small shots and high velocity led to the largest surface stress (456 MPa), the largest maximum stress (597 MPa) and the thinnest layer of compressive residual stresses (0.131mm). Conversely, combination (iii) with large shots and low velocity led to the smallest surface stress (71 MPa), the smallest maximum stress (500 MPa) and the thickest layer of compressive residual stresses (0.141mm). These results suggest that modification of shot size while keeping a constant Almen intensity in a shot peening application may induce unwanted effects, such as lower surface stresses and reduced thickness of the compressive layer, both of which being commonly related to changes in the fatigue life expectancy of the peened component.

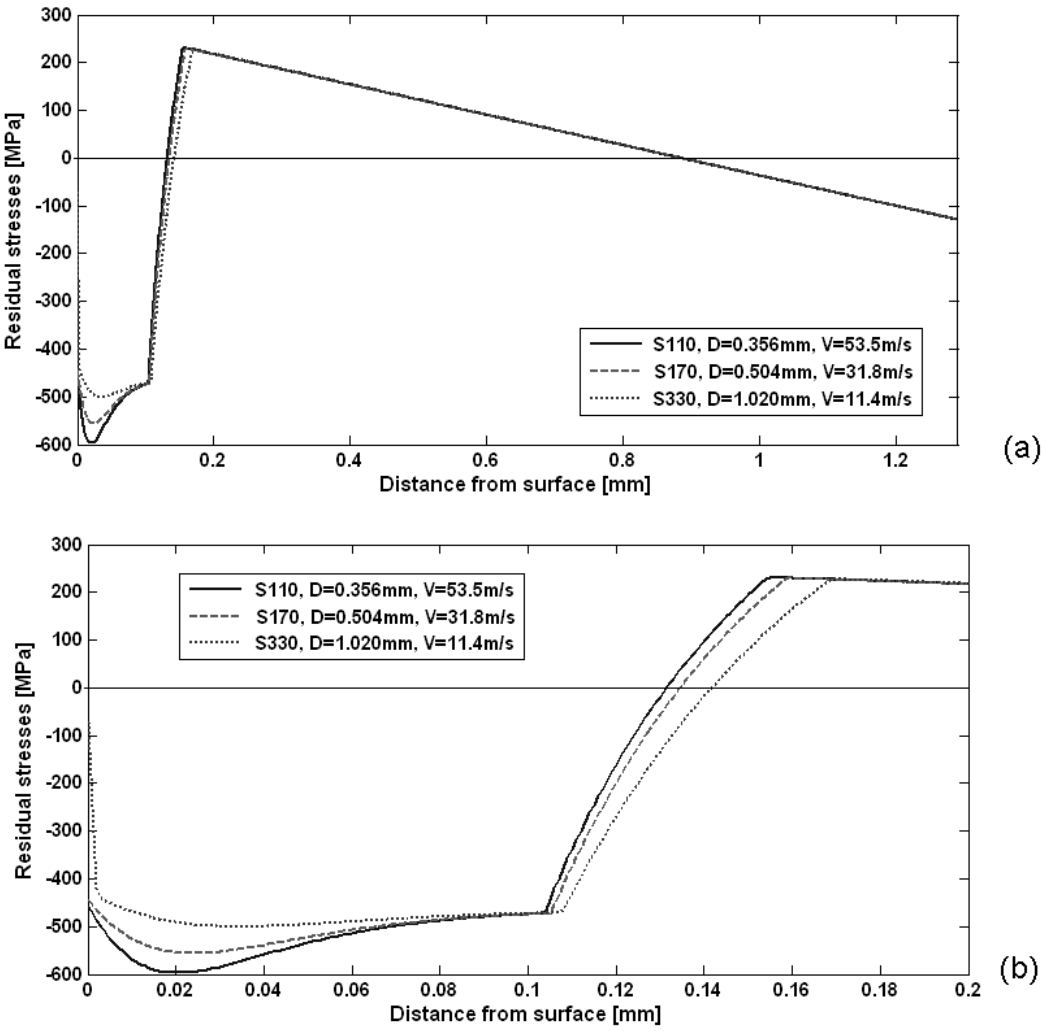

Figure 7.11: Calculated residual stresses for different combinations of peening parameters, with identical Almen intensity (0.2mm A). (a) Residual stress profiles for three cases following the whole depth (1.29mm). (b) Residual stress profiles for three cases on the top surface (0 to 0.2mm).

Figure 7.12 presents the relationship between shot velocity, shot diameter and Almen intensity from a new perspective. In this figure, results are presented as a series of curves corresponding to different levels of Almen intensity (ranging from 0.05 to 0.35mm A), for steel shots and ceramic shots (Figure 7.12 (a) and (b) respectively).

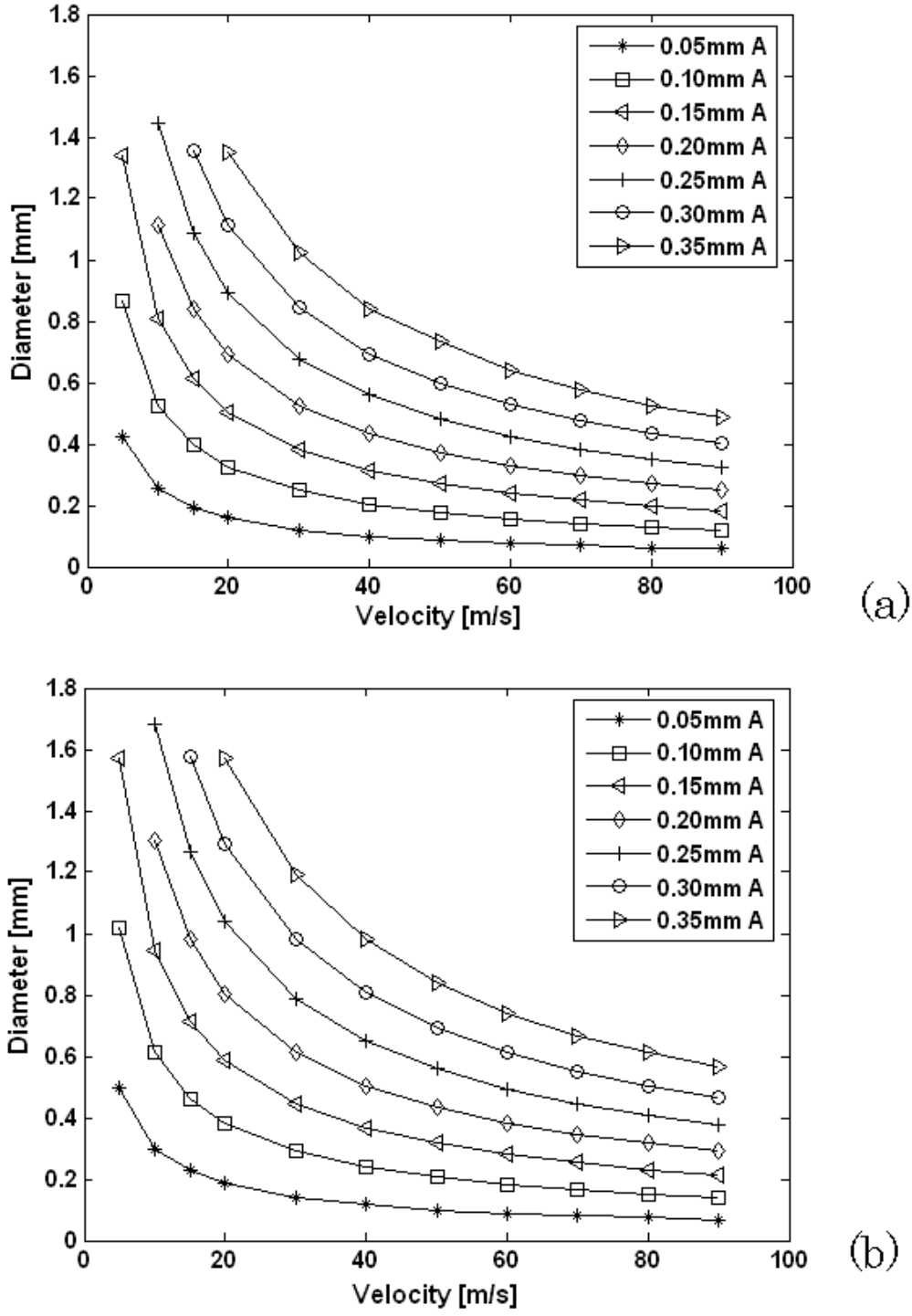

Figure 7.12: Relationship between diameter and velocity for seven different Almen intensities (Almen Type A strip): (a) Steel shot, (b) Ceramic shot.

For both shot materials, results show that to achieve a given Almen intensity, the shot velocity must increase as the shot size (diameter) decreases. At any given shot velocity, a larger ceramic shot diameter is required to achieve the same Almen intensity when compared to a steel shot. For instance, for a shot velocity of 40m/s, it is required to use approximately 0.4mm diameter steel shots or 0.5mm diameter ceramic shots to obtain an intensity 0.2mmA. This can be explained by the following. Calculations took into account two material properties for shots: density and Young's modulus. Steel shots possess a larger density ($\rho_s = 7800\text{kg/m}^3$) when compared with ceramic shots ($\rho_s = 3850\text{kg/m}^3$), which, on the other hand are much harder (Young's modulus $E_s = 300\text{GPa}$) than steel shots (Young's modulus $E_s = 210\text{GPa}$). Thus, we can conclude that the effect of shot density predominates over the effect of Young's modulus when comparing these two shot materials. The results show that to achieve a given Almen intensity, a large variation of shot diameter occurs at low velocity. The required diameter is then almost constant at velocities over 45 m/s. Furthermore, it is nearly impossible to achieve a low intensity with large shots since it would require a very low velocity.

Finally, the results from Figure 7.12 were used to establish empirical relationships between peening parameters and Almen intensity. The trend of the Almen intensity is well described by the following best fit equation for steel shots:

$$A_{H,steel}(D,v) = 0.06735D + 0.01184Dv - 0.00002824Dv^2 - 0.00004991D^2v^2 \quad (7.66)$$

The coefficient of determination for this equation $R^2 = 0.998$. For ceramic shots, the following best fit equation is obtained:

$$A_{H,ceramic}(D,v) = 0.05714D + 0.01019Dv - 0.00002472Dv^2 - 0.00003583D^2v^2 \quad (7.67)$$

The corresponding coefficient of determination $R^2 = 0.998$. For both equations, D is expressed in mm and v is expressed in m/s. These equations are only valid for the range of shot diameter and shot velocity represented in Figure 7.12 and should not be used outside this range of validity as they may lead to unrealistic results, especially for small shot diameters.

The empirical equations for Almen intensity presented above can be used as a tool for determining possible combinations of peening parameters to obtain given Almen intensities. It would also be applicable for substituting parameters in peen forming of spring steel thin

components (or of a similar alloy), as the peening-induced stresses in such metal are likely to be similar to those in Almen strips.

However, although each combination of peening parameters for a given Almen intensity induces similar residual stress profiles, significant differences were found in the magnitude of surface stress and thickness of compressive layer. It would therefore be inappropriate in many shot peening applications for fatigue life enhancement to substitute a set of peening parameters for another set while keeping the Almen intensity constant, as it could influence the fatigue life expectancy of the peened component. Moreover, the present study investigated residual stresses in Almen strips made of SAE1070 spring steel. Combinations of peening parameters leading to similar residual stress profiles in Almen strips may lead to various stress profiles in a different metal such as aluminum. Care must thus be taken when substituting peening parameters while applying shot peening for fatigue life enhancement or peen forming on different metals as it may lead to unwanted and hardly predictable results.

7.6 Conclusions

Shot peening Almen intensity is one of an important shot peening control parameters to ensure repeatability of the shot peening process. In this paper, an analytical model was developed to predict Almen intensity and residual stress distribution for Almen strip. The influence of shot peening parameters, such as shot type (steel and ceramic), size, velocity and peening angle on the Almen intensity have been presented.

The study results revealed the following:

(1) The analytical model can predict the Almen intensity and shot-induced residual stress for Almen strips for any combination of peening parameters (shot type, size, velocity, peening angle). The predicted results were in good agreement with published experimental results, especially for the prediction of Almen intensity.

(2) Shot velocity was found to be the predominant peening parameter for Almen intensity. Shot material also had a substantial effect on Almen intensity.

(3) The analytical model produces different residual stress for the same Almen intensity generated with different combinations of shot peening parameters (shot type, size, velocity, peening angle). Thus, small shots at high velocity will produce larger maximum

compressive residual stress and thinner layer of compressive residual stress, while large shots at low velocity will produce smaller maximum compressive residual stress and thicker layer of compressive residual stress.

(4) Shot peening with normal angle of incidence will produce a larger Almen intensity compared with oblique shot peening, every other parameters kept unchanged. Peening angle induces a scale factor on the shot velocity since only the normal component of velocity onto the surface is considered by the model. However, this assumption may not be completely representative of the real shot peening process since the model ignores friction effects as well as interference effects between incident and reflected shots.

(5) For either shot types, steel or ceramic, the effect of shot velocity and size on the resulting Almen intensity can be expressed as an empirical equation. This equation can be used as a tool for determining possible combinations of peening parameters to obtain given Almen intensities.

Almen test is a useful control procedure for shot peening applications, as it monitors the aggregate energy transfer imparted to the workpiece by the shot peen process and reveals process variations. Any change in a process parameter is reflected by a change in Almen intensity. However, as underlined by the present study, simultaneous change of multiple parameters (e.g. shot diameter and shot velocity) may produce the same Almen intensity and may thus remain unnoticed. It is thus of paramount important to control within certain limits the key process parameters using other means. In particular, tight control of shot diameter should be used. Furthermore, as each combination of shot diameter and shot velocity yields a unique residual stress profile, shot peening for fatigue life enhancement should not be solely specified by Almen intensity, but also by shot diameter. Care must be taken when substituting peening parameters while keeping the Almen intensity constant, as it may change the residual stress profile and may influence the fatigue life expectancy of the peened component.

CHAPITRE 8 DISCUSSIONS

This chapter discusses the results of this study. As an overview, this study produced a number of findings in relation to the objectives listed in Chapter 2. However, as some findings appeared to be related to more than one research objectives, it was decided to discuss the key findings firstly and then discuss them in relation to the research objectives.

8.1 Discussion of key findings

8.1.1 Finding 1: Saturation curve (relationship between resulting arc height and number of shots) was established numerically and experimentally.

Almen intensity is one of the most important control parameters to ensure the repeatability of the shot peening process. It is defined by a saturation curve, a relationship between peening time versus resulting arc height. Almen intensity is conventionally used industrial shot peening applications. In this study, a numerically established saturation curve was firstly presented using the newly developed FE model. In addition, an experimental study of the saturation curve based on the target peening material (aluminum) was carried out in order to relate their relationship to surface coverage and roughness on the same materials.

8.1.2 Finding 2: Surface coverage curve (relationship between surface indentation ratio and number of shots) was established numerically and experimentally.

Surface coverage is another important control parameter in the shot peening process. Most of the studies of surface coverage are based on visual inspection and theoretical models. In the theoretical model, the shot flow is assumed to impact the component's surface at a constant rate and to create circular indents of constant size. In this study, a numerically established surface coverage curve was firstly presented using the newly developed FE model. Then, in the shot peening experiments, imageJava software was used to evaluate surface coverage form surfaces topography images obtained from profiler measurements. This experimentally calculated surface coverage curve was compared with the curve obtained from the Avrami theoretical model.

8.1.3 Finding 3: Surface roughness curve (relationship between surface roughness and number of shots) was established numerically and experimentally.

One detrimental effect of shot peening is to increase surface roughness, which acts as stress concentrations, induces crack initiation and causes a reduction of the fatigue life of the treated component. In this study, a numerically established surface roughness curve (relationship between surface PV roughness and number of shots) was firstly presented using the newly developed FE model. In the experiments, the relationship between surface roughness (Ra roughness and stress concentration factor Kt) and number of shots were presented and best-fitted by equations.

8.1.4 Finding 4: Residuals stress profile after shot peening, conventional peen forming and stress peen forming have been simulated, measured and compared.

Producing compressive residual stresses is the main purpose of shot peening. Figure 1.2 shows the main terms for the description of the residual stress produced by shot peening. In this study, with the developed 3D FE model, it was possible to study the influence of the shot peening parameters on the resulting residual stresses such as: shot size, velocity, density, peening angle, peening time, etc. Residual stresses profile after conventional peen forming and stress peen forming have been measured by X-ray diffraction method and compared to the simulated results.

8.1.5 Finding 5: Experimental and numerical study of the stress peen forming process

A prebending device has been designed to study stress peen forming process. With this device, four prebending moments were applied to the strip in order to study their influence on forming results. Then, a three steps numerical model was developed to simulate this experimental stress peen forming process. With this numerical model, it was possible to predict the deformed shape of the strip after conventional peen forming and stress peen forming. The relationships between the prebending moment and the resulting arc height have been numerically predicted and compared to the experimentally measured values. In addition, the simulated residual stresses

profiles after conventional peen forming and stress peen forming have been calculated and compared with the experimentally measured values.

8.1.6 Finding 6: An analytical model was developed to predict Almen intensity.

An analytical model based on Hertz contact theory was developed using MATLAB to predict Almen intensity and residual stresses profile in an Almen strip. With this model, the principle and the induced stress distribution in the strip during impingement and rebound of shots as well as after release of the boundary conditions of Almen strip were introduced in details. This model was validated to be an effective tool for the prediction of Almen intensity under different shot peening parameters such as shot size, type, velocity and peening angle, etc.

8.2 Discussion of findings in relationship to four articles

As outlined above, a number of key findings associated with this study were discussed. These key findings were presented in this manner because they tended to cut across more than one research question. The purpose of the following section is to discuss these findings in relation to the research objectives as presented in Chapter 3 posed in this thesis.

8.2.1 Discussion of findings in relationship to the first article: On the potential applications of a 3D random finite element model for the simulation of shot peening

In the first article, a novel 3D FE model was developed to simulate random aspect of the shot peening process. With the new model, the quantitative relationship of peening intensity, coverage and roughness with respect to the number of shots have been presented. In addition, residual stresses profile after normal impact and oblique impact have been calculated and compared. Therefore, this first article presents the above listed findings 1 to 4.

8.2.2 Discussion of findings in relationship to the second article: Experimental study of shot peening and stress peen forming

In the second article, quantitative relationships between the saturation, coverage, roughness with respect to peening time have been established on aluminum 2024 test strips. Residual stress profiles after different peening velocities and peening times have been measured by X-ray diffraction method. In the second part of this article, a prebending device with four different prebending radii of curvatures have been designed to perform stress peen forming study. With this device, the quantitative relationships between the prebending moment and the resulting arc height of narrow strips and square strips have been experimentally investigated. In addition, residual stresses profiles after conventional peen forming and stress peen forming have been measured and compared. Therefore, this second article is related to the findings 1 to 5.

8.2.3 Discussion of findings in relationship to the third article: A numerical study of the stress peen forming process

In the third article, a three steps numerical model was established to simulate the stress peen forming process. The second of this three steps numerical model was based on the FE model introduced in the first article. With this model, the relationships between the prebending moments and resulting arc heights as well as residual stresses have been simulated and compared to the experimental measured values. Therefore, this third article presents the above listed findings 4 and 5.

8.2.4 Discussion of findings in relationship to the fourth article: An analytical approach to relate shot peening parameters to Almen intensity

In order to understand the theory of shot peening and to predict Almen intensity with the least calculation resource, the fourth article describes an analytical model for the prediction of Almen intensity considering shot peening parameters such as, shot type (steel and ceramic), size, velocity and peening angle. This model can be used as a tool for determining the various possible combinations of peening parameters combination to obtain given Almen intensity. This article presents the above listed finding 6.

CONCLUSIONS

This thesis focused on the study of the shot peening and stress peen forming processes with numerical, experimental and analytical methods. A 3D FE model was developed firstly in order to simulate the dynamic shot peening process. With this FE model, the shot peening intensity and surface coverage were numerically simulated and the relationship between them and the peening time (number of shots) was quantitatively expressed. Based on this novel 3D random FE model of shot peening, a three-step Implicit-Explicit-Implicit FE model for simulating stress peen forming was established in order to predict the forming results under different prebending conditions. In order to validate the novel FE model, shot peening and stress peen forming experiments were carried out to study of the intensity, coverage and forming results under different prebending conditions. Finally, an analytical model for calculation of Almen intensity and residual stress was constructed in order to further understand the theory of shot peening and to predict the peening results under different peening parameters.

Overall, the results of this study produced a number of interesting findings that contribute to a better understanding of the shot peening and the stress peen forming process. The contributions associated with this study are of particular importance as

Significance and contribution of the research

This research makes four main contributions that could potentially be used for the optimization of the shot peening and stress peen forming processes, namely

1) The 3D random FE model for simulation of shot peening.
2) The quantitative relationship between prebending and forming results with experiments.
3) FE model for simulation of the stress peen forming process.
4) Analytical model for the prediction of Almen intensity.

We summarize these contributions individually in the following subsections.

***Objective 1*:** A novel 3D FE model with multiple randomly distributed shots was developed to simulate the shot peening process. It is the first FE model that takes account the random nature of the shot peening process, such as the shot peening sequence and the impact location. This model

demonstrates a computing strategy to understand most of the important shot peening parameters, such as saturation curve, peening intensity, surface coverage and roughness. Using this model, the relationship between shot peening intensity, surface coverage and surface roughness with respect to number of peening shots was established quantitatively.

***Objective 2*:** A pre-stressing device with four different prebending radii of curvatures which correspond to four different prebending moments was designed in order to study the stress peen forming process. The relationship between the prebending moment and the forming results (radius of curvature and the arc height) were obtained for three different shot velocities. A quantitative relationship between them was established in order to optimize the stress peen forming process.

***Objective 3*:** A three steps Implicit-Explicit-Implicit FE model was established, in order to simulate the stress peen forming process. Firstly, an implicit FEA with ANSYS was performed, with a prebending moment along the spanwise direction of the component, to obtain the initial stress distribution inside the component. Then, an explicit FEA with LS-DYNA simulating shot impact on the pre-stressed component was conducted in order to obtain the resulting stresses inside the component. Finally, another implicit FEA with ANSYS was carried out to calculate the resulting arc height and radius of curvature of the strip. With this FE model, the relationship between prebending moment and resulting arc height was obtained and compared with the experimental results. The numerical results showed good consistency with the experimental results.

***Objective 4*:** An analytical model based on Hertz contact theory was developed to predict Almen intensity and residual stress, that takes into account several shot peening parameters, such as shot size, shot velocity, peening angle, etc. This model incorporates the existing analytical model for prediction of the induced stress in a semi-infinite target component, as well as the method to calculate the deformed arc height and residual stresses from the induced stress in the semi-infinite target component. With this model, the mechanical principle of the shot peening process was explained in detail. In addition, we can predict the Almen intensity and residual stress with minimal calculation time.

Limitation and suggestion for future study

Several interesting research questions are left for future research. For the newly developed 3D random FE model for shot peening process, there exists several assumptions which should be restudied in order to improve the model. Firstly, for the randomly distributed shots, the distance between each shot was assumed to have little influence on the results. Therefore, a further study should be performed with different shot distances in order to confirm this assumption. Secondly, the assumed representative area for the study, such as the shot distribution area, as well as the representative volume for calculation of the average induced stress profiles, should both be further studied. Thirdly, the saturation curve, coverage curve and roughness curve from the numerical simulation should be compared with the experimental results, using the same shot peening parameters. Therefore, more calculations that use the same shot peening parameters and target material properties, to determine which should be used in experiments, should be carried out in order to compare the saturation curve, coverage curve and roughness curve with experimental data.

In the case of the FE model for the simulation of stress peen forming, the induced average stress profiles calculated from a representative volume of the component was assumed to be uniformly distributed in the whole target component in order to calculate the deformation of the whole strip. However, in actual peen forming, the induced stress in the previous peened component has a certain influence on the unpeened component, and the effect should not be ignored. In addition, some experimental results show that peening multiple passes with a fast robot travelling velocity and peening one pass with a low robot travelling velocity produce different forming results for a target with large dimension. Therefore, further studies of these issues could be performed in order to improve the FE model.

In the analytical model for the prediction of Almen intensity, there exist several assumptions which require further validation such as the value of the efficiency coefficient $k = 0.8$, which represented the elastic and thermal dissipation during impact as well as an efficiency factor α, which was defined as the ratio of the radius of maximum plastic indentation to the radius of the maximum elastic contact radius. In addition, in this model, only one impact has been considered and the induced stress profile beneath one impact has been assumed to be uniformly distributed

in the whole plate to predict residual stress profile. Further study would be carried out considering the influence of the sounding impacts on the predicted results.

Compressive residual stresses produced by shot peening have beneficial effect for the improvement of the fatigue life of the peened components. However, surface roughness produced by shot peening has detrimental effect on the peened components. Both numerical study and experimental study in this thesis have provided these two results under different shot peeing conditions. Therefore, future study on the fatigue prediction could be performed considering the residual stress profile and surface roughness in order to obtain the influence of the shot peening parameters on the fatigue improvement abilities.

The stress peen forming process carried out in this thesis was a very rudimentary study and provided only results on the small size components with simple shapes such as rectangle or square strips. Further study would be focused on the components with larger size, more complicated shape or component with ribs, which are more close to the real wing skins. In addition, more practical study of the stress peen forming could be focused on the establishment of a tool to predict the shot peening parameters according to the designed the geometric shape.

REFERENCES

Al-Hassani, S.T.S., 1981. Mechanical aspects of residual stress development in shot peening. *Proceedings of the 1th International Conference on Shot Peening*, pp. 583–602.

Al-Hassani, S.T.S., 1982. The shot peening of metals – mechanics and structures, Aerospace congress - *SAE Technical Paper*, SAE-821452, 13p.

Al-Hassani, S.T.S., 1984. An engineering approach to shot peening mechanics, *Proceedings of the 2nd International Conference on Shot Peening*, pp. 275–282.

Al-Hassani, S.T.S., Kormi, K., and Webb, D.C., 1999. Numerical simulation of multiple shot impact. *Proceedings of the 7th International Conference on Shot Peening*, pp. 217–227.

Almen, J. and Black, J.P.H., 1963. Residual stresses and fatigue in metals. Mcgraw-hill, Toronto, pp. 64–69.

Al-Obaid, Y.F., 1990a. A rudimentary analysis of improving fatigue life of metals by shot-peening. *Journal of Applied Mechanics*, 57pp. 307–312.

Al-Obaid, Y.F., 1990b. Three-dimensional dynamic finite element analysis for shot-peening mechanics. *Computers and structures*, 36(4), pp.681–689.

Al-Obaid, Y.F., 1995. Shot peening mechanics: experimental and theoretical analysis. *Mechanics of Materials*, 19, pp. 251–260.

Balcar, C. and Maltby, F., 1981. Basic curves of surface finish after glass bead peening. *Proceedings of the 1st International Conference on Shot Peening*, pp. 295–301.

Baragetti, S., 2001. Three-dimensional finite element procedures for shot peening residual stress field prediction. *International Journal of Computer Applications in Technology*, 14(1/2/3), pp. 51–63.

Barrett, C.F. and Todd, R., 1984. Investigation of the Effects of Elastic Pre-Stressing Technique on Magnitude of Compressive Residual Stress Induced by Shot Peen Forming of Thick Aluminum Plates. *Proceedings of the 2nd International Conference on Shot Peening*, pp.15-21.

Baughman, D.L., 1984. An Overview of Peen Forming Technology. *Proceedings of the 2nd International Conference on Shot Peening*, pp. 28-33

Bernard, M., Bui-Quoc, T., Julien, D., and April, S., 2004. Literature survey on shot peening process characterization. pp. 2.1–2.90.

Bignonnet, A., Picouet, L., and Lieurade, H.P. 1987. The application of shot peening to improve the fatigue life of welded steel structures. *Proceedings of the 3rd Conference on Steel in Marine Structures*, pp. 669–678.

Cammett, J. 2007. Shot peening coverage - the real deal. *The Shot Peener*, 21(3), 8–14.

Cao, W., Fathallah, R. and Castex, L., 1995. Correlation of Almen arc height with residual stresses in shot peening process. *Materials Science and Technology*, 11(9), pp. 967-973.

Champaigne, J., 2001. The little book on shot peening. On line, http://www.shotpeener.com/learning/tlb.pdf.

Clausen, R., and Stangenberg, J., 1999. Roughness of shot-peened surfaces - definition and measurement. *Proceedings of the 7th International Conference on Shot Peening*, pp. 69–77.

Curtis, S., de los Rios, E.R., Rodopoulos, C.A. and Levers, A., 2003. Analysis of the effects of controlled shot peening on fatigue damage of high strength aluminum alloys. *International Journal of Fatigue*, 25, pp. 59-66.

Davies, R.M., 1949. The determination of static and dynamic yield stresses using a steel ball. *Proceedings of the Royal Society of London A*, 197(1050), pp. 416-432.

Deslaef, D., Rouhaud, E., and Rasouli-Yazdi, S., 2000. 3D finite element models of shot peening processes. *Materials Science Forum*, pp. 347–349.

Ebenau, A., Vöhhringer, O., and Macherauch, E., 1987. Influence of the shot peening angle on the condition of near surface layers in materials. *Proceedings of the 3rd international conference on shot peening*, pp. 253–260.

Edberg, J., Lindgren, L., and Mori, K., 1995. Shot peening simulated by two different finite element formulations. *Simulations of Materials Processing: Theory, Methods and Applications*, ISBN 90 54 10 5534, 425–430.

Fathallah, R., 1994. Modélisation du procédé de grenaillage: incidence des billes et taux de recouvrement. Ph.D. thesis, ENSAM. Aix en Province, France.

Fathallah, R., Inglebert, G. and Castex, L., 1998. Prediction of plastic deformation and residual stresses, *Materials Science and Technology*, 14(7), pp. 631-639.

Flavenot, J.F., Niku-Lari, A., 1977. La mesure des contraintes résiduelles, méthode de la flèche, méthode de la source de contraintes, *Les Mémoires Techniques du CETIM*, 31.

Gardiner, D.S. and Platts, M.J., 1999. Towards Peen Forming Process Optimisation, *Proceedings of the 7th International Conference on Shot Peening*, pp. 235-243.

Gentil, B., Desvignes, M., and Castex, L., 1987. Analyse des surfaces grenaillees: fissuration, rugosite et contraintes residuelles. *Materiaux et technique*, 75(12), pp. 493–497.

Guagliano, M., Vergani, L., Bandini, M., and Gili, F., 1999. An approach to relate the shot peening parameters to the induced residual stresses. *Proceedings of the 7th International Conference on Shot Peening*, pp.274-282.

Guagliano, M., 2001. Relating almen intensity to residual stresses induced by shot peening: a numerical approach. *Journal of Materials Processing Technology*, 110, pp. 277–286.

Guechichi, H., 1986. Prévision des contraintes résiduelles dues au grenaillage de précontrainte, *PhD thesis, ENSAM*.

Han, K., Owen, D.R.J., and Perić, D., 2002. Combined finite/discrete element and explicit/implicit simulations of peen forming process. *Engineering Computations*, 19(1-2), pp. 92–118.

Herzog, R., Zinn, W., Scholtes, B., and Wohlfarth, H., 1996. The significance of Almen intensity for the generation of shot peening residual stresses. *Proceedings of the 6th International Conference on Shot Peening*, pp. 270–281.

Hong, T., Ooi, J.Y., and Shaw, B.A., 2008a. A numerical study of the residual stress pattern from single shot impacting on a metallic component. *Advances in Engineering Software*, 39, pp. 743–756.

Hong, T., Ooi, J.Y., and Shaw, B., 2008b. A numerical simulation to relate the shot peening parameters to the induced residual stresses, *Engineering Failure Analysis*, 15, pp. 1097–1110.

Iida, K., 1984. Dent and affected layer produced by shot peening, *Proceedings of the 2nd International Conference on Shot Peening*, pp. 283-292.

Ilyushin, A.A., 1948. Plasticity [in Russian], *Gostekhizdat*, Moscow, Chapter 2.

Johnson, K.L., 1985. Contact mechanics, *Cambridge University Press,* Cambridge, UK.

Johnson, W., 1972. Impact strength of materials, *Edward Arnold*, London, UK

Karuppanan, S., Romero, J. S., de los Rios, E. R., Rodopoulos, C., and Levers, A., 2002. A theoretical and experimental investigation into the development of coverage in shot peening. *Proceedings of the 8th International Conference on Shot Peening*, pp. 101–107.

Khabou, M. T., Castex, L. and Inglebert, G., 1989. The effect of material behavior law on the theoretical shot peening results, *European Journal of Mechanics -A/Solids*, 9(6), pp. 537-549.

Kirk, D., 1999. Shot peening. *Aircraft Engineering and Aerospace Technology*, 71(4), pp. 349–361.

Kirk, D., 2002. Coverage: development, measurement, control and significance. *The Shot Peener*, 16(4), pp. 33–36.

Kirk, D., 2005. Theoretical principles of shot peening coverage. *The Shot Peener*, 19(2), pp. 24–26.

Kirk, D., and Abyaneh, M. Y., 1993. Theoretical basis of shot peening coverage control. *Proceedings of the 5th International Conference on Shot Peening*, pp. 183–190.

Knotek, O., and Elsing, R., 1987. Computer simulation of different surface topographies of metals produced by blasting processes. *Proceedings of the 3rd International Conference on Shot Peening*, pp. 361–368.

Kobayashi, M., Matsui, T., and Murakami, Y., 1998. Mechanics of creation of compressive residual stress by shot peening. *International Journal of Fatigue*, 20(5), pp. 351–357.

Kopp, R., and Ball, H.W., 1987. Recent developments in shot peen forming. *Proceedings of the 3th International Conference on Shot Peening*, pp. 297–308.

Kyriacou, S., 1996. Shot-peennng mechanics, a theoretical study. *Proceedings of the 6th International Conference on Shot Peening*, pp. 505–516.

Levers, A. and Prior, A., 1995. Finite element simulation of shot peening. *The Shot Peener*, 9(3), pp. 14–16.

Li, J. K., Yao, M., Wang D., and Wang R. Z., 1991. Mechanical approach to the residual stress field induced by shot peening, *Materials Science and Engineering A*, 147, pp. 167-173.

Li, Kuohsiang., 1981. Using stress peen-forming process for integrally stiffened wing panels. *Proceedings of the 1th International Conference on Shot Peening*, pp. 555–563.

Lu, J., 1996. Handbook of measurement of residual stresses, *The Fairmont Press, Inc.*, Lilburn, GA, USA.

Majzoobi, G.H., Azizi, R., and Alavi Nia, A., 2005. A three-dimensional simulation of shot peening process using multiple shot impacts. *Journal of Materials Processing Technology*, 164–165, pp. 1226–1234.

Meguid, S.A., 1975. Mechanics of shot peening. *Ph.D. thesis*, UMIST. UK.

Meguid, S.A., Shagal, G., and Stranart, J.C., 1999a. Finite element modeling of shot peening residual stresses. *Journal of Materials processing Technology*, 92–93, pp. 401–404.

Meguid, S.A., Shagal, G., Stranart, J.C., and Daly, J., 1999b. Three-dimensional dynamic finite element analysis of shot-peening induced residual stresses. *Finite Elements in Analysis and Design*, 31, pp. 179–191.

Meguid, S.A., Shagal, G. and Stranart, J.C., 2002. 3D FE analysis of peening of strain-rate sensitive materials using multiple impingement model, *International Journal of Impact Engineering*, 27, pp.119-134.

Meguid, S.A., Shagal, G., Stranart, J.C., Liew, K.M., and Ong, L.S., 2005. Relaxation of peening residual stresses due to cyclic thermo-mechanical overload. *Transactions of the ASME - journal of engineering Materials and Technology*, 127, pp. 170–178.

Meo, M., and Vignjevic, R., 2003. Finite element analysis of residual stress induced by shot peening process. *Advances in Engineering Software*, 34, pp. 569–575.

Miao, H.Y., Larose, S., Perron, C. and Lévesque, Martin, 2009. On the potential applications of a 3D random finite element model for the simulation of shot peening, *Advances in Engineering Software*, 40, pp. 1023-1038.

Mori, K., Osakada, K., and Matsuoka, N., 1994. Finite element analysis of peening process with plastically deforming shot. *Journal of Materials Processing Technology*, 45(1), pp. 607–612.

Rodopoulos, C.A., Kermanidis, A.Th., Statnikov, E., Vityazev, V. and Korolkov, O., 2007. The effect of surface engineering treatment on the fatigue behavior of 2024-T351 aluminum alloy, Journal of material engineering and performance, 1(1), pp.30-34.

Rodopoulos, C.A., Curtis, S.A., de los Rios, E.R., and Solisromero, J., 2004. Optimisation of the fatigue resistance of 2024-T351 aluminum alloys by controlled shot peening–methodology, results and analysis. *International Journal of Fatigue*, 26, pp. 849–856.

Rouhaud, E., and Deslaef, D., 2002. Influence of shots' material on shot peening, a finite element model. *Materials Science Forum*, 404-407, pp. 153–158.

Rouhaud, E., Ouakka, A., Ould, C., Chaboche, J.L., and François, M., 2005. Finite element model of shot peening, effects of constitutive laws of the material. *Proceedings of the 9th International Conference on Shot Peening*, pp. 107–112.

SAE Surface Enhancement Division, 2009. SAE Standard J2277 - Shot Peening Coverage Determination.

SAE Ams B Finishes Processes And Fluids Committee, 2009. SAE Standard AMS 2430 - Shot Peening, Automatic.

SAE Surface Enhancement Division, 2008. SAE Standard J442 - Test Strip, Holder, and Gage for Shot Peening.

SAE Surface Enhancement Division, 2003. SAE Standard J443 - Procedures for Using Standard Shot Peening Test Strip.

SAE Ams B Finishes Processes And Fluids Committee, 2009. SAE Standard AMS 2430 – Shot Peening, Automatic.

Schiffner, K., and Droste gen. Helling, C., 1999. Simulation of residual stresses by shot peening. *Computers and Structures*, 72, pp. 329–340.

Schwarzer, J., Schulze, V., and Vöhringer, O., 2002. Finite element simulation of shot peening - a method to evaluate the influence of peening parameters on surface characteristics. *Proceedings of the 8th International Conference on Shot Peening*, pp. 507–515.

Schwarzer, J., Schulze, V., and Vöhringer, O., 2003. Evaluation of the influence of shot parameters on residual stress profiles using element simulation. *Materials Science Forum*, 426-432, pp. 3951–3956.

Sharp, P.K., Clayton, J.Q., Clark, G., 1994. The fatigue resistance of peened 7050-T7451 aluminum alloy-repair and re-treatment of a component surface, *Fatigue and Fracture of Engineering Materials and Structures*, 17(3), pp. 243–252

Shen, S., Han, Z. D., Herrera, C. A. and Atluri, S. N., 2004. Assessment, development, and validation of computational fracture mechanics methodologies and tools for shot-peened materials used in rotorcraft principal structural elements, *Final Report-U.S. Department of Transportation: Federal Aviation Administration*, FAA Report No. DOT/FAA/AR-03/76.

Slim, S., 1995, Identification des paramètres d'une loi de comportement élastoplastique pour le grenaillage et application à l'étude des liens entre l'évolution cyclique du matériau et le taux de recouvrement, *thèse de doctorat*, *ENSAM*, Aix en Provence, France.

Tabor, D., 1951. The hardness of metals, Clarendon Press, Oxford, UK.

Tatton, R.J.D., 1987. Shot peen forming-An economical solution. *Proceedings of the 3rd International Conference on Shot Peening*, pp. 309–318.

Torres, M. and Voorwald, H., 2002. An evaluation of shot peening, residual stress and stress relaxation on the fatigue life of AISI 4340 steel. *International Journal of Fatigue*, 24, pp. 877–886.

Vanluchene, R.D., Johnson, J., and Carpenter, R.G., 1995. Induced stress relationships for wing skin forming by shot peening. *Journal of Material Engineering and Performance*, 4(3), pp. 283–290.

Vanluchene, R.D., and Cramer, E. J., 1996. Numerical model of a wing skin peen forming process. *Journal of Material Engineering and Performance*, 5(6), pp. 753–760.

Wang, S., Li, Y., Yao. M. and Wang, R., 1998. Compressive residual stress introduced by shot peening. *Journal of Material Processing Technology*, 73, pp. 64-73

Webster, G.A. and Ezeilo, A.N., 2001. Residual stress distributions and their influence on fatigue lifetimes. *International Journal of Fatigue*, 23, S775–S383.

Wick, A., Holzapfel, H., Schulze, V., and Vöhringer, O., 1999, Effect of shot peening parameters on the surface characteristics of differently heat treated AISI 4140, *Proceedings of the 2nd International Conference on Shot Peening*, pp. 42-53.

Wohlfahrt, H., 1984. The influence of peening conditions on the resulting distribution of residual stress. *Proceedings of the 2nd International Conference on Shot Peening*, pp. 316–331.

Zarka, J. and Casier, J., 1979. Elastic-plastic response of structure to cyclic loading: practical rules, In Nemat Nasser, S. (ed.), Mechanics Today, Pergamon Press, Oxford, pp. 93-198.

Zarka, J. and Inglebert, G., 1985. Simplified analysis of inelastic structures, In *Simplified Analysis of Inelastic Structures Subjected to Statical or Dynamical Loadings*, CISM Seminar, October 7-10.